Extension of the Application Potential of Wheeled Mobile Driving Simulators to Uneven Grounds

Vom Fachbereich Maschinenbau an der
Technischen Universität Darmstadt
zur Erlangung des Grades eines
Doktor-Ingenieurs (Dr.-Ing.)
genehmigte

Dissertation

vorgelegt von

Chris Alexander Zöller, M.Sc.
aus Aachen

Berichterstatter:	Prof. Dr. rer. nat. Hermann Winner
Mitberichterstatter:	Prof. Dr.-Ing. Günther Prokop
Tag der Einreichung:	20.05.2019
Tag der mündlichen Prüfung:	17.09.2019

Darmstadt 2019
D 17

Vorwort

Die vorliegende Arbeit entstand während meiner Tätigkeit als wissenschaftlicher Mitarbeiter am Fachgebiet Fahrzeugtechnik (FZD) der Technischen Universität Darmstadt. Die Arbeit war Teil des von der Deutschen Forschungsgemeinschaft geförderten Projekts „Potentialanalyse einer selbstfahrenden Bewegungsplattform für Fahrsimulatoren“ mit dem Geschäftszeichen WI 3153/8-1. Ich danke der Deutschen Forschungsgemeinschaft für die finanzielle Unterstützung, ohne die diese Arbeit nicht möglich gewesen wäre.

Einen besonderen Dank möchte ich meinem Doktorvater Herrn Prof. Dr. rer. nat. Hermann Winner aussprechen. Das große Interesse und die Zeit, die in die Betreuung der Arbeit geflossen sind, sind nicht selbstverständlich. Der wertvolle Austausch in Rücksprachen und der hohe Anspruch hat nicht nur maßgeblich zum Gelingen dieser Arbeit beigetragen, sondern auch eine enorme fachliche und menschliche Entwicklung herbeigeführt.

Herrn Prof. Dr.-Ing. Günther Prokop vom Institut für Automobiltechnik der Technischen Universität Dresden danke ich herzlich für die Übernahme des Korreferats.

Danken möchte ich auch allen aktuellen und ehemaligen Mitarbeitern von FZD. Das angenehme Arbeitsklima, die wertvollen fachlichen Diskussionen sowie der Zusammenhalt und die Hilfsbereitschaft werden mir stets positiv in Erinnerung bleiben. Ich hoffe, dass die Freundschaften, die hier geknüpft wurden, noch lange erhalten bleiben und das Fachgebiet sich auch in Zukunft diese Eigenschaften erhält.

Neben den wissenschaftlichen Mitarbeitern möchte ich auch den dem Sekretariat und der Administration danken, die ein ums andere Mal auch spontan ein offenes Ohr für meine Fragen hatten. Auch der Werkstatt und insbesondere Robert Korndörfer gebührt großer Dank für Übernahme der manchmal recht kurzfristigen Reparatur- und Fertigungsaufträge.

Ein großer Dank gilt auch allen Studenten, mit denen ich im Verlauf meiner Zeit am Fachgebiet zusammenarbeiten durfte. Dies gilt insbesondere für Torben Albrecht, dessen unermüdlicher Drang nach Verbesserung des Simulators wesentlich zum Gelingen der Arbeit beigetragen hat.

Meiner Familie danke ich für die Unterstützung, die mir auch in schwierigen Phasen immer halt gegeben hat. Die durch euch geförderte Eigenverantwortung war ein wesentlicher Bestandteil für die Fertigstellung dieser Arbeit.

Besonders danken möchte ich meiner Frau Manuela, die mich in dieser anspruchsvollen Phase über alle Maßen entlastet hat, um mir den Freiraum für diese Arbeit zu geben. Deine liebevolle Unterstützung hat mir immer wieder die Kraft gegeben, diese Herausforderung zu bewältigen.

Chris Zöller Darmstadt, Mai 2019

List of Contents

Abbreviations

Abbreviation	Description
ADMA	Automotive Dynamic Motion Analyzer
CLC	Closed-Loop Control Architecture
CLTF	Closed Loop Transfer Function
CG	Centre of Gravity
DB	Disturbance Behavior
DMC	Direction-Dependent Motion Control
DoF	Degree of Freedom
DS	Driving Simulator
DSPMS	Driving Surface Profile Measurement System
EMC	Equal-Distribution Motion Control
FMC	Friction-Optimized Motion Control
HBP	Hexapod Bottom Plate
HTP	Hexapod Top Plate
ICR	Instantaneous Center of Rotation
IMU	Inertial Measurement Unit
JND	Just Noticeable Difference
MC	Motion Control
MRB	Manipulating Reaction Behavior
OLC	Open-Loop Control Architecture
OLTF	Open-Loop Transfer Function
PSD	Power Spectral Density
PT	Pneumatic Tire
ST	Solid Tire
TVV	Total Vibration Value
WMDS	Wheeled Mobile Driving Simulator

Symbols and Indices

Symbol	Unit	Description
a	m/s²	Acceleration
c	N/m	Spring Stiffness
$\boldsymbol{C}$	-	Stiffness Matrix
d	Ns/m	Damper Constant
D	-	Damping Ratio
$\boldsymbol{D}$	-	Damping Matrix
$\boldsymbol{E}$	-	Excitation Transfer Matrix
f	Hz	Frequency
F	N	Force
g	m/s²	Gravitational Acceleration
G	Differing	Transfer Function
h	m	Height
i	-	Index Variable
I	A	Current
J	kgm²	Moment of Inertia
k	Differing	Constant
K	-	Controller Transfer Function
ℓ	m	Length
L	Henry	Electric Inductance
m	kg	Mass
M	Nm	Moment, Torque
$\boldsymbol{M}$	-	Mass Matrix
p	-	Thread lead
q	-	Dimensionless Pacejka Parameter
r	m	Radius
$\vec{r}$	m	Position Vector
R	Ohm	Electric Resistance
s	1/s	Laplace Variable
t	s	Time
T	s	Time Constant
U	V	Voltage
V	-	Gain Factor
v	m/s	Velocity
w	m	Deflection, Stroke, Distance
x	m	Distance in x-Direction
y	m	Distance in y-Direction
z	m	Distance in z-Direction

Symbol	Unit	Description
α	°	Slip Angle
$\vec{\alpha}$	°	Angular Position Vector
γ	-	Factor for Combining Acceleration DoFs to Total Vibration Value
δ	°	Steering Angle
ε	°	Support Angle of Suspension
ζ	-	Time Constant Increase Factor
η	-	Efficiency Factor
ϑ	°	Pitch Angle
θ	°	Angle for Transformation in Polar Coordinates
κ	-	Weber Ratio
μ	-	Friction Coefficient
ξ	°	Force/Acceleration Direction Relative to Simulator Coordinate System
ρ	m	Depth Gauge
ϱ	-	Relative Attenuation between two Values
τ	s	Time window length/Time integration variable
φ	°	Roll Angle
ϕ	-	Control Function
Φ	Differing	Power Spectral Density
ψ	°	Yaw Angle
Ψ	Differing	Autocorrelation Function
ω	rad/s	Angular Frequency/Velocity
Ω	rad/m	Angular Spatial Frequency

Index	Description
0	Initial Value/Natural frequency
2D	Two-Dimensional
4m	Depth Gauge over a Length of 4 m
A	Actuator
a	Acceleration
act	Acting Value
aFix	For a Fixed Acceleration
An	Analytic Signal
B	Body, Sprung Mass of the WMDS with Suspension
c	Spring
CG	Center of Gravity
CLC	Closed-Loop Control
controlled	Controlled
Conv	Power Converter
CR	Command Response Transfer Function
Cut	Signal with Cutted Frequencies
d	Damper
DB	Disturbance Behavior
dem	Demanded
Dist	Disturbance Transfer Function
DMC	Direction-dependent Motion Control
DSE	Driving Surface Excitation
DT	Dead Time
dyn	Dynamic
EMC	Equally-distributed Motion Control
Env	Envelope of Signal
f	Front Wheel (In x-Direction of Simulator-Fixed Coordinate System)
FB	Feedback
FFC	Feed-Forward Control
FixMC	Fixed Dimensioning Value of the Motion Control
FMC	Friction-optimized Motion Control
FW	Frequency-Weighed
Fz	Wheel Load Variations
h	High
H	Horizontal
Hex	Hexapod
Hil	Hilbert-Transform
Ho	Horizontal
HBP	Hexapod Bottom Plate
HTP	Hexapod Top Plate

Index	Description
CG	Center of Gravity
i	Index Variable
I	Current
ICR	Instantaneous Center of Rotation
in	Input value
ind	Induced
Inst	Instantaneous
JND	Just Noticeable Difference
kin	Kinematic
l	Low
lim	Limiting Value
lin	Linear Approximation
Load	Load
max	Maximum
min	Minimum
MP	Motion Platform
MRB	Manipulating Reaction Behavior
OLC	Open-Loop Control
OLTF	Open-Loop Transfer Function
opt	Optimum
Parc	Parchilowskij Parameter
PE	Power Electronics
PF	Pre-Filter
PI	PI Controller
Pos	Position/Position Control Loop
PrF	Projected into Direction of Force
PT	Perception Threshold
r	Polar Coordinates
red	Reduced
ref	Reference
rel	Relative
res	Resultant
rms	Root Mean Square
rrms	Running Root Mean Square
rl	Rear Left Wheel (In x-Direction of Simulator-Fixed Coordinate System)
rr	Rear Right Wheel (In x-Direction of Simulator-Fixed Coordinate System)
rt	Transformation of Rotation to Translation
S	Suspension
Sen	Sensor
set	Set Value

Index	Description
simple	Simplified
Sp	Screw Spindle
stat	Static State
sub	Subject
sum	Summed
Sup	Support Force from Suspension Linkages
t	Triangular Frame of Simulator
T	Tire
TCP	Tire Contact Point
tot	Total
tr	Transformation of Translation to Rotation
TS	Tire-Sprung Mass of the WMDS
TVV	Total Vibration Value
TZ	Transition Zone
U	Voltage
uncon-trolled	Uncontrolled
Vis	Viscous Damping
W	Wheel
Weber	Weber Coefficient
WMDS	Wheeled Mobile Driving Simulator
WO	Washout
x	in x-Direction
y	in y-Direction
yaw	Yaw Fraction of Motion Control Demand
α	Cornering Stiffness
ϑ	in Pitch-Direction
φ	in Roll-Direction
ω	Angular Velocity

Figures and Tables

Kurzzusammenfassung

Fahrsimulatoren stellen bereits heute einen wichtigen Bestandteil der Fahrzeugentwicklung dar, da insbesondere die Auslegung von Fahrerassistenzsystemen die Untersuchung der Fahrer-Fahrzeug-Interaktion erfordert. Zukünftig ist im Hinblick auf das automatisierte Fahren ein noch größeres Anwendungspotential zu erwarten, da bspw. Übergabestrategien in einer sicheren Umgebung untersucht werden können. Heutige Fahrsimulatorkonzepte haben jedoch eine Grenze hinsichtlich der erreichbaren Güte der Bewegungssimulation erreicht. Speziell urbane Fahrszenarien erfordern einen Bewegungsraum, der mit den bei High-End-Systemen verwendeten Schlittensystemen nicht mehr wirtschaftlich darstellbar ist.

Einen Ausweg aus dieser Limitierung stellen selbstfahrende Fahrsimulatoren dar, die die geforderten Beschleunigungen durch Reifenkräfte erzeugen. Dadurch ist eine Verwendung auf verschiedenen Fahrflächen möglich, wodurch sich der Bewegungsraum flexibel an die Anforderungen des zu simulierenden Szenarios anpassen lässt. Aufgrund des Reifen-Fahrbahn-Kontakts dieses Simulatorkonzepts werden durch Unebenheiten jedoch Schwingungen in das System eingeleitet, die die Immersion des Probanden stören. Die im Rahmen einer Recherche ermittelte Forschung zu selbstfahrenden Simulatoren vernachlässigte diesen Aspekt und setzte eine ausreichend ebene Fahrfläche voraus. Unklar ist jedoch, was in diesem Zusammenhang ausreichend bedeutet. Zudem wird der Flexibilitätsvorteil des Konzepts durch die Anforderung einer hohen Qualität der Fahrfläche eventuell deutlich eingeschränkt. Aus diesem Grund werden in dieser Arbeit zum einen die notwendige Fahrflächenqualität quantifiziert und zum anderen Ansätze zur Reduzierung der Störungen durch die Fahrbahn entwickelt und bewertet.

Zunächst wird eine Analyse des aktuellen Entwicklungsstadiums des Fahrsimulators von FZD vorgenommen, welches ein rein reifengefedertes System mit Vollgummi-Reifen umfasst. Diese Analyse zeigt, dass Fahrbahnqualitäten mit einer maximalen Höhenabweichung von 0,01 mm auf einer Länge von 4 m (sog. Stichmaß) zulässig sind, um einen Fahrsimulator dieser Konfiguration ohne Einschränkung der Immersion des Probanden zu nutzen. Diese Qualität ist mit Asphaltflächen, die für WMDS das größte Anwendungspotential aufweisen, nicht erreichbar. Diese erreichen minimale Stichmaße von 2 mm.

Daraufhin wird als Verbesserungsansatz eine aktive Kompensation der fahrbahnerregten Schwingungen mit dem in Simulatoren ohnehin vorhandenen Hexapod entwickelt und untersucht. Durch den aktiven Ansatz wird das zulässige Stichmaß gegenüber dem passiven reifengefederten System um den Faktor 4 erhöht, liegt aber dennoch bei nur 3 % Zielwerts. Insbesondere die Totzeit des Hexapods und die geringe Dämpfung sowie die Parameterschwankungen der Reifen schränken das Potential des Konzepts ein.

Aus diesem Grund wird das Potential der Implementierung einer zusätzlichen Federung in Kombination mit dem aktiven Ansatz untersucht. Um eine niedrige Eigenfrequenz zu erreichen, die im Hinblick auf Schwingungsisolation vorteilhaft ist, wird eine Kinematik entwickelt, die durch Stützkräfte die Fahrwerksbewegungen der omnidirektionalen Bewegungsplattform reduziert. Zudem erfolgt eine Anpassung der Ansteuerung des Fahrsimulators, um mithilfe einer auf das Fahrwerk angepassten Kraftverteilung das Potential der Kinematik möglichst weit auszuschöpfen. Durch diese Maßnahmen werden die durch Fahrwerksbewegungen bedingten Störungen bis zu einer Horizontalbeschleunigung von 4.5 m/s² auf Werte unterhalb der Wahrnehmungsschwelle reduziert. Die Simulation eines Stadtfahrszenarios mit einem Mehrkörpermodell zeigt, dass dies den Großteil der auftretenden Beschleunigungen abdeckt und mehr als 99 % der Simulationszeit keine Störbewegungen oberhalb der Wahrnehmungsschwelle auftreten. Mit Luftreifen lässt sich der Beschleunigungsbereich mit idealer Abstützung auf 5.4 m/s² steigern.

Hinsichtlich der erforderlichen Fahrbahnqualität lässt sich dadurch eine Erhöhung des akzeptablen Stichmaßes auf 0,8 mm erreichen, was einer Verbesserung von fast zwei Größenordnungen gegenüber der Ausgangslage entspricht. Dennoch ist der Wert etwas geringer als der mit Asphaltflächen erreichbare Wert von 2 mm. Der ermittelte Wert ist jedoch nur erforderlich, um mit den Störvibrationen vollständig unterhalb der Wahrnehmungsschwelle zu bleiben. Da Vibrationen in Pkw jedoch nicht ungewöhnlich sind, könnten die negativen Auswirkungen auf die Immersion möglicherweise geringer sein, sodass eine leichte Überschreitung der Wahrnehmungsschwelle zulässig sein könnte. Zukünftige Probandenuntersuchungen müssen diesen Aspekt näher untersuchen.

Summary

Driving simulators are an important element of vehicle development, since the design of driver assistance systems in particular requires the investigation of the driver-vehicle interaction. In the future, an even greater application potential is to be expected with regard to automated driving, since, for example, handover strategies can be investigated in a secure environment. However, today's driving simulator concepts have reached a limit with regard to the achievable quality of motion simulation. Especially urban driving scenarios require a range of motion that is not economically viable with the sled systems applied in current high-end systems.

One way out of this limitation is provided by wheeled mobile driving simulators, which generate the demanded accelerations through tire forces. This enables an application on different driving surfaces, which allows flexible adaptation of the movement area to the requirements of the scenario. However, due to the contact between tire and driving surface, unevenness induces vibrations into the system which disturb the immersion of the subject. The known previous research on wheeled mobile driving simulators gathered in literature neglected this aspect and postulated a sufficient driving surface quality. However, it is unclear what sufficient means in this context. In addition, the flexibility advantage of the concept may be significantly limited by the requirement of a high quality surface. Thus, this work aims at quantifying the required driving surface quality and the development and evaluation of approaches for the reduction of disturbances induced by unevenness.

First, an analysis of the current development state of the driving simulator at FZD, which includes a purely tire-sprung system with solid rubber tires, is conducted. This analysis shows that driving surface qualities with a maximum height deviation of 0.01 mm over a length of 4 m (so-called depth gauge) are required to use a driving simulator of this configuration without deteriorating the immersion of the subject. This quality is not achievable with asphalt surfaces, which offer the highest application potential for WMDS. The minimum achievable depth gauge amounts to 2 mm.

Thereupon, an active compensation of the driving surface-induced vibrations with the Hexapod, which is already available in simulators, is investigated. The active approach increases the tolerable depth gauge by a factor of 4 compared to the passive tire-sprung system. Nevertheless, it is still only 3 % of the target value. Especially the high dead time of the hexapod as well as the low damping and the parameter fluctuations of the tire limit the potential of the concept.

Therefore, the potential of implementing an additional suspension in combination with the active approach is investigated. In order to achieve a low natural frequency, which is advantageous in terms of vibration isolation, a kinematics is developed that reduces the suspension

movements of the omnidirectional motion platform by support forces. In addition, the motion control of the driving simulator is adapted in order to adjust the wheel force distribution to the demands of the suspension. These measures reduce the disturbances caused by suspension movements to values below the perception threshold up to a horizontal acceleration of 4.5 m/s². The simulation of an urban driving scenario with a multibody model shows that this covers the majority of the occurring accelerations and that within more than 99% of the simulation time the disturbance motions remain below the perception threshold. With pneumatic tires, the acceleration range with ideal support can be increased to 5.4 m/s².

With regard to the required driving surface quality, this allows an increase of the acceptable depth gauge to 0.8 mm, which corresponds to an improvement of almost two orders of magnitude compared to the initial situation. Nevertheless, the value is slightly below the minimum of 2 mm achievable with asphalt surfaces. However, the determined value is only required to remain below the perception threshold with the disturbance vibrations. As vibration in vehicles is not uncommon, the negative effects on the immersion could possibly be lower, allowing a slight exceeding of the threshold. Future subject studies must examine this aspect in more detail.

1 Introduction

1.1 Motivation

Driving Simulators (DS) as a development tool in the automotive industry have become increasingly important throughout the last years due to extended research in the field of advanced driver assistance systems[1,2,3,4] and automated driving[5,6,7]. The human-machine interaction resulting from these systems makes an inclusion of the driver in the development process essential. Especially the current trend topic of automated driving requires driver behavior investigations e.g. to analyze handover strategies. The advantages of DS for these investigations are the safety of subjects, the reproducibility of environment conditions and the reduction of development time and costs due to the reduced number of required physical prototypes. However, especially urban driving scenarios, which will become more and more important when the focus of automation shifts from highways to the city, are still a challenge for today's motion systems.[8]

State-of-the-Art DS consisting of a hexapod mounted on a sledge system have shortcomings concerning the movement representation. As shown in Figure 1-1, especially intermediate acceleration frequencies require a wide range of movement of the motion base to be represented accurately at all amplitudes occurring in a vehicle.[9a] The sled system that would be necessary for this workspace would result in a high moving mass of the system. This would increase the power demand and therefore lead to high purchase and operating costs.

An approach to solve this dilemma is the use of Wheeled Mobile Driving Simulators (WMDS) that were first addressed in a patent of Donges[10] and a reference by Slob[11]. The

[1] Cf. Zeeb, E.: Daimler's Driving Simulator (2010).

[2] Cf. Baumann, G. et al.: How to build Europe's largest eight-axes DS (2012).

[3] Cf. Chapron, T.; Colinot, J.-P.: The new PSA Peugeot-Citroën Advanced DS (2007).

[4] Cf. Schöner, H. P.: Erprobung und Absicherung im dynamischen DS (2014).

[5] Cf. Richter, A.; Scholz, M.: The Surveyor's Guide to Automotive Simulation (2016).

[6] Cf. Boer, E. R. et al.: The Role of DS in Developing and Evaluating AD (2015).

[7] Cf. Maurer, M. et al.: Autonomes Fahren (2015), p. 446.

[8] Cf. Schöner, H.-P.: Expectations towards Driving Simulation (2018), p. 15.

[9] Cf. Betz, A.: Diss., Feasibility and Design of WMDS (2014). a: pp. 22f; b: -.

[10] Cf. Donges, E.: Fahrsimulator (2002).

[11] Cf. Slob, J. J. et al.: The Wall is the Limit (2009).

idea behind this concept is to drive the motion platform based on tires instead of a sled system. Therefore, only the available movement area limits the motion representation capabilities but not the system itself. A possible approach on WMDS is proposed by Betz[9b] and its feasibility concerning power, energy and friction demands is proven theoretically. It consists of a motion base mounted on three tires, which are actuated by one drive and one steering motor each. The WMDS prototype MORPHEUS was built at the Institute of Automotive Engineering at TU Darmstadt to investigate these aspects.

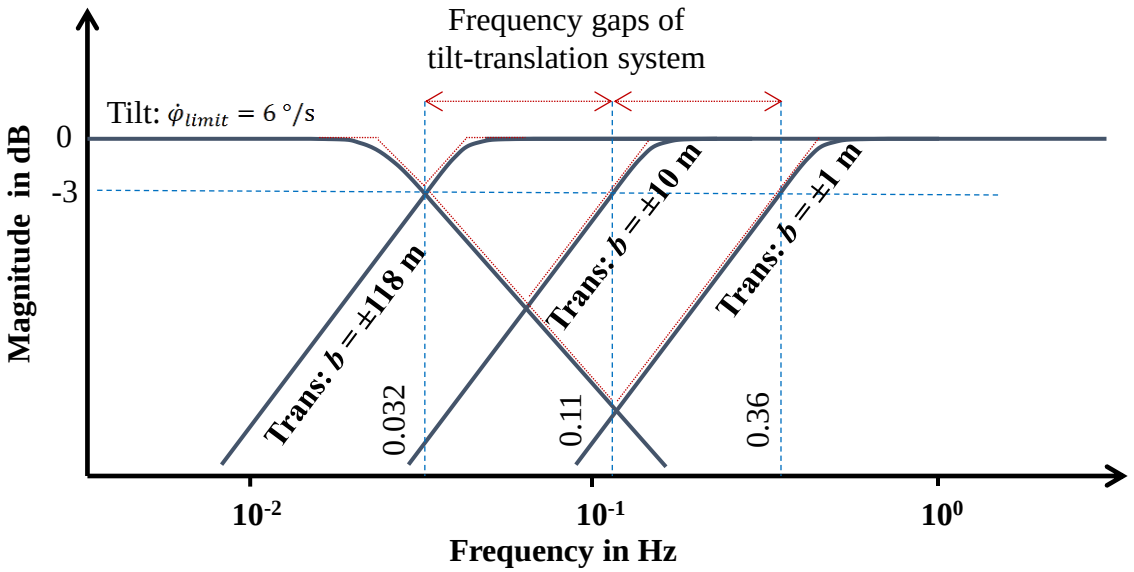

Figure 1-1: Frequency gaps of exemplarily chosen tilt-translation systems.[12]

Nevertheless, as the simulator is mounted and driven on tires, which are in contact with a driving surface of finite evenness, vertical excitations arise during simulation. To avoid a disturbance of the subject's immersion, a limitation of the acceptable driving surface unevenness is required. This, on the other hand, limits the number of suitable driving surfaces and may even require the construction of a new driving surface of adequate quality. Additional costs or reduced movement representation capabilities are the results, so that the main advantages and therefore the application potential of the WMDS concept are detracted. At worst, no driving surface could exist that allows the application of WMDS without an unacceptable disturbance of subjects. Hence, an investigation of the applicability of WMDS on uneven driving surfaces and the development of measures to improve the vertical dynamic behavior are required.

[12] Wagner, P.: Diss., Practical Feasibility WMDS (2018), p. 15. According to Betz, A.: Feasibility and Design of WMDS (2014).

1.2 Research Questions and Working Hypothesis

The main goal of the work is to prove and extend the application potential of the WMDS concept on uneven grounds. To address this goal, the following core research question is formulated:

Which driving surface unevenness is acceptable for the application of a WMDS without additionally disturbing the immersion of subjects compared to a flat surface?

The research question is highly dependent on the applied WMDS system configuration because the vertical dynamic behavior offers a high degree of freedom for adaptions. Therefore, the current work is not limited to the current system state, which is solely sprung by solid tires. Instead, it is aspired to answer the core research question for different system configurations. Thus, the following sub-research question is defined:

What measures are conceivable to extend the application potential of WMDS to uneven grounds of lower quality and how high is their potential for improvement?

In order to address these research questions, the following working hypothesis is defined:

An ideal driving surface without unevenness is required for the application of WMDS without deterioration of the immersion of the subject.

Of course, this consideration is theoretical because a driving surface without unevenness does not exist but nevertheless, it first must be proven that even the smallest excitation is acceptable for the application of WMDS. Hence, the aim of this work is to continuously falsify this hypothesis and adapt it to the acceptable driving surface quality of the respective considered system state. Thus, the hypothesis addresses both research questions. The falsification of the hypothesis yields the answer to the core research question for a given system state. The aspiration of a further falsification of the adapted hypothesis requires answers to the second research question.

1.3 Overall Methodology and Structure

The overall methodology of this work is summarized in Figure 1-2. The structure of the thesis follows this methodology. The first step is the investigation of fundamentals concerning driving surfaces, human motion perception, driving simulation and the WMDS concept. Based on these fundamentals, a detailed analysis of the problem is enabled. Subsequently, a methodology for the falsification of the working hypothesis by determining the acceptable driving surface quality is derived and the required research tools are developed and presented. The next step is the investigation of the initial situation by identifying and modeling the current system configuration. Then the methodology is applied to this system state to

determine the current limitation concerning the acceptable driving surface quality, which enables the first adaption of the working hypothesis.

The next step is the development of concepts for reducing disturbances of the subject induced by the driving surface. Three concepts are developed in detail in the successive chapters to be able to thoroughly evaluate their potential for the further falsification of the working hypothesis:

- Pneumatic Tires
- Hexapod vertical dynamics control in combination with the solely tire-sprung vibration system
- Hexapod vertical dynamics control in combination with a spring-damper-suspension

The last chapter aims at the comparison and the overall evaluation of the developed concepts.

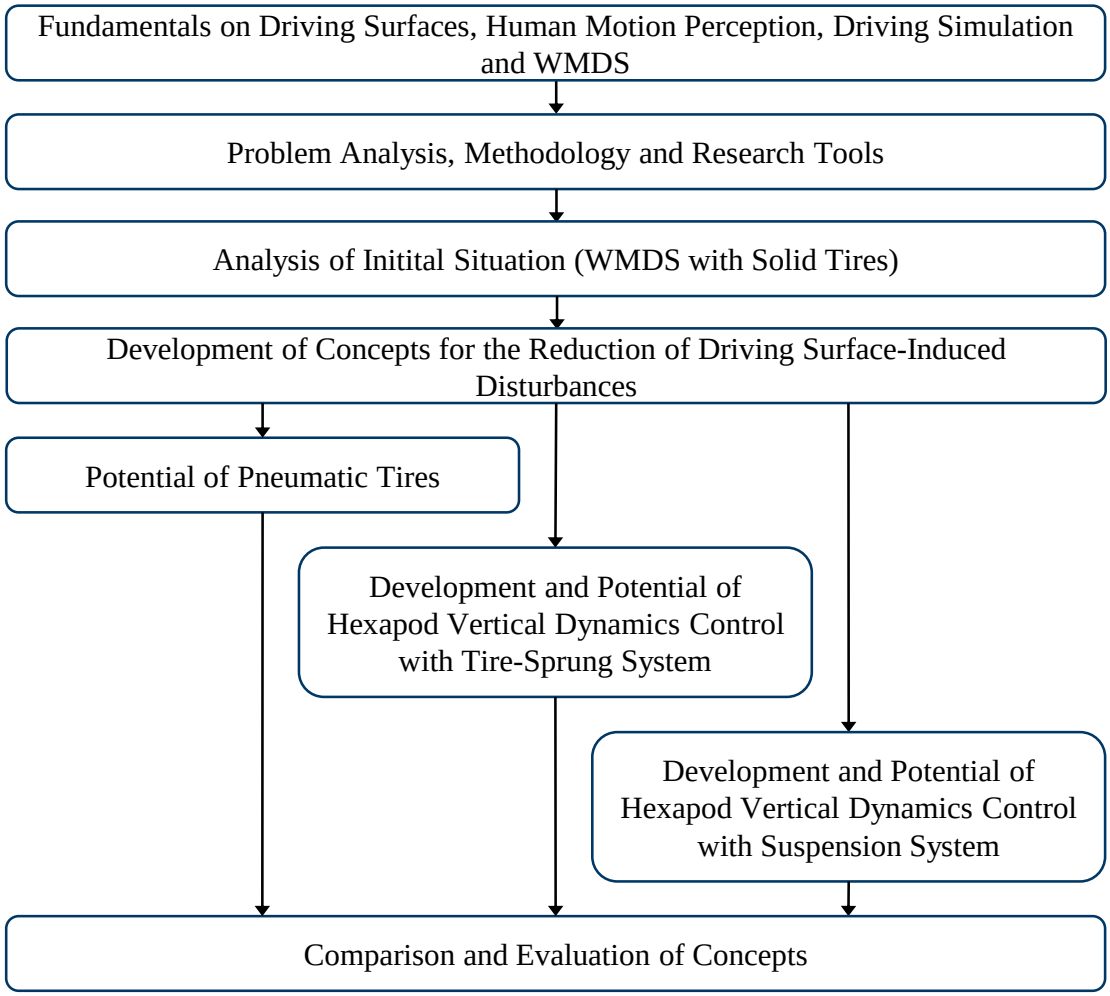

Figure 1-2: Overall methodology.

2 Fundamentals

The following chapter gives an overview of all fundamentals that are required for the further research process. The first step is the introduction of definitions applied in this thesis. Subsequently, the current state of the art is presented. For a better understanding of the problem of disturbances induced by the driving surface, fundamentals of driving simulation are introduced. The next two subchapters address the driving surface as the relevant input and the human perception of motion as the output of the following investigations. The chapter closes with an introduction of FZD's WMDS concept by means of the MORPHEUS prototype.

2.1 Definitions

2.1.1 Coordinate Systems

The applied coordinate system definition for the driving simulator platform is based on ISO 8855[13]. The leveled vehicle system is indicated with the index H.

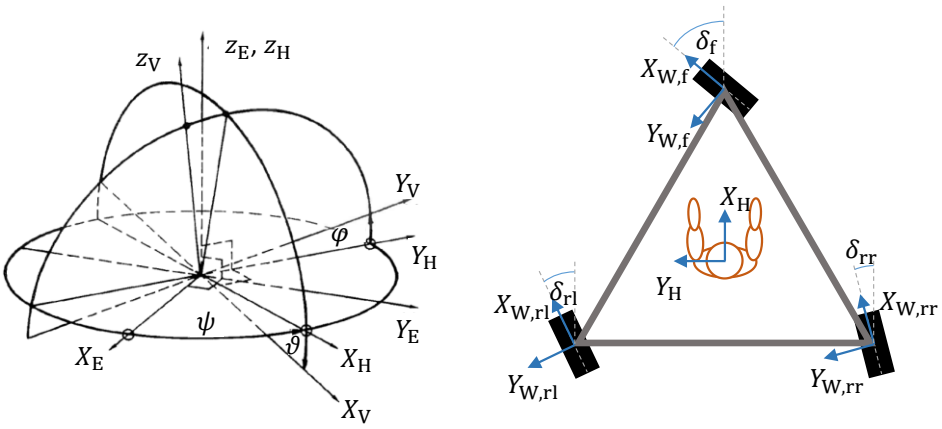

Figure 2-1: Coordinate system definitions[14]

The translational degrees of freedom (DoF) are described with x for surge, y for sway and z for the heave motion. The rotational DoF are denominated ϑ for pitch, φ for roll and ψ for yaw. The x-axis of the leveled simulator coordinate system is oriented according to the direction the subject is facing. This definition of the forward direction yields the naming of the

[13] Cf. Deutsches Institut für Normung e. V.: ISO 8855 - Fahrdynamik Begriffe (2013).

[14] According to Deutsches Institut für Normung e. V.: ISO 8855 - Fahrdynamik Begriffe (2013), p. 11.

respective wheels. Additional to the coordinate system of the driving simulator body, separate coordinate systems are defined for the wheels (W) and the subject seat (S).

2.1.2 Notation

The notation applied in this thesis is exemplified in Figure 2-2. The upper left index describes the domain in which the variable is described. The following indices are applied:

- $\mathcal{F}$=Fourier domain
- $\mathcal{L}$=Laplace domain

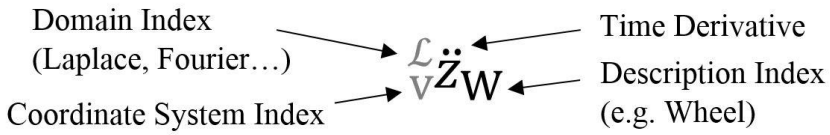

Figure 2-2: Applied notation

Variables without domain index are described in the time domain. The lower left index describes the coordinate system according to the definitions in section 2.1.1. Time derivatives are indicated by dots above the variable in every domain.

2.2 State of the Art

The topic of reducing disturbances induced by the driving surface in WMDS is almost not addressed by the current state of the art. The quantity of published WMDS developments is small and this special aspect is neglected by most of the known concepts. The patents of Donges[15] and Hüsing[16] postulate a flat surface for the application of the WMDS and do not consider surface-induced vibrations.

For another concept developed by the Eindhoven University of Technology together with Bosch Rexroth, the problem is addressed superficially. A “relatively flat floor” is assumed. Additionally, the wheels are able to tilt, which should absorb “2/3 of the excitation”.[17] According to the publication, the vibrations generated by the wheels “will be damped or filtered out”, while there is no closer information on how this is achieved.[17]

The only detailed suspension design for WMDS is described by Tüschen.[18a] Three main requirements on the suspension are mentioned: dynamic requirements, comfort requirements

[15] Cf. Donges, E.: Fahrsimulator (2002).

[16] Cf. Hüsing, K.: Fahrsimulator (2003).

[17] Slob, J. J. et al.: The Wall is the Limit (2009). p. 300.

[18] Cf. Tüschen, T. et al.: Suspensions Design of a WMDS (2016). a: -; b: pp. 15 ff.; c: p. 21; d: p. 16.

and roll and pitch angle requirements. In order to solve the design conflict between driving dynamics and comfort, a dual kinematic is applied, which divides both functionalities. The dual kinematic suspension concept is shown in Figure 2-3. The primary function of the upper kinematic is the reduction of angular motions of the simulator and the achievement of a preferably equal wheel load distribution. The lower kinematic design aims at the reduction of driving surface-induced vibrations.[18b]

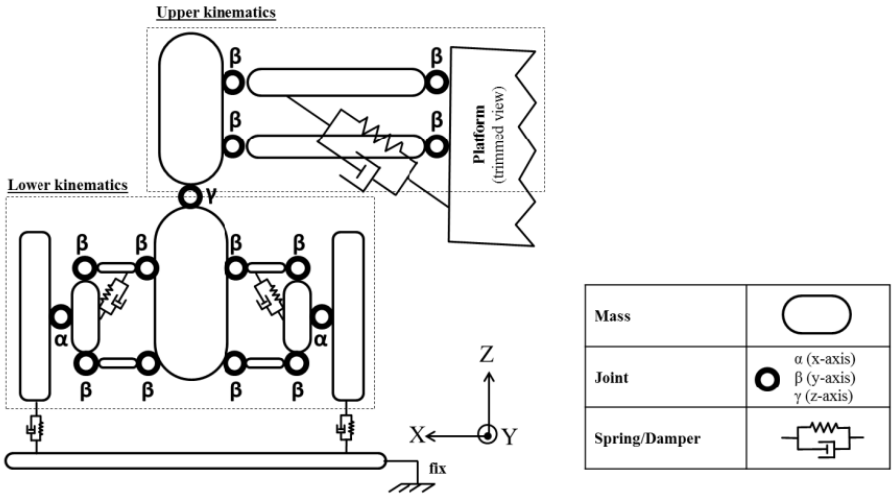

Figure 2-3: Dual kinematic suspension concept.[19]

The focus of the description of the concept is on the dynamic requirements concerning the wheel load distribution among the twin wheels and on the mitigation of angular motions. Especially the design of the instantaneous centers of rotation is considered. The design of the concept is based on a planar consideration with respect to lateral accelerations.[18b] The dual kinematic shows no loss of ground contact in the relevant range up to 10 m/s², while the simple kinematic reaches this limit at about 6 m/s². This also results in a reduction of the angular motions.[18c] The impact of different acceleration directions, the wheel load-dependent force distribution and the relative rotation between the two kinematics due to steering motions is not described.

The comfort aspect, which addresses the disturbances by driving surface unevenness, is limited to vertical excitations by single humps because a sufficient quality of the applied driving surfaces is postulated.[18d] It is not described in detail, how the comfort requirement is addressed with the lower kinematic. Additionally, no evidence is given that the lower kinematic achieves the comfort targets. The design of the spring-damper elements, which is crucial for vibration reduction, is not conducted.[20]

Summarizing, no work has yet considered the application of WMDS on uneven surfaces. An area with sufficient quality is postulated by all authors, while it is unclear what sufficient means. Detailed descriptions of concepts and designs that would enable such an application

[19] Tüschen, T. et al.: Design suspension dynamic driving simulator (2015).

[20] Cf. Tüschen, T.: Diss., Konzeptionierung selbstfahrender Fahrsimulator (2018). p. 65.

are not available in literature. Thus, the focus of this work, which is to quantify an acceptable quality of the driving surface and to extend the application potential to surfaces with higher unevenness, fills a gap within the previous research concerning WMDS.

2.3 Introduction to Driving Simulation

Driving simulators (DS) have the purpose to simulate a scenario to a subject in a safe and reproducible environment. To achieve this, the following sensory channels of human perception have to be addressed:[21]

- Auditory (Ear)
- Visual (Eye)
- Somatosensory System (Skin, Muscles, Joints, Tendons)
- Vestibular System (Equilibrium Organ)

The information from these channels are merged in the human brain, which enables the compensation of weaknesses of the respective systems by supplementing missing information from other sources. Thus, to achieve high immersion, a perfect simulation of all channels is not required but the single channels have to yield a plausible overall picture. A high mismatch of the channels causes disorientation or even nausea of the subject, the so-called simulator sickness.[21]

The focus of research concerning WMDS is motion simulation, which addresses the somatosensory and the vestibular system. Therefore, mainly the fundamentals concerning this aspect are described in the following. An overview over all aspects of driving simulation is given e.g. in the work of Negele.[22]

2.3.1 Motion Simulation and Motion Cueing Algorithm

The motion simulation is typically based on two fractions: a translational motion of the DS motion simulation system and a superposed tilt of the subject. The latter is the so-called tilt coordination (TC) that utilizes a motion perception error of the human. The tilt angle results in an inclination of the gravitational acceleration vector relative to the subject. The subject perceives the resulting sine component in the subject coordinate system as a horizontal acceleration. This enables the simulation of sustained accelerations without any translational motion. However, the human is able to sense rotational accelerations and velocities. Thus, the adjustment of the tilt angle has to be slow so that this principle is only suitable for the

[21] Cf. Fischer, M.: Diss., Motion-Cueing-Algorithmen (2009). p. 8.

[22] Cf. Negele, H. J.: Diss., Konzipierung Fahrsimulatoren (2007).

simulation of low-frequent accelerations. Higher frequencies have to be simulated by translational motions. The purpose of the motion cueing algorithm (MCA) is to translate the acceleration demand of the virtual vehicle, which is generated from the driver inputs and a vehicle dynamics model, to the motions of the DS that simulate this demand. This comprises the division between translational and tilt motion, but also the scaling of the accelerations and the return of the simulator to its initial position, the so-called washout.

The scaling of the accelerations means the multiplication of the desired input accelerations by a frequency-independent, constant factor. Because of the limited discrimination of acceleration magnitudes, this does not necessarily affect the subject's immersion.[23] Common scaling factors are 1, 0.7 and 0.5.[21,23]

The purpose of the washout is to return the simulator to its initial position in order to provide the maximum range of motion for the oncoming acceleration demands without violating the human motion perception thresholds.

2.4 Human Motion Perception

The following subchapter gives a short introduction to the topic of human motion perception. First, the vestibulum, which is the main organ for the perception of accelerations[24], is described. Additionally, the special considerations concerning the perception of vibrations are presented. The last sections give an overview of human motion perception thresholds.

2.4.1 Vestibular Organ

The vestibular organ is located in the inner ear. It consists of two maculae, the utricle and the saccule, for sensing translational accelerations and three semi-circular canals, which are oriented orthogonally to each other, for sensing rotational motions.[25a]

In the macula organs, sensory hairs are connected to a gelatinous layer, which is filled with otoliths with a high relative density and is therefore called the otolithic membrane. The resulting higher inertia relative to the surrounding endolymph leads to a deflection of this membrane under translational accelerations, which is sensed by the sensory hairs.[25a]

The cupula, which is the sensing element of the semi-circular canals, has a similar structure as the otolithic membrane. However, it contains no otoliths so that the cupula and the surrounding endolymph have an equal relative density and thus, no deflection occurs under translational accelerations. For rotational accelerations, on the other hand, the inertia of the

[23] Cf. Greenberg, J. et al.: Lateral motion cues during simulated driving (2003).

[24] Cf. Dobbeck, R.: Diss., Beschleunigungen in Fahrsimulatoren (1974), p. 11.

[25] Cf. Schmidt, R. et al.: Physiologie des Menschen (2005). a: pp. 358 ff.; b: pp. 287 f.

endolymph results in relative motion between the liquid and the wall of the semi-circular canal, resulting in a deflection of the cupula and, therefore, a sensing of the rotational motion by the sensory hairs. For short rotational motions of the head, the semi-circular canals also sense the rotational velocity.[25a] Summarizing, the following motion quantities are perceptible by the vestibular organ (given in subject seat coordinate system):

- Translational accelerations ${}_S\ddot{x}$, ${}_S\ddot{y}$, ${}_S\ddot{z}$
- Rotational velocities ${}_S\dot{\vartheta}$, ${}_S\dot{\varphi}$, ${}_S\dot{\psi}$
- Rotational accelerations ${}_S\ddot{\vartheta}$, ${}_S\ddot{\varphi}$, ${}_S\ddot{\psi}$

2.4.2 Vibration Perception

The human perception of vibrations, which is the most relevant aspect of perception for this work due to the vibrational characteristic of the disturbances resulting from driving surface unevenness, has been addressed by many studies and standards.[26,29a,27] The aim of these standards is to offer objective characteristic values for the assessment of the subjective human perception of vibrations. This enables the design of vibration reduction measures based on simulated and measured quantities.

The standards differentiate between whole-body vibrations, which are transmitted to the human body via the buttocks and the back of the seated person, and hand-transmitted vibrations, which are transmitted via the steering wheel. The frequency range relevant for the impairment of comfort by whole-body vibrations is between 0.5 and 80 Hz.[28a] In the following, objective characteristics for the assessment of whole-body vibrations are described.

As discussed in section 2.4.1, the human senses translational and rotational accelerations, which is therefore the main characteristic described by the standards. The human perception of vibrations is frequency dependent. Therefore, a frequency weighting function is applied to the relevant translational and rotational acceleration signals in order to assess the human feeling of the objective vibration. Frequency weighting functions are defined for different postures of the human as well as for different vibration directions.[27] An example is given in the appendix in Figure A.1 - 1. The r.m.s. of these frequency-weighed accelerations a_{FW} is determined as a characteristic value for the assessment of vibration comfort. However, for long tests with occasional shocks and transient vibration, a running r.m.s. method with a short integration time constant τ_{rrms} is recommended:[29b]

---

[26] Cf. DIN Deutsches Institut für Normung e.V.: ISO 8041-1 - Human Response to Vibration (2017).

[27] Cf. VDI, Verein Deutscher Ingenieure: VDI 2057 - Ganzkörper-Schwingungen (2017).

[28] VDI, Verein Deutscher Ingenieure: VDI 2057 - Ganzkörper-Schwingungen (2017). a: p. 6.; b: p. 29.

[29] Cf. ISO: ISO 2631-1 - Mechanical Vibration (1997). a: -; b: p. 9; c: p. 12.; d: p. 15.

$$\mathrm{a}^2_{\mathrm{FW,rrms}}(t,\tau_{\mathrm{rrms}}) = \sqrt{\frac{1}{\tau_{\mathrm{rrms}}}\int_{t-\tau_{\mathrm{rrms}}}^{t} \mathrm{a}^2_{\mathrm{FW}}(t')dt'} \tag{2.1}$$

An integration time constant of 1 s is recommended for the assessment of specific quantiles of this running r.m.s. value.[29b] This characteristic value is determined separately for each vibration direction. If multiple directions are acting simultaneously, the respective directions are combined to the total vibration value (TVV) a_{TVV}:[29c]

$$a_{\mathrm{TVV}} = \sqrt{\gamma_x^2 \ddot{x}^2_{\mathrm{FW,rrms}} + \gamma_y^2 \ddot{y}^2_{\mathrm{FW,rrms}} + \gamma_z^2 \ddot{z}^2_{\mathrm{FW,rrms}} + \gamma_\vartheta^2 \ddot{\vartheta}^2_{\mathrm{FW,rrms}} + \gamma_\varphi^2 \ddot{\varphi}^2_{\mathrm{FW,rrms}}} \tag{2.2}$$

The constants γ are factors weighing the impact of the vibration in the respective DoF on the overall vibration perception. The TVV is recommended for the assessment of comfort. Values for the combination factors are given in ISO 2631-1.[29d]

2.4.3 Perception Thresholds

An extensive overview of perception thresholds determined in several studies is given by Betz.[30] From this summary he derived the following perception thresholds, which are also applied in this thesis for the sake of consistency and comparability:[31]

- Rotational Velocity Threshold: 6 °/s
- Rotational Acceleration Threshold: 6°/s²
- Translational Acceleration Threshold: 0.2 m/s²

These thresholds apply to the perception of approximately constant accelerations with low variations. This is useful for example for the design of washout-filters in order to determine acceptable accelerations of the return motions. Concerning the perception of vibrations, a perception threshold of 0.015 m/s² is given for the total vibration value from section 2.4.2, which is calculated from the frequency-weighted accelerations.[28b] Although this is one order of magnitude below the perception threshold of Betz, the frequency weighting has to be considered. The perception filter characteristic reduces at low frequencies, resulting in a lower perceptibility of constant accelerations.

2.4.4 Just Noticeable Difference

The aforementioned perception thresholds are valid for a state in which no other stimuli are acting. If a reference stimulus is already available, the perceptibility of superposed disturbances reduces because they are masked by the reference signal. In that case, the Just Noticeable Difference (JND) is the relevant threshold characteristic. For many sensory channels,

[30] Cf. Betz, A.: Diss., Feasibility and Design of WMDS (2014). p. 16.

[31] Betz, A.: Diss., Feasibility and Design of WMDS (2014). p. 15.

the relation between reference stimulus a_{ref} and just noticeable difference Δa_{JND} is proportional for medium stimulus intensities according to Weber's Law:[25b]

$$\Delta a_{\mathrm{JND}} = k_{\mathrm{Weber}} a_{\mathrm{ref}} \tag{2.3}$$

With the Weber coefficient k_{Weber} that describes the relation. Studies document that whole-body vibrations obey to Weber's Law.[32,33] An overview of several Weber coefficients gathered in literature is given in Table 2-1.

Table 2-1: Overview of Weber coefficients k_{Weber}, directions in subject frame.

Reference	${}_S\ddot{x}$	${}_S\ddot{y}$	${}_S\ddot{z}$	${}_S\dot{\psi}$
Bellmann[34]			0.185 ± 0.11	
MacNeilage et al.[35]	0.42 ± 0.24		0.39 ± 0.26	
Mallery et al.[36]				0.03
Mansfield et al.[37]			Median 0.131	
Matsumoto et al.[38]			0.065	
Morioka et al.[39]			0.092 - 0.116	
Müller et al.[40]	0.027			
Naseri et al.[41]	a_{ref} 0.5 $\frac{\mathrm{m}}{\mathrm{s}^2}$: 0.1 a_{ref} 2 $\frac{\mathrm{m}}{\mathrm{s}^2}$: 0.063			
Pielemayer et al.[42]			0.075 – 0.225	
Winkel et al.[43]				0.27 ± 0.094
Zaichik et al.[44]	0.6	0.4	0.9	

[32] Cf. Mansfield, N. J.; Griffin, M. J.: Difference thresholds automobile seat vibration (2000).

[33] Cf. Zaichik, L. et al.: Acceleration perception (1999).

[34] Bellmann, M. A.: Diss., Perception of Whole-Body Vibrations (2002). pp. 86 ff.

[35] MacNeilage, P. R. et al.: Vestibular heading discrimination (2010). p. 9088.

[36] Mallery, R. M. et al.: Discrimination of rotational velocities (2010). p. 16.

[37] Mansfield, N. J.; Griffin, M. J.: Difference thresholds automobile seat vibration (2000). p. 260.

[38] Matsumoto, Y. et al.: Difference Thresholds Whole-Body Vibration (2002). p. 317.

[39] Moroika, M.; Griffin, M. J.: Difference thresholds for intensity perception (2000). p. 9.

[40] Müller, T. et al.: JND Longitudinal Acceleration (2013).

[41] Naseri, A. R.; Grant, P. R.: Human discrimination of translational accelerations (2012). p. 460.

[42] Pielemeier, W.J., Jeyabalan, V. et al.: JND vertical vibration automobile seat (1997). According to: Mansfield, N.J.; Griffin, M. J.: Difference thresholds automobile seat vibration (2000). p. 256.

[43] Winkel, K. N. de et al.: Perception of angular self-motion (2013). p. 213.

[44] Zaichik, L. et al.: Acceleration perception (1999). p. 518.

The values show a high variation between 0.027 and up to 0.9. Nevertheless, many studies found thresholds around 0.1. Therefore, this value is chosen as JND threshold for this thesis.

This value, however, only describes the amplitude discrimination threshold for an acting acceleration. Another aspect is the JND concerning the direction of acceleration. MacNeilage determined a threshold of 6° for horizontal accelerations.[35]

2.5 Driving Surfaces

2.5.1 Description of Driving Surfaces

The vertical profile of driving surfaces can be considered as a stochastic excitation process. Therefore, it can be described with a power spectral density (PSD) in the frequency domain in dependency of the spatial frequency.[45a] Figure A.1 - 2 in the appendix shows power spectral densities of different asphalt and concrete road surfaces measured by Braun. It is recognizable that the PSD of the measured road surfaces decreases with increasing frequency. An exponentiation approximation of the measured PSDs results in straights on a double logarithmic scale. The resulting approximation of the PSD of the driving surface excitation Φ_{DSE} is described by the following function: [46a]

$$\Phi_{\mathrm{DSE}}(\Omega) = \Phi_{\mathrm{DSE}}(\Omega_0)\left(\frac{\Omega}{\Omega_0}\right)^{-w} \tag{2.4}$$

With the PSD defined as follows:

$$\Phi_{\mathrm{DSE}}(\Omega) = \frac{1}{\Delta\Omega}\left|{}^{\mathcal{F}}z_{\mathrm{DSE}}(\Omega)\right|^2;\ {}^{\mathcal{F}}z_{\mathrm{DSE}}(\Omega) = \mathcal{F}\left(z_{\mathrm{DSE}}(x)\right) \tag{2.5}$$

With the spatial frequency resolution $\Delta\Omega$ and the driving surface excitation z_{DSE}. The parameter w adjusts the decline of the PSD towards higher frequencies. For typical driving surfaces it varies around a value of 2.[46] The power spectral density $\Phi_{\mathrm{DSE}}(\Omega_0)$ at the reference frequency $\Omega_0 = 1\,\frac{\mathrm{rad}}{\mathrm{m}}$, in the following referred to as the **roughness coefficient**, describes the quality of a driving surface. A classification of driving surface qualities based on this quantity is given in Table 2-2 for $w = 2$. An alternative description by Parchilowskij avoids the infinite power spectral density at low frequencies:[47]

---

[45] Cf. Mitschke, M.; Wallentowitz, H.: Dynamik der Kraftfahrzeuge (2014). p. 334 ff..

[46] Mitschke, M.; Wallentowitz, H.: Dynamik der Kraftfahrzeuge (2014). p. 342.

[47] Parchilowskij, J. G.: Verteilungsdichte der Unebenheiten (1961). According to: Mitschke, M.; Wallentowitz, H.: Dynamik der Kraftfahrzeuge (2014). p. 343.

$$\Phi_{\mathrm{DSE}}(\Omega) = \frac{k_{\mathrm{Parc},1}}{k_{\mathrm{Parc},2}^2 + \Omega^2} \tag{2.6}$$

The parameter $k_{\mathrm{Parc},2}$ generates a constant magnitude for low frequencies. At high frequencies, the spatial frequency becomes dominant compared to the parameter $k_{\mathrm{Parc},2}$ and the equation corresponds to formula (2.4) with $w = 2$. Hence, the parameter $k_{\mathrm{Parc},1}$ is equal to the roughness coefficient.

Table 2-2: Classification of Driving Surfaces.[48]

Driving Surface Class	$\Phi_{\mathrm{DSE}}(\Omega_0)$ in cm³			Subjective Assessment
	Lower Limit	Mean	Upper Limit	
A	0	1	2	Very good
B	2	4	8	Good
C	8	16	32	Medium
D	32	64	128	Bad
E	128	256	512	Very Bad

An alternative quantity to describe the quality of a driving surface is the so-called **depth gauge**. It is defined as the distance of the lowest point of the measured surface from a connecting line between two maximum turning points.[49] It has a higher practical relevance in the construction field because it is measurable with a boning rod. Additionally, it is more conceivable than the abstract roughness coefficient. Hence, both quantities are applied for the description of the driving surface quality in this work. A relation between both characteristics is unknown yet and will be derived in section 3.2.2.

2.5.2 Achievable Driving Surface Qualities

Concerning the achievable driving surface quality of typical asphalt materials, the literature mentions minimum roughness coefficients of 0.3 cm³ for highways in Germany.[50] An expert discussion with Mathias Schollmaier, head of the test center Dudenhofen from Opel GmbH, yielded that the driving dynamics area of the test center has an average depth gauge of 2 mm over a length of four meters. According to his statement, a high effort was required to reach this quality and the possibility of further improvements is doubted.[51]

[48] ISO: ISO 8608-1 - Road surface profiles (1995). According to Mitschke, M.; Wallentowitz, H.: Dynamik der Kraftfahrzeuge (2014). p.343.

[49] Cf. Deutsches Institut für Normung e. V.: DIN 18202 - Toleranzen im Hochbau (2005), p. 4.

[50] Braun, H.: Meßergebnisse von Straßenunebenheiten (1991). According to Mitschke, M.; Wallentowitz, H.: Dynamik der Kraftfahrzeuge (2014), p.343.

[51] Schollmaier, M.: Expert Interview - Quality of Driving Dynamics Area (2017).

Therefore, to extend the application potential of WMDS to available driving dynamics areas, this target value for the acceptable driving surface quality must be reached.

2.6 Overview of FZD's WMDS Concept

The MORPHEUS prototype, which is the prototype implementation of FZD's WMDS concept, together with a designation of the major components is presented in Figure 2-4. It consists of three wheel units, each equipped with a drive and a steering motor. Additionally, the emergency braking system and the hexapod, which is required for the TC, are depicted. A comprehensive overview of the MORPHEUS prototype and its components can be found in the thesis of Betz[52] and Wagner[53]. Hereinafter, only the hardware and software components that are relevant for the aspired investigations and developments are described.

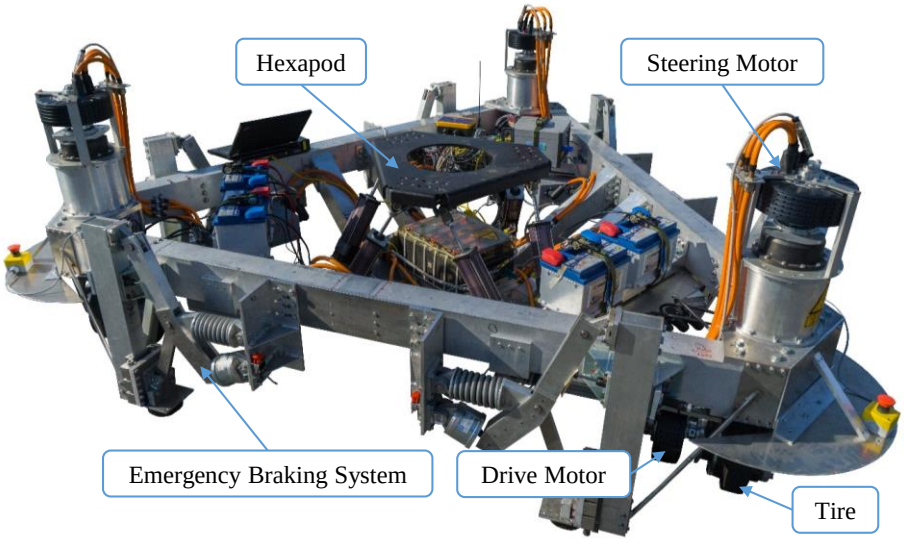

Figure 2-4: Overview of MORPHEUS prototype.

2.6.1 Hardware Components

2.6.1.1 Tires

The tires applied in the MORPHEUS prototype are solid press-on-band slick tires of type Softy, which are provided by Gumasol Rubber-Tec GmbH.[54] The radius amounts to 150 mm, the width is 75 mm. The tires offer a high load capacity at compact dimensions and low acceleration-induced angular motions of the WMDS. The horizontal tire force characteristics

[52] Cf. Betz, A.: Diss., Feasibility and Design of WMDS (2014).

[53] Cf. Wagner, P.: Diss., Practical Feasibility WMDS (2018).

[54] Cf. Gumasol Rubber-Tec GmbH: Datasheet Gumasol-Softy (2014).

were determined in tests with the prototype. It achieves a maximum friction coefficient of 0.8.[55] The tire has a low cornering stiffness and requires high longitudinal slip and slip angles to reach its maximum friction coefficient.[55]

2.6.1.2 Hexapod

The hexapod applied in the prototype MORPHEUS is a Mevea 1200E[56]. It consists of a bottom and a top plate, connected by six electric linear actuators. One possible input interface of the system are the positions in the six degrees of freedom (DoF). The positions are converted into the corresponding actuator lengths by an inverse kinematic calculation. The result is target values, which are the input to the internal cascade control of the actuators. Alternatively, the actuator lengths can be set directly.

The actuators are of type GSM30 of the company Exlar[57] and are each driven by a brushless DC-motor. The transformation from rotational to linear motion is realized by planetary screw spindle drives without self-locking. A representation and datasheet of the hexapod together with a datasheet of the implemented actuators are given in the appendix from Figure D.1 - 1 to Figure D.1 - 3.

2.6.1.3 Measurement Instrumentation

Several sensors are installed in the MORPHEUS prototype. The most relevant instrumentation for this work is the Automotive Dynamic Motion Analyzer (ADMA).[58] It consists of an inertial measurement unit that measures translational accelerations and rotational velocities and is combinable with GPS/DGPS in order to determine positions without drift. The separately determined signals are combined by an internal processing unit including a Kalmanfilter. The outputs are leveled and internally transformed into the center of gravity by correcting the installation offset.

2.6.2 Software Components

2.6.2.1 Control Architecture

The control architecture applied in MORPHEUS is shown in Figure 2-5. The scenario input is the demanded accelerations to be simulated, which would normally result from the driver

[55] Cf. Zöller, C. et al.: Vertical Dynamics WMDS (2019), p. 70.

[56] Cf. Mevea Ltd.: Mevea Motion Platform 1200E (2014).

[57] Cf. Exlar Automation: Exlar GSM (2014).

[58] Cf. GeneSys Elektronik GmbH: ADMA (2018).

input but also synthetically generated signals are applicable. The MCA transforms this acceleration demand into desired horizontal accelerations of the motion platform. The motion control determines the required steering angles and drive moments to achieve this motion. The control of the respective electric drives convert these set values, which results in a motion according to the dynamic characteristics of the platform.

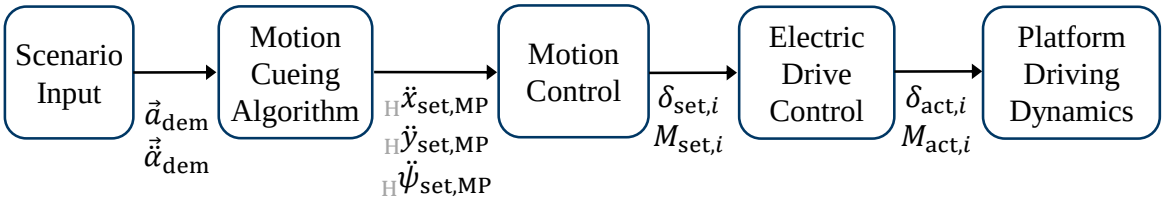

Figure 2-5: Control Architecture of the MORPHEUS prototype.

The respective components, especially the MCA, are comprehensively described by Betz.[52] In the following, the motion control (MC) is introduced because it affects the horizontal tire force distribution. Therefore, it is important for the impact of horizontal dynamics on the motions of the elastic elements within the WMDS.

2.6.2.2 Motion Control

The task of the motion control (MC) is to translate the motion demands from the MCA to the actuator inputs drive torque and steering angle. An overview of the MC applied in MORPHEUS, which was developed by Betz[59], is given in the appendix in Figure A.1 - 3.

The first step is to determine the required tire forces to generate the desired motions (step (a)). For this purpose, the acceleration and yaw demand are transformed into a force and a moment acting on the WMDS' center of gravity (CG). The determination of the required wheel forces to generate this overall demand is split into a translational and a yaw task according to Figure 2-6. For the translational task, all wheel forces are aligned in the same direction as the overall translational force in the CG, whereas the forces for the yaw demand are perpendicular to the triangle's symmetry axes.

For the translational task, the force distribution between the three wheels is adjusted to achieve equal friction utilization. This is done by calculating the dynamic wheel load at each wheel based on the desired acceleration of the CG and multiplying it with the friction coefficient resulting from the acceleration demand. The forces for the yaw demand are distributed equally between the wheels in order to avoid disturbances of the translational task. Prior to the determination of the required drive torque to generate this wheel force demand, the orientation of the wheel needs to be known in order to calculate the required longitudinal and lateral forces in the wheel coordinate system.

[59] Cf. Betz, A. et al.: Driving Dynamics Control of a WMDS (2013).

"To determine the necessary steering angle of the wheels, a kinematic model is used (step (b)). The velocity vectors resulting from the desired translational and rotational accelerations of the motion platform are calculated for each wheel. The angle between the resulting velocity vector and the x-axis of the driving simulator coordinate system is the necessary static steering angle if slip angles are neglected."[60]

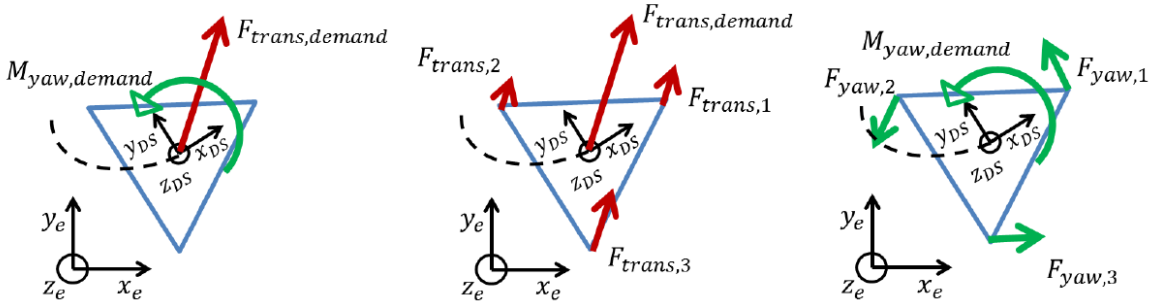

Figure 2-6: Division between translational and yaw demand.[61]

"An enhanced algorithm of the MC also considers slip angles. It is based on the target lateral force in tire coordinates resulting from the force demand calculation. The geometric relations for this calculation are shown in Figure A.1 - 3 step (c). The required slip angle to reach the target lateral force is calculated with a local numerical root-finding algorithm on the assumption of a linear cornering stiffness $c_{\alpha,i}$. Therefore, the following deviation between the target lateral force ${}_{\mathrm{W}}F_{\mathrm{W},y,i}$ and the linear force approximation $c_{\alpha,i}\alpha_i$ is minimized iteratively:

$$\Delta = \left|\vec{F}_{\mathrm{W},i}\right| \cdot \sin\left(\xi_i - \delta_{\mathrm{W,kin},i} - \alpha_i\right) - c_{\alpha,i}\alpha_i \tag{2.7}$$

With the force direction ξ. Afterwards, the estimated slip angle is added to the static steering angle to determine the required overall steering angle for each wheel."[60]

Based on the determined steering angle, the force demand is transformed into the wheel coordinate system. This enables the calculation of the drive torque from the desired longitudinal tire force and the effective roll radius.

[60] Zöller, C. et al.: Vertical Dynamics WMDS (2019).

[61] Betz, A. et al.: Concept Analysis of a WMDS (2012).

3 Methodology and Research Tools

3.1 Problem Analysis and Methodology

3.1.1 Problem Analysis

In this section, the problem that has been formulated in the working hypothesis is analyzed in more detail based on the presented fundamentals. Especially the question, in which ways the immersion is deteriorated has to be answered in order to derive suitable evaluation parameters. An overview of the problem is given in Figure 3-1. The simulator generates stimuli for all relevant channels presented in subchapter 2.3 with the shown components of the simulation system. As discussed in subchapter 2.3, a high immersion requires the plausibility of these channels.

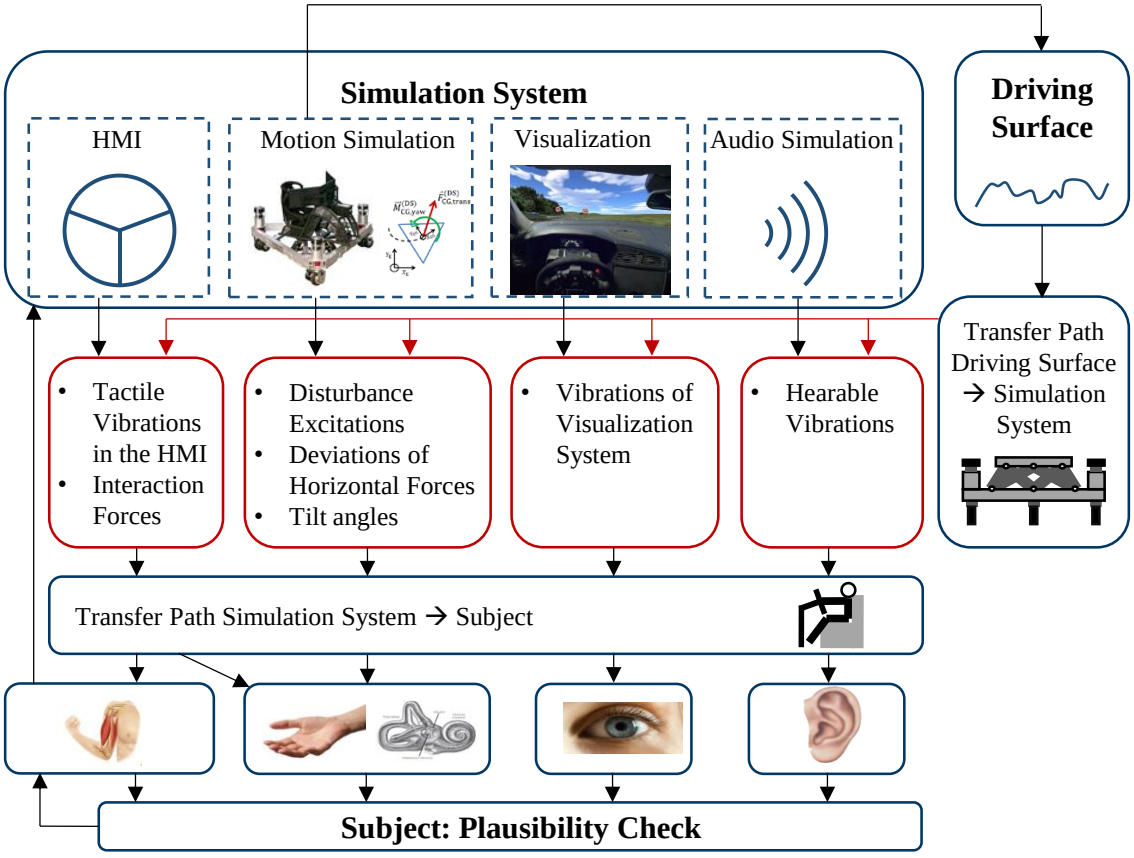

Figure 3-1: Problem description of driving surface induced vibrations.

The driving surface excitation, which is dependent on the trajectory given by the motion simulation, generates disturbances on the respective channels that are subject to the dynamics of the transfer path from excitation to simulation system. These disturbances generally

result in implausible signals of the sensory channels, which reduce the immersion and lead to simulator sickness in the worst case. Thus, to fulfill the criterion given by the working hypothesis of not deteriorating the immersion of the subject, the implausibility of the sensory channels must not exceed a perceptible degree.

Nevertheless, the consideration of all sensory channels and disturbances would go beyond the scope of this thesis. Therefore, boundaries of the investigated combinations are defined. According to Reason, especially the sensory mismatch between visual and vestibular perception is responsible for the occurrence of simulator sickness.[62] Therefore, it is assumed that the implausibility of these channels is the major impact on the immersion. Thus, this work focusses on the motion disturbances, which are whole-body vibrations in the range from 0.5 to 80 Hz according to section 2.4.2.

Other mismatches as for example the auditory disturbances also have an impact on immersion. Nevertheless, the problem is of another kind and has to be addressed with other measures (high-frequent acoustic damping). Future research has to investigate this aspect.

3.1.2 Methodology of Driving Surface Determination

The investigation of the working hypothesis requires a methodology for the determination of the acceptable driving surface quality, which is presented in Figure 3-2.

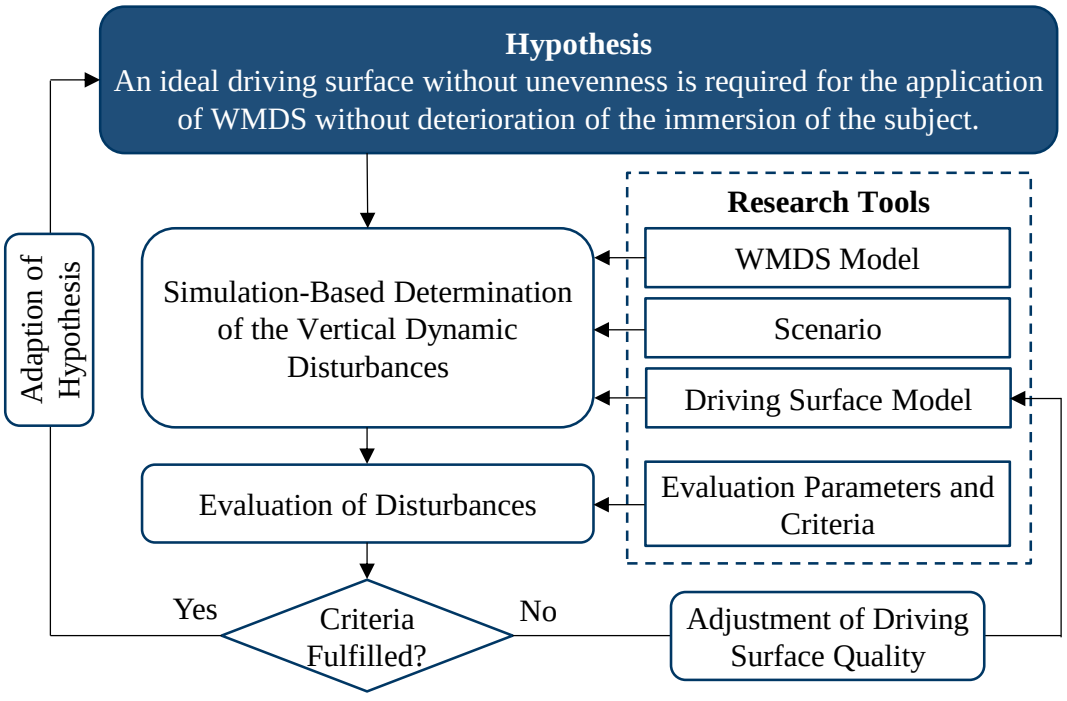

Figure 3-2: Methodology for the investigation of the working hypothesis.

[62] Reason, J. T.; Brand, J. J.: Motion Sickness (1975). According to: Fischer, M.: Diss., Motion-Cueing-Algorithmen (2009). p. 13.

An iterative simulation-based approach is applied for the determination of the acceptable driving surface quality. Based on a model of the WMDS and its components and a driving surface model, a representative scenario that is a typical application of WMDS is simulated. The resulting disturbances are evaluated based on pre-defined parameters. For each of these parameters, criteria are defined to determine if the disturbances are acceptable. If the criteria are not fulfilled, the driving surface quality is adjusted and the procedure is repeated. This is done until the criteria are met, which enables an adaption of the working hypothesis to the determined acceptable driving surface quality. A simulation-based approach is mandatory for the determination of the acceptable driving surface quality because an adjustment of the driving surface would not be practically feasible. In the following subchapters, the research tools labeled in Figure 3-2 are described.

3.2 Driving Surface Model

In the following, a driving surface model is derived that serves as input for the vertical dynamic simulation. Subsequently, based on this model, a description of the relation between the quality characteristics roughness coefficient and depth gauge is given. This step is required to assess the acceptable driving surface qualities determined in this work relative to the achievable qualities given in section 2.5.2.

3.2.1 Model

Contrary to passenger vehicles, a WMDS has no pre-defined driving direction but can move in any direction. Therefore, a surface model in two horizontal dimensions is required for the simulation of the WMDS' vertical dynamic behavior. However, the known road profile descriptions presented in subchapter 2.5 are given for one horizontal dimension. Therefore, an approach by Mack is applied in order to transform the 1D-description into a 2D-PSD assuming radial symmetry.[63] This requires the description of the stochastic process as an autocorrelation function. According to the Wiener-Khinchin theorem, the autocorrelation function of the 1D-PSD description in equation (2.6) is its inverse Fourier transform:

$$\Psi_{\mathrm{DSE}} = \frac{k_{\mathrm{Parc},1}}{2k_{\mathrm{Parc},2}} e^{-k_{\mathrm{Parc},2} r} \tag{3.1}$$

With the radius r for the position in polar coordinates. The next step is a 2D-Fourier transform in polar coordinates:

$${}^{\mathcal{F}}\Phi_{\mathrm{DSE,2D}} = \int_0^{\infty} \int_0^{2\pi} \Psi_{\mathrm{DSE}}(r) e^{-i2\pi\Omega_r \cos(\theta-\theta_0)} r dr d\theta \tag{3.2}$$

[63] Cf. Mack, C. A.: Analytic form of PSD (2011). pp. 1 f.

By calculating this equation based on the Hankel transform and substituting the polar spatial frequency Ω_r by the Cartesian spatial frequencies Ω_x and Ω_y, the following 2D-PSD description for a driving surface is derived:

$$ {}^{\mathcal{F}}\Phi_{\mathrm{DSE,2D}} = \frac{\pi k_{\mathrm{Parc,1}}}{\left[k_{\mathrm{Parc,2}}^2 + 4\pi^2\left(\Omega_x^2 + \Omega_y^2\right)\right]^{\frac{3}{2}}} \tag{3.3} $$

The next step is the generation of a driving surface description in the spatial domain. For that purpose, the 2D-amplitude spectrum is calculated from the PSD and multiplied with equally distributed random phases to account for the stochastic characteristic.[64] The resulting spectrum is transformed into the spatial domain with a 2D inverse Fourier transform.

To verify the derived model, the average PSD is determined for both directions. The results are shown in Figure 3-3 on the left. The model follows the description by Braun.[65] Additionally, at a frequency of 1 rad/m, the roughness coefficient of 1 cm³ is attained according to the setting of the parameter $k_{\mathrm{Parc,1}}$.

Another characteristic of a driving surface is the correlation between adjacent lanes, which are linearly dependent for sufficiently large wavelengths. This characteristic is described by the coherence.[66a] On the right side of Figure 3-3, this characteristic is compared to a coherence model proposed by Ammon.[66b]

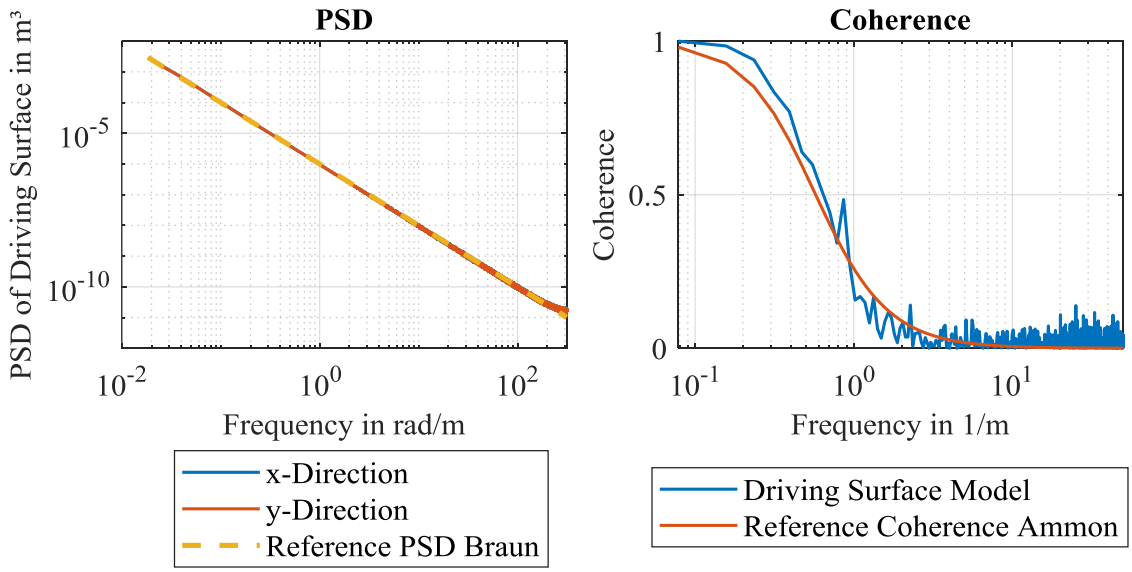

Figure 3-3: PSD and coherence of developed driving surface model.

[64] Quarz, V.: Diss., Generierung von Fahrwegstörungen (2004). p. 56.

[65] Cf. Braun, H.: Meßergebnisse von Straßenunebenheiten (1991).

[66] Cf. Ammon, D.: Problems in Road Surface Modelling (1992). a: p. 29; b: p. 35.

3.2.2 Relation of Quality Characteristics

The relation between the quality characteristics depth gauge and roughness coefficient described in section 2.5.1 is determined by analyzing the average depth gauge of the modelled stochastic driving surface with varying roughness coefficients over a length of four meters. The result is shown in Figure 3-4. The relation between depth gauge over a length of 4 m $\rho_{4\mathrm{m}}$ and roughness coefficient $\Phi_{\mathrm{DSE}}(\Omega_0)$ can be described by the following equation:

$$\rho_{4\mathrm{m}} = k_{\rho\Phi}\sqrt{\Phi_{\mathrm{DSE}}(\Omega_0)} \tag{3.4}$$

The coefficient $k_{\rho\Phi}$ is determined to 2.17 $\frac{\mathrm{mm}}{\sqrt{\mathrm{cm}^3}}$. Although the unit of the coefficient seems circumstantial, it is selected according to the units that are typically given in literature for the respective quality characteristics (cf. subchapter 2.5). Following from that, the **depth gauge of 2 mm**, which is the **target quality** for the application of WMDS according to section 2.5.2 approximately corresponds to a **roughness coefficient of 1 cm³**.

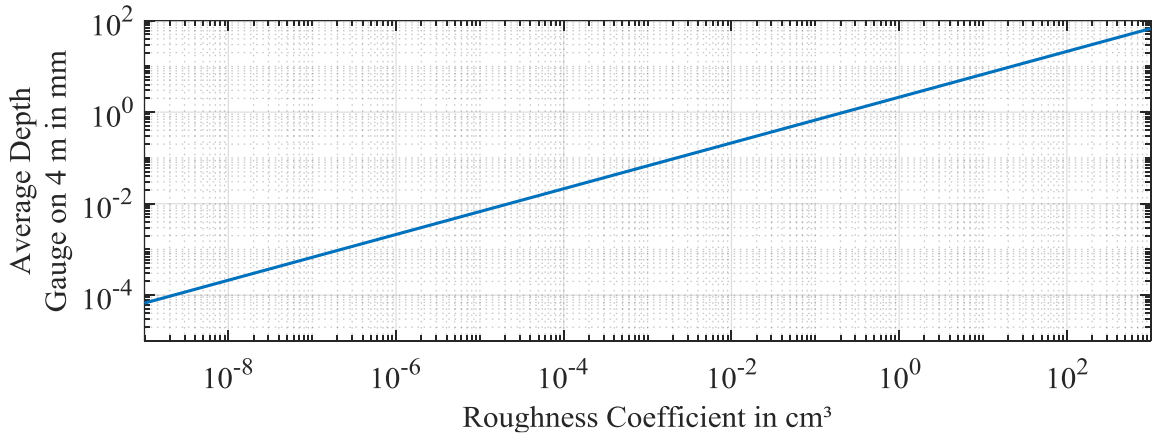

Figure 3-4: Relation between depth gauge and roughness coefficient determined by varying the roughness coefficient of the developed driving surface model.

3.3 Simulation Scenario

The trajectory of the simulator has a high impact on the disturbances induced by the driving surface. For example, higher velocities generate higher vibration magnitudes because the natural frequencies of the system are shifted to higher amplitudes of the excitation. Thus, to assess the impact of the disturbances, the investigation of a scenario that is a representative application for WMDS is required. The main motivation for WMDS is their potential in urban driving simulation resulting from their high range of motion. Therefore, a representative urban driving scenario is investigated that was developed within the project.[67] It was

[67] Cf. Graupner, M.: Bachelor Thesis, Entwicklung Stadtparcours (2011).

applied by Betz to analyze the requirements on the WMDS's motion capabilities.[68] These are shown in Figure 3-5. The requirements were determined based on a model in IPG Carmaker, which included the control architecture from section 2.6.2.1 and the mechanical parameters of the prototype.

It is recognizable that the scaling factor (cf. section 2.3.1) influences the velocity distribution. As discussed previously, this has an impact on the driving surface-induced disturbances and, thus, on the acceptable driving surface quality. In order to assess the impact of this aspect, the **three common scaling factors 0.5, 0.7 and 1 are investigated** concerning their acceptable driving surface qualities. For the adaption of the working hypothesis, the scaling factor of 0.7 is assessed because subjects are typically not able to differentiate this scaling to a factor of 1[69] and therefore the immersion is not disturbed, which is postulated by the hypothesis.

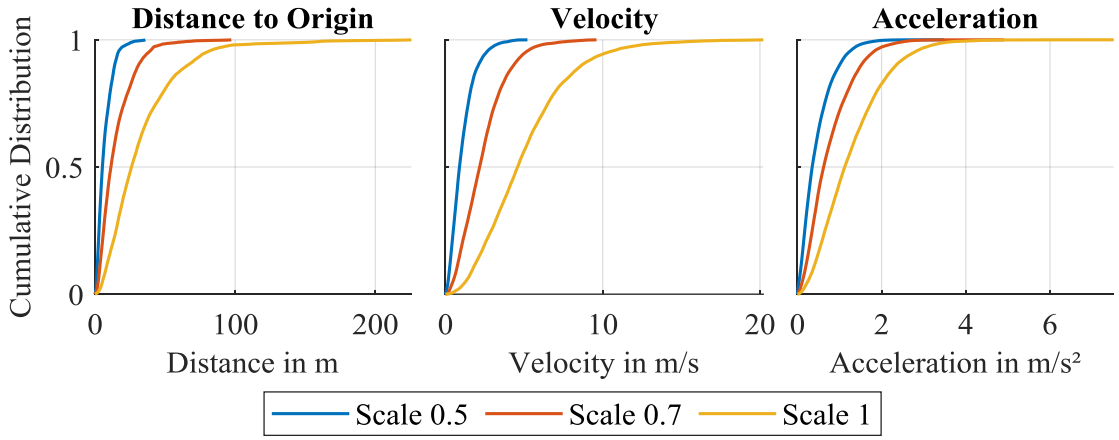

Figure 3-5: Simulator motions occurring during an urban driving scenario for different scaling factors determined with IPG Carmaker model including the control architecture from section 2.6.2.1.

3.4 Evaluation Parameters

In order to determine suitable evaluation parameters, the disturbances of the driving surface unevenness on the motions perceived by the vestibular organ are gathered. These are categorized as follows:

- **Direct disturbances:** Disturbances that are directly generated by the driving surface
- **Indirect disturbances:** Disturbances that are indirectly generated by the driving surface because a specific operational state is required
- **Horizontal dynamic disturbances:** Disturbances due to motions induced by horizontal accelerations

[68] Cf. Betz, A.: Diss., Feasibility and Design of WMDS (2014). pp. 93 ff.

[69] Cf. Berthoz, A. et al.: Motion Scaling for DS (2013).

The evaluation parameters have to address the human perception of the disturbance motions. Thus, the following parameters that are introduced in subchapter 2.4 are conceivable for the evaluation:

- Absolute, unfiltered accelerations isolated for each DoF
- Total vibration value
- Just noticeable difference (JND) described by Weber's Law

The aforementioned categories require different evaluation parameters. Therefore, the categories are analyzed for suitable evaluation parameters separately in the following.

3.4.1 Direct Disturbances

This aspect comprises all disturbances that are generated by the driving surface unevenness without requiring a specific operation state (except a velocity higher than zero):

- Translational and rotational motions due to driving surface excitation of the vibration system
- Horizontal translational motions due to the combination of rotational accelerations and the offset between pivot and position of the subject
- Horizontal translational disturbances due to tilt angles and resulting fractions of the gravitational acceleration

It is expected that the disturbances are partially not feeling unrealistic to the subject as these are typical motions occurring in a vehicle. Therefore, the JND could be applied to include the impact of superposed motions of the virtual vehicle into the evaluation. However, this would only be acceptable if a correlation between the driving surface excitation and the acceleration of the virtual vehicle were to exist. Otherwise, the evaluation would be based on a random coincidence of the acceleration of the virtual vehicle and intense excitations. This could result in an acceptable rating of a disturbance because at the same time a high acceleration of the virtual vehicle is acting at random, while it is unacceptable for other situations.

A correlation between acceleration and disturbance excitation intensity, which would allow this evaluation method, could result from a correlation between acceleration and driving velocity. However, an analysis of the scenario from subchapter 3.4 shows that this is not valid. A simple and relevant example scenario for the virtual vehicle is strong braking to a standstill after a long period of constant velocity. The simulator is returned to its origin by the washout due to the period without acceleration demand. Then the simulator is accelerated to simulate the braking motion. When the virtual vehicle reaches zero velocity, the simulator is at its maximum velocity. In that situation, strong disturbances occur while the subject expects no vibrations from the driving surface due to the standstill of the simulated vehicle.

Thus, it is demanded that the disturbance motions remain below the perception threshold independent of the motions of the virtual vehicle. The oscillatory characteristic of the dis-

turbances requires the consideration of the frequency dependence of human motion perception. Therefore, the **total vibration value** (cf. section 2.4.2) is selected as the evaluation parameter for this disturbance category. Not exceeding the **perception threshold of 0.015 m/s²** within the whole scenario is the criterion for the acceptability of a driving surface by means of the working hypothesis. Nevertheless, as discussed previously, a slight exceeding of the perception threshold is probably acceptable because the driver expects vibrations in a vehicle. Thus, the acceptable driving surface quality is also determined for an allowed exceeding occurrence of 10 % and 50 % to determine the improvement potential if vibrations turn out to be acceptable and to assess the sensitivity to the evaluation criterion.

3.4.2 Indirect Disturbances

Contrary to the previously analyzed category, the indirect disturbances can only occur if a specific operation state of the WMDS is fulfilled. This mainly applies to the disturbance of the horizontal tire forces by wheel load variations, which results in deviations from the desired horizontal accelerations.

Thus, contrary to the direct disturbances, a causal correlation between the motion of the virtual vehicle and the disturbance exists. Therefore, the evaluation of this disturbance is conducted based on the **just noticeable difference (JND)**. A shortcoming of the description in equation (2.3) is that the JND gets close to zero for small reference accelerations. For a reference stimulus of zero, however, the perception threshold would apply. Therefore, the following Weber ratio κ is defined for the evaluation based on the acceleration perception threshold a_{PT} and the Weber coefficient k_{Weber}:

$$\kappa = \frac{\Delta a}{\max(a_{\mathrm{PT}}, k_{\mathrm{Weber}} a_{\mathrm{ref}})} \tag{3.5}$$

This means a normalization of the acceleration deviation to the acting perception threshold. Therefore, a value of 1 corresponds to a disturbance that exactly meets the perception threshold. The value of a_{PT} is set to the absolute, unfiltered perception threshold of 0.2 m/s² from section 2.4.3.

3.4.3 Horizontal Dynamic Disturbances

This category comprises the disturbances that result from motions of the elements along the transfer path due to horizontal accelerations and are not excited by the driving surface. An example is motions of suspension springs for the support of wheel load transfers. A distinction is made between two types of disturbances: dynamic disturbances during transient acceleration variations and static, sustained disturbances that act during periods of constant acceleration. The dynamic disturbances are vertical, pitch and roll accelerations resulting from the moments of the horizontal forces and vertical support forces around the center of

gravity. These moments only occur until a new equilibrium state is reached. The static disturbances are generated by the tilt angles resulting from the motions required for this equilibrium. The tilt angles generate a horizontal component of the gravitational acceleration in the subject coordinate system, which leads to a sustained offset even during a constant acceleration period.

The first aspect is evaluated based on the **absolute and unfiltered disturbance accelerations**. Due to the lower variations of the horizontal accelerations compared to the excitations induced by the driving surface, the specific characteristics of vibration perception are not considered.

The evaluation criteria for this disturbance are the perception thresholds from section 2.4.3. Although a reference motion of the virtual vehicle exists during this phase, which could result in a realistic feeling of the motions, the motions of the WMDS will generally not match those of the virtual vehicle. On the one hand, especially the angular motions of the WMDS could have another direction than those of the virtual vehicle because of support forces. On the other hand, the natural frequency and damping of the WMDS are generally different from those of the virtual vehicle. Therefore, the disturbance motions should remain below the perception thresholds to avoid these mismatches.

The second aspect is only relevant if a reference acceleration is acting that generates a sustained tilt of the subject. Therefore, similar to the indirect disturbances by wheel load variations, a causal correlation between horizontal acceleration and disturbance applies. Thus, the **JND** is selected as an evaluation parameter. However, in this case not only the acceleration magnitude but also the direction could be disturbed because the disturbance direction induced by the tilt angle might not match the direction of the reference acceleration. Therefore, both aspects are evaluated. The magnitude deviation is assessed based on the Weber ratio from equation (3.5). Additionally, the difference between desired and disturbed direction is evaluated and the perception threshold of 6° from section 2.4.4 is applied as a criterion.

3.4.4 Interaction of the Disturbances

The previous sections showed that different evaluation parameters have to be applied to different sources of disturbance. The impact of the interaction of these disturbances, however, is unknown. For example, if indirect and direct disturbances both exactly meet their respective perception thresholds, it is unclear whether the superposed disturbances are perceptible. Nevertheless, as discussed, the compliance of the direct disturbances to the perception threshold is already a strong criterion, yielding a conservative estimation of the acceptable driving surface. Additionally, especially in the described critical situation with the virtual vehicle at standstill and the simulator at high velocity, no disturbance other than the direct one can occur due to the lack of horizontal accelerations. Thus, for this thesis, it is assumed that if the direct disturbances are below the perception threshold, their influence on the evaluation of the indirect and horizontal dynamic disturbances is negligible due to the additional masking effect of the horizontal acceleration.

This enables the isolated investigation of the respective disturbance categories. First, the acceptable driving surface quality is determined for direct disturbances. Subsequently, the impact of the indirect and horizontal dynamic disturbances is determined on this driving surface. Although the interaction of the disturbances is not assessed by this methodology, it enables the evaluation of the impact of the different sources of disturbances.

3.4.5 Summary

The derived evaluation parameters and evaluation criterions are summarized in Table 3-1. The main aspect for the determination of the acceptable driving surface quality is the direction disturbance. In subsequent investigations, it is evaluated whether the other disturbances are also below an acceptable level.

Table 3-1: Evaluation Parameters.

Disturbance Source	Explanation	Evaluation Parameter	Evaluation Criterion
Direct	Vibrations excited by the driving surface	Total vibration value	<0.015 m/s²
Indirect	Horizontal force deviations due to wheel load variations	Weber Ratio	<1
Transient Horizontal Dynamic	Accelerations of WMDS due to moments resulting from horizontal forces	Absolute Accelerations rot. Velocities	<0.2 m/s²; 6 °/s; 6°/s²
Static Horizontal Dynamic	Static angles of the WMDS due to moments resulting from horizontal forces	Weber Ratio	<1
		Direction Deviation	<6°

3.5 Model Structure

The models applied for the investigation of the evaluation parameters are dependent on the considered system configuration. Therefore, the models are presented for each system configuration in the respective chapters. However, the applied model structure that addresses the evaluation parameters shown in Figure 3-6 is derived. The top-level input into the model structure is the urban driving scenario from subchapter 3.3. The demanded translational and rotational accelerations are transferred to the Carmaker model of the WMDS developed by Betz.[70] It contains the control architecture and the driving dynamics of the motion platform.

[70] Cf. Betz, A.: Diss., Feasibility and Design of WMDS (2014). pp. 95 ff.

The output trajectory of the WMDS is sampled by the driving surface model from subchapter 3.2 to obtain the vertical driving surface excitation, which is the input for the vertical dynamics model. This model determines the evaluation parameters for the direct and the horizontal disturbances. Additionally, the wheel loads and their variations are determined and fed to an isolated horizontal tire model. That enables the isolated investigation of the wheel load variation impact for different reference accelerations. The tire is described based on a fully nonlinear single contact point transient tire model combined with the Magic Formula 5.2.[71] The model parameterization and validation were done in previous works based on tests with the MORPHEUS prototype.[72] The resulting Weber ratio for the indirect disturbances and the output evaluation parameters of the vertical dynamics model are then evaluated concerning their perceptibility.

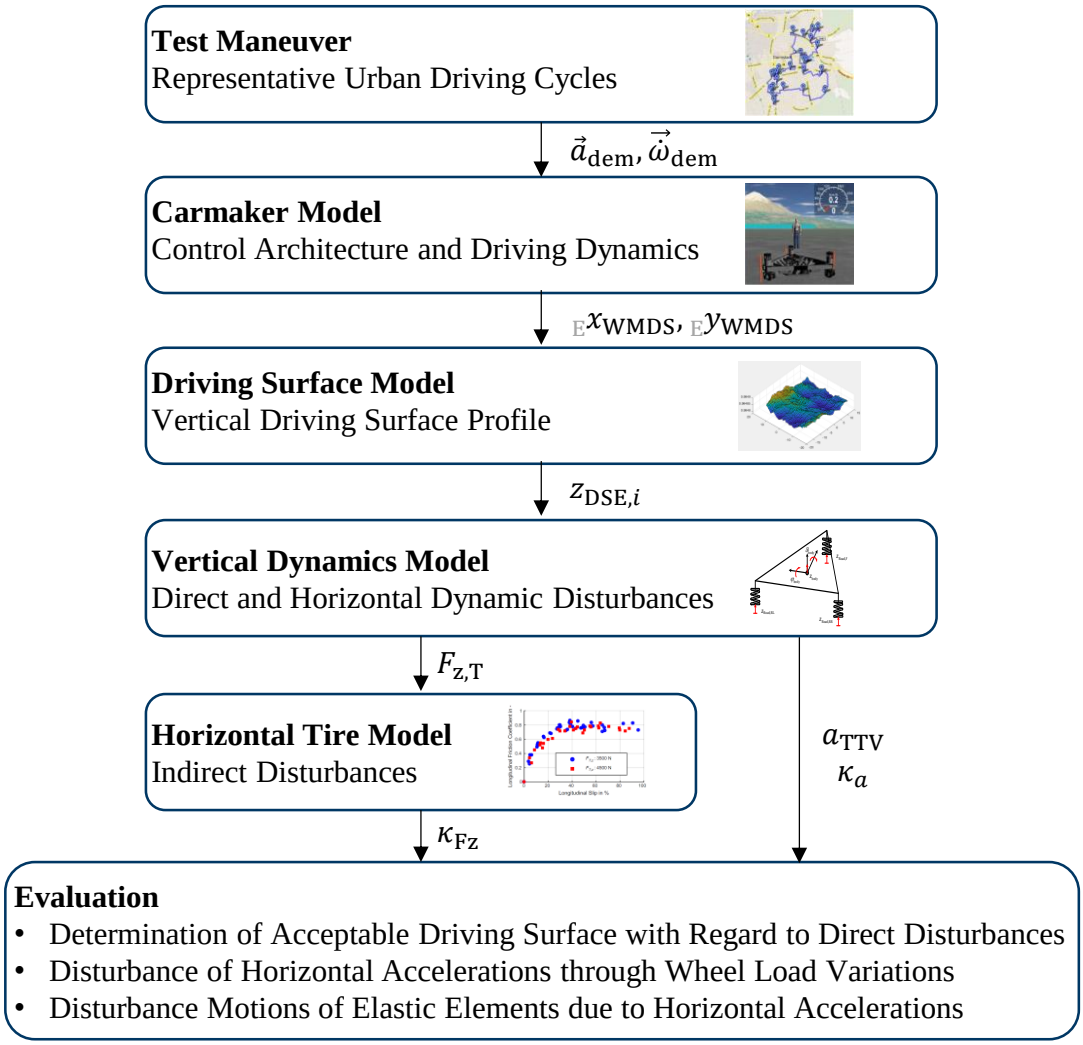

Figure 3-6: Applied model structure.

[71] Cf. Pacejka, H. B.; Besselink, I.: Tire and vehicle dynamics (2012).

[72] Cf. Zöller, C.: Masterthesis, Reifenmodell WMDS (2015).

4 Analysis of Initial Situation

Based on the developed methodology and research tools, this chapter aims at investigating the current system configuration of the MORPHEUS prototype, which is equipped with solid tires. This allows the assessment of the initial situation and of the demand for further improvements of the vertical dynamic behavior. The methodology of this chapter is shown in Figure 4-1. The first step is the measurement-based system identification, which is divided into the component identification of the tire and the identification of the overall system. Based on the determined system characteristics, a vertical dynamic model is derived. The model is then validated in further experiments. Subsequently, the validated model enables the evaluation of the acceptable driving surface quality.

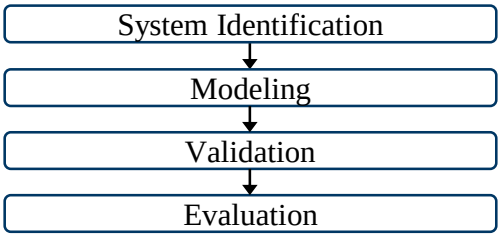

Figure 4-1: Methodology of the analysis of the initial situation.

4.1 System Identification

The system identification is started on component level for a better understanding of the system behavior. The dominant elastic component along the transmission path from the driving surface to the subject is the tire, which is therefore identified statically on a hydraulic shaker. The analysis is restricted to the determination of the stiffness. Findings from the research concerning pneumatic tires have shown that the damping of a rolling tire could be a factor 10 smaller compared to the static condition.[73] Additionally, other damping effects for example from joint patches or material damping could have a relevant impact on the overall damping. Therefore, the damping is only determined for the overall system in the next step. This overall system identification is also conducted to adapt the determined static stiffness to the rolling condition.

[73] Cf. Pacejka, H. B.; Besselink, I.: Tire and vehicle dynamics (2012). p. 636.

4.1.1 Component Identification: Tire Stiffness

In order to identify the elastic properties of the tire, experiments are conducted on a hydraulic shaker. A plate is pressed vertically against the tire in discrete steps of 0.2 mm. The resulting force is measured with a load cell. The resulting force deflection characteristic is shown in Figure 4-2. Two tire conditions are tested to identify the time variance of the behavior. The new tire has a radial rubber thickness of 3 cm, the worn tire 2 cm. Highly nonlinear behavior is recognizable. The reason for this is the growth of the tire contact patch. Each radial element has an elastic behavior that increases the element force over its deflection. Additionally, a larger contact patch results in a higher amount of radial elements that contribute to the overall force.

The nonlinear elastic force $F_{z,c,\mathrm{T}}$ can be described with a quadratic function of the tire deflection Δz_T:

$$F_{z,c,\mathrm{T}} = c_{\mathrm{T},2}\Delta z_\mathrm{T}^2 + c_{\mathrm{T},1}\Delta z_\mathrm{T} \tag{4.1}$$

With the parameters $c_{\mathrm{T},2}$ (New Tire: 113.7 N/mm², Worn Tire: 441.5 N/mm) and $c_{\mathrm{T},1}$ (New Tire: 353.7 N/mm, Worn Tire: 265.9 N/mm). The stiffness characteristic is approximated with the following linear approach at the static wheel load:

$$c_{\mathrm{T,lin}} = 2c_{\mathrm{T},2}\left(-\frac{c_{\mathrm{T},1}}{2c_{\mathrm{T},2}} + \sqrt{\left(\frac{c_{\mathrm{T},1}}{2c_{\mathrm{T},2}}\right)^2 + \frac{F_{z,\mathrm{stat}}}{c_{\mathrm{T},2}}}\right) + c_{\mathrm{T},1} \tag{4.2}$$

Wear has a high impact on the stiffness characteristic of the tire because the length of the radial elements reduces. The linear approximation of the new tire at the static wheel load yields a stiffness of 1300 N/mm, whereas that of the worn tire amounts to 2480 N/mm. With a third of the overall platform mass of 1052 kg this corresponds to estimated natural frequencies of 9.7 Hz and 13.4 Hz.

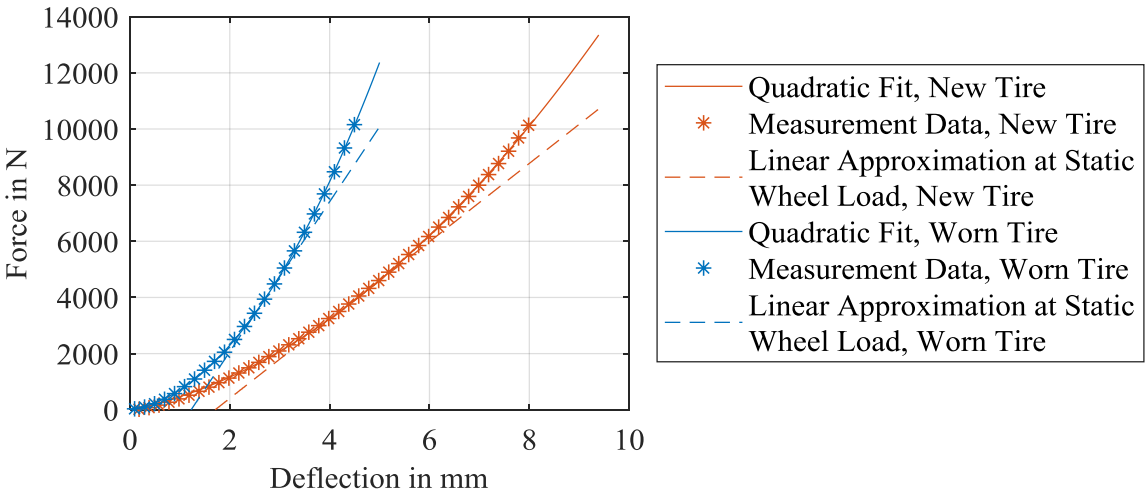

Figure 4-2: Static force-deflection characteristic of the solid tire determined on a hydraulic shaker.

4.1.2 Overall System Identification

The described component identification of the static tire only yields a first estimation of its characteristic. The typical behavior known from pneumatic tires is a reduction of the vertical stiffness of a rolling compared to a static tire. Earlier research has shown that this is mainly due to a reduction of the sidewall stiffness.[74] Therefore, the rubber-metal structure seems to have the highest impact on the stiffness difference. Thus, the influence of rolling on the behavior of solid tires is expected to be even higher. Therefore, an adaption of the determined static stiffness to the rolling condition is conducted in this section. Additionally, the overall system damping is determined.

4.1.2.1 Methodology

The system behavior is determined based on an analysis of its step response. The excitation is generated by a metal bar with a height of 6 mm and a width of 50 mm. In order to avoid multiple excitations that interfere with each other, only one wheel of the simulator is driven across the metal bar. The vertical acceleration and the pitch and roll rates are determined with the ADMA that is described in section 2.6.1.3. The angular accelerations are determined by calculating the derivative of the measured angular rates.

The tests were conducted on the August-Euler-Airfield in Griesheim. Although a place with low surface unevenness is selected for the tests, disturbance excitations cannot be avoided. To compensate for the influence of these undesired disturbances, the metal bar is relocated every fifth trial of the tests. This procedure is conducted 10 times, resulting in an overall scope of 50 trials. The maximum amplitude of the vertical accelerations is applied as an indicator for the time of crossing the step in order to synchronize the specific measurement results to each other. The accelerations resulting from disturbance excitations have random phases, resulting in a mutual distinction of these oscillations when the results are averaged for the different positions of the metal bar. Because of the synchronization, the step response has equal phases for all measurements, so that it is isolated from the disturbance excitations. The remaining step response allows the determination of the system parameters.

4.1.2.2 Natural Frequency Determination

The dominant natural frequency is determined based on a Fourier-transform of the measured vertical and angular accelerations. The complex Fourier descriptions are averaged over all conducted trials. The resulting PSD spectra are shown in Figure 4-3.

The natural frequency of the vertical accelerations amounts to 8 Hz, which is 82% of the natural frequency estimated from the component identification in section 4.1.1. Thus, the

[74] Cf. Zegelaar, P. W.: Diss., Dynamic response of tyres (1998). pp. 164 ff.

expected influence of rolling on the tire stiffness is recognizable. To account for this, a velocity reduction factor k_{Roll} is introduced that is multiplied with the total tire force from equation (4.1), so that both fractions of the force are equally reduced. It is determined from the linear approximation of the stiffness in equation (4.2). The linearized stiffness around the static wheel load is required to be 67 % lower to achieve the desired reduction of the natural frequency, which is described by the stiffness reduction factor $k_{c,\mathrm{red}}$. By inserting these factors into equation (4.2) and solving it for the velocity reduction factor k_{Roll}, the following relation is found:

$$k_{\mathrm{Roll}} = \frac{c_{\mathrm{T,lin}}^2 k_{c,\mathrm{red}}^2}{2F_{z,\mathrm{stat}} c_{\mathrm{T},2} + \sqrt{4F_{z,\mathrm{stat}}^2 c_{\mathrm{T},2}^2 + c_{\mathrm{T,lin}}^2 c_{\mathrm{T},1}^2 k_{c,\mathrm{red}}^2}} \tag{4.3}$$

Substitution of the respective parameters with their numeric values from section 4.1.1 yields a velocity reduction factor of 0.49.

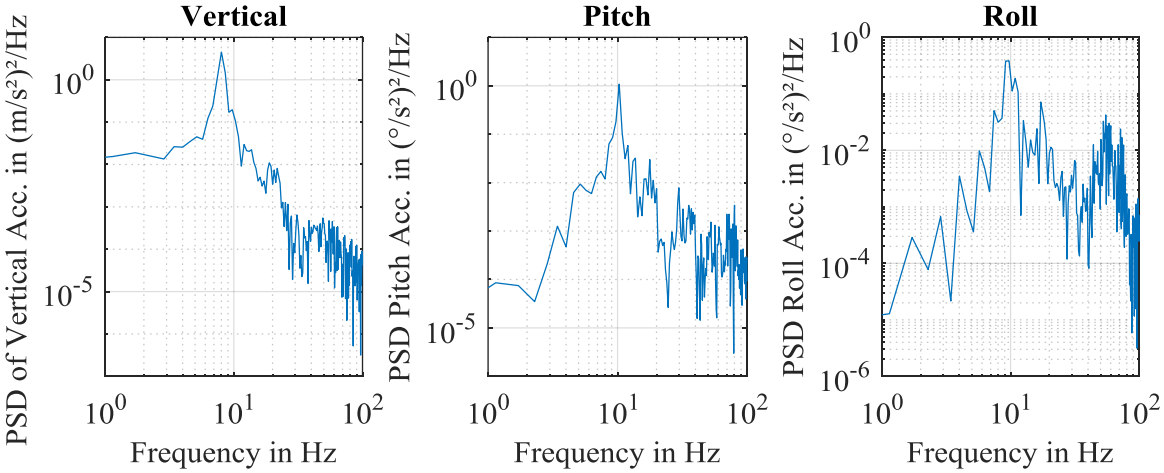

Figure 4-3: PSD spectra of measured accelerations resulting from step excitation.

4.1.2.3 Damping Determination

The determination of the damping characteristic is based on the analytic signal, which is determined with the Hilbert transform. The transformation is conducted according to the steps given in appendix A.4. To limit the disturbances induced by high-frequent fractions, only frequencies around the natural frequency between 4 and 12 Hz are considered. Based on the resulting envelope of the acceleration signal ${}_{\mathrm{H}}\ddot{z}_{\mathrm{Env,CG,Cut}}$, the damping characteristic is determined from an analysis of the decay behavior. For viscous damping behavior, the following behavior applies for the envelope of the oscillation signal:[75]

$${}_{\mathrm{H}}\ddot{z}_{\mathrm{Env,Vis}} = {}_{\mathrm{H}}\ddot{z}_{\mathrm{Env,Vis,0}} e^{-D\omega_0 t} \tag{4.4}$$

The derivative of this envelope can be written as follows:

[75] Cf. Magnus, K. et al.: Schwingungen (2016), p. 63.

$$\frac{\mathrm{d}\left({}_{\mathrm{H}}\ddot{z}_{\mathrm{Env,Vis}}\right)}{\mathrm{dt}} = -D\omega_0 {}_{\mathrm{H}}\ddot{z}_{\mathrm{Env,Vis}} = -\frac{d_{\mathrm{T}}}{\frac{2}{3}m_{\mathrm{WMDS}}} {}_{\mathrm{H}}\ddot{z}_{\mathrm{Env,Vis}} \tag{4.5}$$

Thus, by determining the gradient of the acceleration dependent on its magnitude, the damping coefficient of the tires can be derived. If the measurement results follow this relation of a constant gradient over the acceleration amplitude, the viscous behavior is the dominant damping fraction.

The gradient of ${}_{\mathrm{H}}\ddot{z}_{\mathrm{Env,CG,Cut}}$ is calculated separately for each trial with a step width of 0.01 s and the discrete points of the gradient vs. magnitude are summarized in a resulting vector. Because of disturbances from undesired excitations, a high variation between the different trials arises. In order to determine a trend within these varying values, which results from the equal step excitation in all trials, an averaging is conducted. The resulting relation between gradient and magnitude as well as a linear approximation is shown in Figure 4-4.

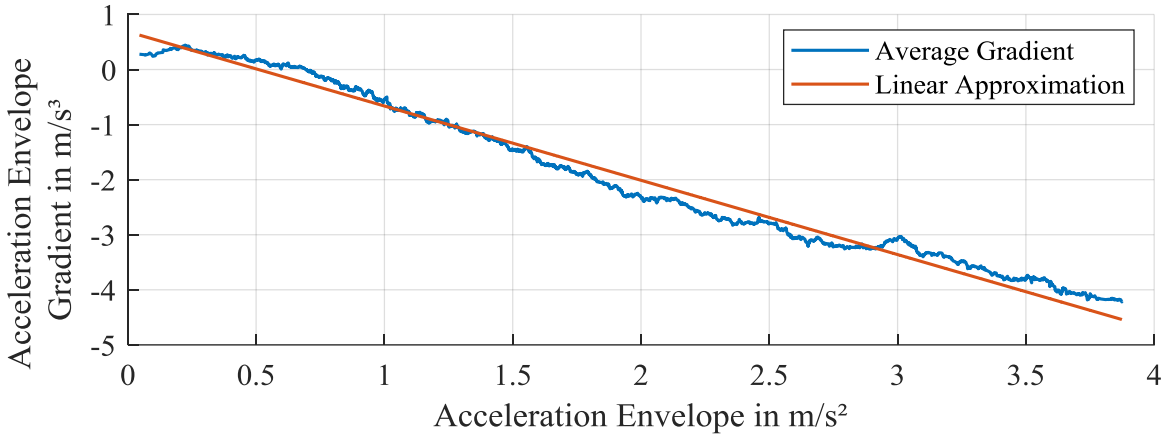

Figure 4-4: Acceleration envelope gradient vs. acceleration envelope determined in and averaged over 30 measurements of a step response. With regard to the time course, the graph is read from the bottom right (highest acceleration magnitude directly after the step).

The linear approximation of the gradient offers a high coefficient of determination (R^2=0.98) and is therefore suitable for the description of the decay characteristic. Thus, the viscous fraction is the dominant damping component. The damping constant is determined to 0.95 Ns/m.

4.2 Modeling

The model for the vertical vibration system is depicted in Figure 4-5. It consists of the body and the tire springs, which are, as described, the main elastic element along the transmission path from the driving surface to the subject and, thus, are dominant for the dynamics of the system. The differential equations for this system are derived with Newton's Second Law:

$$m_{\mathrm{B}} {}_{\mathrm{H}}\ddot{z}_{\mathrm{B}} = {}_{\mathrm{H}}F_{z,(c,d),\mathrm{T,f}} + {}_{\mathrm{H}}F_{z,(c,d),\mathrm{T,rl}} + {}_{\mathrm{H}}F_{z,(c,d),\mathrm{T,rr}} \tag{4.6}$$

$$J_{\mathrm{B},y}^{(\mathrm{CG})}\,{}_{\mathrm{H}}\ddot{\vartheta}_{\mathrm{B}} = -\frac{1}{\sqrt{3}}\,{}_{\mathrm{H}}F_{z,(c,d),\mathrm{T,f}}\ell_{\mathrm{t}} + \frac{1}{2\sqrt{3}}\ell_{\mathrm{t}}\left({}_{\mathrm{H}}F_{z,(c,d),\mathrm{T,rl}} + {}_{\mathrm{H}}F_{z,(c,d),\mathrm{T,rr}}\right) \tag{4.7}$$

$$J_{\mathrm{B},x}^{(\mathrm{CG})}\,{}_{\mathrm{H}}\ddot{\varphi}_{\mathrm{B}} = \frac{1}{2}\ell_{\mathrm{t}}\left({}_{\mathrm{H}}F_{z,(c,d),\mathrm{T,rl}} - {}_{\mathrm{H}}F_{z,(c,d),\mathrm{T,rr}}\right) \tag{4.8}$$

with the body mass m_{B} and the mass moments of inertia around the center of gravity $J_{\mathrm{B}}^{(\mathrm{CG})}$. The geometric quantity ℓ_{t} is the distance between the wheels, which is equal to the edge length of the equilateral triangle connecting them. The tire stiffness is described as a square function of the deflection with the tire stiffness coefficients $c_{\mathrm{T},1}$ and $c_{\mathrm{T},2}$, according to the findings from section 4.1.1. This characteristic is adapted with a roll factor k_{Roll} to account for the reduced natural frequency that has been determined for the rolling tire in section 4.1.2.2. The determined decay behavior from section 4.1.2.3 showed an exponential behavior. Therefore, tire damping is modeled as a viscous damper with the damping constant d_{T}. This results in the following description of the tire forces as a function of the driving surface excitation $z_{\mathrm{DSE},i}$:

$${}_{\mathrm{H}}F_{z,c,\mathrm{T},i} = k_{\mathrm{Roll}}\left(c_{\mathrm{T},1}\left({}_{\mathrm{H}}z_{\mathrm{DSE},i} - {}_{\mathrm{H}}z_{\mathrm{B,W},i}\right)^2 + c_{\mathrm{T},2}\left({}_{\mathrm{H}}z_{\mathrm{DSE},i} - {}_{\mathrm{H}}z_{\mathrm{B,W},i}\right)\right) \tag{4.9}$$

$${}_{\mathrm{H}}F_{z,d,\mathrm{T},i} = d_{\mathrm{T}}\left({}_{\mathrm{H}}\dot{z}_{\mathrm{DSE},i} - {}_{\mathrm{H}}\dot{z}_{\mathrm{B,W},i}\right) \tag{4.10}$$

The required motions of the body at the wheel positions ${}_{\mathrm{H}}z_{\mathrm{B,W},i}$ are calculated from the motions in the center of gravity (CG) of the body, which is the center of the WMDS:

$${}_{\mathrm{H}}z_{\mathrm{B,W,f}} = {}_{\mathrm{H}}z_{\mathrm{B}} - \frac{1}{\sqrt{3}}\,{}_{\mathrm{H}}\vartheta_{\mathrm{B}}\ell_{\mathrm{t}} \tag{4.11}$$

$${}_{\mathrm{H}}z_{\mathrm{B,W,rl}} = {}_{\mathrm{H}}z_{\mathrm{B}} + \frac{1}{2}\,{}_{\mathrm{H}}\varphi_{\mathrm{B}}\ell_{\mathrm{t}} + \frac{1}{2\sqrt{3}}\,{}_{\mathrm{H}}\vartheta_{\mathrm{B}}\ell_{\mathrm{t}} \tag{4.12}$$

$${}_{\mathrm{H}}z_{\mathrm{B,W,rr}} = {}_{\mathrm{H}}z_{\mathrm{B}} - \frac{1}{2}\,{}_{\mathrm{H}}\varphi_{\mathrm{B}}\ell_{\mathrm{t}} + \frac{1}{2\sqrt{3}}\,{}_{\mathrm{H}}\vartheta_{\mathrm{B}}\ell_{\mathrm{t}} \tag{4.13}$$

All motions are defined to zero in the static equilibrium state.

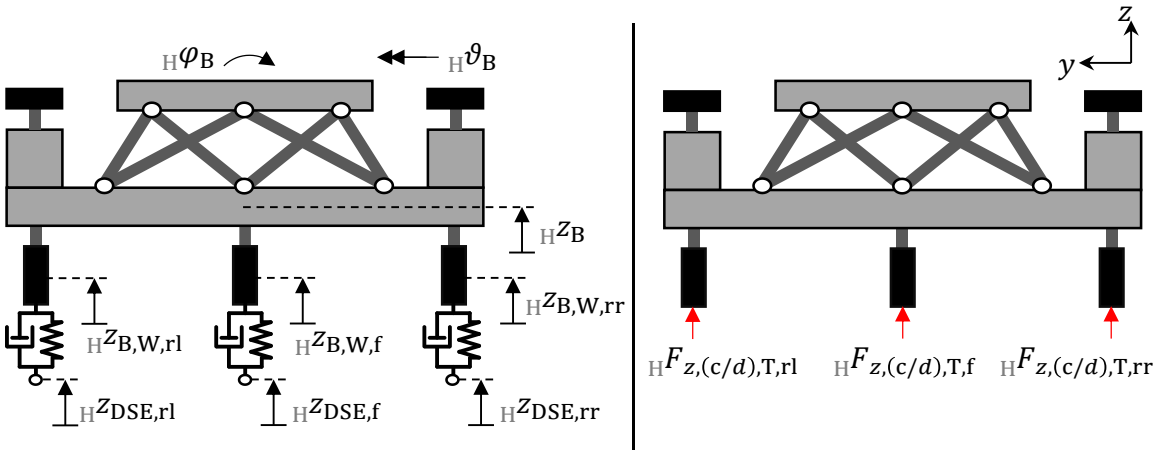

Figure 4-5: Vertical vibration system model.

4.3 Validation

The methodology for the validation is shown in Figure 4-6. The first step is the selection of a real driving surface profile for the validation test drive. This profile needs to be digitalized to serve as an input for the comparison simulation. Subsequently, test drives and simulations are conducted and compared in order to assess the simulation's validity and its limitations.

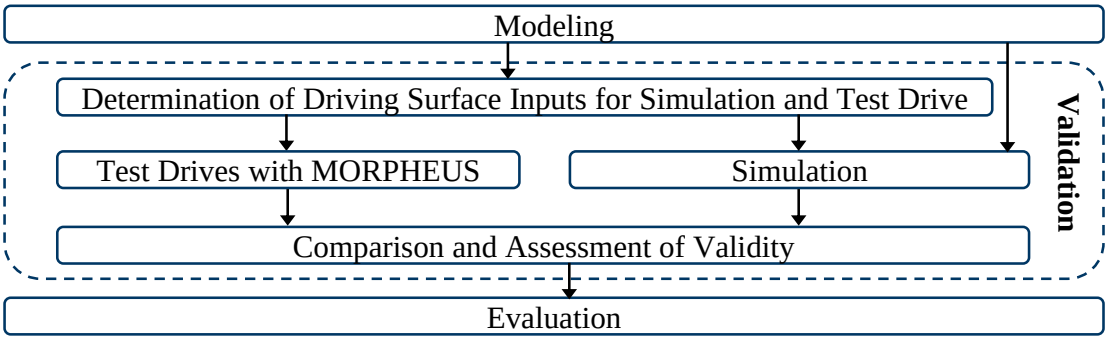

Figure 4-6: Validation methodology.

4.3.1 Determination of Input Signals

4.3.1.1 Methodology

For the determination of driving surface profiles that serve as an input for the validation simulation, the driving surface profile measurement system (DSPMS) from Figure 4-7 is applied.[76] The main part of the DSPMS is the laser-ground-sensor (LGS), which is moved along a linear guide by an electric drive. It measures the distance to the ground with an accuracy of 0.5 mm[77] and the velocity over ground, from which the longitudinal movement distance is integrated with an accuracy of 6 m/h[77]. The linear guide is connected to two base units by spherical joints. The height of the spherical joints is adjustable via vertical adjustment guides.

The aim of this mechanism is to hold a constant height relative to the start point of the measurement independently of the driving surface unevenness over a long distance. Therefore, the system is placed along the track to be measured and the base units are fixed. The vertical adjustment guides together with a precise level (accuracy: 0.02 mm/m) are used to adjust an inclination of 0°. In the next step, the LGS measures the first section of the driving surface profile from the beginning to the end of the linear guide. To measure the next section, the rear base unit is rotated around the spherical joint of the front base unit. Afterward, the height of the spherical joint of the displaced base unit is again adjusted with the help of the vertical

[76] Cf. Banic, M. et al.: Advanced Design Project 82/16, Anlage Vermessung Fahrbahnprofile (2016).

[77] Cf. A&D GmbH: Vehicle Measurement System Description (2013).

adjustment guide to an inclination of 0°. Because the height of the stationary base unit is still the same, the level of the linear guide and therefore the LGS relative to the start point remain constant, even if the base unit is displaced vertically by driving surface unevenness.

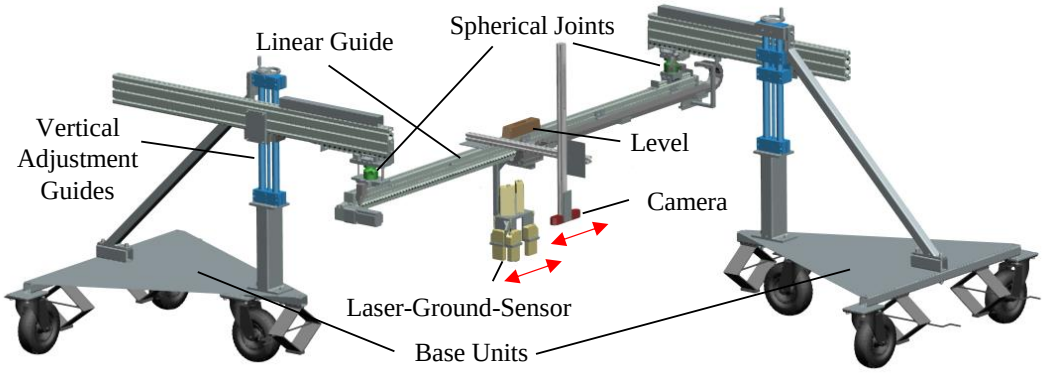

Figure 4-7: Driving surface profile measurement system.

The system is only suitable for the measurement of line profiles. Therefore, three lanes for the respective wheels of the simulator are measured over a length of 40 m.

4.3.1.2 Results

The results of the driving surface profile measurement are shown in Figure 4-8.

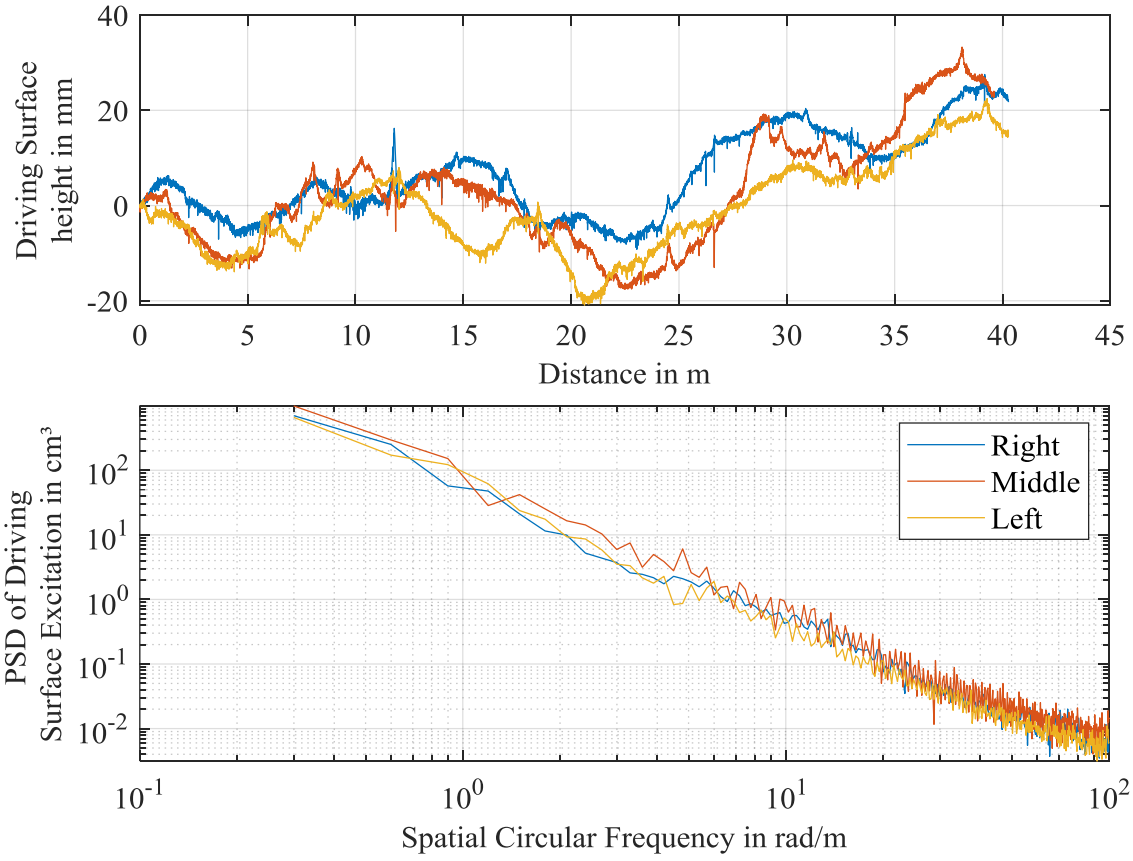

Figure 4-8: Results of driving surface profile measurement in spatial and frequency domain.

The maximum height deviation over a length of 40 m amounts to 48 mm. The Power spectral densities of the three measured lanes are in a similar range. The slope of the PSD is approximately -20 dB/decade and therefore matches the value for typical roads from the literature that was described in subchapter 2.5. The roughness coefficient (PSD at reference frequency 1 rad/m) lies between 40 and 100 cm³, which corresponds to a class D surface according to Table 2-2.

4.3.2 Test methodology

The general test setup is to drive the prototype along the measured lanes and record the vertical accelerations and the angular rates. However, the compliance to the measured lane is difficult because the prototype is steered manually. Therefore, 30 trials are conducted so that on average the correct excitation is acting on the WMDS. Additionally, based on the multiple trials, a range of the measurement results is determined, which serves as a validity criterion. This is sufficient since the main purpose of the model is to determine the vertical excitations on stochastic driving surfaces, which inherently always show variations. This stochastic variation is included here as a deviation from the measured lane. Based on the range of the measurement results, the accuracy of the driving surface determination can be estimated.

4.3.3 Validation Results

The results are evaluated in the frequency domain. The signals are zero-phase filtered with a Butterworth filter of second order at a limit frequency of 100 Hz, which is the relevant range of whole-body vibrations according to section 2.4.2. The signals are windowed with a Hanning window to reduce the influence of side lobes resulting from leakage and then Fourier transformed. Subsequently, based on the determined spectra, the octave r.m.s. are calculated according to an approach by Claus[78]. The respective minimum and maximum values of the trials are determined for each octave. The resulting PSD spectra are shown in Figure 4-9. Despite a slight undercut at the first and the fifth middle frequency, the vertical r.m.s. values of the simulation are within the range of the measured values. The pitch frequency is valid up to the fifth octave, beyond which the model estimates too low magnitudes. For the roll frequency, the limit of validity is reached at the fourth octave and the deviations beyond that limit are higher than for the pitch DoF.

However, for the purpose of the model, the level of validity is considered to be sufficient even though not the whole frequency range of whole-body vibrations is valid. The fraction of the vertical DoF on the total vibration value (cf. section 2.4.2), which is the criterion for the determination of the acceptable driving surface quality, is about 99.3 %. Therefore, the

[78] Cf. Claus, S.: Diss., Kompensation Verzugszeiten semiaktive Fahrwerkregelung (2016). pp. 31-32.

impact of the deviations due to the angular DoFs is small. This is probably the reason for the deviation between measurement and simulation at high frequencies. The natural frequency oscillations excited by the driving surface have low power, resulting in an increased influence of other high-frequent excitations that are not modeled, e.g. from the drivetrain.

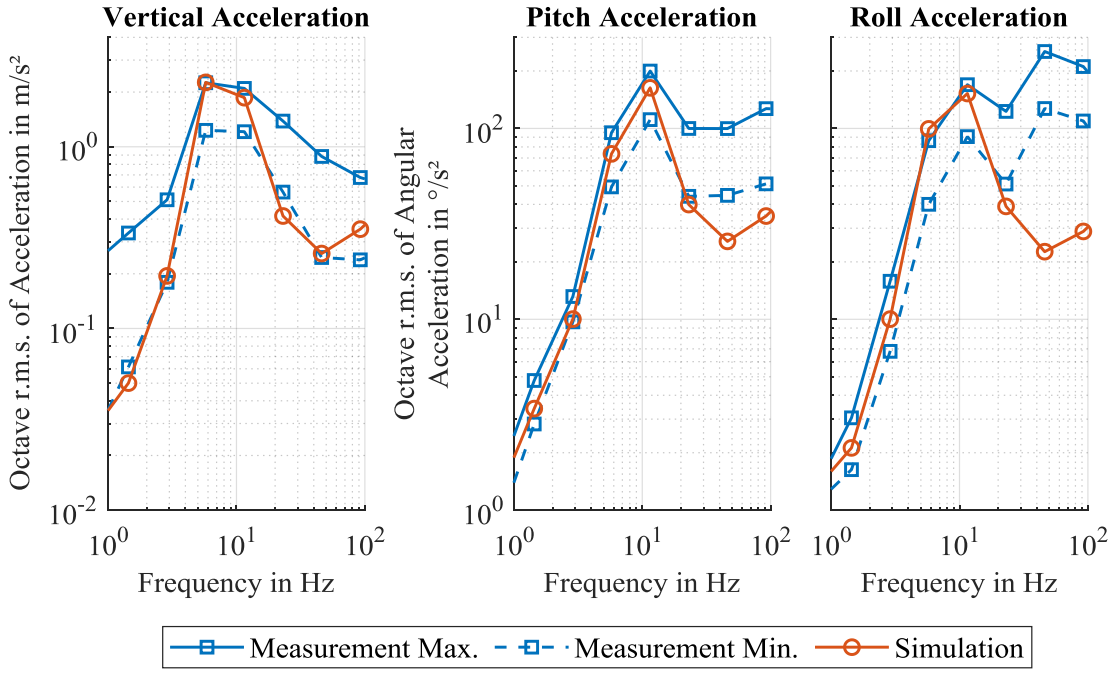

Figure 4-9: Comparison of octave r.m.s. between simulation (model from subchapter 4.2) and measurement for vertical, pitch and roll DoF determined on the measured validation driving surface. The maximum and minimum r.m.s. over 30 trials are shown for the measurement results.

In order to determine the uncertainty resulting from the inaccuracies of the validation, a comparison of the total vibration values (cf. section 2.4.2) between measurement and simulation is conducted. The cumulative distribution of the total vibration value is shown in Figure 4-10.

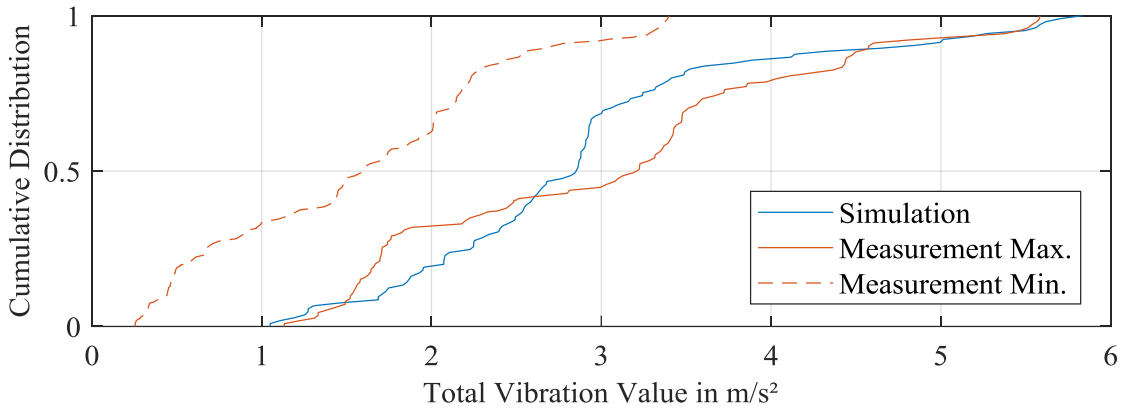

Figure 4-10: Cumulative distribution comparison of total vibration value (introduced in section 2.4.2) between simulation (model from subchapter 4.2) and measurement determined on the measured validation driving surface. The maximum and minimum distribution functions over 30 trials are shown for the measurement results.

It is recognizable that the simulation is close to the maximum values determined in the measurement. The minimum 100%-quantile of the measurement amounts to 3.4 m/s², the 100%-quantile of the simulation is 5.83 m/s². The acceleration and therefore the total vibration value are approximately linearly dependent on the reference amplitude of the driving surface unevenness. Therefore, the reference amplitude of the acceptable driving surface quality determined with the model could be a factor of 1.7 higher due to the uncertainty. This corresponds to an uncertainty factor of the roughness coefficient of 2.9. Although this seems high, the classification of driving surfaces follows a logarithmic scale so that the uncertainty has a limited influence on the determined class of the driving surface. For example, the difference between a roughness coefficient of 2 and 6 cm³ is still a driving surface of good quality according to Table 2-2.

4.4 Evaluation

In the following section, the initial system configuration is evaluated based on the evaluation parameters presented in subchapter 3.4 and summarized in Table 3-1. First, the acceptable driving surface quality is determined for pure direct disturbances from the driving surface. Subsequently, the impact of indirect disturbances of the horizontal accelerations resulting from wheel load variations is analyzed. The disturbance motions from tire deflections due to horizontal accelerations of the platform are not evaluated. The wheel load transfer at the maximum acceleration together with the stiffness of the tires yields a maximum tilt of 0.15°. This corresponds to a disturbance acceleration of 0.02 m/s², which is one order of magnitude below the absolute, unfiltered perception threshold (cf. section 2.4.3).

4.4.1 Acceptable Driving Surface Quality

The acceptable driving surface quality is determined with the methodology from subchapter 3.1 for direct disturbances from the driving surface according to the definition in section 3.4.1. For that purpose, the model described in subchapter 4.2 is applied to simulate an urban driving scenario according to subchapter 3.3 and the total vibration value (cf. section 2.4.2) resulting from driving surface excitations is determined. The driving surface quality is iteratively reduced until the occurrence of exceedings of the perception threshold remains below different specified values. The results are presented in Figure 4-11 by means of the acceptable roughness coefficients of the driving surface.

According to equation (3.4), the shown values of the acceptable roughness coefficient correspond to a range of maximum depth gauges between 0.008 mm and 0.087 mm over a length of 4 m. Even if the determined uncertainty of the validation is considered, a depth gauge range in the submillimeter range between 0.014 mm and 0.148 mm is required. Reduced scaling factors or accepting higher exceedance of the perception threshold improve the vertical dynamic behavior by at least half an order of magnitude.

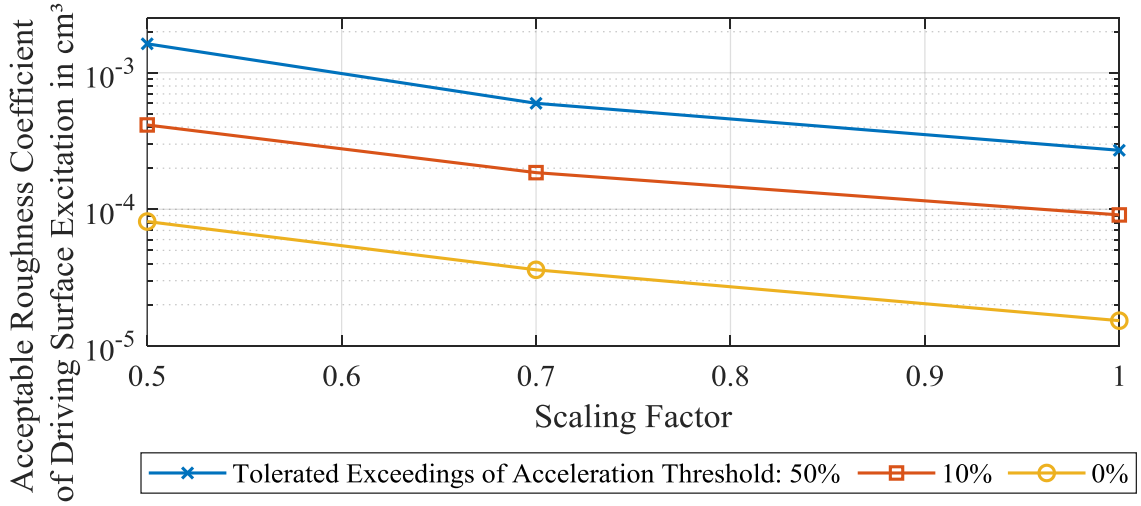

Figure 4-11: Acceptable driving surface qualities for a tire-sprung system with solid tires in dependence on acceleration scaling factor and allowed exceedings of perception threshold. The quality was determined with the model from subchapter 4.2 in an urban driving scenario by iteratively reducing the surface roughness until the total vibration value (section 2.4.2) is below the perception threshold.

4.4.2 Impact of Wheel Load Variations

In this section, the impact of the disturbances of the desired horizontal accelerations resulting from wheel load variations is investigated. For that purpose, the wheel load variations occurring on the acceptable driving surface determined in the previous section are transferred to a magic formula tire model (cf. subchapter 3.5). The input into the model are moments corresponding to constant straight accelerations of different magnitude, which are the reference stimuli. The deviations from that reference stimuli resulting from wheel load variations are converted to Weber ratios according to equation (3.5) in order to evaluate the perceptibility (Perception threshold: 1). Different quantiles of the Weber ratios at each of the simulated reference accelerations are shown in Figure 4-12.

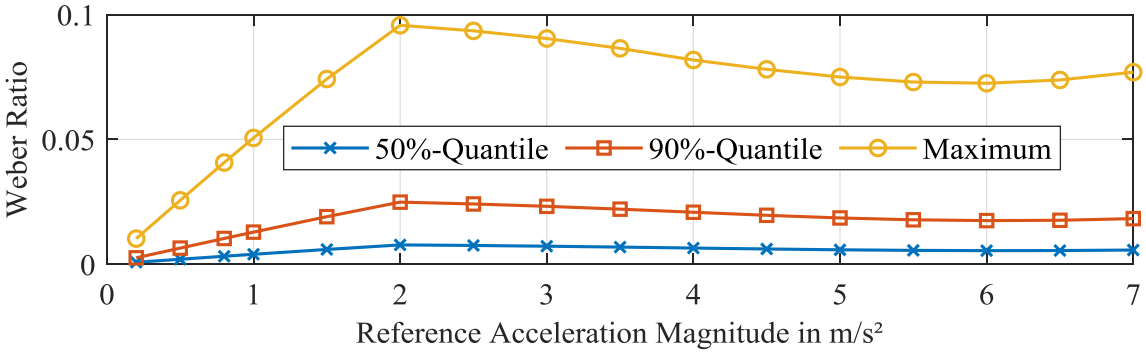

Figure 4-12: Disturbance of horizontal reference acceleration through wheel load variations by means of Weber ratio (cf. equation (3.5), perception threshold: 1). Determined from wheel load variations on acceptable driving surface from section 4.4.1 with isolated horizontal tire model (cf. subchapter 3.5) and different input moments corresponding to the shown reference acceleration.

The maximum ratios remain one order of magnitude below the perception threshold. Therefore, the impact of wheel load variations is negligible. This is an expected result because the wheel load variations of the tire-sprung system are directly correlated with the vertical accelerations. The high driving surface quality determined in section 4.4.1 generates low wheel load variations.

4.5 Conclusion

The determined acceptable driving surface qualities are far below the desired values of 1 cm^3 from section 2.5.2, which are achievable with asphalt or concrete driving surfaces, even if the uncertainty of the validation is considered. The depth gauge of 0.148 mm over a length of 4 m is a high accuracy requirement and even if this is achieved, 50 % exceedings of the perception threshold and a scaling factor of 0.5 reduce the simulation quality.

Thus, concepts for the reduction of the disturbances resulting from driving surface excitations are required to extend the application potential of WMDS to uneven surfaces such as driving dynamic testing grounds. The working hypothesis is adapted to the determined driving surface quality for a scaling factor of 0.7 and no exceeding of the perception threshold (cf. subchapter 3.3 and section 3.4.1):

> A driving surface with a roughness coefficient of 0.036 mm^3 is required for the application of WMDS without deterioration of the immersion of the subject.

This corresponds to a depth gauge of 0.013 mm. The following chapters aim at falsifying this hypothesis by reducing the driving surface-induced disturbances.

5 Concept Development

The following chapter aims at developing concepts that reduce the disturbances induced by the driving surface in order to extend the application potential of WMDS to surfaces of lower quality. The most promising concepts are selected and developed throughout the following chapters.

5.1 Methodology

The concept development is based on the problem analysis in Figure 3-1. The aim of the concepts to be developed is to reduce the mismatch between visual and vestibular channel that is generated by the driving surface disturbances. Therefore, the signal path of these two channels is analyzed from subject to simulation system and disturbance in order to identify potentials to reduce the mismatch. Subsequently, the identified separate concepts are investigated concerning their compatibility to generate combined concepts as additional solution approaches.

5.2 Concepts for the Reduction of Driving Surface-Induced Immersion Disturbances in WMDS

In the following, the visual and the vestibular signal path are investigated separately for possible adaptions. Subsequently, combinations are assessed.

5.2.1 Visual Path

5.2.1.1 Visual Adaption

Though the dominant origin of the mismatch between visual and vestibular channel is the motion disturbance, the reduction of this disturbance is not the only option to improve the immersion. Alternatively, the visualization can be adapted in order to make the disturbances feel more realistic. This would comprise two aspects. On the one hand, the relevant perceptible driving surface disturbances have to be implemented into the visualization. This would require a preview-detection of the driving surface unevenness and a variable visualization of the road in the simulation environment. On the other hand, the disturbance reaction of virtual vehicle and WMDS have to be adapted to each other. Especially the natural frequency and

the damping of both have to match to generate a plausible feeling of the vibrations. However, the shortcoming that the most critical situation, a vehicle at standstill and a simulator at nonzero velocity, cannot be solved by this concept, prevents its application as a singular concept for disturbance mitigation. Therefore, it is not further considered in this work, although it could be combined with other approaches along the vestibular path in the future to enhance the immersion.

5.2.2 Vestibular Path

Along the vestibular path, the following options for a reduction of the mismatch induced by the driving surface are conceivable:

- Adjustment of the transfer path
  - Pneumatic Tires
  - Passive elements (spring-damper system)
  - Active elements
- Compensation of the disturbances with a hexapod vertical dynamics control
- Adjustment of the trajectory of the WMDS to avoid strong excitations
- Reduction of the driving surface unevenness
- Masking with superposed signals to increase perception threshold

In the following, these options are analyzed concerning their advantages and disadvantages.

5.2.2.1 Pneumatic Tires

Unlike solid tires, which carry the entire load with the rubber structure, air pressure is the main support of pneumatic tires. Increased loads are mainly compensated by a larger area of the contact patch at a constant surface pressure. On the other hand, the elastic behavior of solid tires is based on two effects. The first is the radial stiffness of the rubber elements. The second is an increase in the number of effective elements with increasing deflection of the tire. This results in the nonlinear characteristic of the solid tire. Thus, the application of pneumatic tires promises a lower natural frequency than the solid tires. The nonlinearity of the stiffness is expected to be much smaller with pneumatic tires. The impact of wear on the stiffness of the pneumatic tire is lower because of the reduced influence of the rubber structure on the overall stiffness. In addition to the vertical dynamic behavior, the horizontal force characteristic of pneumatic tires is preferable. The friction coefficient is typically between 0.9 and 1.1 on dry asphalt[79] compared to a maximum of 0.8[80] for the solid tires.

[79] Roth, J.: Diss., Kraftübertragung Pkw-Reifen (1993). p. 50.

[80] Zöller, C. et al.: Vertical Dynamics WMDS (2019). p. 71.

Disadvantageous are the larger dimensions of the pneumatic tire and the lower damping compared to solid tires as well as an additional eigenmode at approximately 80 Hz due to the dynamics of the tire belt.[81] Due to the low damping, an appreciable improvement compared to the solid tire is not expected even though the lower natural frequency extends the filtering range. Nevertheless, due to the mentioned advantages, the application of pneumatic tires is a promising improvement of the vertical and horizontal dynamic behavior of the WMDS and will therefore be investigated further.

5.2.2.2 Passive Suspension

The introduction of additional spring-damper elements allows a further reduction of the natural frequency compared to the solid tires. Damping can be increased in order to reduce the peak at the natural frequency. Additionally, the behavior of the two-mass oscillator generates a slope of the disturbance power of -40 dB/decade above the second natural frequency, resulting in strong filtering of high-frequent accelerations.

Disadvantageous is the introduction of a high second natural frequency. Additionally, passive suspensions always are subject to a tradeoff between the impact of the natural frequency and the reduction of high-frequent oscillations, which is adjustable by the damper characteristic. Thus, although an improvement compared to the solely tire-sprung system is expected, a complete compensation of the relevant oscillations is not achievable. Additionally, a low natural frequency that is required for effective filtering of driving surface excitations results in increased motions of the WMDS's body due to horizontal forces. Therefore, the improvements concerning the isolation of direct vibrations is bought with additional disturbances induced by the horizontal dynamics.

5.2.2.3 Active Suspension Elements

The aforementioned shortcomings of a passive suspension can be overcome by the introduction of active elements. This enables a more or less free adjustment of the transfer behavior, which is of course limited by the performance of the implemented actuator. Additionally, a complete compensation of the motions that are induced by the horizontal dynamics is possible. Therefore, concerning the vibration isolation and the extension of the application potential of WMDS, it is a superior approach. The main disadvantages are the high costs, the weight and the installation space of the required actuators as well as the increased energy demand that is relevant for a mobile approach as the WMDS.

---

[81] Pacejka, H. B.; Besselink, I.: Tire and vehicle dynamics (2012). p. 475.

5.2.2.4 Hexapod Control

This approach is assignable to the aforementioned active approaches. However, the hexapod is already available in the WMDS concept due to the required tilt coordination function. Therefore, the disadvantages of the active elements concerning costs, weight and installation space do not apply. The flexibility in adjusting the transfer behavior is of course limited to the performance of the implemented hexapod. Additionally, the other functions are probably impeded by an additional vertical dynamics control due to the limitations of the actuators concerning stroke, velocity and force. Therefore, the suitability of the hexapod for this function is unknown. Nevertheless, it is a promising approach because of the low required hardware adjustments.

5.2.2.5 Trajectory Adjustment

The main target of the trajectory planning of the WMDS is the adequate representation of the demanded accelerations. However, human motion perception thresholds provide a scope for the adjustment of the trajectory. The driven trajectory on position level is less relevant for WMDS because no lanes have to be kept. Therefore, a further optimization criterion for the trajectory could be the prevention of strong driving surface induced excitations. This would either require preview detection of oncoming or memory of past strong excitations, whereas the latter would be disadvantageous because the strong disturbances will at least act once during a simulation. Although the concept is suitable for the mitigation of singular obstacles with high magnitudes, the general reduction of vibrations resulting from stochastic excitations is not possible. Therefore, it is more of a complementary approach that could improve the behavior in combination with another approach for the reduction of vibrations.

5.2.2.6 Reduction of Driving Surface Unevenness

A reduction of the immersion disturbances is also possible by reducing its source. However, if the flexibility advantage of the WMDS concept should be maintained, a solution that does not require potential users to construct a special driving surface is desired. This could be achieved by a transportable driving surface that can be flexibly placed on different areas. However, to achieve the required driving surface quality for the solid tire-sprung system determined in section 4.4.1 with a transportable solution is expected to be challenging. Therefore, it is also an approach that could improve the behavior in combination with another solution concept that reduces the vibrations.

5.2.2.7 Masking with Superposed Signals

Instead of reducing the mismatch between visual and vestibular channel, an increase of the acceptable mismatch is possible. The Weber law described in section 2.4.4 shows that a ref-

erence signal increases the perception threshold. Thus, by applying other, preferably plausible vibration signals (e.g. road vibrations or motor vibrations for standstill) the perceptibility of the disturbances induced by the driving surface could be reduced.

5.2.3 Combination of Concepts

The following concepts are complementary approaches and can be combined with each of the other solutions:

- Adaption of visualization
- Trajectory adaption
- Portable high-quality driving surface
- Masking of signals

Therefore, the suitable combinations are gathered from the other remaining concepts. These are as follows:

- Passive suspension + pneumatic tires
- Active elements + pneumatic tires
- Hexapod vertical dynamics control + pneumatic tires
- Active elements + passive suspension + (pneumatic tires)
- Hexapod vertical dynamics control + passive suspension + (pneumatic tires)

The combination of pneumatic tires is possible for every concept in order to reduce the first (tire-sprung system) or the second (suspension) natural frequency. On the one hand, this improves the filtering of high-frequent vibrations, while it possibly shifts the second natural frequency into a range of increased perceptibility (cf. Figure A.1 - 1). The impact of this tradeoff has to be investigated in detail. Especially the combination with an active approach could benefit from the lower natural frequency with pneumatic tires because the required bandwidth of the actuators is reduced.

This is also the main advantage of the combination of an active control with a passive suspension. The suspension provides filtering of high-frequent excitations, while the active controller damps the remaining natural frequencies of the suspension system. The implementation of the suspension is expected to reduce the requirements on the actuator and thus, probably enables the application of the hexapod for the control.

5.3 Evaluation and Selection

The complementary concepts have the potential to improve the other approaches in specific situations, while they are not suitable to reduce the immersion disturbances throughout a whole scenario. Nevertheless, the focus of this work is to generally reduce the disturbance in a large part of the scenario duration. Therefore, these solutions are not further considered

in this work, although a future development is recommended, especially concerning the trajectory adaption and the masking approach.

The approaches with active elements promise the highest potential concerning vibration isolation. Dependent on the selected actuator, a full compensation of the disturbances is possible. With the already available hexapod, however, an active approach without further hardware changes is theoretically possible. Thus, the potential of the hexapod should be investigated prior to the introduction of an additional actuator in order to avoid the associated technical and financial effort. Therefore, the focus of this work is set on the development and investigation of the hexapod concept. First, the improvement potential for the solely tire-sprung system is analyzed. Subsequently, the combination with an additional suspension system that serves as a low-pass filter in combination with the high-pass hexapod is investigated.

The introduction of pneumatic tires is a simple hardware change. It is unclear yet, which tire concept suits best for the respective concepts. The solid tire has a high stiffness, resulting in a shift of the natural frequency towards higher frequencies for which humans are less sensitive, especially combined with a suspension system. The pneumatic tire with its low stiffness, on the other hand, could be advantageous within the active system due to the reduced natural frequency, while the impact of the belt eigenmode is unknown yet. Additionally, the smaller nonlinearities, the lower sensitivity to wear and the higher friction coefficient are advantageous. Thus, a superior tire concept cannot be identified currently. Therefore, both tire concepts are investigated for each concept. Additionally, the potential of a tire-sprung system with pneumatic tires is investigated.

5.4 Summary

Summarized, the following concepts will be developed and evaluated in the following chapters:

- Tire-sprung system with pneumatic tire
- Hexapod vertical dynamics control + solid tire
- Hexapod vertical dynamics control + pneumatic tire
- Hexapod vertical dynamics control + suspension + solid tire
- Hexapod vertical dynamics control + suspension + pneumatic tire

6 Pneumatic Tires

The expected advantages of the application of pneumatic tires are summarized in section 5.2.2.1. This chapter aims at investigating the improvement potential by determining the acceptable driving surface quality for pneumatic tires and comparing the two tire concepts. The basic methodology for the determination of the acceptable driving surface quality is the same as for solid tires. However, unlike solid tires, pneumatic tires are widespread due to their application in passenger cars and extensive research is available concerning their characteristics, modeling and parameterization.[82a,83,84,85] Therefore, no experimental system identification is conducted. Instead, available tire models and parameterizations are researched and applied for the investigation.

6.1 Modeling

The Short Wavelength Intermediate Frequency Model (SWIFT) is applied for the investigation of the improvement potential of pneumatic tires. It is a comfort-oriented model and valid up to frequencies of 80 Hz, which corresponds to the limit of whole-body vibrations considered in this work, and low wavelengths of 10 cm.[82b] The configuration of the model is depicted in Figure 6-1. The main difference to a simple single-contact-point model is the division of the tire into contact patch and belt. The additional belt mass between the rim and the contact patch that is in contact with the driving surface introduces an additional eigenmode.

The belt mass is connected to the body-fixed wheel rim via the sidewall stiffness and damping and to the contact patch through a residual spring, so that the overall static tire stiffness equals that of the simple model without consideration of the belt mass. The following equations are derived from Pacejka.[82c] This results in the following dynamic equation of the belt mass:

$$m_{\mathrm{Belt}\,\mathrm{H}}\ddot{z}_{\mathrm{Belt},i} = {}_{\mathrm{H}}F_{z,c,\mathrm{T},i} + {}_{\mathrm{H}}F_{z,d,\mathrm{T},i} + {}_{\mathrm{H}}F_{\mathrm{z,Rsdl},i} \tag{6.1}$$

The involved elastic and damping forces acting between body and wheel according to Figure 4-5 are now calculated dependent on the belt deflection:

$${}_{\mathrm{H}}F_{z,c,\mathrm{T},i} = c_{\mathrm{Belt}}\left({}_{\mathrm{H}}z_{\mathrm{B,W},i} - {}_{\mathrm{H}}z_{\mathrm{Belt},i}\right) \tag{6.2}$$

[82] Cf. Pacejka, H. B.; Besselink, I.: Tire and vehicle dynamics (2012). a: -; b: pp. 412 ff.; c: pp. 454 ff.; d:

[83] Cf. Gipser, M.: FTire (2007).

[84] Cf. Oertel, C.; Fandre, A.: Reifenmodell RMOD-K (2001).

[85] Cf. Schmeitz, A.J.C.: Diss., Semi-Empirical Pneumatic Tyre Model (2004).

$$ {}_{\mathrm{H}}F_{z,d,\mathrm{T},i} = d_{\mathrm{Belt}}\left({}_{\mathrm{H}}\dot{z}_{\mathrm{B,W},i} - {}_{\mathrm{H}}\dot{z}_{\mathrm{Belt},i}\right) \tag{6.3} $$

The force ${}_{\mathrm{H}}F_{\mathrm{z,Rsdl}}$ of the residual spring between belt and contact patch is approximated by a third-order polynomial:[82c]

$$ {}_{\mathrm{H}}F_{\mathrm{z,Rsdl},i} = k_1\,{}_{\mathrm{H}}\Delta z_{\mathrm{Rsdl},i} + k_2\,{}_{\mathrm{H}}\Delta z^2_{\mathrm{Rsdl},i} + k_3\,{}_{\mathrm{H}}\Delta z^3_{\mathrm{Rsdl},i} + d_{\mathrm{Rsdl}}\,{}_{\mathrm{H}}\Delta \dot{z}_{\mathrm{Rsdl},i} \tag{6.4} $$

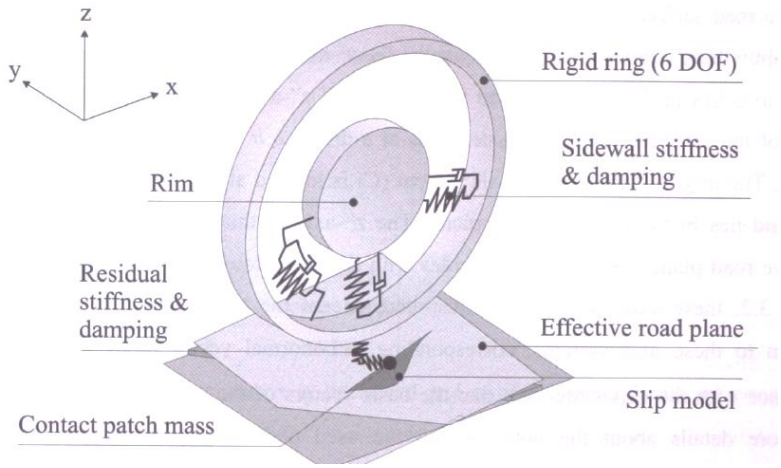

Figure 6-1: Basic SWIFT model configuration[86]

The deflection of the residual spring ${}_{\mathrm{H}}\Delta z_{\mathrm{Rsdl},i}$ is defined as follows:

$$ {}_{\mathrm{H}}\Delta z_{\mathrm{Rsdl},i} = {}_{\mathrm{H}}z_{\mathrm{DSE},i} - {}_{\mathrm{H}}z_{\mathrm{Belt},i} \tag{6.5} $$

The constant parameters in equation (6.4) are calculated based on the belt stiffness:

$$ k_1 = \frac{c_{\mathrm{Belt}} q_{\mathrm{Fz},1} \frac{F_0}{r_0}}{c_{\mathrm{Belt}} - q_{Fz,1} \frac{F_0}{r_0}} \tag{6.6} $$

$$ k_2 = \frac{c^3_{\mathrm{Belt}} q_{\mathrm{Fz},2} \frac{F_0}{r_0^2}}{\left(c_{\mathrm{Belt}} - q_{Fz,1} \frac{F_0}{r_0}\right)^3} \tag{6.7} $$

$$ k_3 = \frac{c^4_{\mathrm{Belt}} \left(q_{\mathrm{Fz},2} \frac{F_0}{r_0^2}\right)^2}{\left(c_{\mathrm{Belt}} - q_{Fz,1} \frac{F_0}{r_0}\right)^5} \tag{6.8} $$

The model parameters of a 205/60R15 91V tire, which would be suitable for the MORPHEUS prototype concerning the maximum wheel load, at an inflation pressure of 2.2 bar are given by Pacejka.[87] The model was validated in the work of Schmeitz on a tire test stand by driving over oblique steps with different inclinations and at different velocities

[86] Schmeitz, A.J.C.: Diss., Semi-Empirical Pneumatic Tyre Model (2004). p. 45.

[87] Pacejka, H. B.; Besselink, I.: Tire and vehicle dynamics (2012). pp. 629 ff.

and static vertical loads. The results showed that the model is valid for frequencies up to 100 Hz.[88]

6.2 Evaluation

Based on the described model, the potential of pneumatic tires is investigated in the following subchapter. First, the acceptable driving surface quality is determined and the influence of wheel load variations on the horizontal dynamics is presented. Finally, a comparison of the tire concepts is conducted for a better understanding of the differences. As for the solid tire, the disturbances through tire deflections resulting from horizontal accelerations are not evaluated. The tilt resulting from wheel load transfer at the maximum acceleration amounts to 0.63°, which corresponds to an acceleration of 0.11 m/s² (half of the perception threshold).

6.2.1 Acceptable Driving Surface Quality

The acceptable driving surface quality is determined with the methodology presented in subchapter 3.1. A detailed description of the application of the methodology is given for the solid tire in section 4.4.1. The results are presented in Figure 6-2. According equation (3.4), the shown values of the acceptable roughness coefficient correspond to a range of maximum depth gauges between 0.011 and 0.07 mm on a length of 4 m. Reduced scaling factors improve the vertical dynamic behavior by at least half an order of magnitude.

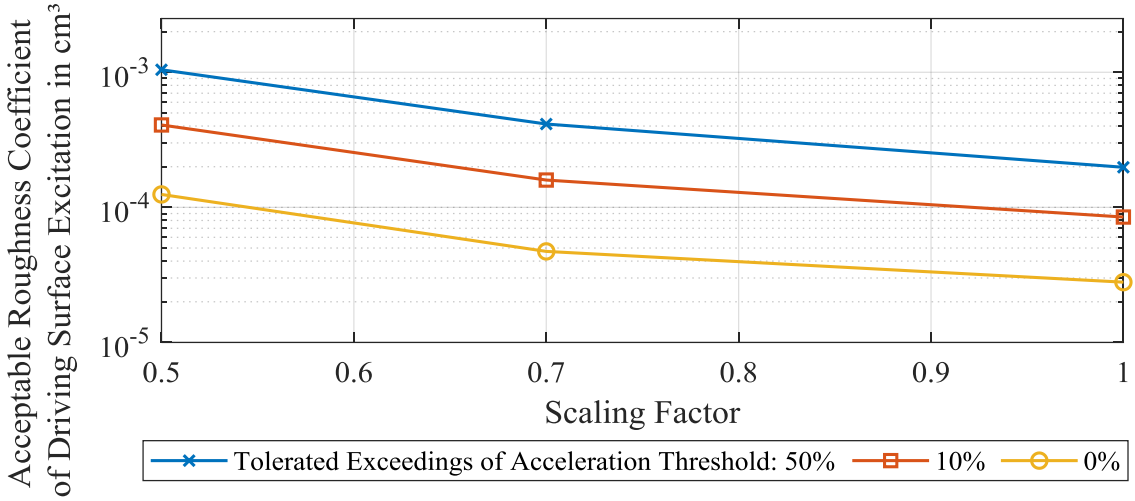

Figure 6-2: Acceptable driving surface qualities for a tire-sprung system with pneumatic tires in dependence on acceleration scaling factor and allowed exceedings of perception threshold. The quality was determined with the model from subchapter 6.1 in an urban driving scenario by iteratively reducing the surface roughness until the total vibration value (section 2.4.2) is below the perception threshold.

[88] Cf. Schmeitz, A.J.C.: Diss., Semi-Empirical Pneumatic Tyre Model (2004). pp. 208 ff.

Compared to solid tires, almost no clear improvement is recognizable. At an allowed exceeding occurrence of 50 %, the solid tire (Scaling 0.7: $6.0 \cdot 10^{-4}$ cm^3) achieves slightly higher acceptable roughness coefficients than the pneumatic tire (Scaling 0.7: $4.1 \cdot 10^{-4}$ cm^3). If no exceeding of the acceleration threshold is allowed, the pneumatic tire (Scaling 0.7: $4.7 \cdot 10^{-5}$ cm^3) is advantageous compared to the solid (Scaling 0.7: $3.6 \cdot 10^{-5}$ cm^3).

Nevertheless, the deviations are within the uncertainty of the model validity, so that the tire performance concerning the vertical dynamics is equal. The reason for this finding will be investigated in section 6.2.3.

6.2.2 Impact of Wheel Load Variations

Hereinafter, the disturbances of the desired horizontal accelerations due to driving surface-induced wheel load variations are investigated. The detailed methodology is described for the solid tire in section 4.4.2. The horizontal tire model parameters for the pneumatic tire are adapted according to Pacejka.[87] The resulting Weber ratios are shown in Figure 6-3 (cf. equation (3.5), perception threshold: 1). The values are lower than for the solid tires. The reason for this is the higher slip stiffness of the pneumatic tires. A wheel load reduction generates a reduced tire force. Due to the ideal control, the moment on the wheel remains the same. Thus, the wheel is accelerated until the force and the moment are again at equilibrium. The lower the slip stiffness, the more time is needed to adapt to the reduced force and therefore the deviation between desired and acting force is increased. The Weber ratios are far below the perception threshold for the same reasons as already discussed in section 4.4.2.

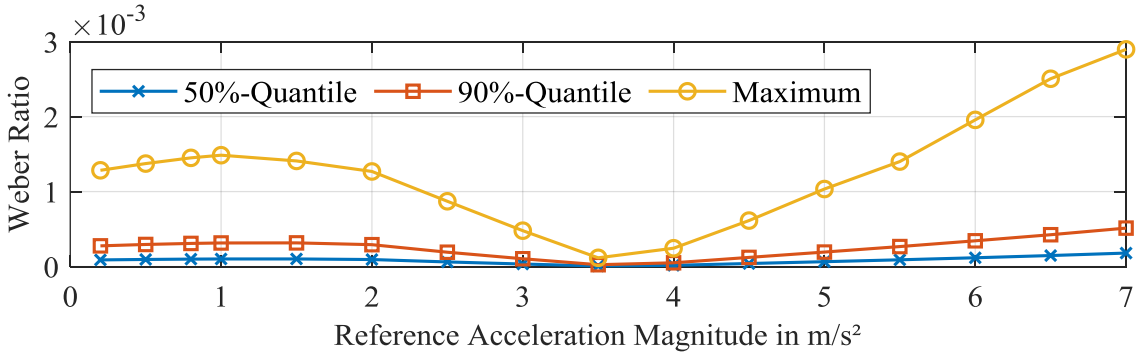

Figure 6-3: Disturbance of horizontal reference acceleration through wheel load variations by means of Weber ratio (cf. equation (3.5), perception threshold: 1). Determined from wheel load variations on acceptable driving surface from section 6.2.1 with isolated horizontal tire model (cf. subchapter 3.5) and different input moments corresponding to the shown reference acceleration.

6.2.3 Comparison of Tire Concepts

The comparison between both tire concepts is conducted by means of the vertical acceleration. The frequency-weighed PSD spectra of both tires with equal driving surface input

(roughness coefficient 0.036 mm³, acceptable quality for solid tire) is shown in Figure 6-4. The reason for the almost equal acceptable driving surface quality is a slightly different damping in combination with the dominant impact of the natural frequency. Although the high natural frequency of the solid tire leads to increased powers at high frequencies, their impact is small. At 12.5 Hz, 99 % of the overall power within the range from 0.1 to 100 Hz is reached for the solid tire. For the pneumatic tire, the same applies for a frequency of 4 Hz. Therefore, the higher damping of the solid tire compensates the impact of the increased powers at high frequencies and the wider main lobe, resulting in a similar overall acceleration power.

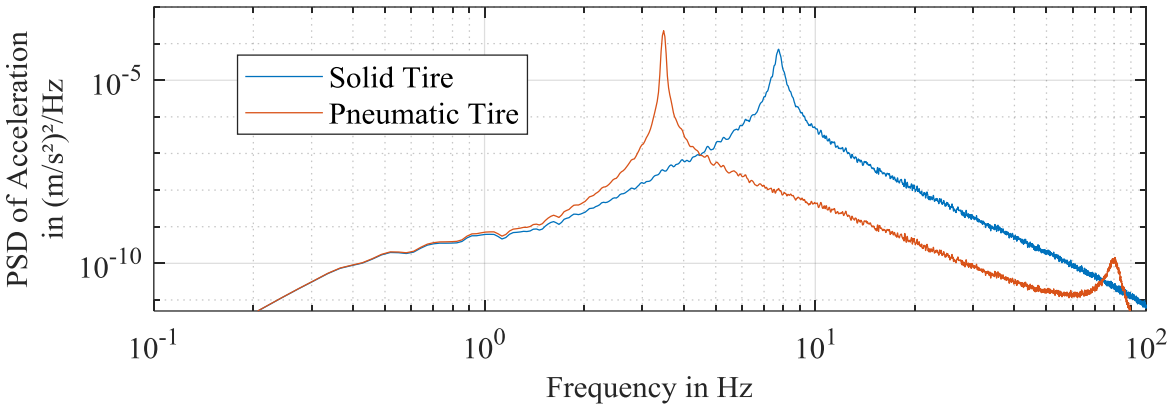

Figure 6-4: Comparison of vertical frequency-weighed acceleration PSD between solid and pneumatic tire determined with the models from subchapters 4.2 and 6.1 in an urban driving scenario on the acceptable driving surface quality of the solid tire determined in section 4.4.1.

6.3 Conclusion

The improvement resulting from the application of pneumatic tires is marginal. The determined acceptable driving surface qualities are still far below the desired values from section 2.5.2. Nevertheless, the working hypothesis is further adapted according to the results of a scaling factor of 0.7 and no exceeding of the perception threshold (cf. subchapter 3.3 and section 3.4.1):

A driving surface with a roughness coefficient of 0.047 mm³ is required for the application of WMDS without deterioration of the immersion of the subject.

The next step is the investigation of the potential of a hexapod vertical dynamics control, which is introduced into the tire-sprung system.

7 Hexapod Vertical Dynamics Control and Tire-Sprung System

7.1 Methodology

The development methodology is shown in Figure 7-1. First, system architectures are developed including the main components and the interfaces between them. This step is followed by the development of a linear model description of the WMDS system, which allows a thorough synthesis of the controller. The ascertained control approaches are validated with a nonlinear multibody model. Subsequently, based on this model, the controller is evaluated by determining the acceptable driving surface quality and comparing it to the performance of the uncontrolled system. Additionally, the requirements on the hexapod are determined dependent on the quality of the driving surface. The specific methodologies applied for the development steps are described in the respective subchapters.

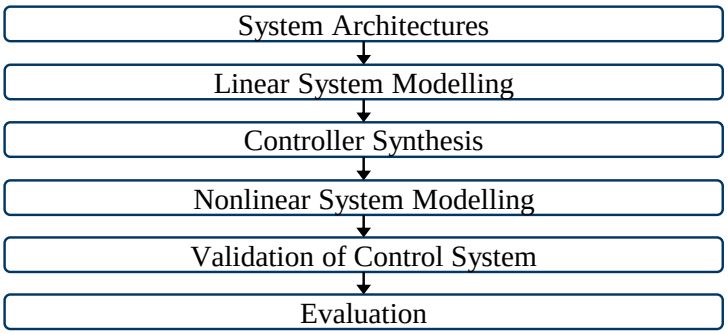

Figure 7-1: Methodology of the hexapod vertical dynamics control development

7.2 System Architecture Development

The considerations concerning the initial system architecture, the output, control and command variables in the following subchapter were conducted in the master thesis of Seebold. The control system architectures were initially developed in her master thesis and extended by the author of this work by the washout and the combination with a feed forward control.[89]

The aim of the system architecture development is to define possible concepts for the control system architecture, including output variables, control or command variables, and manipulated variables. The applied development methodology is depicted in Figure 7-2.

[89] Cf. Supervised Theses: Seebold, L.A., Master Thesis Nr. 615/16, 2016, pp. 23 ff.

Initially, an analysis of the applied hexapod is conducted to identify the relevant properties and interfaces. The respective information are summarized in section 2.6.1.2. Subsequently, based on the initial system architecture on component level, an analysis of the effect chain from the driving surface excitation to the disturbance of the subject is conducted to identify potential variables that can be applied for the control. Based on the defined variables, possible control system architectures are derived.

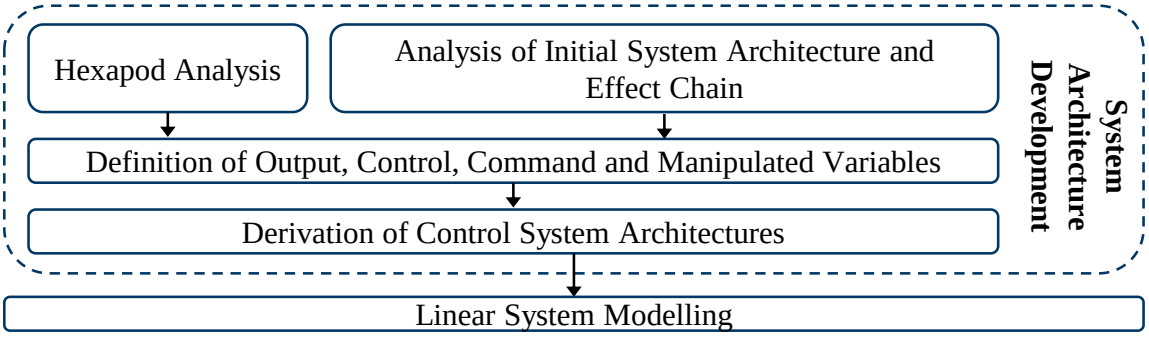

Figure 7-2: Methodology of system architecture development.

7.2.1 Initial System Architecture and Effect Chain

An overview of the initial system architecture is given in Figure 7-3. The input are the driving surface excitations $z_{\mathrm{DSE},i}$ acting on the three tires with elastic and damping properties. The driving surface excitations are transmitted through the frame to the hexapod bottom plate (HBP).

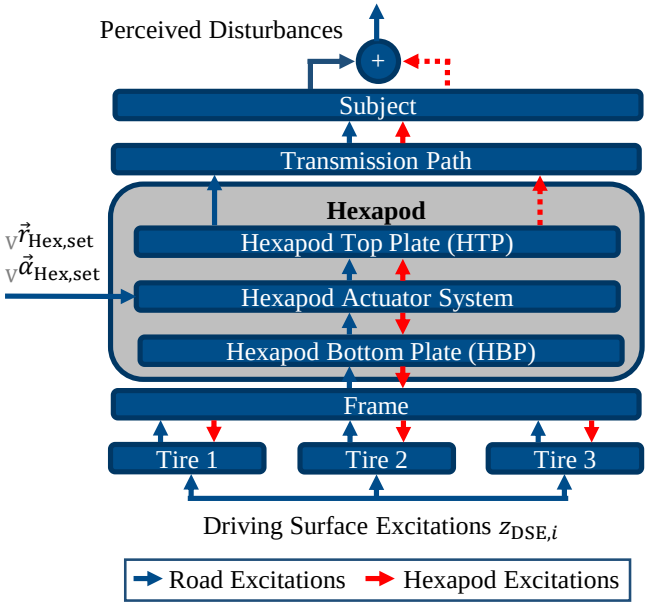

Figure 7-3: Initial system architecture and effect chain.[90]

[90] According to: Seebold, L. A.: Masterthesis, Hexapod Regelung WMDS (2016). p. 25.

The linear actuators partly transmit these oscillations directly because of internal friction and their rotational inertia, even if the motors themselves are not active. Additionally, the control of the motors adjusts the torque so that the set values for the actuator lengths are met. If no external hexapod control is active and the set values remain zero, the vibrations are completely transmitted to the hexapod top plate (HTP) and then transferred to the subject via further transmission components, e.g. the seat.

The hexapod with its inputs ${}_{\mathrm{V}}\vec{r}_{\mathrm{Hex,set}}$ and ${}_{\mathrm{V}}\vec{\alpha}_{\mathrm{Hex,set}}$ in the non-leveled vehicle frame containing the translational components ${}_{\mathrm{V}}x_{\mathrm{Hex,set}}$, ${}_{\mathrm{V}}y_{\mathrm{Hex,set}}$, ${}_{\mathrm{V}}z_{\mathrm{Hex,set}}$ and rotational inputs ${}_{\mathrm{V}}\vartheta_{\mathrm{Hex,set}}$, ${}_{\mathrm{V}}\varphi_{\mathrm{Hex,set}}$, ${}_{\mathrm{V}}\psi_{\mathrm{Hex,set}}$ also induces oscillations into the system even if no driving surface excitations are acting. This manipulating reaction behavior has to be considered during the controller development. The resulting oscillations of the hexapod are superposed with the excitations induced by the driving surface, so that the sum of both is the perceived disturbance of the subject. From the shown components and the effect chain, the relevant variables can be deduced.

7.2.2 Output Variables

First, the relevant output variables are defined. These are the stimulated disturbances that can be perceived by the subject, which have been introduced in section 2.4.1. The driving surface unevenness directly stimulates mainly the translational movements in vertical direction and the rotational movements around the pitch and roll axes. As discussed in section 3.4.2, the horizontal, translational, and yaw movements are mainly stimulated indirectly through dynamical wheel load changes (despite the excitations resulting from angular motions). However, this is only possible if horizontal accelerations are already acting because otherwise there are no wheel forces, which a wheel load change could affect. In that case, the perception thresholds are higher because the vestibular organ is less sensitive to disturbances if a reference stimulus is acting according to Weber's Law from section 2.4.4. Hence, to avoid hitting the limits of the manipulated variables, the focus is set on the directly excited variables. Therefore, the following output variables are defined:

- Vertical acceleration of subject ${}_{\mathrm{H}}\ddot{z}_{\mathrm{sub}}$
- Roll acceleration and velocity of subject ${}_{\mathrm{H}}\ddot{\varphi}_{\mathrm{sub}}/{}_{\mathrm{H}}\dot{\varphi}_{\mathrm{sub}}$
- Pitch acceleration and velocity of subject ${}_{\mathrm{H}}\ddot{\vartheta}_{\mathrm{sub}}/{}_{\mathrm{H}}\dot{\vartheta}_{\mathrm{sub}}$

The aim of the hexapod vertical dynamics control is to hold these variables at zero despite acting disturbances.

7.2.3 Control/Command Variables

The aim of this section is to define input variables for the control that can be applied to control the output variables defined above. The questions are:

- Which quantities have to be measured?
- Where are the quantities measured?

Possible quantities that allow conclusions about the output variables are all positions along the effect chain and the respective derivatives. This also includes the virtual position of the driving surface, which can be interpreted as a movement. To avoid phase shifts through integrations, it is desired to apply the accelerations directly instead of positions or velocities. This is well feasible for the translational acceleration, which can be measured by an inertial measurement unit (IMU). One exception is the driving surface profile, which actually induces no real movement, so that only a position measurement is possible. The rotational movements are also measured by most IMUs, however, only on rate level. Nevertheless, this is accepted in favor of higher practicability.

Alternatively, the forces that generate the movements can be used as input variables for a control. However, forces either require a fractionation of the transmission path to implement a load cell, or a model is required to determine the force from a deflection. There is no advantage in the force determination that could counterbalance this problem, so that the force determination is neglected as input variable. Hence, possible input variables are:

- Translational accelerations
- Rotational velocities
- Driving surface profile on position level

The next step is the determination of the positions, at which these quantities are measured. The position of the driving surface measurement is obvious. The information can be used for an open-loop control based on an inverse model of the transmission path between driving surface and subject.

The accelerations can be measured at every component along the transfer path shown in Figure 7-3. The direct measurement of the subject movements would be a classical closed-loop control with the output variable as control variable. However, the measurement of the subject movements is not feasible, because a sensor mounted directly on the subject could cause an additional disturbance. Hence, the influence of the seat transmission is neglected and the subject movements are set equal to those of the HTP.

An alternative measurement point is the HBP. The gathered signals could be used as a negative input for the desired acceleration of the hexapod, which would be an open-loop control of the output variables. Both points are also eligible for measuring the rotational velocities.

The transmission path along the frame is a continuum so that the measurement position has to be adjusted to the modal order. The lowest eigenmode has its maximum deflection at the HBP, so that no additional information could be gathered from a measurement at the frame.

Measurement at the tires would require a model of the transmission path to determine the necessary hexapod movements for a compensation of the vertical excitations. The advantage would be a slightly earlier information about the movement of the platform. However, this is negligible because the natural frequency of the frame is much higher (above 30 Hz) than

that of the tire-body-mass system, which has to be controlled (8 Hz). Hence, this slight advantage does not justify the inaccuracies resulting from the model assumptions. The next step is the generation of system architectures from the gathered quantities.

7.2.4 System Architectures

The variables determined above generally allow three independent system architectures, which have already been mentioned:

- Closed-loop control of HTP translational and rotational accelerations and rotational velocities (CLC)
- Open-loop control with compensation of the HBP's translational and rotational accelerations and rotational velocities (OLC)
- Open-loop control with preview of the driving surface unevenness and an inverse model of the transmission path (FFC)

The performance of the last variant strongly depends on the model validity and the accuracy of the measurement of the driving surface profile. A combination with one of the other approaches would compensate these inaccuracies. Therefore, the third approach could be implemented into the other system architectures as a feed-forward control (FFC) for the compensation of reaction times, which result e.g. from the inverse kinematic calculations of the hexapod. However, the measurement accuracy of investigated sensors[91] requires a signal to noise ratio (equivalent to driving surface excitation power) that is above the acceptable driving surface qualities determined in this work. Therefore, the concept is not investigated further but future improvements in sensor technology and signal processing could raise the potential of the approach.

Yet, only translational accelerations and rotational velocities are controlled. Measurement inaccuracies or high slopes of the driving surface would lead to a drift of the hexapod to the limits of its range of motion. Therefore, an overlaid washout is required, which returns the hexapod back to its initial position. It generates low accelerations ${}_{\mathrm{H}}\ddot{z}_{\mathrm{WO}}$, ${}_{\mathrm{H}}\ddot{\vartheta}_{\mathrm{WO}}$, ${}_{\mathrm{H}}\ddot{\varphi}_{\mathrm{WO}}$ below the perception thresholds and adds them to the input values for the control. The summation has to be conducted before the controller because otherwise it would act like a disturbance in the control loop. In that case, it would be compensated by the controller.

Additional to the set values of the acceleration control, the hexapod receives inputs ${}_{\mathrm{H}}z_{\mathrm{Hex,in}}$ ${}_{\mathrm{H}}\vartheta_{\mathrm{Hex,in}}$, ${}_{\mathrm{H}}\varphi_{\mathrm{Hex,in}}$ from other functions. For example, the tilt coordination for the simulation of low-frequent accelerations described in section 2.3.1 has to be considered. The closed-loop controller is focused on the reduction of disturbances from the driving surface and, thus, could impede the command response to these inputs. In order to compensate this negative influence of the controller, a pre-filter could be required.

[91] Cf. Zöller, C. et al.: Preview Driving Surface Unevenness in WMDS (2018).

The resulting system architecture for the closed-loop control (CLC) is shown in Figure 7-4. The manipulated variables are the hexapod positions. The only alternative interface would be the pod lengths, which would have no advantages but would require additional kinematic calculations within the self-developed part of the system. The inputs to the hexapod ${}_{\mathrm{V}}\vec{r}_{\mathrm{Hex,set}}$ and ${}_{\mathrm{V}}\vec{\alpha}_{\mathrm{Hex,set}}$ have to be defined in the non-leveled vehicle reference frame. Hence, a transformation of the control inputs from the leveled H-frame into the V-frame is required.

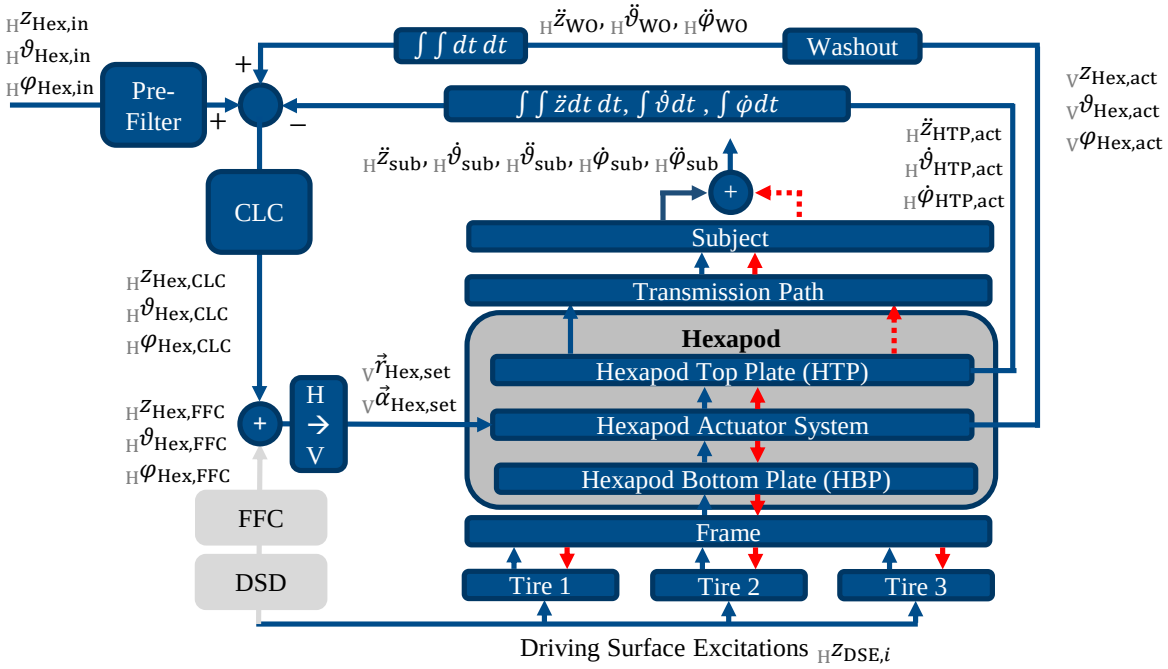

Figure 7-4: Closed-loop control system architecture.

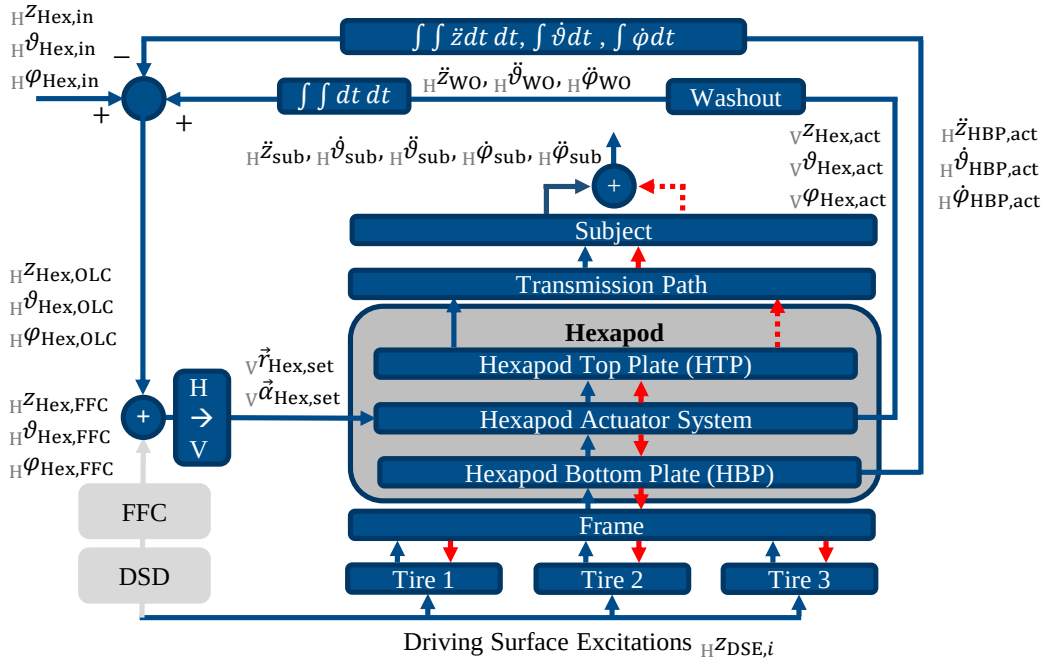

Figure 7-5: Open-loop control system architecture.

The system architecture for the open-loop control (OLC) is depicted in Figure 7-5. It is a simple approach because no special controller has to be developed. The measured control quantities are just the negative movements at the lower hexapod plate. Assuming ideal actuator dynamics, this would lead to a complete compensation of the disturbances. However, it has to be tested how the approach works with non-ideal actuator dynamics.

7.3 Linear System Modelling

The following subchapter aims at the development of a linear model for the controller synthesis. From the system architecture in Figure 7-4, two necessary main components of the model can be identified:

- Hexapod-Actuator
- Mechanical vertical vibration system

7.3.1 Hexapod-Actuator Model

The hexapod-actuator model described in this section was developed in the master thesis of Mehren and the parameterization was adjusted by the author.[92] The basic structure of the hexapod actuator is shown in Figure 7-6.

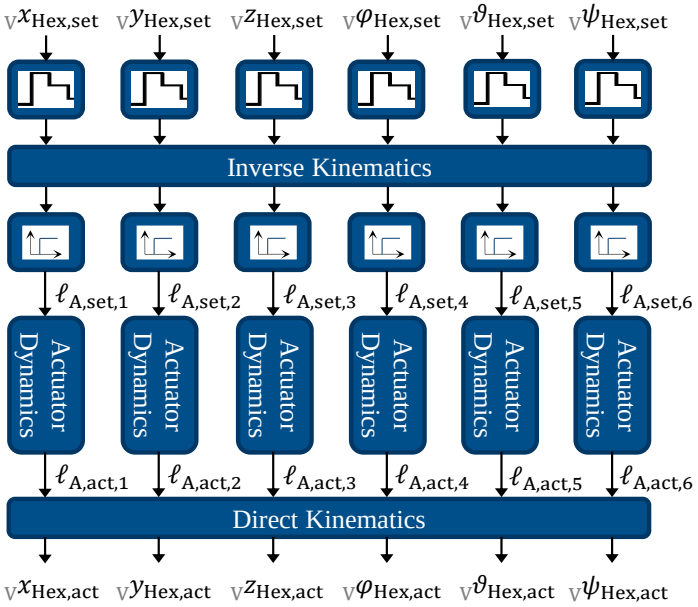

Figure 7-6: Hexapod actuator structure.[93a]

[92] Cf. Supervised Theses: Mehren, M., Master Thesis Nr. 643/17, 2017, pp. 24 ff.

[93] According to Supervised Theses: Mehren, M., Master Thesis Nr. 643/17, 2017, a: p. 30; b: p. 24; c: p. 26; d: p. 26; e: p. 28.

The input values are the set translational and rotational positions of the hexapod as described in the overall system architecture. These values are sampled and held at the input of the hexapod. Afterwards, the positions are converted to the corresponding pod lengths $\ell_{\mathrm{A,set},i}$ by an inverse kinematic calculation.

The latency resulting from that calculation and other internal filters is modelled as a dead-time element at the output of the inverse kinematics. Afterwards, a model of the linear actuators translates the set lengths to the acting lengths $\ell_{\mathrm{A,act},i}$. These are retransformed to the hexapod positions by a direct kinematic description. The system can be characterized as a multiple-input multiple-output system (MIMO). The modeling of the mentioned components is described in the following sections.

7.3.1.1 Modelling of Actuator Dynamics

The aim of modeling the actuator is to establish a behavior that is as close as possible to a real hexapod. Therefore, the internal controllers are designed according to literature methodologies and based on available datasheets[94]. Additionally, the known behavior of hexapods, which has been determined in measurements, will be included in the modeling.

The first step in the description of the actuator dynamics is to model the internal control architecture. According to Schröder, the control of a brushless DC motor is done with a cascade control.[95a] The applied cascade consists of a position control, an angular velocity (ω_{A}) control, and a current (I_{A}) control, as shown in Figure 7-7. This controller acts on the controlled system, which consists of the electric motor components and the rotational dynamics of the actuator. The shown limitations of the manipulated variables are not applied in the linear model but in the nonlinear model.

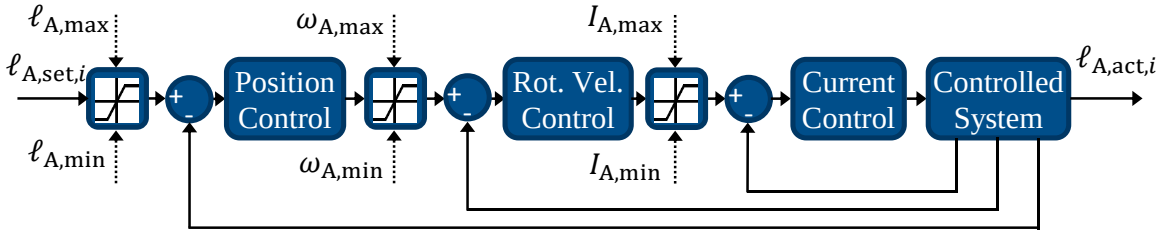

Figure 7-7: Structure of actuator dynamics model.[93b]

The next step is to design the shown controllers. The controllers are designed from the innermost cascade, the current controller, to the outermost. The respective inner control circuits are designed independently from the surrounding ones. Afterwards, the overlaid control circuits are designed based on the inner ones.

---

[94] Cf. Exlar Automation: Exlar GSM (2014).

[95] Cf. Schröder, D.: Regelung von Antriebssystemen (2015). a: p. 262; b: pp. 47-49; c: pp. 263-265; d: pp. 46-60.

Current Control Loop

The current control circuit consists of the following components:

- Electric Power Converter
- Electric Motor
- Current Sensor
- Current Controller

The electric energy converter as well as the current sensor are modelled as PT1 elements with the time constants $T_{I,\mathrm{Sen}}$ and $T_{U,\mathrm{Conv}}$.[95b] The dynamics of the electric motor in the Laplace space with the voltage U_A as input and the current $I_\mathrm{A,act}$ as output result from the resistance R_A and the inductance L_A:

$$\mathcal{L}I_\mathrm{A,act}(s) = \frac{1}{R_\mathrm{A} + L_\mathrm{A}s}\left(\mathcal{L}U_\mathrm{A}(s) - \mathcal{L}U_\mathrm{ind}(s)\right) \tag{7.1}$$

The induced voltage U_ind is compensated by an internal feed-forward control and is therefore neglected.[95c] The current controller is implemented as a PI controller to avoid stationary deviations despite disturbances. The resulting current control loop is shown in Figure 7-8.

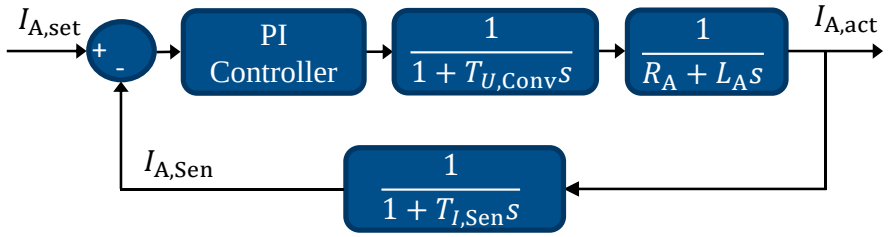

Figure 7-8: Current control loop.[93c]

The PI controller is designed according to the magnitude optimum method.[95d] The time constant of the motor is dominant compared to that of the current sensor and the converter. Following from that, a compensation of the motor time constant is aspired. The resulting control law is formulated as follows:

$$\mathcal{L}G_{\mathrm{PI},I}(s) = \frac{1}{2T_\mathrm{PE}}\frac{R_\mathrm{A} + L_\mathrm{A}s}{s} \tag{7.2}$$

The gain is defined dependent on the summed time constants of the power electronics T_PE:

$$T_\mathrm{PE} = T_{I,\mathrm{Sen}} + T_{U,\mathrm{Conv}} \tag{7.3}$$

This results in the following transfer function of the current control loop:

$$\mathcal{L}G_I(s) = \frac{\mathcal{L}I_\mathrm{A,act}(s)}{\mathcal{L}I_\mathrm{A,set}(s)} = \frac{T_{I,\mathrm{Sen}}s + 1}{2T_\mathrm{PE}s\left(T_{U,\mathrm{Conv}}s + 1\right)\left(T_{I,\mathrm{Sen}}s + 1\right) + 1} \tag{7.4}$$

The time constant $2T_\mathrm{PE}$ is dominant compared to that of the sensor and the converter. Hence, for the controller synthesis, this equation is simplified by the following transfer function:

$$\mathcal{L}G_{I,\mathrm{simple}}(s) = \frac{1}{2T_\mathrm{PE}s + 1} \tag{7.5}$$

In the nonlinear model, the extended description (7.4) will be applied. Based on this current controller, the rotational velocity controller is designed.

Rotational Velocity Control Loop

The control loop for the rotational actuator velocity, which transforms the set angular velocity $\omega_{\mathrm{A,set}}$ to the acting $\omega_{\mathrm{A,act}}$ is shown in Figure 7-9. To avoid stationary deviations due to load torques M_{Load}, a PI controller is applied. The constant k_{A} describes the correspondence between motor current and output torque. The motor torque is reduced by the efficiency factor for the transformation from rotational to translational velocity $\eta_{\mathrm{A,rt}}$, whereas the load torque is reduced by the factor for translational to rotational transformation $\eta_{\mathrm{A,tr}}$. The difference between both torques is converted to a rotational acceleration by the mass moment of inertia $J_{\mathrm{A,red}}$, which is reduced to the output of the motor and includes the rotational inertia of the actuator and the mass on the hexapod top plate.

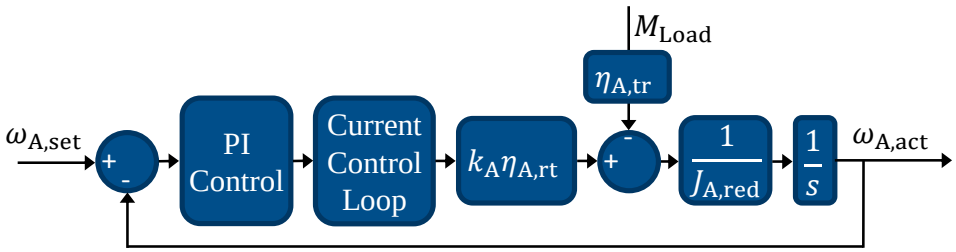

Figure 7-9: Rotational velocity control loop.[93d]

The two I elements of the controller and the controlled system generate a phase difference of -180°. Together with the -90° phase, which is induced by the current control loop, this would result in an unstable system. Therefore, the zero of the PI controller is positioned to heave the phase at a frequency lower than the limiting frequency of the current control loop $1/2T_{\mathrm{PE}}$.

The symmetric optimum methodology, which is common for this kind of problem, is applied for the design of the controller.[96a] According to this method, the controller law is formulated dependent on the time constant increase factor ζ:

$$^{\mathcal{L}}G_{\mathrm{PI},\omega}(s) = \frac{J_{\mathrm{A,red}}}{4 \cdot T_{\mathrm{PE}}^2 \eta_{\mathrm{A}} k_{\mathrm{A}} \zeta^3} \frac{1 + 2T_{\mathrm{PE}}\zeta^2 s}{s} \tag{7.6}$$

To achieve the best compromise between a high phase reserve, a low overshoot, and high dynamics, the time constant of the controller is set 4 times higher than that of the controlled system ($\zeta = 2$).[96b] This results in the following transfer function of the closed-loop:

$$^{\mathcal{L}}G_{\omega}(s) = \frac{^{\mathcal{L}}\omega_{\mathrm{A,act}}(s)}{^{\mathcal{L}}\omega_{\mathrm{A,set}}(s)} = \frac{2T_{\mathrm{PE}}\zeta^2 s + 1}{8T_{\mathrm{PE}}^3\zeta^3 \mathrm{s}^3 + 4T_{\mathrm{PE}}^2\zeta^3 \mathrm{s}^2 + 2T_{\mathrm{PE}}\zeta^2 \mathrm{s} + 1} \tag{7.7}$$

[96] Cf. Schröder, D.: Regelung von Antriebssystemen (2015). a: pp. 60-74; b: p. 66.

The zero of this transfer function has a negative impact on the command reaction of the loop. Hence, a pre-filter ${}^{\mathcal{L}}G_{\mathrm{PF},\omega}$ is designed to compensate the zero of the closed-loop without affecting the dynamics of the disturbance compensation:

$$ {}^{\mathcal{L}}G_{\mathrm{PF},\omega}(s) = \frac{1}{2T_{\mathrm{PE}}\zeta^2 s + 1} \tag{7.8} $$

The respective parameter values are derived from the datasheet of the actuators.[97]

Position Controller

The position control loop is shown in Figure 7-10. The components are the controller, the rotational velocity control loop with the pre-filter, and the transformations of the rotation to a translation by the slope of the screw spindle p_{Sp}.

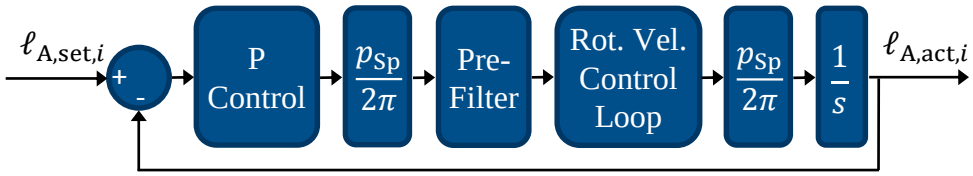

Figure 7-10: Position control loop.[93e]

A P controller is sufficient for the position control because all acting disturbances are controlled by the underlying loops. Measurements of the real hexapod system have shown that no overshoot occurs on position level.[98] Therefore, the controller gain is increased iteratively until the step response of the actuator dynamics begins to overshoot. This results in a position controller gain of $V_{\mathrm{Pos}} = 116$.

Overall Actuator Dynamics

The resulting system dynamics of the actuator are described with the following transfer function:

$$ {}^{\mathcal{L}}G_{\mathrm{A}}(s) = \frac{{}^{\mathcal{L}}\ell_{\mathrm{A,act}}(s)}{{}^{\mathcal{L}}\ell_{\mathrm{A,set}}(s)} = \frac{V_{\mathrm{Pos}}}{8T_{\mathrm{PE}}^3\zeta^3 s^4 + 4T_{\mathrm{PE}}^2\zeta^3 \mathrm{s}^3 + 2T_{\mathrm{PE}}\zeta^2 \mathrm{s}^2 + \mathrm{s} + V_{\mathrm{Pos}}} \tag{7.9} $$

This transfer behavior is dependent on the following three characteristics:

- Gain of the position controller V_{Pos}
- Zero of the rotational velocity controller defined by the time constant factor ζ
- Time constant T_{PE}

The time constant T_{PE} is derived from the known limit frequency of the current controller (1.1 kHz) to 0.45 ms. The T_{95} time of the overall control loop amounts to 18 ms.

[97] Cf. Exlar Automation: Exlar GSM (2014).

[98] Cf. Kässens, A.: Bachelorthesis, Modellbildung Hexapod MORPHEUS (2016). a: p. 45; b: -.

7.3.1.2 Kinematics and MIMO behavior

Until now, the dynamics of one single actuator were described. However, six actuators have to be controlled in a hexapod. The correspondence between the six actuators has a possible influence on the controller synthesis. Whether this influence has to be considered will be analyzed in the following.

The system structure is shown in Figure 7-6. The input values of the respective actuators are transformed from the set positions of the hexapod by an inverse kinematic. After these set values are transferred to the acting values by the actuator dynamics, the calculation of the direct kinematic results in the acting positions of the hexapod. In a linear system, an exchange of these elements is possible.

Nevertheless, the kinematic calculations are nonlinear due to cosine and sine transformations. A linearization around the operation point is required for this step. If the operation points of inverse and direct kinematic are the same, the inverse and the direct kinematic element can be superposed, which results in a unity matrix. This would allow an independent synthesis of the controllers for the respective degrees of freedom.

However, it has to be kept in mind that the operation point of the inverse kinematic is defined by the set values of the hexapod, but the direct kinematic operation point is given by the acting values. To estimate the influence of this difference, an operation point difference is applied to the direct kinematics and the result of the matrix multiplication of inverse and direct kinematic is analyzed. The maximum difference between set and acting values determined in measurements amounts to 25 mm.[98b] This difference results in a maximum deviation of the matrix coefficients from the unity matrix of 0.01.

Therefore, it is stated that the kinematics can be neglected for the controller synthesis and an independent design of the respective degrees of freedom is possible. Hence, the actuator transfer function describes the following correlations:

$$ {}^{\mathcal{L}}G_{\mathrm{A}}(s) = \frac{{}^{\mathcal{L}}_{\mathrm{V}}z_{\mathrm{Hex,act}}(s)}{{}^{\mathcal{L}}_{\mathrm{V}}z_{\mathrm{Hex,set}}(s)} \equiv \frac{{}^{\mathcal{L}}_{\mathrm{V}}\varphi_{\mathrm{Hex,act}}(s)}{{}^{\mathcal{L}}_{\mathrm{V}}\varphi_{\mathrm{Hex,set}}(s)} \equiv \frac{{}^{\mathcal{L}}_{\mathrm{V}}\vartheta_{\mathrm{Hex,act}}(s)}{{}^{\mathcal{L}}_{\mathrm{V}}\vartheta_{\mathrm{Hex,set}}(s)} \tag{7.10} $$

The assumptions made in this section will be validated with the nonlinear model, which includes the kinematics.

7.3.1.3 Dead Time

According to statements of the hexapod manufacturers Bosch-Rexroth and PI, hexapods typically have dead times of approximately 10 ms[99,100], which mainly results from the kinematic and trajectory calculations. However, this value varies and could reach higher values.[100]

[99] Swart, R. d.: Expert Interview - Bosch Dead Times (2017).

[100] Cf. Mehren, M.: Masterthesis, Hexapod Vertikaldynamikregelung (2017), p. 83.

Dead times have a strong influence on the stability of control loops. Hence, to ensure a robust controller development, the dead time is set to 20 ms in the model for the controller synthesis. To enable the application of pole-zero-maps and root-locus methods in the controller development, a padé-approximation of 4th order is applied to formulate an analytical transfer function ${}^{\mathcal{L}}G_{\mathrm{DT}}$ for the dead time behavior.

7.3.2 Vertical Vibration System Model

The vertical vibration system model from Figure 7-11 is based on that for the investigation of the tire-sprung system described in subchapter 4.2. For the investigation of the hexapod control a division between hexapod bottom plate (HBP) and hexapod top plate (HTP) is introduced and the forces generated by the hexapod between both parts are considered. For the controller synthesis, the elastic tire behavior determined in section 4.1.1 is linearized to the constant value c_{T} around the static deflection at a wheel load of 4000 N. Hence, the tire forces are described as a function of the driving surface excitation $z_{\mathrm{DSE},i}$:

$${}_{\mathrm{H}}F_{z,c,\mathrm{T},i} = c_{\mathrm{T}}\left({}_{\mathrm{H}}z_{\mathrm{DSE},i} - {}_{\mathrm{H}}z_{\mathrm{HBP,W},i}\right) \tag{7.11}$$

$${}_{\mathrm{H}}F_{z,d,\mathrm{T},i} = d_{\mathrm{T}}\left({}_{\mathrm{H}}\dot{z}_{\mathrm{DSE},i} - {}_{\mathrm{H}}\dot{z}_{\mathrm{HBP,W},i}\right) \tag{7.12}$$

The required motions of the HBP at the wheel positions ${}_{\mathrm{H}}z_{\mathrm{HBP,W},i}$ are calculated according to equations (4.11) to (4.13). The forces and torques between the hexapod and the HBP have to be equal to the product of the accelerations of the top plate and its mass m_{HTP} respectively mass moment of inertia around the center of gravity $J_{\mathrm{HTP}}^{(\mathrm{CG})}$:

$${}_{\mathrm{H}}F_{\mathrm{Hex},z} = -m_{\mathrm{HTP}}\,{}_{\mathrm{H}}\ddot{z}_{\mathrm{HTP}} \tag{7.13}$$

$${}_{\mathrm{H}}M_{\mathrm{Hex},x} = -J_{\mathrm{HTP},x}^{(\mathrm{CG})}\,{}_{\mathrm{H}}\ddot{\varphi}_{\mathrm{HTP}} \tag{7.14}$$

$${}_{\mathrm{H}}M_{\mathrm{Hex},y} = -J_{\mathrm{HTP},y}^{(\mathrm{CG})}\,{}_{\mathrm{H}}\ddot{\vartheta}_{\mathrm{HTP}} \tag{7.15}$$

The motions at the HTP are equal to the superposed motions of the HBP and the Hexapod:

$${}_{\mathrm{H}}\ddot{z}_{\mathrm{HTP}} = {}_{\mathrm{H}}\ddot{z}_{\mathrm{HBP}} + {}_{\mathrm{H}}\ddot{z}_{\mathrm{Hex,act}} \tag{7.16}$$

$${}_{\mathrm{H}}\ddot{\varphi}_{\mathrm{HTP}} = {}_{\mathrm{H}}\ddot{\varphi}_{\mathrm{HBP}} + {}_{\mathrm{H}}\ddot{\varphi}_{\mathrm{Hex,act}} \tag{7.17}$$

$${}_{\mathrm{H}}\ddot{\vartheta}_{\mathrm{HTP}} = {}_{\mathrm{H}}\ddot{\vartheta}_{\mathrm{HBP}} + {}_{\mathrm{H}}\ddot{\vartheta}_{\mathrm{Hex,act}} \tag{7.18}$$

Next, the force and torque equilibriums for the HBP are formulated similar to equations (4.6) to (4.8) under consideration of the hexapod forces and moments and the HBP motion is substituted by the aforementioned equations. After a transformation into the Laplace space, the output accelerations are calculated dependent on the input quantities, namely the driving surface excitation z_{DSE} and the hexapod motions z_{Hex}, φ_{Hex}, ϑ_{Hex}. The DoFs are decoupled. By setting one of the respective input values zero, the transfer function for the other is calculated. Setting the hexapod motions to zero results in the disturbance behavior (DB):

$$ {}^{\mathcal{L}}G_{\mathrm{DB},z}(s) = \frac{{}^{\mathcal{L}}_{\mathrm{H}}\ddot{z}_{\mathrm{HTP,DB}}(s)}{{}^{\mathcal{L}}_{\mathrm{H}}z_{\mathrm{DSE}}(s)} = \frac{3(c_{\mathrm{T}} + d_{\mathrm{T}}s)s^2}{(m_{\mathrm{HBP}} + m_{\mathrm{HTP}})s^2 + 3d_{\mathrm{T}}s + 3c_{\mathrm{T}}} \tag{7.19} $$

$$ {}^{\mathcal{L}}G_{\mathrm{DB},\varphi}(s) = \frac{{}^{\mathcal{L}}_{\mathrm{H}}\ddot{\varphi}_{\mathrm{HTP,DB}}(s)}{{}^{\mathcal{L}}_{\mathrm{H}}z_{\mathrm{DSE}}(s)} = \frac{2(c_{\mathrm{T}} + d_{\mathrm{T}}s)\ell_{\mathrm{t}}s^2}{2\left(J^{(S)}_{\mathrm{HBP},x} + J^{(S)}_{\mathrm{HTP},x}\right)s^2 + d_{\mathrm{T}}\ell_{\mathrm{t}}^2 s + c_{\mathrm{T}}\ell_{\mathrm{t}}^2} \tag{7.20} $$

$$ {}^{\mathcal{L}}G_{\mathrm{DB},\vartheta}(s) = \frac{{}^{\mathcal{L}}_{\mathrm{H}}\ddot{\vartheta}_{\mathrm{HTP,DB}}(s)}{{}^{\mathcal{L}}_{\mathrm{H}}z_{\mathrm{DSE}}(s)} = \frac{\sqrt{3}(c_{\mathrm{T}} + d_{\mathrm{T}}s)\ell_{\mathrm{t}}s^2}{2\left(J^{(S)}_{\mathrm{HBP},y} + J^{(S)}_{\mathrm{HTP},y}\right)s^2 + d_{\mathrm{T}}\ell_{\mathrm{t}}^2 s + c_{\mathrm{T}}\ell_{\mathrm{t}}^2} \tag{7.21} $$

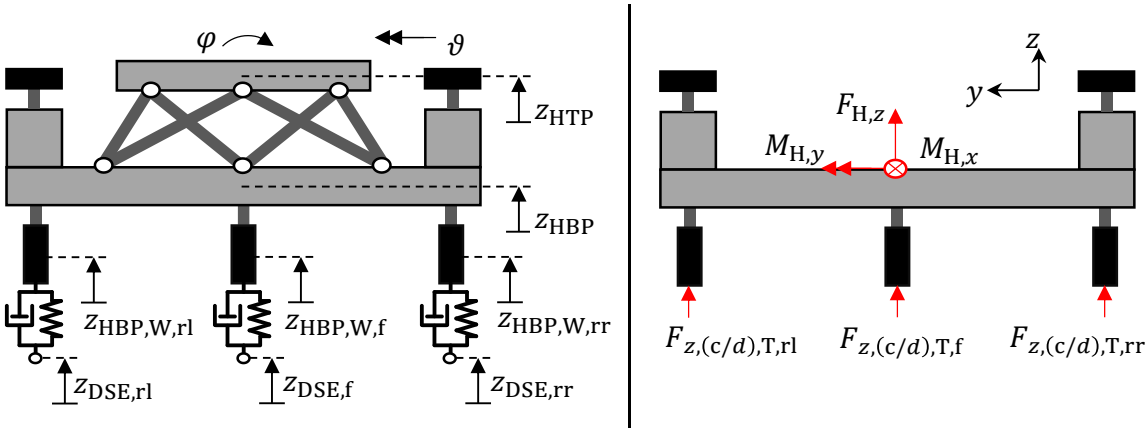

Figure 7-11: Vertical vibration system model.

For this step, the driving surface excitations at the respective wheels are adjusted so that isolated excitations of the DoFs are achieved. Secondly, setting the driving surface excitations to zero leads to the manipulation reaction behavior (MRB):

$$ {}^{\mathcal{L}}G_{\mathrm{MRB},z}(s) = \frac{{}^{\mathcal{L}}_{\mathrm{H}}\ddot{z}_{\mathrm{HTP,MRB}}(s)}{{}^{\mathcal{L}}_{\mathrm{H}}z_{\mathrm{Hex,act}}(s)} = \frac{(m_{\mathrm{HBP}}s^2 + 3d_{\mathrm{T}}s + 3c_{\mathrm{T}})s^2}{(m_{\mathrm{HBP}} + m_{\mathrm{HTP}})s^2 + 3d_{\mathrm{T}}s + 3c_{\mathrm{T}}} \tag{7.22} $$

$$ {}^{\mathcal{L}}G_{\mathrm{MRB},\varphi}(s) = \frac{{}^{\mathcal{L}}_{\mathrm{H}}\ddot{\varphi}_{\mathrm{HTP,MRB}}(s)}{{}^{\mathcal{L}}_{\mathrm{H}}\varphi_{\mathrm{Hex,act}}(s)} = \frac{\left(2J^{(S)}_{\mathrm{HBP},x}s^2 + (d_{\mathrm{T}}s + c_{\mathrm{T}})\ell_{\mathrm{t}}^2\right)s^2}{2\left(J^{(S)}_{\mathrm{HBP},x} + J^{(S)}_{\mathrm{HTP},x}\right)s^2 + d_{\mathrm{T}}\ell_{\mathrm{t}}^2 s + c_{\mathrm{T}}\ell_{\mathrm{t}}^2} \tag{7.23} $$

$$ {}^{\mathcal{L}}G_{\mathrm{MRB},\vartheta}(s) = \frac{{}^{\mathcal{L}}_{\mathrm{H}}\ddot{\vartheta}_{\mathrm{HTP,MRB}}(s)}{{}^{\mathcal{L}}_{\mathrm{H}}\vartheta_{\mathrm{Hex,act}}(s)} = \frac{\left(2J^{(S)}_{\mathrm{HBP},y}s^2 + \ell_{\mathrm{t}}^2(d_{\mathrm{T}}s + c_{\mathrm{T}})\right)s^2}{2\left(J^{(S)}_{\mathrm{HBP},y} + J^{(S)}_{\mathrm{HTP},y}\right)s^2 + \ell_{\mathrm{t}}^2(d_{\mathrm{T}}s + c_{\mathrm{T}})} \tag{7.24} $$

The overall motions at the HTP are equal to the sum of MRB output and DB output.

7.4 Controller Synthesis

The next step is the controller synthesis for the developed system architectures. The methodology for this subchapter is depicted in Figure 7-12. Prior to the controller synthesis, an

evaluation quantity is defined, which is applied for the parameter optimization and the evaluation of the controller performance. Based on the developed linear model, a system analysis is conducted to be able to derive a suitable controller law for the CLC. Subsequently, a parameterization of the controller law is possible. Based on this controller, the command behavior is analyzed and, if necessary, the design of a pre-filter is conducted. As described above, the OLC approach has no controller to be designed. However, a system analysis is conducted for an insight into its behavior and the comparison to the CLC. The last step is the comparison of the system architecture approaches based on the linear model for a first estimation of the differences in their performance.

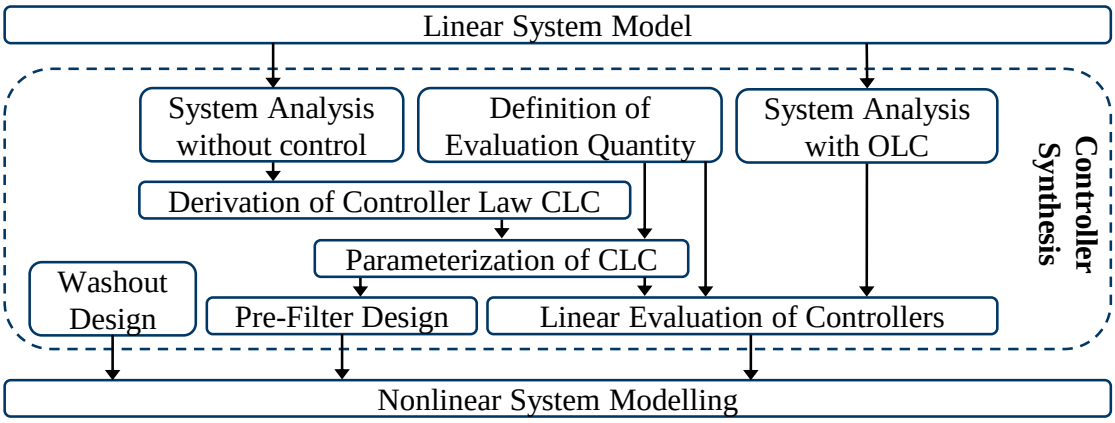

Figure 7-12: Methodology of controller synthesis.

7.4.1 Evaluation Parameter for Linear Analysis

In order to assess and compare different controller designs, the root mean square (r.m.s.) of the output acceleration $\ddot{z}_{\mathrm{HTP,act}}$ is applied. In order to receive the output acceleration from the disturbance transfer function $G_{\mathrm{Dist},z}$, it is multiplied with $1/f$. This corresponds to the description of the driving surface excitation in equation (2.4). The gain of the driving surface excitation is set to one because only relative considerations are conducted and so the absolute acceleration value is irrelevant. The evaluation parameter must also take into account the frequency-dependent human motion perception. This is achieved by applying a motion perception frequency weighing filter ${}^{\mathcal{F}}G_{\mathrm{FW}}$ according to section 2.4.2 to the output acceleration.[101] These considerations result in the frequency-weighed output acceleration:

$$ {}^{\mathcal{F}}_{\mathrm{H}}\ddot{z}_{\mathrm{HTP,act,FW}}(f) = {}^{\mathcal{F}}G_{\mathrm{FW}}(f)\,\frac{1}{f}\,{}^{\mathcal{F}}G_{\mathrm{Dist},z}(f) \tag{7.25} $$

The r.m.s. of the frequency-weighed output acceleration is calculated in the relevant frequency range for whole body vibrations between $f_{\mathrm{l}} = 0.5$ Hz and $f_{\mathrm{h}} = 80$ Hz:[102]

[101] Cf. ISO: ISO 2631-1 - Mechanical Vibration (1997).

[102] VDI, Verein Deutscher Ingenieure: VDI 2057 - Ganzkörper-Schwingungen (2017), p. 11.

$$ {}_{\mathrm{H}}\ddot{z}_{\mathrm{HTP,rms,FW}} = \sqrt{\frac{1}{f_\mathrm{h} - f_\mathrm{l}} \int_{f_\mathrm{l}}^{f_\mathrm{h}} \left({}_{\mathrm{H}}^{\mathcal{F}}\ddot{z}_{\mathrm{HTP,act,FW}}(f) \right)^2 df} \tag{7.26} $$

The relative attenuation ϱ between controlled and uncontrolled system that is applied in the optimization of the controller parameterization and the evaluation is determined as follows:

$$ \varrho = \frac{{}_{\mathrm{H}}\ddot{z}_{\mathrm{HTP,rms,FW,controlled}}}{{}_{\mathrm{H}}\ddot{z}_{\mathrm{HTP,rms,FW,uncontrolled}}} \tag{7.27} $$

7.4.2 Controller Synthesis Closed-Loop Architecture (CLC)

7.4.2.1 System Analysis

The control loop structure of the decoupled z-DoF, which is derived from the system architecture in Figure 7-4 and the actuator structure in Figure 7-6, is shown in Figure 7-13. It contains the transfer functions, which have been formulated in the sections 7.3.1.1 and 7.3.2, as well as the control law K, the Washout transfer function G_{WO}, and the pre-filter transfer function for the adjustment of the command response $G_{\mathrm{PF,CR}}$. The control loops for the pitch- and roll-DoFs are identical. Due to the similar system behavior of the three DoFs, the controller synthesis is exemplary conducted for the z-DoF. From this control loop structure, the disturbance transfer function G_{Dist} is derived:

$$ {}^{\mathcal{L}}G_{\mathrm{Dist,CLC},z} = \frac{{}_{\mathrm{H}}^{\mathcal{L}}\ddot{z}_{\mathrm{HTP,act}}(s)}{{}_{\mathrm{H}}^{\mathcal{L}}z_{\mathrm{DSE}}(s)} = {}^{\mathcal{L}}G_{\mathrm{DB},z} \frac{1}{1 + {}^{\mathcal{L}}G_{\mathrm{OLTF,CLC},z}} \tag{7.28} $$

With the open-loop transfer function (OLTF) ${}^{\mathcal{L}}G_{\mathrm{OLTF,CLC},z}$ describing the relation between the hexapod-excited acceleration of the top plate $\ddot{z}_{\mathrm{HTP,MRB}}$ and the control error:

$$ {}^{\mathcal{L}}G_{\mathrm{OLTF,CLC},z} = \frac{{}_{\mathrm{H}}^{\mathcal{L}}\ddot{z}_{\mathrm{HTP,MRB}}}{{}_{\mathrm{H}}^{\mathcal{L}}\ddot{z}_{\mathrm{HTP,set}} - {}_{\mathrm{H}}^{\mathcal{L}}\ddot{z}_{\mathrm{HTP,act}}} = \frac{1}{s^2} {}^{\mathcal{L}}K \, {}^{\mathcal{L}}G_{\mathrm{DT}} \, {}^{\mathcal{L}}G_{\mathrm{A}} \, {}^{\mathcal{L}}G_{\mathrm{MRB}} \tag{7.29} $$

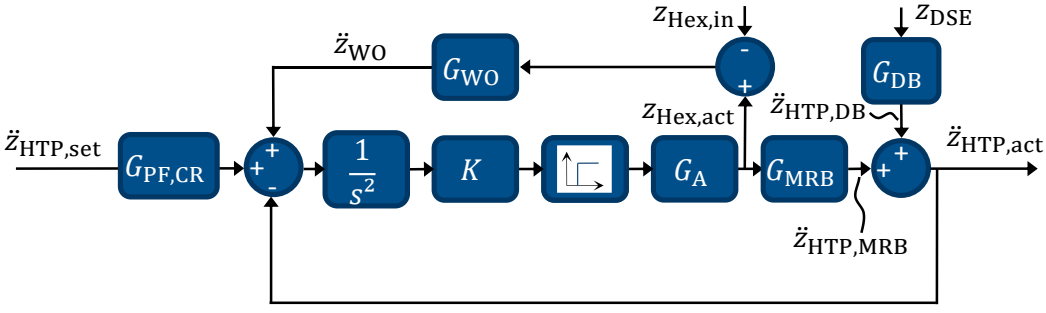

Figure 7-13: Control-loop structure CLC, exemplarily for z-DoF.

The Washout is neglected for the first analytical system analysis for a better understanding of the system influences. The dynamics of the washout are far below the relevant control frequencies, so that no influence on the controller development is expected. This assumption

will be proven in the validation. The controller synthesis is conducted based on the OLTF of the disturbance loop. The first step is the derivation of specifications on the OLTF from the aspired control aims. Without a controller (${}^{\mathcal{L}}G_{\mathrm{OLTF,CLC},z} = 0$), the acceleration of the hexapod top plate results only from the disturbance behavior ${}^{\mathcal{L}}G_{\mathrm{DB}}$, which cannot be affected by the controller. For a reduction of the disturbance accelerations, the feedback function of ${}^{\mathcal{L}}G_{\mathrm{Dist,CLC},z}$ has to be as small as possible, especially in the frequency regions where ${}^{\mathcal{L}}G_{\mathrm{DB},z}$ is large (natural frequency of the vibration system). On the other hand, no other relevant peaks should be created by the controller. From these considerations, the following specifications for the OLTF can be derived:

- The magnitude of the OLTF should be as high as possible, especially in the range of the natural frequency of the vibration system.
- The phase and gain margins of the system must be as high as possible to avoid the insertion of new peaks into the disturbance transfer function.

For the derivation of a controller law suitable to attain these specifications, the OLTF is analyzed for a proportional controller with gain one ($K = 1$). The corresponding Bode plot is shown on the left side of Figure 7-14 as blue curve.

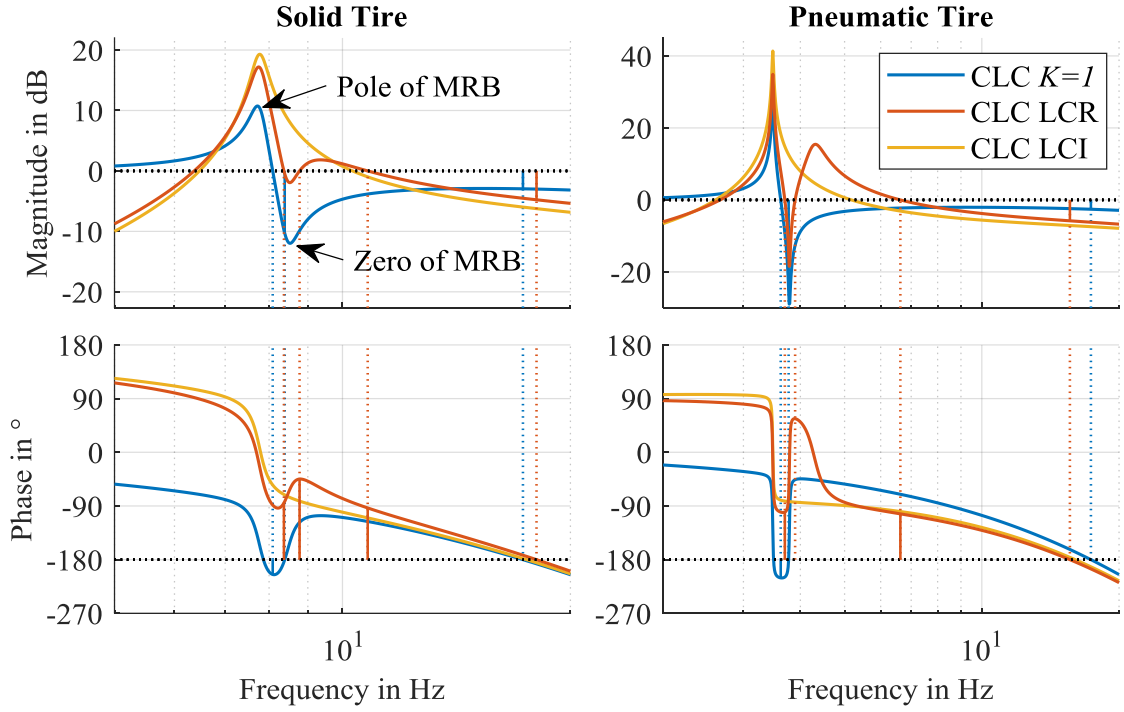

Figure 7-14: Bode plot of open-loop transfer function (OLTF) of closed-loop system architecture (cf. Figure 7-4) determined with linear model from subchapter 7.3. Comparison between proportional controller with gain 1, robust lead compensator control (LCR) and ideal lead compensator (LCI).

The first specification is already well fulfilled due to the pole of the manipulating reaction behavior (MRB) transfer function ${}^{\mathcal{L}}G_{\mathrm{MRB},z}$ at 7.8 Hz. However, due to the high group delay resulting from the low tire damping, the phase margin behind the pole of the MRB is negative, which indicates an unstable system. Additionally, the following zero of the MRB leads

to a magnitude increase at higher frequencies, which results in a low gain margin. This generates peaks in the feedback function, which result in higher amplitudes than in the uncontrolled system. A further increase of the gain, which would be necessary to increase the amplitude at the natural frequency of the vibration system, would lead to a further reduction of the gain margin.

7.4.2.2 Derivation of Controller Law

The dynamics of the controller have to address the mentioned margin problems by raising the phase in the range of the pole of the MRB and at the same time reducing the amplitude at higher frequencies. This task is typical for a lead compensator. The phase has to be raised by placing zeroes of the controller at low frequencies. The resulting positive magnitude slope has to be compensated by poles above the critical crossover frequencies.

The given system has the positive characteristic of a conjugate complex zero of the MRB, which follows the pole directly at 8.5 Hz. The compensation of this zero with the controller pole has two advantages. First, no additional peak is generated by the controller pole, which would lead to higher crossover frequencies. Second, the magnitudes above the crossover frequency are reduced, which results in a higher gain margin. The conjugate complex pole of the controller allows the implementation of a conjugate complex zero that raises the phase by 180°. The disadvantage of decreasing magnitudes at low frequencies is bearable because the disturbance magnitudes also decrease due to the double derivative behavior on acceleration level. Hence, a second order lead compensator is applied.

7.4.2.3 Parameterization of Controller

The available parameters of the second order lead compensator are the conjugate complex pole, the conjugate complex zero, and the controller gain. It has already been discussed that the conjugate complex pole should compensate the zero of the MRB. However, an additional problem is the robustness of the controller to variations of the natural frequency. An increase of the natural frequency shifts the phase-heaving zero towards higher frequencies, while the pole of the controller remains at the same position. Because of the high group-delays resulting from the low damping of the controller pole, this could yield a phase below -180° and thus, an unstable system. Therefore, although the pole should compensate the zero, its damping ratio is increased to 10 %. The reduced group delays of the pole enable an increase of the systems natural frequency by 1.5 Hz without getting unstable (cf. section 7.4.4.1).

Concerning the conjugate complex zero, there are two demands:

- It must be placed at a frequency so far below the natural frequency of the disturbance behavior (DB) that the amplitude of the OLTF is not affected at that frequency.
- The phase-raising of the zero must be maximum at the relevant crossover frequencies to achieve the maximum phase margin.

Both demands are fulfilled if the zero is placed in the origin. No relevant disadvantages result from that design because in this region the closed-loop transfer function is dominated by the disturbance behavior, which shows falling amplitudes towards low frequencies.

The parameterization of the controller gain is subject to a trade-off between reducing the amplitude of the closed-loop transfer function at the natural frequency of the disturbance behavior (high amplitude of OLTF) and increasing peaks at higher frequencies (reducing phase margin of OLTF). An additional requirement is a phase margin of at least 60° to achieve robust stability.[103]

In order to optimize this tradeoff, the evaluation parameter ϱ defined in equation (7.27) is applied. The gain is parameterized by minimizing this value while maintaining the stability margin of 60°. The resulting OLTF is shown in Figure 7-14 on the left for the robust control design and the ideal design with full compensation of the zero of the MRB for comparison. It is recognizable that the stated requirements, a high amplitude at the natural frequency of the disturbance behavior and a high phase margin of 80°, are achieved. Although the amplitude at the natural frequency and the gain margin is lower for the robust design, this is tolerable for the sake of improved robustness concerning fluctuations of the natural frequency.

7.4.2.4 Adaptions for Pneumatic Tires

The following differences between solid and pneumatic tires probably affect the considerations of the controller synthesis described above:

- The lower natural frequency requires less phase heave around that frequency, so that the zeros can be placed at higher frequencies resulting in an increased gain margin.
- The reduced damping of the pneumatic tire increases the group delays and the slope of the magnitudes around the natural frequency. This could result in a lower robustness. On the other hand, the impact of wear on the natural frequency is lower due to the reduced impact of the rubber structure on the overall stiffness. Therefore, the range of the natural frequency fluctuation is lower.
- The belt eigenmode introduces a peak into the OLTF, which could yield stability issues of the closed loop if an additional intersection of the 0 dB line is generated.

In order to investigate these aspects, the residual stiffness of the SWIFT model from subchapter 6.1 is linearized to generate a linear description for the controller synthesis. The rest of the model is already linear and is adopted. As for the solid tire, the OLTF is analyzed based on a proportional controller with gain 1. The resulting Bode plot of the OLTF is shown on the right side of Figure 7-14.

The belt eigenmode is not recognizable in the MRB and is therefore negligible for the controller synthesis. As expected, the large group delays have a high impact on the controller

[103] Lunze, J.: Regelungstechnik (2010). p. 445.

stability. Thus, one zero is placed in the origin to increase the phase by 90°, so that an exceeding of a phase of -180° due to the pole of the MRB is avoided. The phase increase of the zero of the MRB is steep so that the impact on lower frequencies is reduced. Therefore, in order to achieve robustness, it is not sufficient to increase the damping of the controller pole but also the frequency has to be adapted. Therefore, the damping of the controller pole is increased to 5 % and the natural frequency is set 0.5 Hz above the zero of the MRB. The gain is parameterized according to the methodology of the solid tire. The location of the second zero is a tradeoff between the gain margin and the phase margin. Thus, an optimization is conducted with respect to the evaluation parameter ϱ. The resulting OLTFs are shown on the right side of Figure 7-14 for the robust lead compensator and the ideal compensator. A high amplitude and phase margin above 80° are achieved with the design.

7.4.2.5 Command Response

The previously developed controller is focused on the reduction of disturbance vibrations resulting from driving surface unevenness. However, the inputs from other functions as the tilt coordination require a command response behavior that does not impede these functions in the relevant frequency range. Although the main function of the tilt coordination is the simulation of low-frequent accelerations (cf. section 2.3.1) it also has to represent high-frequent angular accelerations resulting from the horizontal dynamics of the virtual vehicle. These motions require a representable frequency range up to 5 Hz.[104]

In order to investigate if this requirement is fulfilled by the command behavior, the following command response (CR) transfer function is derived from the control loop architecture in Figure 7-13:

$$ {}^{\mathcal{L}}G_{\mathrm{CR,CLC},z} = \frac{{}^{\mathcal{L}}_{\mathrm{H}}\ddot{z}_{\mathrm{HTP,act}}(s)}{{}^{\mathcal{L}}_{\mathrm{H}}\ddot{z}_{\mathrm{HTP,set}}(s)} = {}^{\mathcal{L}}G_{\mathrm{PF,CR},z}\,\frac{{}^{\mathcal{L}}G_{\mathrm{OLTF,CLC},z}}{1+{}^{\mathcal{L}}G_{\mathrm{OLTF,CLC},z}} \tag{7.30} $$

With the pre-filter transfer function ${}^{\mathcal{L}}G_{\mathrm{PF,CR},z}$ that is applied to adjust the command behavior independent of the disturbance behavior. The resulting transfer function for the CLC controller with no pre-filter (${}^{\mathcal{L}}G_{\mathrm{PF,CR},z} = 1$) is shown in Figure 7-15 as red curve. The original command response behavior without a feedback loop is shown as blue curve for comparison. It is recognizable that the developed disturbance controller significantly impedes the command behavior. This is mainly due to the zeros of the controller that result in decreasing magnitudes towards lower frequencies. The tilt coordination function with its low frequencies is highly affected by this behavior. Thus, the pre-filter ${}^{\mathcal{L}}G_{\mathrm{PF,CR},z}$ is designed to compensate the zeros of the controller. The two poles required for this compensation enable the introduction of two additional zeros, which are applicable to mitigate the impact of the pole of the manipulating reaction behavior (MRB). The resulting command response transfer

[104] Adamski, D.: Simulation Fahrwerktechnik (2014). p. 101.

function is shown in Figure 7-15 as yellow curve. It is recognizable that the compensation of the zeros of the controller yields an ideal transfer behavior (0 dB) in the low frequency range up to 7 Hz, which is sufficient for the simulation of vehicle dynamics with the hexapod. The compensation of the pole of the MRB even leads to an improvement of the command response compared to the original uncontrolled system, which also suffers from the characteristics of the vibration system.

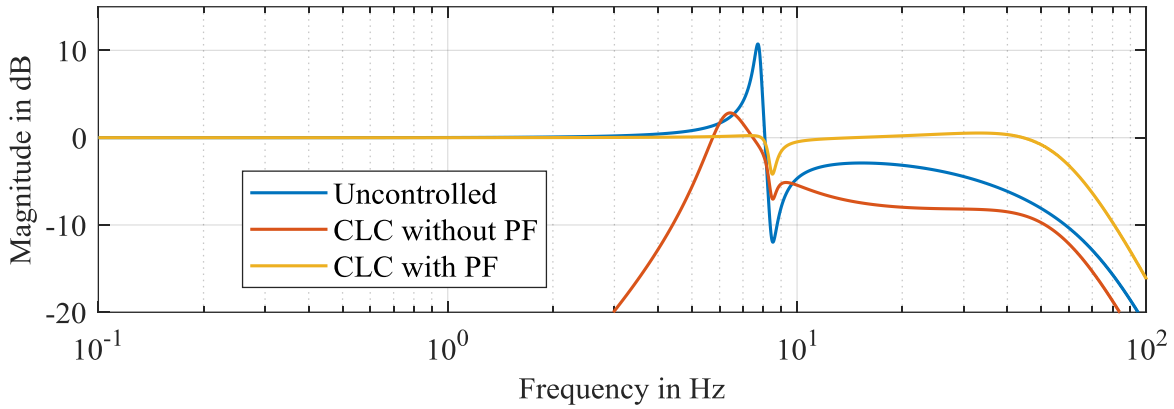

Figure 7-15: Command response transfer function determined with linear model from subchapter 7.3 for original uncontrolled system, the closed-loop architecture without pre-filter (CLC without PF) and the CLC with pre-filter (CLC with PF).

7.4.3 System Analysis Open-Loop Architecture (OLC)

For the OLC, the input into the actuator is the negative bottom plate acceleration, which can be formulated dependent of the top plate acceleration:

$$-{}_{\mathrm{H}}\ddot{z}_{\mathrm{HBP,act}} = {}_{\mathrm{H}}\ddot{z}_{\mathrm{Hex,act}} - {}_{\mathrm{H}}\ddot{z}_{\mathrm{HTP,act}} \tag{7.31}$$

This results in the control loop structure for the OLC shown in Figure 7-16. The actuator feedback transfer function ${}^{\mathcal{L}}G_{\mathrm{A,FB}}$, which consists of the blocks bordered by dashed lines, is calculated with the actuator dynamics ${}^{\mathcal{L}}G_{\mathrm{A}}$ and the dead time approximation ${}^{\mathcal{L}}G_{\mathrm{DT}}$:

$${}^{\mathcal{L}}G_{\mathrm{A,FB}} = \frac{{}^{\mathcal{L}}G_{\mathrm{DT}}\,{}^{\mathcal{L}}G_{\mathrm{A}}}{1 - {}^{\mathcal{L}}G_{\mathrm{DT}}\,{}^{\mathcal{L}}G_{\mathrm{A}}} \tag{7.32}$$

Inserting the transfer function of the actuator dynamics leads to:

$${}^{\mathcal{L}}G_{\mathrm{A,FB}} = \frac{V_{\mathrm{Pos}}\,{}^{\mathcal{L}}G_{\mathrm{DT}}}{8T_{\mathrm{PE}}^3\zeta^3 s^4 + 4T_{\mathrm{PE}}^2\zeta^3 \mathrm{s}^3 + 2T_{\mathrm{PE}}\zeta^2 \mathrm{s}^2 + \mathrm{s} + V_{\mathrm{Pos}}\left(1 - {}^{\mathcal{L}}G_{\mathrm{DT}}\right)} \tag{7.33}$$

For a dead time of zero, the constant fraction of the denominator is omitted and, thus, an integral behavior is induced. This leads to an optimal compensation of low-frequent excitations. The open-loop transfer function (OLTF) for the OLC is formulated as follows:

$${}^{\mathcal{L}}G_{\mathrm{OLTF,OLC},z} = \frac{{}^{\mathcal{L}}_{\mathrm{H}}\ddot{z}_{\mathrm{HTP,MRB}}}{{}^{\mathcal{L}}_{\mathrm{H}}\ddot{z}_{\mathrm{HTP,set}} - {}^{\mathcal{L}}_{\mathrm{H}}\ddot{z}_{\mathrm{HTP,act}}} = \frac{1}{s^2}\,{}^{\mathcal{L}}G_{\mathrm{A,FB}}\,{}^{\mathcal{L}}G_{\mathrm{MRB}} \tag{7.34}$$

The overall disturbance transfer function can be calculated according to the closed-loop architecture in equation (7.28). The Bode plot of the OLTF is shown in Figure 7-17 for a dead time of zero and a dead time of 20 ms.

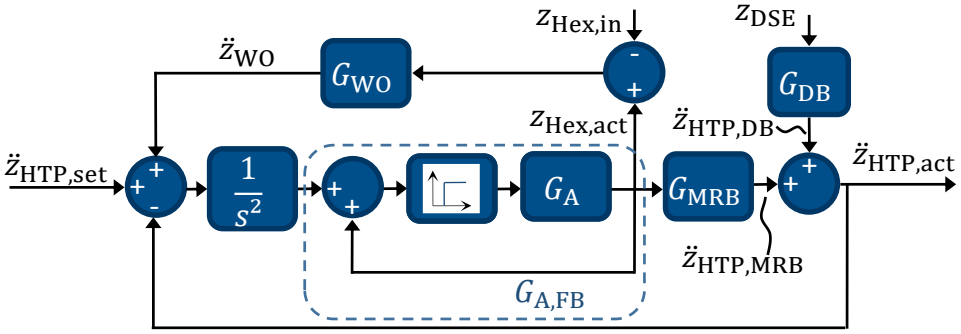

Figure 7-16: Control-loop structure OLC.

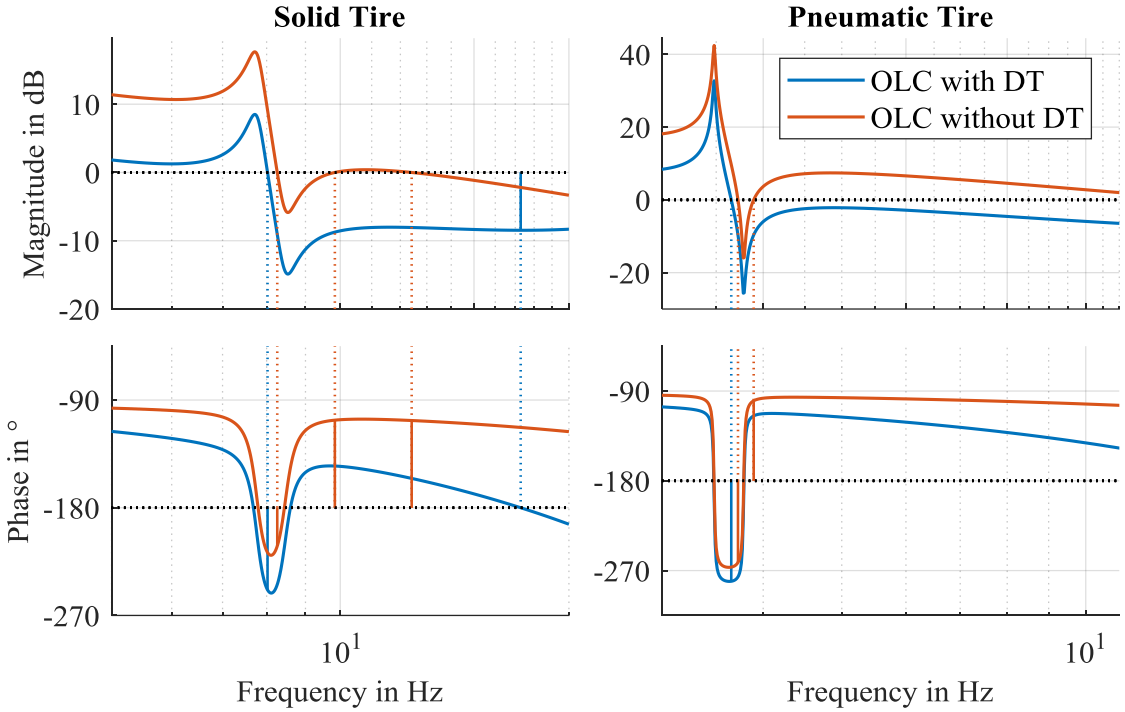

Figure 7-17: Bode plot of open-loop transfer function (OLTF) for open-loop system architecture (OLC, cf. Figure 7-5) determined with linear model from subchapter 7.3. Comparison between dead time of zero (without DT) and dead time of 20 ms (with DT).

It is recognizable that the system is unstable for both tire types. The high group delay at the natural frequency resulting from the low damping in combination with the I-behavior of the control loop results in an exceeding of the -180° phase limit. Even if no dead time would act in the system, no stability could be achieved. Summarizing, the OLC in this form is not suitable for the solely tire-sprung system due to the low damping of the tires. An improvement is possible by implementing additional phase heaving elements to compensate the phase reduction of the integral term. However, this would require a parameterization and, hence, dissolve the greatest advantage of the OLC. Additionally, the nonlinear dependence of the OLC-OLTF from the actuator dynamics would impede the parameterization.

7.4.4 Controller Robustness

The controller robustness is investigated concerning two aspects: the deviation of the vibration system parameters and the variations of the dead time.

7.4.4.1 Vibration System Parameter Deviations

In order to determine the robustness of the developed controller, the vibration system parameters natural frequency and damping ratio of the linear model are varied while the control law and parameterization are maintained. The results for the vertical DoF are shown for both tire types in Figure 7-18 as the negative relative attenuation from equation (7.27) in dB (positive values indicate an improvement by the controller) dependent on the parameter deviations together with the 0 dB plane that indicates a deterioration of the original behavior. Missing values indicate an unstable system configuration. The results for the pitch and roll DoF are given in the appendix in Figure B.2 - 1 and Figure B.2 - 2.

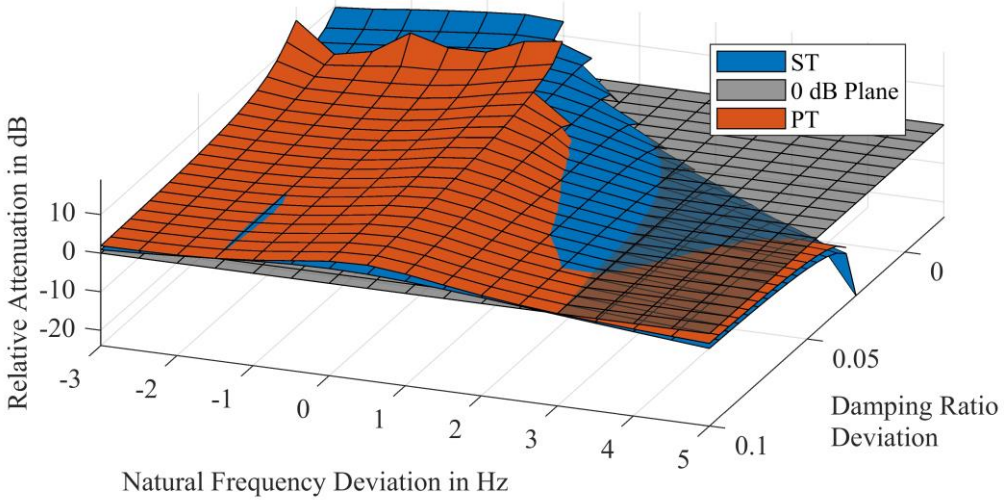

Figure 7-18: Robustness of controller against deviations of vibration parameters for solid (ST) and pneumatic tire (PT) in vertical DoF. Positive values (above 0 dB plane) indicate an improvement by the controller. Determined with linear model from subchapter 7.3 by varying parameters of the vibration system for a fixed control design and evaluating relative attenuation (cf. equation (7.27)).

It is recognizable that especially an increase of the damping is uncritical in terms of stability. The reason for the reduction of the relative attenuation is that the natural frequency becomes less dominant, resulting in a reduced impact of the controller that focusses on the reduction of the magnitudes at this frequency. For the solid tire, the increase of the natural frequency by more than 1.5 Hz results in an unstable system due to the phase reduction by the controller pole that is compensated at too high frequencies by the zero of the manipulating reaction behavior (MRB). This is especially a problem because of the large impact of wear on the natural frequency of the solid tire that is indicated in Figure 4-2. To assure robustness for a natural frequency fluctuation of 4 Hz would impede the controller performance by far. Thus, for a robust controller function, an online parameter identification will be required to continuously adapt the controller parameters to that of the vibration system. A low dynamic of

this adaption is sufficient because the wear rate is low. Probably, the control function even needs to be deactivated at a certain wear state due to the limitations of the actuator dynamics. For all other variations resulting from tire nonlinearities, the margin of 1.5 Hz is sufficient. The same applies for the margin of 0.5 Hz for the pneumatic tire.

7.4.4.2 Dead Time Variations

The robustness of the developed controller against dead time variations is investigated by applying various dead times on a given system and controller configuration. The results are given as the negative relative attenuation from equation (7.27) in dB (positive values indicate an improvement by the controller). It is recognizable that the controller generates a positive impact up to dead times of 44 ms for the solid and 52 ms for the pneumatic tire. This results from the robust controller design with a phase margin of at least 60°. The sensitivity of the solid tire to deviations around the design dead time (20 ms) is slightly higher than that of the pneumatic tire, but with a difference of 1 dB at a dead time deviation of 10 ms, sufficient control performance is still achieved. The results for the pitch and roll DoF given in the appendix in Figure B.2 - 3 and Figure B.2 - 4 are similar.

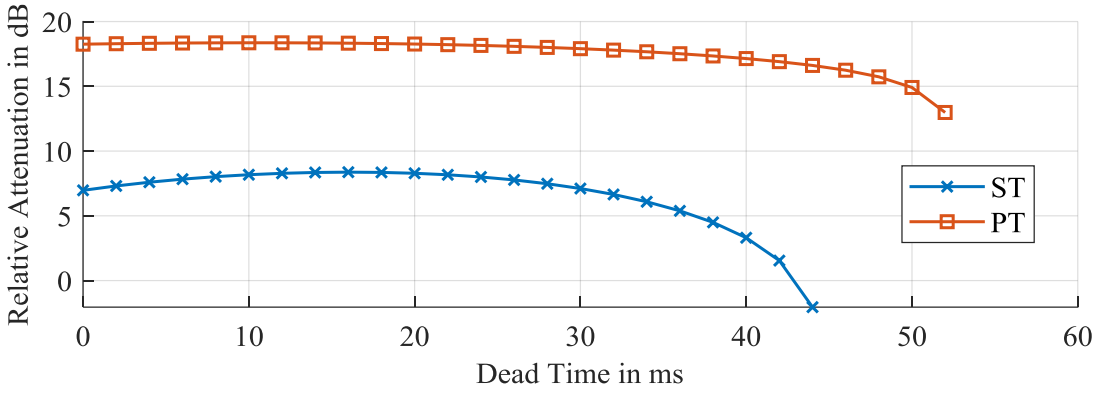

Figure 7-19: Robustness of controller against deviations of dead time for solid (ST) and pneumatic tire (PT) in vertical DoF. Determined with linear model from subchapter 7.3 by varying dead time for a fixed control design and evaluating relative attenuation (cf. equation (7.27)).

7.4.5 Washout

The washout is required to keep the hexapod in the middle of its range of motion. The control function itself does not require a washout because the average acceleration and therefore the position resulting from driving surface unevenness is zero. Nevertheless, due to errors in the acceleration determination, the control or high amplitudes of the driving surface e.g. from large wavelengths the hexapod could drift into its stroke limitation. Nevertheless, these error sources do not require a high dynamic. Additionally, the motions of the washout should maintain a sufficient margin to the perception thresholds to avoid an exceeding in combination with other disturbances. Thus, the washout is designed as a second order low-pass filter with a low natural frequency and damping ratio of 1 to avoid an oscillatory behavior that has an increased effect on the human motion perception:

$$ {}_{\mathrm{H}}\ddot{z}_{\mathrm{WO}} = \omega_{\mathrm{WO}}^2\left({}_{\mathrm{H}}z_{\mathrm{Hex,in}} - {}_{\mathrm{H}}z_{\mathrm{Hex,act}}\right) + 2\omega_{\mathrm{WO}} D_{\mathrm{WO}}\, {}_{\mathrm{H}}\dot{z}_{\mathrm{Hex,act}} \tag{7.35} $$

The natural frequency is designed so that an acceleration fraction $k_{a,\mathrm{WO}}$ of the perception threshold a_{PT} acts on the hexapod top plate at the maximum stroke of the hexapod:

$$ \omega_{o,\mathrm{WO}}^2 = \frac{k_{a,\mathrm{WO}} a_{\mathrm{PT}}}{{}_{\mathrm{H}}z_{\mathrm{Hex,max}}} \tag{7.36} $$

The factor $k_{a,\mathrm{WO}}$ is set to 0.1. This dynamic is assumed to be sufficient to account for the small drift effects so that the limitation of the acceleration is set conservatively to leave enough margin for other disturbances. If a higher drift of the hexapod is expected, for example due to a high inclination of the driving surface, the factor $k_{a,\mathrm{WO}}$ can be increased.

7.4.6 Linear Controller Performance Evaluation

The performance of the controllers is evaluated by examining the frequency-weighed output accelerations at the hexapod top plate ${}^{\mathcal{F}}_{\mathrm{H}}\ddot{z}_{\mathrm{HTP,act,FW}}$, ${}^{\mathcal{F}}_{\mathrm{H}}\ddot{\vartheta}_{\mathrm{HTP,act,FW}}$ and ${}^{\mathcal{F}}_{\mathrm{H}}\ddot{\varphi}_{\mathrm{HTP,act,FW}}$ from (7.25) for the different control approaches. The resulting Bode plots of the vertical DoF are shown in Figure 7-20. The pitch and roll DoF are given in the appendix in Figure B.1 - 1 and Figure B.1 - 2. As already mentioned, the closed-loop control (CLC) design is a compromise between damping the peak at the natural frequency and increasing the magnitude at higher frequencies. The targets of damping the main peak and, at least with the ideal controller, generating a more uniform course of the magnitude are achieved. The impact of the newly generated high-frequent excitations is mitigated by the reduced sensitivity of the human motion perception at high frequencies. The required robust design impedes the behavior due to the shift of the controller pole relative to the zero of the MRB.

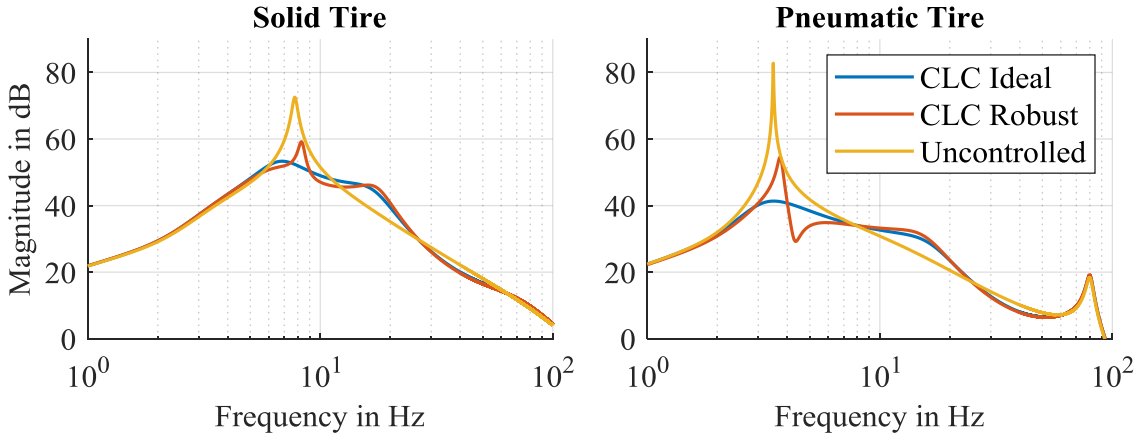

Figure 7-20: Bode plot of vertical frequency-weighed output acceleration (cf. equation (7.25)) comparing the ideal and robust closed-loop control (CLC) approaches to the uncontrolled system. Determined with linear model from subchapter 7.3.

This is also evident in the summarized results for all DoF in Table 7-1. Shown is the relative attenuation ϱ from equation (7.27) of the two control approaches for the three DoFs. In order to quantify the influence of the robust design that impedes the compensation of the zero of

the MRB, the robust and the ideal controller design are also compared. The impact of the robust design on the attenuation is small especially in vertical direction, while it enables a high fluctuation of the systems natural frequency without becoming unstable. The CLC has a higher attenuation in the z-DoF than in the pitch- and roll-DoF. The reason for this is the slightly higher natural frequency of each of the angular DoFs, which requires reduced gains in order to maintain the stability margins. The OLC is unstable for all tire types and DoFs.

Summarizing from the linear considerations, the CLC improves the vertical dynamic behavior of the system. The next step is to validate this finding with an alternative model.

Table 7-1: Relative attenuation ϱ (cf. equation (7.27)) of the control approaches (open-loop system architecture, OLC; closed-loop system architecture, CLC) for solid (ST) and pneumatic (PT) tire.

DoF	z		ϑ		φ	
Tire Type	ST	PT	ST	PT	ST	PT
CLC ideal	34 %	10 %	46 %	9 %	47 %	11 %
CLC robust	37 %	14 %	47 %	19 %	48 %	24 %
OLC	Unstable	Unstable	Unstable	Unstable	Unstable	Unstable

7.5 Theoretical Validation

7.5.1 Validation and Evaluation Model

In order to validate the developed control approaches, an alternative nonlinear modeling approach is applied. The following effects have to be considered by the model:

- Kinematic influences like the changing angles of the hexapod actuators
- Restrictions of the manipulated variables of the hexapod actuators
- Multiple Input-Multiple Output behavior of the hexapod
- Nonlinear characteristics of the solid tires applied in the system
- Real dead times instead of approximations
- Limited sampling rate of hexapod input signals

In order to address these aspects, a multibody model is applied. The basic mechanical setup is similar to that shown in Figure 7-11. Instead of linear tire springs, the nonlinear characteristic determined in sections 4.1.1 and 4.1.2 is applied. The six hexapod actuators are connected to the top and bottom plate bodies by cardan joints. The actuators are modelled as two bodies connected by an actuated prismatic joint. The input into the actuated joint is the pod length output of the actuator dynamics model in Figure 7-7. The joint calculates the resulting reaction force and applies it as a load torque to the actuator dynamics model. In contrast to the linear approach, the actuator model considers restrictions of the manipulated variables as indicated in Figure 7-7 as well as the discretization of the hexapod input signals,

the inverse kinematic calculation, and dead times according to Figure 7-6. The input into the multibody model are the driving surface excitations $z_{\mathrm{DSE},i}$.

7.5.2 Theoretical Validation of Control System Function

In this section, a validation of the developed control approaches is conducted based on the described nonlinear multibody model. The spectra of the occurring frequency-weighed output accelerations are shown in Figure 7-21 for solid and pneumatic tires.

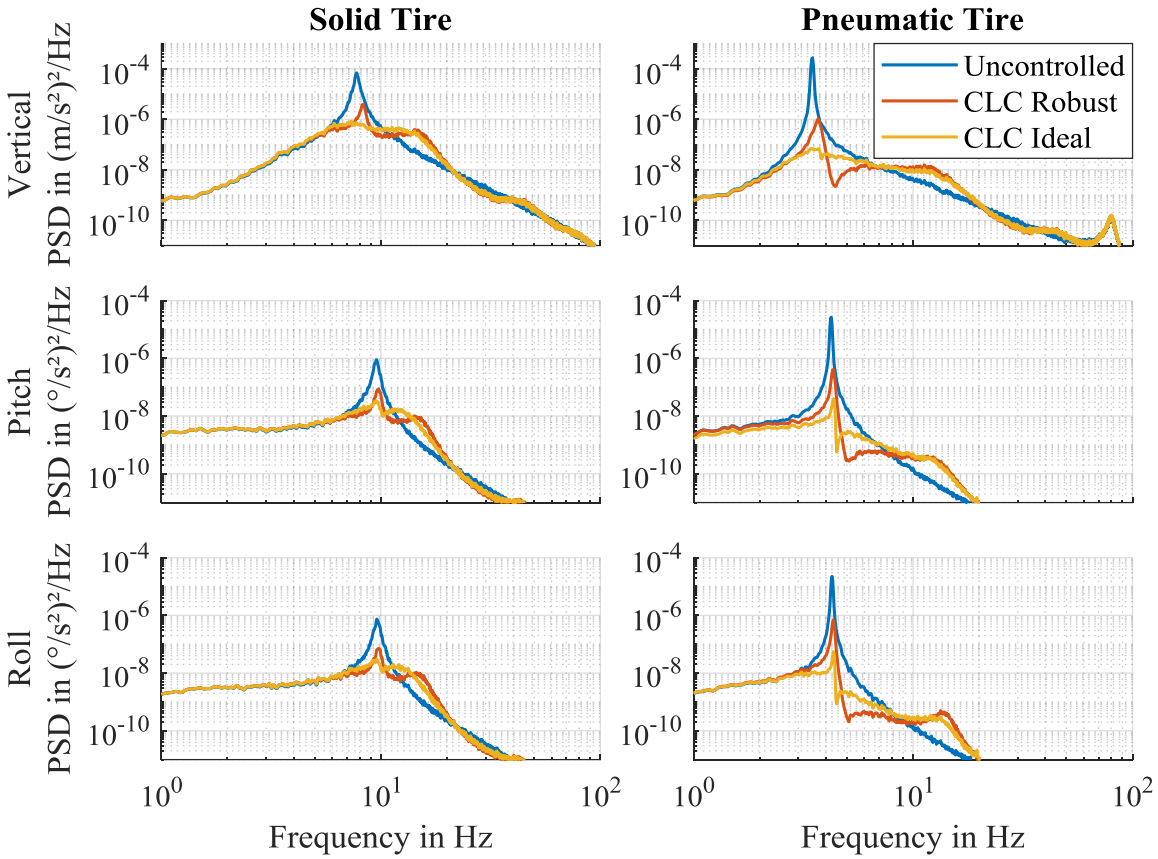

Figure 7-21: Theoretical validation of control system function by means of frequency weighed acceleration power spectral density for ideal and robust closed-loop architecture (CLC) compared to uncontrolled system for vertical, pitch and roll DoF. Determined with multi-body model from section 7.5.1 in urban driving scenario on reference driving surface roughness of 0.036 mm³.

For both tire types, the CLC leads to a damping of the natural frequency, while the ideal controller results in a more uniform course at least for the solid tire. Especially for the pitch and roll direction of the pneumatic tire, even for the ideal controller a high variation is recognizable around the natural frequency. This results from a slight deviation between the natural frequency of the linear model and the multibody model, which is generated by the deflection of the center of gravity through rotation. This effect is comparable to an inverse pendulum. The low damping of the pneumatic tire in combination with the slight deviation of the natural frequency results in this control behavior. This substantiates the necessity of a robust control design, especially for this tire type. For the other DoF, a high qualitative agreement to the linear model in Figure 7-20 is recognizable.

Summarizing, the controller developed with the linear model proves itself also in the non-linear case and the simplifications made during the development of the linear controller were acceptable.

The controller behavior is also recognizable in the time domain as shown in the cumulative distribution function (CDF) in Figure 7-22. Depicted is the total vibration value a_{TTV} introduced in section 2.4.2, which occurs during an urban driving scenario with the acceptable driving surface quality of the solid tire-sprung system. The improvement for the pneumatic tire is higher due to the increased impact of the natural frequency that is damped by the controller. On the other hand, the impact of the robust design is higher for the pneumatic tire due to the higher group delays compared to the solid tire, which is almost not affected.

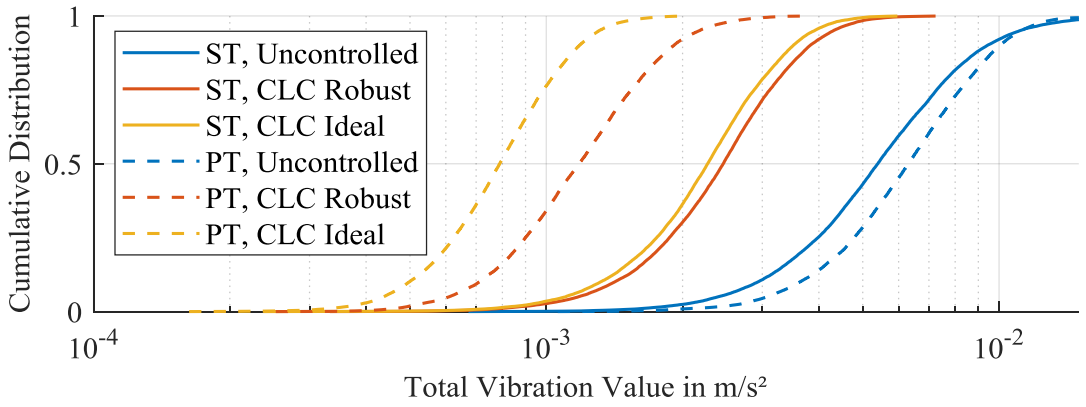

Figure 7-22: Cumulative distribution of total vibration value (cf. section 2.4.2) for ideal and robust closed-loop architecture (CLC) compared to uncontrolled system for solid (ST) and pneumatic (PT) tires. Accelerations determined with multibody model from section 7.5.1 in urban driving scenario on reference driving surface roughness of 0.036 mm³.

7.6 Evaluation

The next step is the evaluation of the developed control concepts. This comprises the evaluation parameters from Table 3-1 that have already been applied for the passive tire-sprung systems. Therefore, the acceptable driving surface quality is determined with regard to direct disturbances from the driving surface. Then the disturbances of the horizontal accelerations due to wheel load variations are analyzed. Additionally, the requirements on the hexapod to achieve the control aims of the active system are investigated.

7.6.1 Acceptable Driving Surface Quality

The acceptable driving surface quality is determined with the methodology from subchapter 3.1. A detailed description of the application of the methodology is given for the passive tire-sprung system in section 4.1.1. The results are presented in Figure 7-23. It is recognizable that the pneumatic tire is advantageous because of its lower natural frequency and the low damping, which is compensated by the active approach. According to equation (3.4), the

shown values of the acceptable roughness coefficient correspond to a range of maximum depth gauges between 0.026 and 0.2 mm over a length of 4 m for the solid tire and 0.048 to 0.388 mm for the pneumatic tire. Reduced scaling factors or accepting more exceedings of the perception threshold improve the behavior by at least half an order of magnitude.

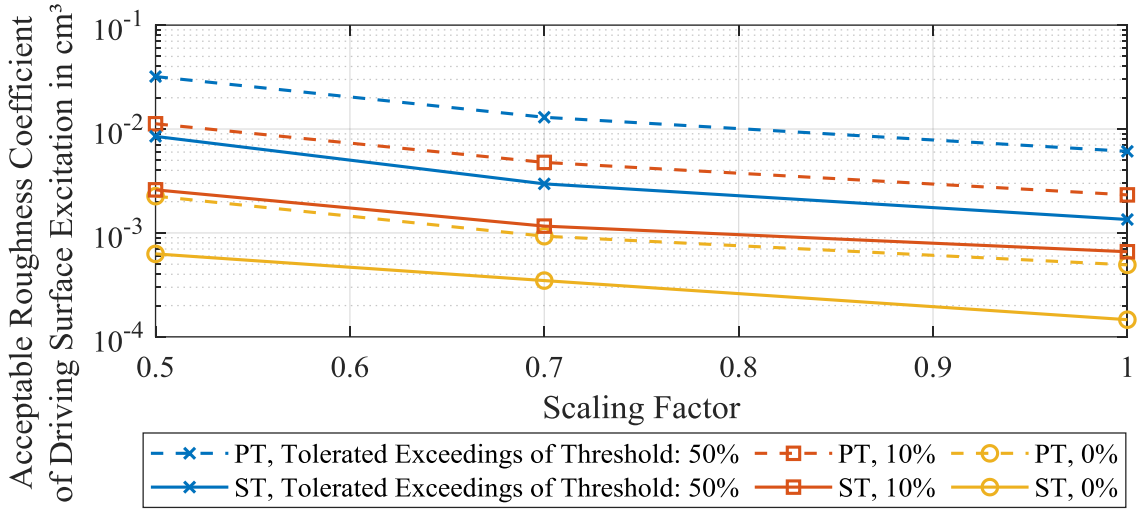

Figure 7-23: Acceptable roughness coefficients for solid (ST) and pneumatic (PT) tire with closed-loop control approach for different scaling factors and allowed exceedings of perception threshold. The quality was determined with the model from section 7.5.1 in an urban driving scenario by iteratively reducing the surface roughness until the total vibration value (section 2.4.2) is below the perception threshold.

7.6.2 Impact of Wheel Load Variations

The disturbances of the horizontal accelerations due to wheel load variations are analyzed by means of the Weber ratios in Figure 7-24.

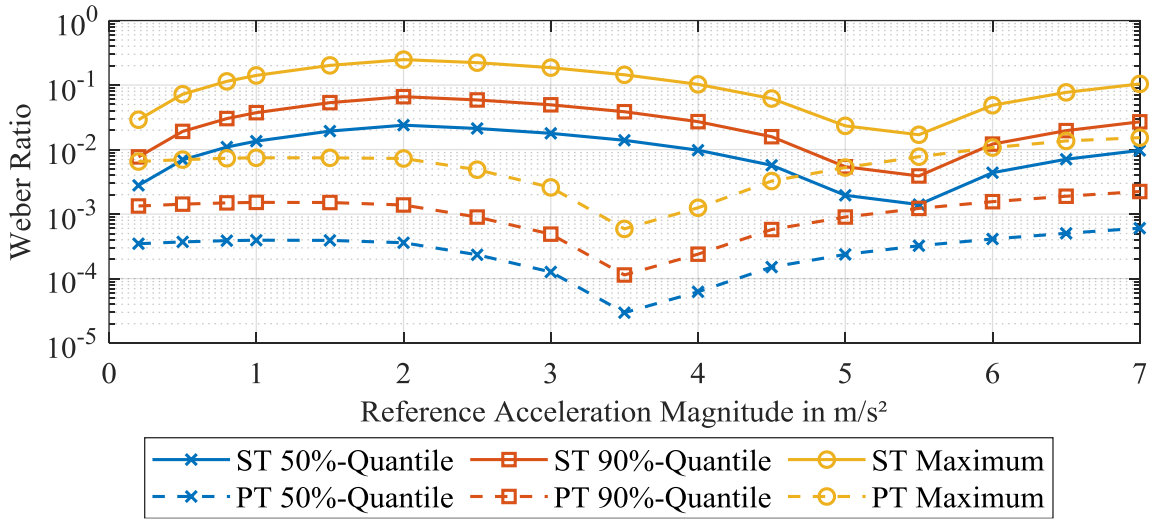

Figure 7-24: Disturbance of horizontal reference acceleration through wheel load variations by means of Weber ratio (cf. equation (3.5), perception threshold: 1) for solid (ST) and pneumatic (PT) tire. Determined from wheel load variations on acceptable driving surface from section 7.6.1 with isolated horizontal tire model (cf. subchapter 3.5) and different input moments corresponding to the shown reference acceleration.

The methodology of the determination is described in section 4.4.2. Compared to the passive tire-sprung system, the maximum Weber ratio is twice as high. This is an expected result because the decoupling between hexapod top plate and hexapod bottom plate motion enables higher wheel load variations without generating vibration disturbances of the subject. Thus, due to the lower acceptable driving surface quality, the wheel load variations increase and so do the horizontal tire forces. Nevertheless, with a maximum value of 0.2, the margin to the perception threshold is still high. The pneumatic tire shows even lower values due to the reasons discussed in section 6.2.2.

7.6.3 Hexapod Requirements

The requirements on the motion capabilities of the hexapod are shown in Figure 7-25 for different driving surface qualities.

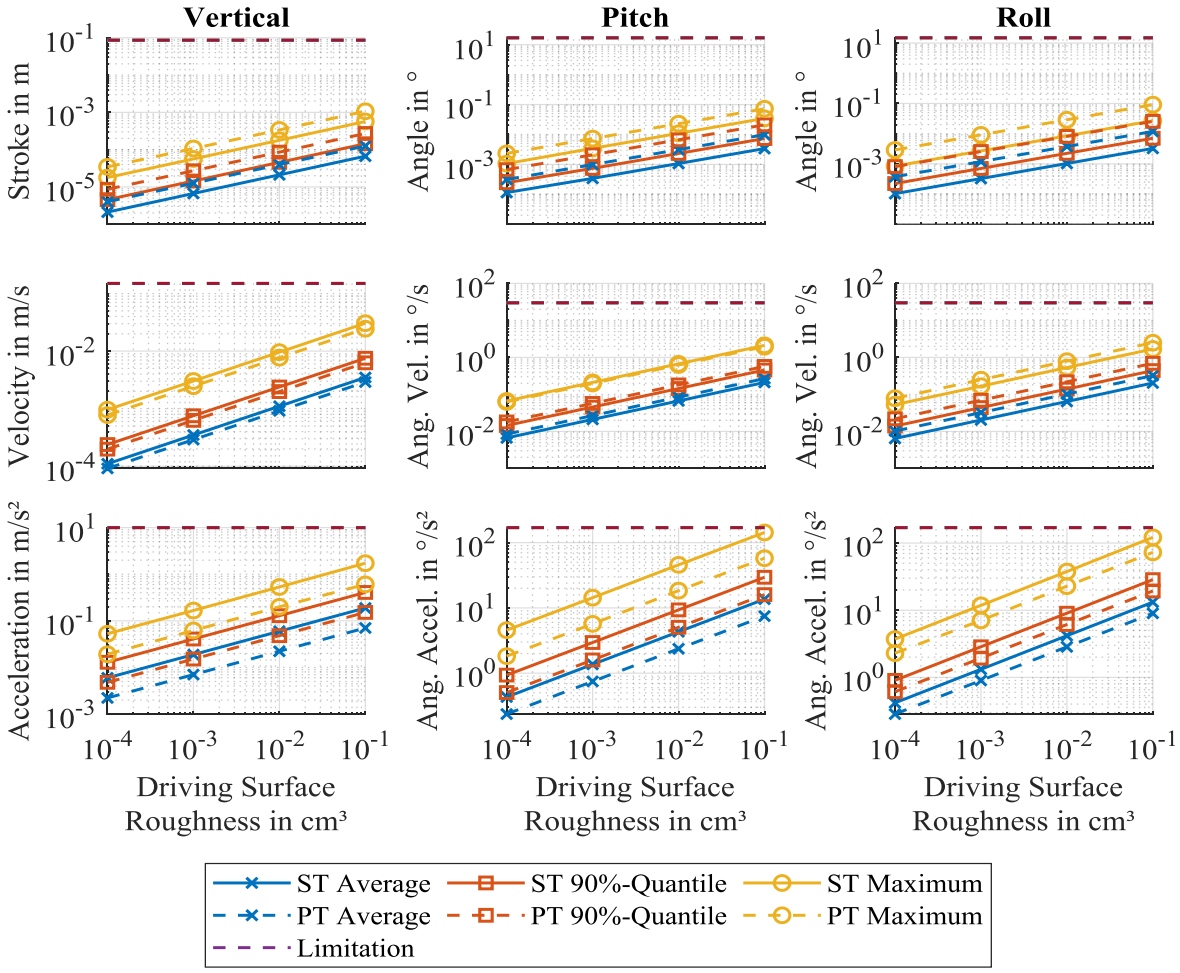

Figure 7-25: Hexapod requirements for solid (ST) and pneumatic tires (PT) determined with the multibody model from section 7.5.1 in urban driving scenario on different driving surface qualities.

It is recognizable that especially in the range of the acceptable driving surface qualities, the requirements are fulfilled by the applied Mevea hexapod. The critical aspect is the angular acceleration, which exceeds the limit at a roughness coefficient of 0.1 cm³ for the solid tire.

Thus, for the target driving surface quality of 1 cm³ from section 2.5.2, the control would reach its limitations so that the improvement potential is further reduced. The maximum angles required for the control at a roughness coefficient of 1 cm³ amount to 0.1° so that the tilt coordination function is not impeded by the vertical dynamics control. The pneumatic tire offers slightly lower requirements on acceleration level due to the reduced control frequency. Although this leads to higher requirements on stroke level, this aspect is less critical due to the higher margin to the limitation. Nevertheless, also to pneumatic tire reaches the limitation at the target roughness coefficient.

7.7 Summary and Conclusion

According to the previous theoretical considerations, the active hexapod closed-loop control architecture has the potential to improve the vertical dynamic behavior of the solely tire-sprung system and extends the amount of driving surfaces suitable for an application of WMDS by one order of magnitude. The pneumatic tire is preferable concerning all evaluation aspects due to its lower natural frequency and the higher slip stiffness. However, the lower limit of the applicable driving surfaces is still very low compared to the target driving surface quality with a roughness coefficient of 1 cm³ determined in section 2.5.2, which is required to extend the application potential of WMDS to e.g. driving dynamics test areas. Especially the high dead times and the robustness requirements resulting from the low damping impede an improved control performance of the active system. Additionally, the hexapod limitations are exceeded at the target driving surface roughness coefficient.

Hence, further measures are required to improve the vertical dynamic behavior of WMDS. The next step is the implementation of a suspension to improve the filtering of high-frequent excitations. The remaining low-frequent excitations are compensated by the hexapod control. Nevertheless, the working hypothesis is adapted to the new system configuration according to the results of a scaling factor of 0.7 and no exceeding of the perception threshold (cf. subchapter 3.3 and section 3.4.1):

A driving surface with a roughness coefficient of 0.93 mm³ is required for the application of WMDS without deterioration of the immersion of the subject.

This corresponds to a depth gauge of 0.066 mm and is therefore a factor of 5 higher than the value of the solid tire-sprung system.

8 Hexapod Vertical Dynamics Control and Suspension System

The following chapter aims at the development and evaluation of a vertical dynamics system for WMDS, consisting of an active hexapod control combined with a passive suspension.

The development methodology is summarized in Figure 8-1. The first step is a functional analysis to determine the necessary sub-functions that must be fulfilled by the suspension. From these functions, the free parameters that have to be determined during the development process are derived. The next step is to gather the demands on these parameters resulting from the aspects of stability, vibration isolation and horizontal driving simulator dynamics. In order to determine the vibration isolation demands for the active system, the hexapod vertical dynamics controller has to be redesigned to meet the requirements of the suspension. The influence of the suspension parameters on the control design has to be investigated to be able to optimize the control on every variant of the suspension parameters.

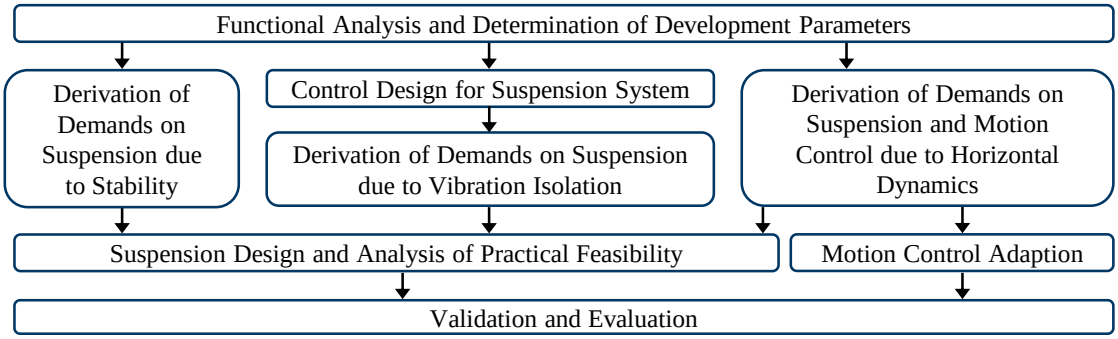

Figure 8-1: Methodology of Suspension Development.

Based on the gathered demands, suspension designs are developed and analyzed concerning their practical feasibility. As a result of this investigation, a practically feasible suspension concept that best meets the stated demands is selected. Based on the demands from the horizontal dynamics, an adaption of the MC that is introduced in subchapter 2.6, is conducted. Finally follows the validation and evaluation of the developed approaches.

8.1 Functional Analysis and Free Parameters

The aim of this subchapter is to define the free parameters of the suspension, which have to be determined during the development process. Additionally, possible parameter values respectively limitations are presented. This is done based on the following functions that have to be covered by the suspension:

- **Function DoF**: At least one DoF between driving surface and subject in vertical, pitch and roll direction must be implemented by the suspension while maintaining a connection in longitudinal, lateral, and yaw direction.
- **Function static weight support**: The static weight of the mass above the DoF has to be held despite the introduced DoF.
- **Function energy dissipation**: The energy induced by the driving surface excitations has to be dissipated to avoid increasing vibration energy in the DS system.

Hereinafter, these functions are analyzed for their free parameters and possible parameter variants, which are then varied to determine the demands on these parameters in subchapters 8.3 and 8.5.

8.1.1 Function DoF

The first free parameter is the **joint configuration** to achieve the desired DoF. Theoretically, an unlimited number of revolute and prismatic joints can be introduced into the system. In order to reduce the solution diversity, only one intersection along the transmission path between each wheel and the subject is considered for the implementation of the DoF. This restriction results in the two joint configurations shown in Figure 8-2. The difference between the configurations is the connection of the wheels. If the wheels are not rigidly connected to each other (configuration A), one prismatic joint between each wheel and the subject is sufficient. If the wheels are rigidly connected (configuration B), one prismatic joint and two revolute joints for the pitch and roll DoFs are required.

The second free parameter is the **joint position**, which can be placed at every point along the transmission path between driving surface and subject. In order to reduce the solution volume for this parameter, discrete positions for the DoFs are determined that substantially differ from each other. This could be a dominant additional mass between excitation input and DoF or a functional difference as the steer moment transmission. The resulting intersection points are shown in Figure 8-3.

The characteristics of the intersection points are as follows:

1. **Wheel Hub:** Intersection point with the lowest possible tire-sprung mass.
2. **Below Steering Bearing:** Dominant mass of the drivetrain and no drive moment transmission over the DoF required. Additionally, the last intersection that offers a steered DoF.
3. **Above Steering Bearing:** Dominant mass of the drivetrain and first intersection that offers an unsteered DoF.
4. **Between Frame and Steering Unit:** Dominant mass of the steering unit and first intersection that does not require a steering moment transmission over the DoF.
5. **Between Frame and Hexapod-Frame-Connection:** Dominant mass of the motor controllers, the low voltage batteries and the frame. Additionally, the last intersection point that allows joint configuration A.

6. **Between Hexapod-Frame-Connection and HBP:** Lowest mass below the hexapod and the first intersection point for joint configuration B.
7. **Between HTP and Mockup:** Lowest sprung mass and changing system behavior because of solely tire-sprung hexapod.

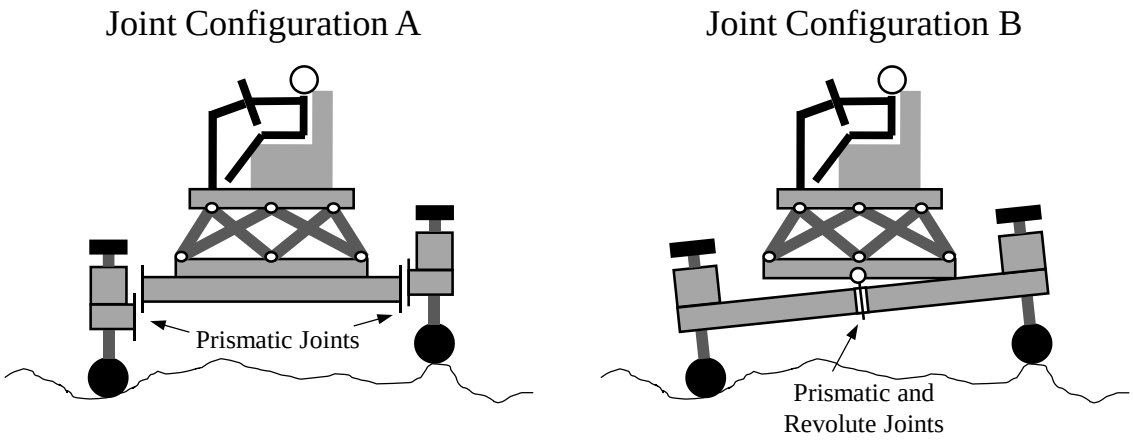

Figure 8-2: Joint configurations to achieve the desired DoF with one intersection point between each wheel and the subject.

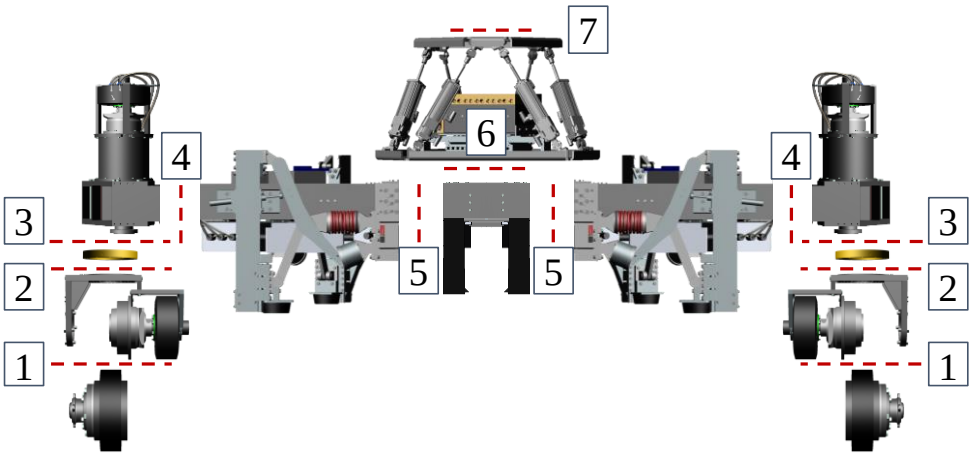

Figure 8-3: Possible intersections for the introduction of a DoF.

The joint configurations 6 and 7 are not addressed in this work. Configuration 6 has a small mass below the hexapod, which is expected to deteriorate the control behavior. Configuration 7 requires an alternative control approach because the hexapod indirectly affects the subject. The potential of this approach is investigated in future research.

Though the joints in Figure 8-2 are depicted as prismatic joints, this is only to show which DoF must be provided. Nevertheless, it is also possible to achieve this joint DoF by a kinematic arrangement. Hence, another free parameter is the **kinematic characteristic** of the DoF. Based on the kinematic characteristics known from passenger cars[105], the following kinematic parameters are defined for WMDS:

[105] Vgl. Ersoy, M.; Gies, S.: Chassis Handbook Fundamentals (2011), pp. 18–28.

- **Suspension stroke:** The required positive and negative stroke of the suspension around the static equilibrium state. This is a crucial aspect of the practical feasibility. Therefore, the stroke that is demanded in order to design the suspension has to be determined.
- **Toe angle (Dynamic):** Steering angle resulting from the suspension motion, which is added to the steering angle of the steering motor. A static toe angle is not defined for WMDS because each wheel is independently steerable and no system-inherent relative steering angle between the wheels exists.
- **Camber angle (Static and dynamic):** Angle of the wheel around the longitudinal wheel axis.
- **Force-support angle/Diagonal springing (Static and dynamic):** The classical definition of the brake and traction support angles of a suspension is given by the direction of the velocity of the tire contact point (TCP) in the x-z-plane of a vehicle resulting from the kinematic motion.[106] However, in order to account for the omnidirectional behavior of the WMDS, in this work, the definition is given in polar coordinates. The effective support angle ε is defined dependent on the direction ξ of the resultant tire force $F_{\mathrm{T,res}}$ that has to be supported, as shown in Figure 8-4. The velocity of the tire contact point $\vec{v}_{\mathrm{TCP,kin}}$ resulting from the kinematic motion of the suspension is projected on the plane spanned by the resultant tire force and the leveled z-axis. From the direction of the projected velocity vector $\vec{v}_{\mathrm{TCP,kin,PrF}}$, the effective support angle is calculated as follows:

$$\varepsilon = -\frac{\vec{v}_{x,\mathrm{TCP,kin,PrF}}(\xi)}{\vec{v}_{z,\mathrm{TCP,kin,PrF}}} \tag{8.1}$$

  The sign of the support angle results from the fact that a positive vertical support force is generated if the projected x-velocity and the tire force are acting in the opposite direction.

- **Caster angle (Static and Dynamic)**: Angle of the steering axis relative to the z-axis of the leveled vehicle coordinate system in the x-z-plane of the wheel coordinate system.
- **Caster trail (Static and Dynamic):** Distance between the tire contact point and the intersection of the steering axis with the ground plane in the x-z-plane of the wheel coordinate system.
- **Kingpin inclination (Static and Dynamic)**: Angle of the steering axis relative to the z-axis of the leveled vehicle coordinate system in the y-z-plane of the wheel coordinate frame.

[106] Vgl. Matschinsky, W.: Radführungen der Straßenfahrzeuge (2007), p. 136.

- **Scrub radius (Static and Dynamic):** Distance between the tire contact point and the intersection of the steering axis with the ground plane in the y-z-plane of the wheel coordinate system.

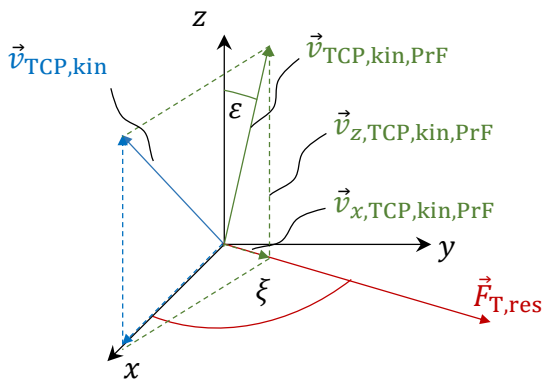

Figure 8-4: Definition of the effective support angle.

8.1.2 Function Static Weight Support

The free parameters of this function are strongly influenced by the applied solution concept. Hence, in order to define these parameters, possible solution approaches have to be investigated and pre-selected.

The implementation of a DoF into the system results in an unbound mass, which would fall down if its weight load was not supported. This also comprises the support of moments resulting from the acceleration of the unbound mass in the horizontal plane. An ideal solution would apply a constant force and moment for a given horizontal acceleration state, which is not affected by driving surface-induced motions of the DoF. However, an active system would be required to achieve this because the force and moment have to be continuously adapted to be robust against small disturbances, which affect the equilibrium state (e.g. slight fluctuations of the center of gravity). Additionally, no solution is known to the author that achieves this without energy loss even in the static and undisturbed state that does not require control interventions. Examples would be the application of electric linear motors at the DoF (energy loss due to resistance) or the support of the unbound mass based on aerodynamics similar to a drone (aerodynamic energy loss). In order to avoid this additional drain of energy, which would result in an increased accumulator mass or reduced operation time, a passive solution is aspired in this work. However, if the potential of this approach turns out to be insufficient, active systems could lead to further improvement.

The most common passive solution for the investigated function is the application of elastic elements, which increase the force in dependence of and opposite to their deflection. Several solutions exist for the implementation of such an elastic element, ranging from coil or leaf springs to gas springs or even passive magnets, which have opposing poles. The selection of a solution is dependent on the respective suspension concept and will be done in subchapter 8.6. However, at this point, the basic characteristic of the elastic element is defined to be

linear. This is advantageous with respect to the hexapod vertical dynamics control because it is expected that it has to be adapted to the oscillation system. A nonlinear element would impede the controller synthesis and probably also require a nonlinear control. On the other hand, no advantages are expected from a nonlinear element because e.g. no high variation of the static load occurs in a WMDS (only varying subject mass), which would require an adaption of the spring stiffness to the mass.

The defining parameter of a linear elastic element is its stiffness. However, the oscillation behavior of a system results from the combination of the stiffness of the elastic suspension element c_S and the sprung body mass m_B, which yields the natural frequency:

$$f_0 = \frac{1}{2\pi}\sqrt{\frac{c_S}{m_B}} \tag{8.2}$$

Though this is actually only valid for a single-mass-oscillator, it is used as an approximation for the real natural frequency of the sprung mass of the two-mass-oscillator.[107a] Hence, the natural frequency is defined as the free parameter of the function “static weight support”.

8.1.3 Function Energy Dissipation

The general characteristic of dissipating elements is the generation of a force that acts opposite to the relative velocity of both ends of the element and, hence, reduces the kinetic energy of a connected mass.[108] This general definition covers a wide range of passive and active, linear and nonlinear elements. The most common elements are viscous dampers and friction damping.[108]

In the case of the controlled system, the dissipation function can also be fulfilled solely by the hexapod. Nevertheless, a low oscillation system damping results in high group delays at the poles and zeros of the open control loop. Therefore, an additional damping element is intended and a soft parametrization could be adjusted in order to transfer the dissipation function to the hexapod.

For the same reason as for the elastic element chosen in section 8.1.2, a linear element is aspired in order to improve the controller performance. Though details of the damping characteristic, which are state of the art in vehicle technology (e.g. different tension and compression characteristic or declining slope for higher velocity amplitudes)[109] could be tuned in the practical implementation, at this point a purely linear approach is chosen for the following investigations. This can be described by the dimensionless damping ratio parameter

[107] Haken, K.-L.: Grundlagen der Kraftfahrzeugtechnik (2015). a: p. 109; b: p. 111.

[108] Vgl. Markert, R.: Strukturdynamik (2013), pp. 34–38.

[109] Vgl. Pischinger, S.; Seiffert, U.: Vieweg Handbuch Kraftfahrzeugtechnik (2016), p. 867.

D, which is dependent on the suspension damping constant d_S, the sprung body mass m_B and the natural frequency of the suspension according to (8.2):[110]

$$D = \frac{d_S}{4\pi m_B f_0} \tag{8.3}$$

8.1.4 Summary

In this subchapter, the following parameters of the suspension development were defined:

- Joint position (Joint configuration results directly from their position)
- Suspension stroke
- Suspension kinematics
    - Toe angle
    - Camber angle
    - Support angle
    - Steering axis inclination
    - Caster
- Natural frequency
- Damping ratio

The subsequent subchapters aim at determining the demands from the stability, the vibration isolation and the horizontal dynamics on these free parameters in order to select a suitable parameter set. However, the controller influences these demands. Therefore, the controller development is conducted beforehand in the following subchapter.

8.2 Control Design for Suspension System

The general development steps in Figure 7-1 remain the same as for the tire-sprung system and many of the discussed approaches can be transferred. Hence, only necessary adaptions for the sprung system are discussed hereinafter.

8.2.1 System Architecture Development

The general considerations from the tire-sprung system are transferable to the system equipped with a suspension. An additional option for the control variables results from the newly introduced DoF between body and wheel. This enables the measurement of the force acting between wheel and body by measuring the deflection of the spring damper system. However, as already discussed for the tire-sprung system, this requires an accurate model of

[110] Pischinger, S.; Seiffert, U.: Vieweg Handbuch Kraftfahrzeugtechnik (2016), p. 866.

the force-deflection characteristic. Especially the damper generates a high inaccuracy because of its probably varying behavior (e.g. temperature dependence). On the other hand, no advantage results from the application of this variable because the information is received by the controller at the same time as if the accelerations are measured directly. Therefore, this concept is neglected and the same system architectures as for the tire-sprung system are investigated hereinafter.

8.2.2 Linear System Modelling

The actuator model developed for the tire-sprung system is directly transferable to the sprung system. The vertical vibration system model has to be completely revised due to the new system design.

8.2.2.1 Vertical Vibration System Model

The applied linear model is depicted in Figure 8-5. The spring force $F_{z,c,\mathrm{S},i}$ and damper force $F_{z,d,\mathrm{S},i}$ of the suspension are calculated as follows with the suspension spring stiffness c_S and the suspension damper constant d_S:

$$ {}_\mathrm{H}F_{z,c,\mathrm{S},i} = c_\mathrm{S}\left({}_\mathrm{H}z_{\mathrm{W},i} - {}_\mathrm{H}z_{\mathrm{HBP,W},i}\right) \tag{8.4} $$

$$ {}_\mathrm{H}F_{z,d,\mathrm{S},i} = d_\mathrm{S}\left({}_\mathrm{H}\dot{z}_{\mathrm{W},i} - {}_\mathrm{H}\dot{z}_{\mathrm{HBP,W},i}\right) \tag{8.5} $$

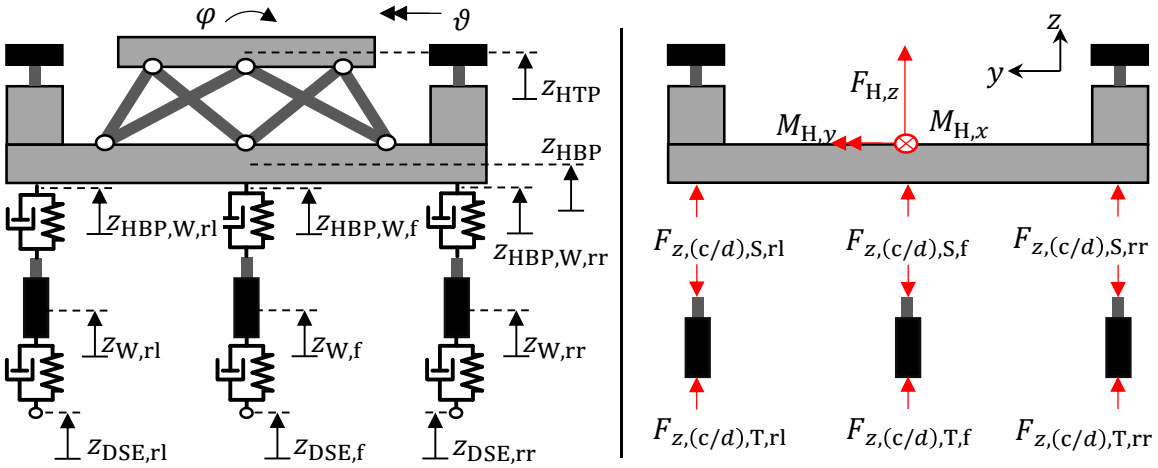

Figure 8-5: Vertical vibration system model for sprung system.

Based on these forces and the forces of the hexapod in (7.13) to (7.15), the motion equations for the hexapod bottom plate (HBP) and the wheel masses are formulated. By inserting the kinematic equations from (4.11) to (4.13) and substituting the HBP motion for the expressions in (7.16) to (7.18), the linear equation systems are derived.

The driving surface excitation is defined separately for each DoF so that only isolated motions are induced. This leads to the following decoupled system equations in z-direction:

$$ {}^{\mathcal{L}}\boldsymbol{C}_{\mathrm{dyn},z}\begin{pmatrix} {}^{\mathcal{L}}_{\mathrm{H}}\ddot{z}_{\mathrm{W}} \\ {}^{\mathcal{L}}_{\mathrm{H}}\ddot{z}_{\mathrm{HTP}} \end{pmatrix} = {}^{\mathcal{L}}\boldsymbol{E}_{z}\begin{pmatrix} {}^{\mathcal{L}}_{\mathrm{H}}z_{\mathrm{DSE}} \\ {}^{\mathcal{L}}_{\mathrm{H}}z_{\mathrm{Hex}} \end{pmatrix} \tag{8.6} $$

With the dynamic stiffness matrix ${}^{\mathcal{L}}\boldsymbol{C}_{\mathrm{dyn},z}$ (same definition for pitch- and roll-direction):

$$ {}^{\mathcal{L}}\boldsymbol{C}_{\mathrm{dyn},z} = \boldsymbol{M}_{z} + \frac{1}{s}\boldsymbol{D}_{z} + \frac{1}{s^{2}}\boldsymbol{C}_{z} \tag{8.7} $$

$$ \boldsymbol{M}_{z} = \begin{pmatrix} m_{\mathrm{W}} & 0 \\ 0 & (m_{\mathrm{HBP}} + m_{\mathrm{HTP}})/3 \end{pmatrix} \tag{8.8} $$

$$ \boldsymbol{D}_{z} = \begin{pmatrix} d_{\mathrm{S}} + d_{\mathrm{T}} & -d_{\mathrm{S}} \\ -d_{\mathrm{S}} & d_{\mathrm{S}} \end{pmatrix} \tag{8.9} $$

$$ \boldsymbol{C}_{z} = \begin{pmatrix} c_{\mathrm{S}} + c_{\mathrm{T}} & -c_{\mathrm{S}} \\ -c_{\mathrm{S}} & c_{\mathrm{S}} \end{pmatrix} \tag{8.10} $$

And the excitation transfer matrix ${}^{\mathcal{L}}\boldsymbol{E}_{z}$:

$$ {}^{\mathcal{L}}\boldsymbol{E}_{z} = \begin{pmatrix} c_{\mathrm{T}} + d_{\mathrm{T}}s & -c_{\mathrm{S}} - d_{\mathrm{S}}s \\ 0 & c_{\mathrm{S}} + d_{\mathrm{S}}s + \dfrac{m_{\mathrm{HBP}}}{3}s^{2} \end{pmatrix} \tag{8.11} $$

For the roll-DoF, the following equations are derived:

$$ {}^{\mathcal{L}}\boldsymbol{C}_{\mathrm{dyn},\varphi}\begin{pmatrix} {}^{\mathcal{L}}_{\mathrm{H}}\ddot{z}_{\mathrm{W,rl}} \\ {}^{\mathcal{L}}_{\mathrm{H}}\ddot{z}_{\mathrm{W,rr}} \\ {}^{\mathcal{L}}_{\mathrm{H}}\ddot{\varphi}_{\mathrm{HTP}} \end{pmatrix} = {}^{\mathcal{L}}\boldsymbol{E}_{\varphi}\begin{pmatrix} {}^{\mathcal{L}}_{\mathrm{H}}z_{\mathrm{DSE}} \\ {}^{\mathcal{L}}_{\mathrm{H}}\varphi_{\mathrm{Hex}} \end{pmatrix} \tag{8.12} $$

$$ {}^{\mathcal{L}}\boldsymbol{E}_{\varphi} = \begin{pmatrix} c_{\mathrm{T}} + d_{\mathrm{T}}s & -\ell_{\mathrm{t}}(c_{\mathrm{S}} + d_{\mathrm{S}}s) \\ -c_{\mathrm{T}} - d_{\mathrm{T}}s & \ell_{\mathrm{t}}(c_{\mathrm{S}} + d_{\mathrm{S}}s) \\ 0 & 2\ell_{\mathrm{t}}^{2}(c_{\mathrm{S}} + d_{\mathrm{S}}s) + J_{\mathrm{HBP},x}^{(\mathrm{CG})}s^{2} \end{pmatrix} \tag{8.13} $$

$$ \boldsymbol{M}_{\varphi} = \begin{pmatrix} m_{\mathrm{W}} & 0 & 0 \\ 0 & m_{\mathrm{W}} & 0 \\ 0 & 0 & J_{\mathrm{HBP},x}^{(\mathrm{CG})} + J_{\mathrm{HTP},x}^{(\mathrm{CG})} \end{pmatrix} \tag{8.14} $$

$$ \boldsymbol{D}_{\varphi} = \begin{pmatrix} d_{\mathrm{S}} + d_{\mathrm{T}} & 0 & -\ell_{\mathrm{t}}d_{\mathrm{S}} \\ 0 & d_{\mathrm{S}} + d_{\mathrm{T}} & \ell_{\mathrm{t}}d_{\mathrm{S}} \\ -\ell_{\mathrm{t}}d_{\mathrm{S}} & \ell_{\mathrm{t}}d_{\mathrm{S}} & 2\ell_{\mathrm{t}}^{2}d_{\mathrm{S}} \end{pmatrix} \tag{8.15} $$

$$ \boldsymbol{C}_{\varphi} = \begin{pmatrix} c_{\mathrm{S}} + c_{\mathrm{T}} & 0 & -\ell_{\mathrm{t}}c_{\mathrm{S}} \\ 0 & c_{\mathrm{S}} + c_{\mathrm{T}} & \ell_{\mathrm{t}}c_{\mathrm{S}} \\ -\ell_{\mathrm{t}}c_{\mathrm{S}} & \ell_{\mathrm{t}}c_{\mathrm{S}} & 2\ell_{\mathrm{t}}^{2}c_{\mathrm{S}} \end{pmatrix} \tag{8.16} $$

For the pitch-DoF the following equation system is determined:

$$ {}^{\mathcal{L}}\boldsymbol{C}_{\mathrm{dyn},\vartheta}\begin{pmatrix} {}^{\mathcal{L}}_{\mathrm{H}}\ddot{z}_{\mathrm{W,f}} \\ {}^{\mathcal{L}}_{\mathrm{H}}\ddot{z}_{\mathrm{W,r}} \\ {}^{\mathcal{L}}_{\mathrm{H}}\ddot{\vartheta}_{\mathrm{HTP}} \end{pmatrix} = {}^{\mathcal{L}}\boldsymbol{E}_{\vartheta}\begin{pmatrix} {}^{\mathcal{L}}_{\mathrm{H}}z_{\mathrm{DSE}} \\ {}^{\mathcal{L}}_{\mathrm{H}}\vartheta_{\mathrm{Hex}} \end{pmatrix} \tag{8.17} $$

$$
{}^{\mathcal{L}}\boldsymbol{E}_{\vartheta} = \begin{pmatrix} c_{\mathrm{T}} + d_{\mathrm{T}}s & \frac{1}{\sqrt{3}}\ell_{\mathrm{t}}(c_{\mathrm{S}} + d_{\mathrm{S}}s) \\ -c_{\mathrm{T}} - d_{\mathrm{T}}s & -\frac{1}{\sqrt{3}}\ell_{\mathrm{t}}(c_{\mathrm{S}} + d_{\mathrm{S}}s) \\ 0 & \frac{1}{2}\ell_{\mathrm{t}}^2(c_{\mathrm{S}} + d_{\mathrm{S}}s) + J_{\mathrm{HBP},y}^{(\mathrm{CG})}s^2 \end{pmatrix} \tag{8.18}
$$

$$
\boldsymbol{M}_{\vartheta} = \begin{pmatrix} m_{\mathrm{W}} & 0 & 0 \\ 0 & 2m_{\mathrm{W}} & 0 \\ 0 & 0 & J_{\mathrm{HBP},y}^{(\mathrm{CG})} + J_{\mathrm{HTP},y}^{(\mathrm{CG})} \end{pmatrix} \tag{8.19}
$$

$$
\boldsymbol{D}_{\vartheta} = \begin{pmatrix} d_{\mathrm{S}} + d_{\mathrm{T}} & 0 & \frac{1}{\sqrt{3}}\ell_{\mathrm{t}}d_{\mathrm{S}} \\ 0 & 2(d_{\mathrm{S}} + d_{\mathrm{T}}) & -\frac{1}{\sqrt{3}}\ell_{\mathrm{t}}d_{\mathrm{S}} \\ \frac{1}{\sqrt{3}}\ell_{\mathrm{t}}d_{\mathrm{S}} & -\frac{1}{\sqrt{3}}\ell_{\mathrm{t}}d_{\mathrm{S}} & \frac{1}{2}\ell_{\mathrm{t}}^2 d_{\mathrm{S}} \end{pmatrix} \tag{8.20}
$$

$$
\boldsymbol{C}_{\vartheta} = \begin{pmatrix} c_{\mathrm{S}} + c_{\mathrm{T}} & 0 & \frac{1}{\sqrt{3}}\ell_{\mathrm{t}}c_{\mathrm{S}} \\ 0 & 2(c_{\mathrm{S}} + c_{\mathrm{T}}) & -\frac{1}{\sqrt{3}}\ell_{\mathrm{t}}c_{\mathrm{S}} \\ \frac{1}{\sqrt{3}}\ell_{\mathrm{t}}c_{\mathrm{S}} & -\frac{1}{\sqrt{3}}\ell_{\mathrm{t}}c_{\mathrm{S}} & \frac{1}{2}\ell_{\mathrm{t}}^2 c_{\mathrm{S}} \end{pmatrix} \tag{8.21}
$$

By inverting the dynamic stiffness matrices and multiplying with the right sides of the equations, the solution of the system is derived. The lowest rows yield the relevant output accelerations of the top plate dependent of the driving surface input z_{DSE} and the hexapod motions. By isolating the inputs from each other, the single-input single-output transfer functions ${}^{\mathcal{L}}G_{\mathrm{DB}}$ for the driving surface excitations and ${}^{\mathcal{L}}G_{\mathrm{MRB}}$ of the hexapod are derived. The resulting transfer functions are given in the appendix in equations (B1.1) to (B1.6).

8.2.3 Controller Synthesis

The basic methodology for the controller synthesis from Figure 7-12 is transferred to the sprung system. Additionally, the influence of the suspension parameters on the controller performance is investigated to be able to determine a suitable system parameterization.

8.2.3.1 Controller Synthesis Closed-Loop Architecture (CLC)

The disturbance transfer function ${}^{\mathcal{L}}G_{\mathrm{Dist}}$ in (7.28) remains the same for the sprung system. Only the transfer functions for the vertical vibration system are adapted. The discussed requirements on the open-loop transfer function (OLTF) of the tire-sprung system have to be refined. Instead of one dominant peak, there are also relevant amplitudes in the frequency

range between both natural frequencies of the suspension system. Especially in the vertical direction, the human perception is sensitive to these frequencies, which compounds this effect. Therefore, the following aspects have to be considered for the z-DoF:

- Either the magnitude of the OLTF should stay above 0 dB or the phase should remain above 90° in the frequency range with a high perception sensitivity to avoid a deterioration of the system behavior by the controller.
- The magnitude of the OLTF at the first natural frequency of the vibration system should be high enough to damp the peak.
- The gain margin of the system must be as high as possible to mitigate the influence of the peak generated by the controller feedback.

The requirements of a high amplitude in the sensitive frequency range and a high gain margin conflict each other. For a high gain margin, the amplitudes have to be reduced before the phase reaches 180°. Hence, it is preferred to accept low amplitudes but to keep the phase above 90° in the sensitive frequency range. This leads to a reduction of the amplitudes compared to the uncontrolled system while keeping the influence of the new peak at a minimum.

A natural frequency of 1 Hz and a damping ratio of 0.1 are applied as suspension parameters. The impact of these parameters on the controller design is discussed in section 8.2.3.4.

The system behavior is analyzed for the closed-loop architecture (CLC, cf. Figure 7-4) with gain one to derive the necessary changes that have to be induced by the controller (blue curve Figure 8-6 on the left). As for the tire-sprung system, the zero of the manipulating reaction behavior (MRB) leads to a reduction of the amplitude at the natural frequency. Therefore, one pole of the controller is set to compensate this zero.

Additional zeros are required that lift the phase to compensate the pole of the MRB. In order to keep the phase above 90° despite the pole, one zero is placed in the origin. The placing of the second zero is subject to a tradeoff between a high phase margin and the reduction of the magnitudes to achieve a high gain margin. Thus, to determine the preferable position, an optimization based on the evaluation parameter from section 7.4.1 is conducted. For each position of the zero, the respective optimum gain is calculated according to the methodology depicted in section 7.4.2.3. The zero with the lowest attenuation factor is implemented. The gain parameterization is determined simultaneously.

For the pitch and roll DoF, the perception is more sensitive at lower frequencies. Therefore, to achieve a higher magnitude at low frequencies, both zeros are placed above the pole of the natural frequency. The optimization procedure from the vertical DoF is adopted. The resulting OLTF of the CLC is shown in Figure 8-6 for the z-DoF.

8.2.3.2 System Analysis Open-Loop Architecture (OLC)

The OLTF for the OLC is shown in Figure 8-6 as yellow curve. Because of the I-behavior at low frequencies, the amplitude at the natural frequency is higher than that of the CLC.

However, this behavior also leads to a reduced phase in the sensitive frequency range. Therefore, the good compensation of the natural frequency is probably mitigated by the deterioration at high frequencies due to the lower phase and gain margins compared to the CLC.

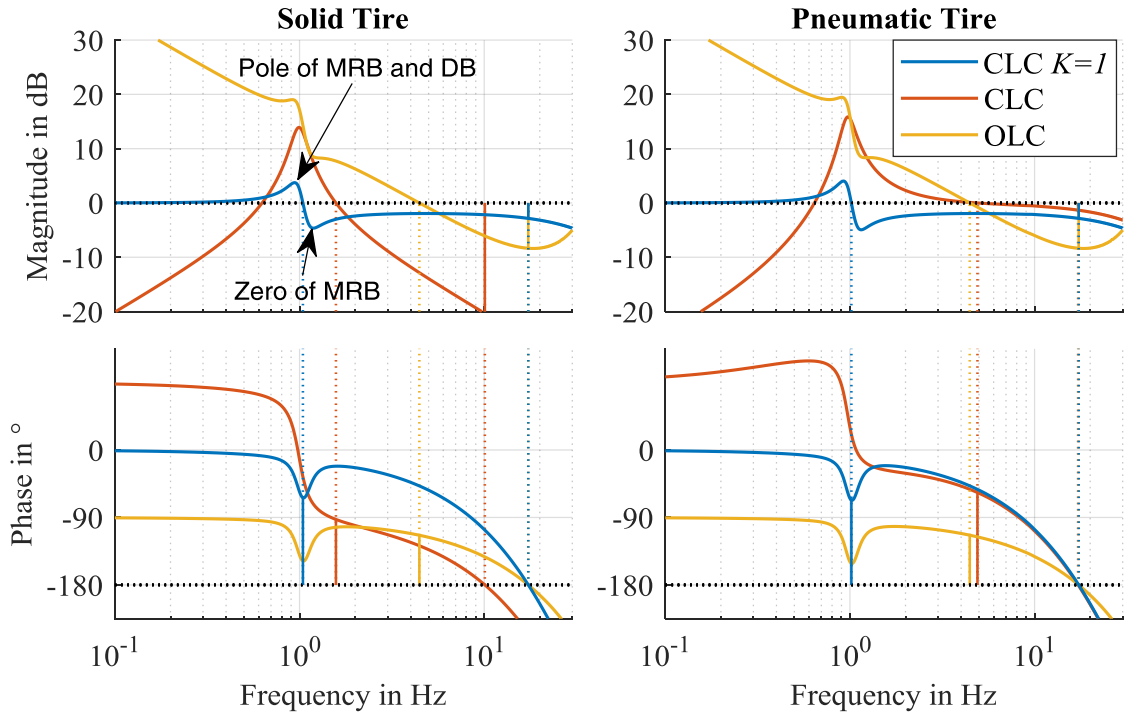

Figure 8-6: Bode plot OLTF comparison between closed-loop proportional controller with gain 1 (CLC K=1), closed-loop lead compensator control (CLC), and open-loop control (OLC) determined with linear model from section 8.2.2.

8.2.3.3 Controller Robustness

Contrary to the tire-sprung system, the controller robustness is also subject to the parameters of the suspension. Thus, the controller robustness concerning parameter deviations is investigated by designing the controller for different damping ratios and then varying the actual system parameters of the linear model. The negative relative attenuation factor from section 7.4.1 is shown in dB in Figure 8-7 for different design damping ratios.

It is recognizable that high damping ratios leave a higher margin concerning fluctuations of the natural frequency. The reason for this behavior is similar to that of the tire-sprung system. A low damping increases the group delays, so that a shift of the zero of the manipulating reaction behavior (MRB) relative to the controller pole results in an exceeding of a phase of -180°. For a damping ratio of 0.1, the controller improves the behavior for frequency variations up to 0.4 Hz. Thus, a lower damping is not recommended and this is selected as the lower value for this thesis. The results for the other DoFs and the pneumatic tire a given in the appendix from Figure B.2 - 5 to Figure B.2 - 9.

For the robustness against dead time variations, the pitch DoF is analyzed. The higher gains of the angular DoFs that result from the reduced sensitivity of the human motion perception

at high frequencies result in a lower stability margin than the vertical DoF. The results are shown in Figure 8-8. For both tire types a stable control is achieved up to 40 ms. The results for the other DoFs are given in the appendix in Figure B.2 - 10 and Figure B.2 - 11.

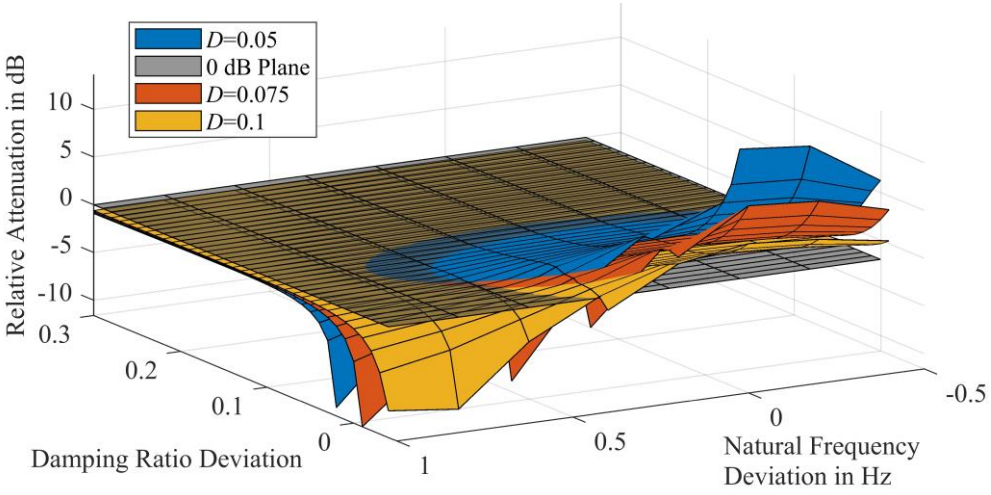

Figure 8-7: Robustness of controller against deviations of vibration parameters for solid tire for different design damping ratios of the controller in vertical DoF. Positive values (above 0 dB plane) indicate an improvement by the controller. Determined with linear model from 8.2.2 by varying parameters of the vibration system for a fixed control design and evaluating relative attenuation (cf. equation (7.27)).

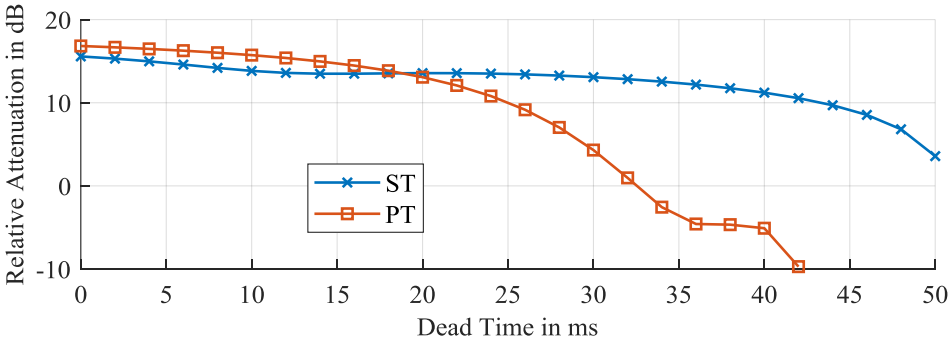

Figure 8-8: Robustness of controller against deviations of dead time for solid (ST) and pneumatic tire (PT) in vertical DoF. Determined with linear model from 8.2.2 by varying dead time for a fixed control design and evaluating relative attenuation (cf. equation (7.27)).

8.2.3.4 Influence of Suspension Parameters on Controller Design

An increasing natural frequency of the suspension shifts the poles to higher frequencies. This could lead to reduced phase margins because the crossover frequencies are higher. However, in the range of typical suspension natural frequencies between 1 and 2 Hz, the margins are sufficient and no additional considerations concerning the control law have to be made.

A reduction of damping results in a more dominant natural frequency and a reduced influence of high-frequent fractions. This is of advantage especially for the *z*-DoF because reduced gain and phase margins can be accepted. This enables higher gain factors and therefore a stronger attenuation of the dominant natural frequency.

8.2.3.5 Influence of Suspension Parameters on Controller Performance

The influence of the suspension parameters on the controller performance is investigated by varying the parameters and redesigning the controller for every parameter set. The position of the controller zero and the gain is optimized for every parameter set to reach the minimum frequency-weighed output acceleration $\ddot{z}_{\mathrm{HTP,rms,FW}}$ according to equation (7.25). The resulting output accelerations are shown in Figure 8-9. As expected from the discussions above, it is clearly visible that low damping and a low natural frequency are advantageous for the controller. However, the damping ratio should not be reduced below 0.1 because this results in high group delays at the poles as described in section 8.2.3.3.

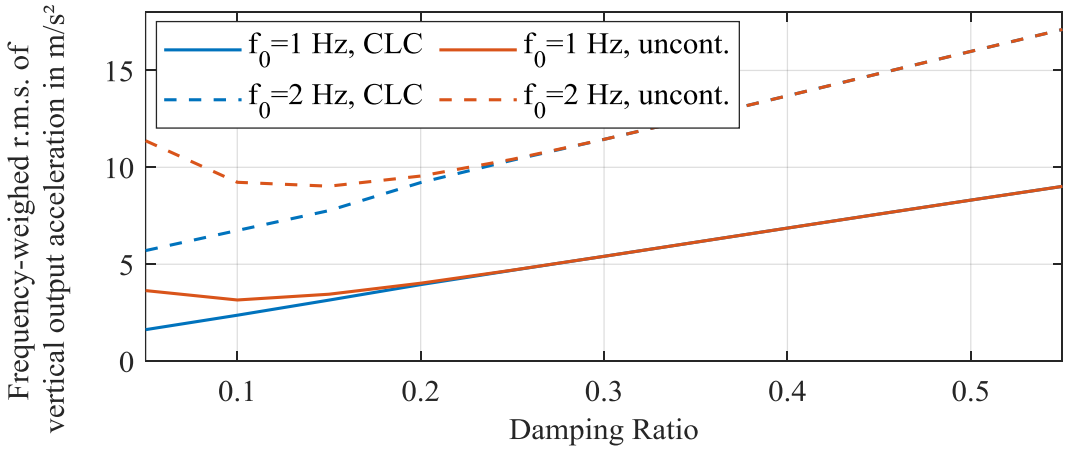

Figure 8-9: Dependence of r.m.s. of vertical frequency-weighed output acceleration (cf. equation (7.25)) from suspension parameters for closed-loop control (CLC) and uncontrolled system. Determined with linear model from section 8.2.2 and optimized control for each parameter set.

8.2.3.6 Linear Controller Performance Evaluation

The expected shortcoming of the OLC is also recognizable in the Bode plot of the closed-loop transfer function shown in Figure 8-10. The damping of the natural frequency is similar to the CLC but at higher frequencies a stronger deterioration of the system behavior occurs.

This results in a worse overall behavior, which is summarized in Table 8-1. The OLC approach worsens the behavior in the vertical direction due to the impact of the second natural frequency, while it improves the angular DoF due to the lower sensitivity at high frequencies.

Table 8-1: Relative attenuation ϱ (cf. equation (7.27)) of the closed-loop (CLC) and open-loop control (OLC) to the uncontrolled system for Solid (ST) and pneumatic (PT) tires.

DoF	***z***		***ϑ***		***φ***	
Tire Type	ST	PT	ST	PT	ST	PT
CLC	88 %	77 %	22 %	22 %	21 %	23 %
OLC	123 %	120 %	32 %	35 %	32 %	35 %

For the CLC, it is recognizable that the vertical DoF suffers from the high sensitivity of the human perception at frequencies above the first natural frequency. This effect reduces the potential of the controller significantly.

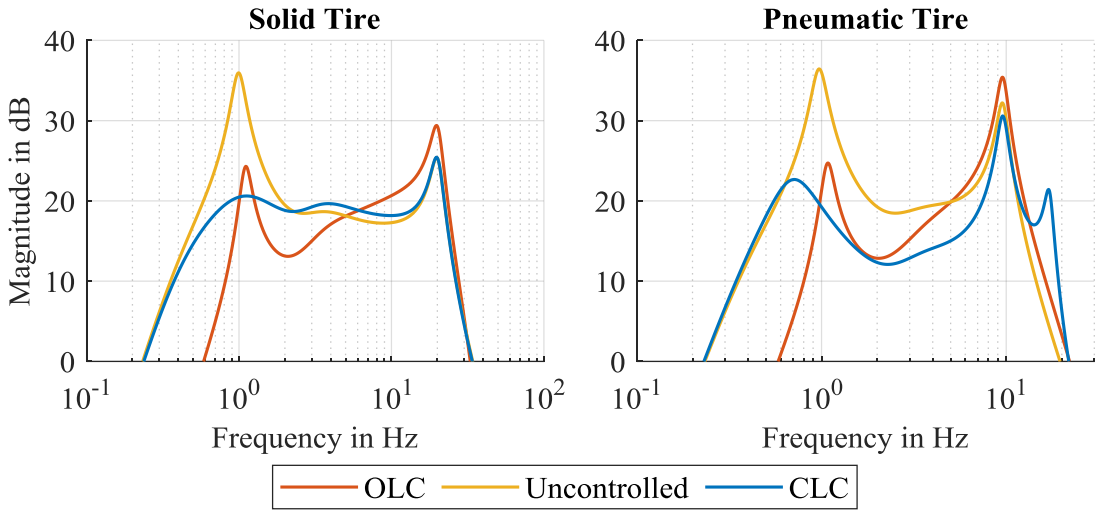

Figure 8-10: Bode plot of vertical frequency-weighed output acceleration (cf. equation (7.25)) comparing the control approaches (open-loop system architecture, OLC; closed-loop system architecture, CLC) to the uncontrolled system. Determined with linear model from subchapter 8.2.2.

8.2.4 Nonlinear System Modelling

The nonlinear multibody model developed for the tire-sprung system in section 7.5.1 is extended by an additional prismatic joint between wheel mass and hexapod bottom plate. The joint is equipped with a linear spring damper system. No further changes are made to the model. The natural frequency of the system is set to 1 Hz, which is the lowest value found to be practically feasible (cf. section 8.6.2). The damping ratio is set to 0.1.

8.2.5 Theoretical Component Validation of Controller Design

As for the tire-sprung system, the theoretical validation is based on the alternative multibody model approach. The PSD of the frequency-weighed output accelerations for the three DoFs are shown in Figure 8-11 for the closed-loop architecture (CLC), the open-loop architecture (OLC) and the uncontrolled system. Compared to the linear system behavior in Figure 8-10 a high qualitative agreement is recognizable. This validates the developed linear model of the suspension. For the vertical DoF, the disadvantage of the OLC of high magnitudes in the sensitive frequency range is recognizable compared to the CLC. For the pitch and roll DoFs, the advantage of the reduced sensitivity of the human perception at high frequencies is visible, allowing higher gains of the CLC and therefore a better performance than the OLC. The dominant peak at 10.5 Hz results from lower gain margins of the open-loop transfer function (OLTF). On the other hand, higher amplitudes of the OLTF at low frequencies are enabled, so that a distinct damping of the natural frequency is achieved.

The CDF of the total vibration values occurring on the acceptable reference driving surface quality of 0.036 mm³ from section 4.4.1 are shown in Figure 8-12.

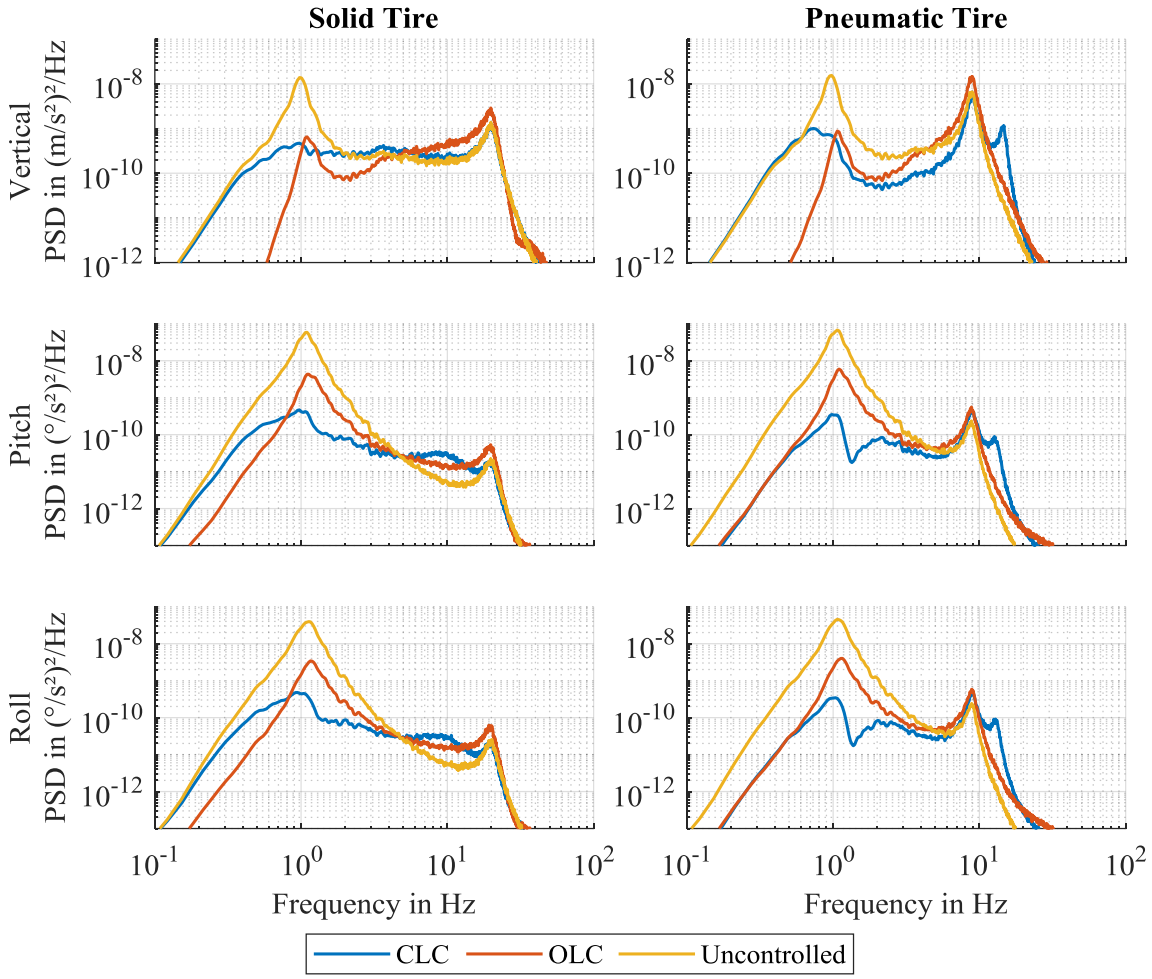

Figure 8-11: Theoretical validation of control system function by means of frequency-weighed accelerations for closed-loop control (CLC), open-loop control (OLC) compared to uncontrolled system for vertical, pitch and roll DoF. Accelerations determined with multi-body model from section 8.2.4 in urban driving scenario on reference driving surface roughness of 0.036 mm³.

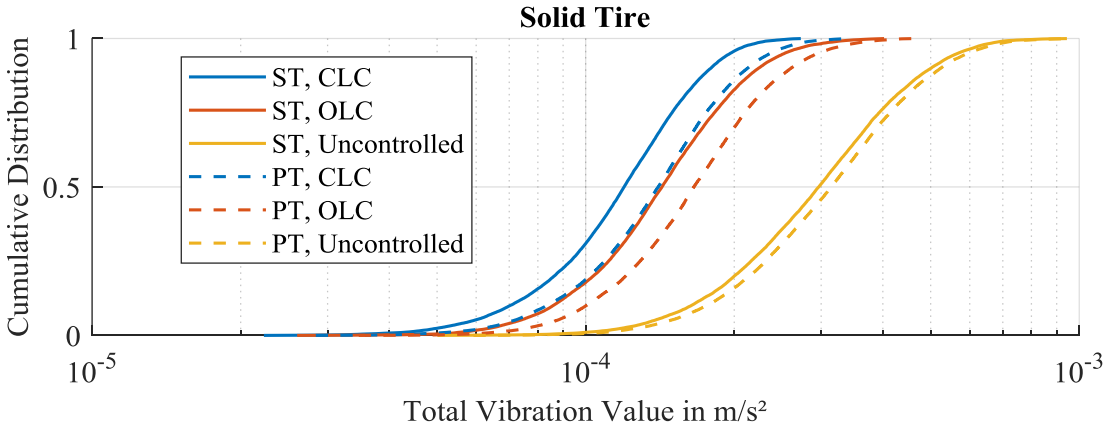

Figure 8-12: Cumulative distribution of total vibration value (cf. section 2.4.2) for closed-loop architecture (CLC), open-loop architecture (OLC, without vertical control) compared to uncontrolled system. Accelerations determined with multi-body model from section 8.2.4 in urban driving scenario on reference driving surface roughness of 0.036 mm³.

For the OLC the control of the vertical DoF is inactive due to the deterioration of the behavior. The passive system has an almost equal performance for both tire types. The positive impact of the controller is higher for the solid tire, although the difference is small. The reduction of the total vibration by the OLC is close to that of the CLC. Thus, it is suitable as a control approach with low development effort for the angular DoFs. Especially for a new system with unknown behavior, it could be implemented as initial control. Nevertheless, the CLC is considered for the following evaluations due to its higher vibration isolation potential. The following subchapters aim at determining the demands on the suspension.

8.3 Demand from Stability of Oscillation System

A lower limit for the natural frequency is given by the demand for a stable system. In many vertical dynamics models of passenger cars, the effect of the shift of the center of gravity due to pitch and roll angles is neglected. However, if the stiffness of the suspension spring is too low and the masses and the center of gravity heights of the connected bodies are too high, the moments resulting from a tilt of the body cannot be compensated by the springs. This effect is similar to an inverse pendulum held by a rotational spring. If the moment resulting from the shift of the mass is higher than the compensating moment of the spring, which results in a negative coefficient in the characteristic polynomial of the system equation, the pendulum turns over. The lower limit of stable natural frequencies is dependent on the intersection point where the DoF is implemented because it depends on the joint configuration and the masses and center of gravity heights of the separated bodies. The stability limits are determined with the multibody model described in 8.2.4 by iteratively reducing the natural frequency. The resulting lower stability limits are shown in Table 8-2 for the different DoF positions of the suspension.

Table 8-2: Stability limitations for natural frequency at different DoF positions of suspension.

DoF Position	**1**	**2/3**	**4**	**5**
Stability Limit	0.3 Hz	0.4 Hz	0.5 Hz	0.7 Hz

8.4 Demands on Suspension due to Vibration Isolation

The demands on the suspension resulting from the function of vibration isolation are determined with the control validation multibody model from section 8.2.4. Different combinations of natural frequencies, damping ratios and DoF positions are simulated in urban driving scenarios on a driving surface with a roughness coefficient of 1 cm³ with active and inactive

hexapod closed-loop control. The controller parameterization is redesigned for each parameter set based on the methodology described in section 8.2.3 in order to determine its maximum potential. The results are given in Figure 8-13. For each parameterization, the optimum damping is determined and the respective total vibration value is shown.

It is recognizable that the DoF position and the control approach can influence the total vibration value by one order of magnitude. Three findings are derived from the results:

- The natural frequency should be as low as possible.
- The DoF position should be as close to the wheel as possible. Especially positions above intersection point 2/3 should be avoided.
- The control improves the behavior for all DoF positions, but the potential reduces at higher intersection points. The demands on the DoF position and the natural frequency are the same for controlled and uncontrolled system.

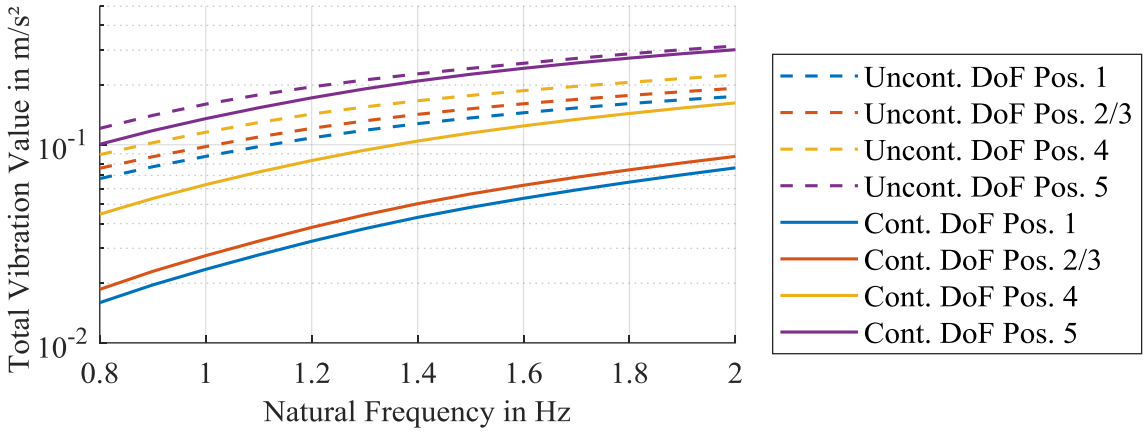

Figure 8-13: Maximum total vibration values determined in urban driving scenario on driving surface with roughness coefficient 1 cm³ with model from section 8.2.4 and different positions and natural frequencies of the suspension DoF. Comparison between controlled and uncontrolled system.

The required suspension strokes due to driving surface unevenness were determined on a driving surface with a roughness coefficient of 100 cm³ (Class D driving surface). The maximum suspension stroke at the natural frequency of 0.5 Hz amounts to 30 mm.

8.5 Demands on Suspension and Motion Control due to Horizontal Dynamics

This subchapter aims at investigating the demands on the suspension that result from the horizontal dynamics of the driving simulator. With regard to the parameters summarized in section 8.1.4, the following questions arise:

- Which kinematic characteristics are demanded from the tire-ground-contact and the steering?

- Which kinematic characteristics are desired in order to support the load transfers resulting from horizontal forces?
- Which adjustments of the MC are required in order to adapt it to the kinematics?
- Which joint position should be chosen?
- Which suspension stroke is required from the horizontal dynamics?

The methodology to address these questions is depicted in Figure 8-14. The demands from the horizontal dynamics mainly affect the kinematic parameters from section 8.1.4. Hence, an analysis of the impact of these parameters on the horizontal dynamics and the usability for affecting the behavior of WMDS is conducted. Following from that, target kinematic parameters are determined. The motion control and the kinematics, especially the support angles, are to be coordinated and, hence, are developed in parallel. Based on the kinematic parameters, an estimation of the required stroke resulting from the horizontal dynamics is possible. Additionally, the joint position demands resulting from kinematic considerations are determined.

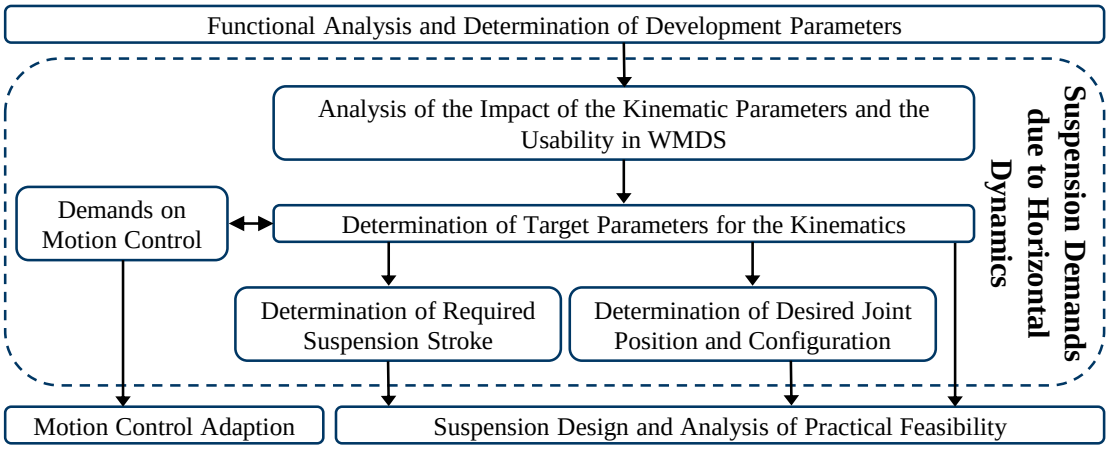

Figure 8-14: Methodology for determination of demands on suspension due to horizontal dynamics.

8.5.1 Impact and Usability of Kinematic Parameters in WMDS

The following section aims at investigating which impact the kinematic parameters from section 8.1.4 have on the behavior of WMDS and if there is a potential for a positive affection of this behavior. For all kinematic parameters, a difference has to be made between a steered kinematic, which is steered together with the wheel body (joint positions 1 and 2), and a non-steered kinematic (joint positions 3 to 7).

8.5.1.1 Toe Angle

Steered Kinematic: The toe angle is a stroke-dependent steering angle, which is superposed to the angle adjusted by the steering motors. This enables an adjustment of the steering angle that is approximately dependent on the wheel load in order to compensate for changing lateral tire forces resulting from driving surface unevenness. However, this also changes the

direction of the longitudinal tire force that was intended by the motion control. Due to the higher portion of the longitudinal tire forces in the overall acceleration generation and the low cornering stiffness of the tires, the impact of this error is worse than that of the changing lateral forces. Hence, no application potential of a dynamically changing toe angle exists.

Non-Steered Kinematic: A non-steered kinematic is unable to affect the toe angle in the given system because it can only rotate the body-fixed part of the steering bearing while the steering angle is still set by the motor. A mixed solution with parts of the kinematic connected to the steered bodies would not be possible due to the unlimited steering angle of the WMDS.

8.5.1.2 Camber Angle

The camber angle is defined as the inclination of the tire relative to the ground according to section 8.1.1. A static camber angle is not feasible in the given WMDS concept. The lack of opposing tires would lead to a sustained and undesired force on the WMDS body.

Steered Kinematic: The dynamic camber could be used to increase the lateral tire friction potential on the tires with increased wheel loads. Disadvantageous is the generation of undesired lateral forces due to the unevenness of the driving surface, which are also not compensated by an opposing tire with the same kinematic motion. Additionally, the longitudinal force potential is reduced by the camber.

Non-Steered Kinematic: If the kinematic were non-steered, no clear relation between the tire direction and the camber, which is generated by the kinematic, would exist. Hence, the increasing lateral friction potential due to camber would be randomly dependent on the steering angle, while the disadvantages mentioned for the non-steered system would remain.

Summarizing, a camber angle relative to the ground is not desired. However, the kinematic motion of the DoF generates an inclination of the wheel relative to the body. In case of a non-steered kinematic, the inclination for a given suspension stroke is not dependent on the steering angle and hence is constant in the driving simulator coordinate system. Thus, it enables compensation of the body inclination in order to reduce the ground-related camber of the wheel. The aim of the suspension camber design should be to generate a wheel inclination relative to the body that minimizes the camber of the wheel relative to the ground in all relevant operation states.

8.5.1.3 Support Angle

In order to reduce the pitch and roll motions resulting from horizontal accelerations, the support angles in combination with the tire forces at each wheel must generate vertical forces acting on the body that compensate the pitch and roll moments so that no additional spring force is required. The required suspension forces to support the moments are calculated based on the system in Figure 8-15.

The summed vertical suspension forces ${}_{\mathrm{H}}F_{z,\mathrm{S,sum},i}$ consist of the spring force ${}_{\mathrm{H}}F_{z,\mathrm{S},c,i}$, the damper force ${}_{\mathrm{H}}F_{z,\mathrm{S},d,i}$ and the support force resulting from the kinematic force transmission ${}_{\mathrm{H}}F_{z,\mathrm{S,Sup},i}$:

$$ {}_{\mathrm{H}}F_{z,\mathrm{S,sum},i} = {}_{\mathrm{H}}F_{z,\mathrm{S},c,i} + {}_{\mathrm{H}}F_{z,\mathrm{S},d,i} + {}_{\mathrm{H}}F_{z,\mathrm{S,Sup},i} \tag{8.22} $$

The damper force is zero due to the consideration of the static equilibrium state. The force and moment equilibriums are as follows:

$$ \sum F_{z,i} = {}_{\mathrm{H}}F_{z,\mathrm{S,sum,f}} + {}_{\mathrm{H}}F_{z,\mathrm{S,sum,rl}} + {}_{\mathrm{H}}F_{z,\mathrm{S,sum,rr}} - m_{\mathrm{B}} g = 0 \tag{8.23} $$

$$ \sum M_{x,i}^{(\mathrm{CG})} = \frac{{}_{\mathrm{H}}F_{z,\mathrm{S,sum,rl}} \ell_{\mathrm{t}}}{2} - \frac{{}_{\mathrm{H}}F_{z,\mathrm{S,sum,rr}} \ell_{\mathrm{t}}}{2} + {}_{\mathrm{H}}F_{y,\mathrm{H,res}} h_{\mathrm{CG,B}} = 0 \tag{8.24} $$

$$ \sum M_{y,i}^{(\mathrm{CG})} = -\frac{{}_{\mathrm{H}}F_{z,\mathrm{S,sum,f}} \ell_{\mathrm{t}}}{\sqrt{3}} + \frac{{}_{\mathrm{H}}F_{z,\mathrm{S,sum,rl}} \ell_{\mathrm{t}}}{2\sqrt{3}} + \frac{{}_{\mathrm{H}}F_{z,\mathrm{S,sum,rr}} \ell_{\mathrm{t}}}{2\sqrt{3}} - {}_{\mathrm{H}}F_{x,\mathrm{H,res}} h_{\mathrm{CG,B}} = 0 \tag{8.25} $$

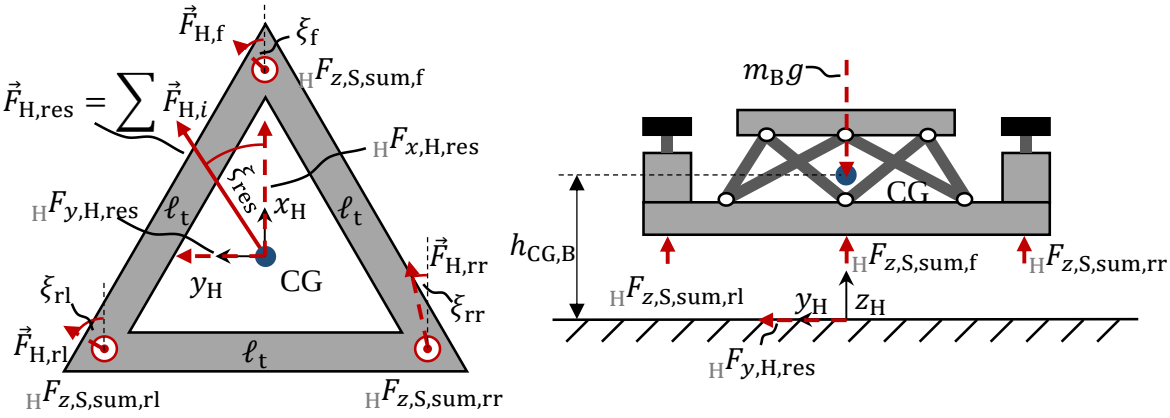

Figure 8-15: Calculation of wheel load transfer resulting from horizontal forces.

The horizontal force components are described in polar coordinates dependent on the resultant horizontal force $F_{\mathrm{H,res}}$, which is the vector sum of all horizontal forces acting on the body (mainly tire forces from the respective wheels, aerodynamics neglected), and its direction ξ_{res} relative to the leveled vehicle frame. The horizontal force $F_{\mathrm{H,res}}$ is equal to the horizontal acceleration $a_{\mathrm{H,res}}$ of the WMDS' body multiplied with its mass m_{B}:

$$ {}_{\mathrm{H}}F_{x,\mathrm{H,res}} = F_{\mathrm{H,res}} \cos \xi_{\mathrm{res}} = m_{\mathrm{B}} a_{\mathrm{H,res}} \cos \xi_{\mathrm{res}} \tag{8.26} $$

$$ {}_{\mathrm{H}}F_{y,\mathrm{H,res}} = F_{\mathrm{H,res}} \sin \xi_{\mathrm{res}} = m_{\mathrm{B}} a_{\mathrm{H,res}} \sin \xi_{\mathrm{res}} \tag{8.27} $$

By inserting these equations into the linear equation system and solving it, the following wheel loads are determined:

$$ {}_{\mathrm{H}}F_{z,\mathrm{S,sum,f}} = \frac{m_{\mathrm{B}} g}{3} - \frac{2 h_{\mathrm{CG,B}}}{\sqrt{3} \ell_{\mathrm{t}}} m_{\mathrm{B}} a_{\mathrm{H,res}} \cos \xi_{\mathrm{res}} \tag{8.28} $$

$$ {}_{\mathrm{H}}F_{z,\mathrm{S,sum,rl}} = \frac{m_{\mathrm{B}}g}{3} + \frac{h_{\mathrm{CG,B}}}{\sqrt{3}\ell_{\mathrm{t}}} m_{\mathrm{B}} a_{\mathrm{H,res}} \left(\cos\xi_{\mathrm{res}} - \sqrt{3}\sin\xi_{\mathrm{res}}\right) \tag{8.29} $$

$$ {}_{\mathrm{H}}F_{z,\mathrm{S,sum,rr}} = \frac{m_{\mathrm{B}}g}{3} + \frac{h_{\mathrm{CG,B}}}{\sqrt{3}\ell_{\mathrm{t}}} m_{\mathrm{B}} a_{\mathrm{H,res}} \left(\cos\xi_{\mathrm{res}} + \sqrt{3}\sin\xi_{\mathrm{res}}\right) \tag{8.30} $$

A further simplification based on addition theorems results in:

$$ {}_{\mathrm{H}}F_{z,\mathrm{S,sum,f}} = \frac{m_{\mathrm{B}}g}{3} + {}_{\mathrm{H}}\Delta F_{z,\mathrm{S,sum,f}} = \frac{m_{\mathrm{B}}g}{3} - \frac{2h_{\mathrm{CG,B}}}{\sqrt{3}\ell_{\mathrm{t}}} m_{\mathrm{B}} a_{\mathrm{H,res}} \cos\xi_{\mathrm{res}} \tag{8.31} $$

$$ {}_{\mathrm{H}}F_{z,\mathrm{S,sum,rl}} = \frac{m_{\mathrm{B}}g}{3} + {}_{\mathrm{H}}\Delta F_{z,\mathrm{S,sum,rl}} = \frac{m_{\mathrm{B}}g}{3} - \frac{2h_{\mathrm{CG,B}}}{\sqrt{3}\ell_{\mathrm{t}}} m_{\mathrm{B}} a_{\mathrm{H,res}} \cos(120° - \xi_{\mathrm{res}}) \tag{8.32} $$

$$ {}_{\mathrm{H}}F_{z,\mathrm{S,sum,rr}} = \frac{m_{\mathrm{B}}g}{3} + {}_{\mathrm{H}}\Delta F_{z,\mathrm{S,sum,rr}} = \frac{m_{\mathrm{B}}g}{3} - \frac{2h_{\mathrm{CG,B}}}{\sqrt{3}\ell_{\mathrm{t}}} m_{\mathrm{B}} a_{\mathrm{H,res}} \cos(240° - \xi_{\mathrm{res}}) \tag{8.33} $$

With the load transfers ${}_{\mathrm{H}}\Delta F_{z,\mathrm{S,sum},i}$ resulting from the horizontal forces. This shows that the description of the load transfer is equal for all wheels despite a shift of the force direction of 120°. The resulting load transfers are shown for the three wheels in Figure 8-16 for an acceleration of 8 m/s². In order to prevent pitch and roll motions due to these load transfers, the spring force in equation (8.22) must not increase relative to the static load. Hence, the following condition is required for an ideal force support:

$$ {}_{\mathrm{H}}\Delta F_{z,\mathrm{S,sum},i} = {}_{\mathrm{H}}F_{z,\mathrm{S,Sup},i} \tag{8.34} $$

Following from that, the vertical forces generated by the support angles at each wheel must match the forces shown in Figure 8-16. In order to analyze the available parameters to adjust this behavior, the generation of support forces is analyzed. The force relations at the tire-sprung mass are shown in the plane of the resultant tire force in Figure 8-17.

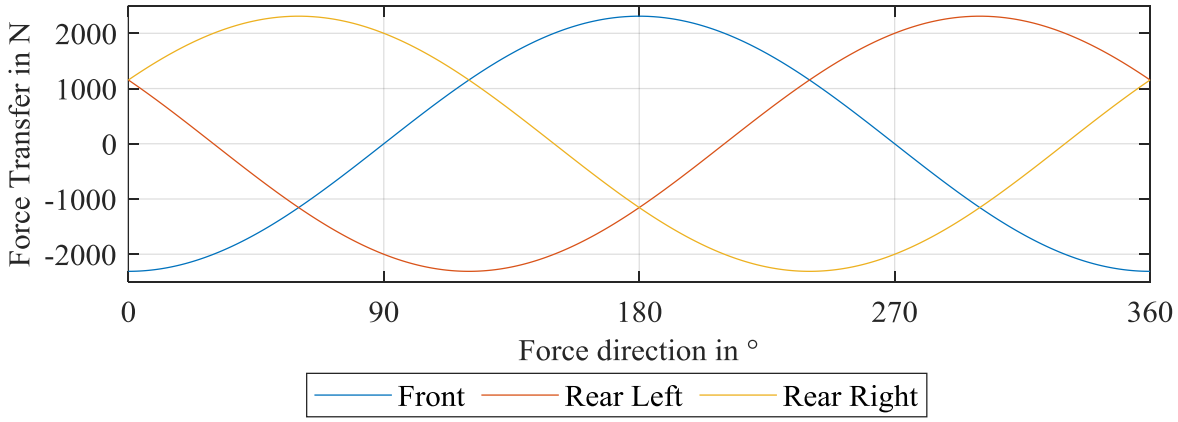

Figure 8-16: Force transfer between the three wheels dependent on force direction in CG for an acceleration magnitude of 8 m/s².

The forces and moments generated by the tire force and the wheel mass acceleration are supported in the instantaneous center of rotation (ICR) in the plane of the resultant force. The following static equilibriums are derived (steady-state, no damper force):

$$\sum F_{z,i} = {}_{\mathrm{H}}F_{z,\mathrm{T}} - {}_{\mathrm{H}}F_{z,\mathrm{S},c,i} - {}_{\mathrm{H}}F_{z,\mathrm{S},\mathrm{Sup},i} - m_{\mathrm{TS}}g = 0 \tag{8.35}$$

$$\sum F_{x,i} = F_{\mathrm{T,res}} - F_{x,\mathrm{ICR,PrF}} - m_{\mathrm{TS}}a_{\mathrm{H,res}} = 0 \tag{8.36}$$

$$\sum M_i^{(\mathrm{ICR})} = F_{\mathrm{T,res}}h_{\mathrm{CG,TS}} - {}_{\mathrm{H}}F_{z,\mathrm{S},\mathrm{Sup},i}\ell_{\mathrm{ICR}} + F_{x,\mathrm{ICR,PrF}}\left(h_{\mathrm{ICR}} - h_{\mathrm{CG,TS}}\right) = 0 \tag{8.37}$$

Solving this equation system results in the following expression for the vertical support force:

$${}_{\mathrm{H}}F_{z,\mathrm{S},\mathrm{Sup},i} = \left(F_{\mathrm{T,res}} - m_{\mathrm{TS}}a_{\mathrm{H,res}}\right)\frac{h_{\mathrm{ICR}}}{\ell_{\mathrm{ICR}}} + m_{\mathrm{TS}}a_{\mathrm{H,res}}\frac{h_{\mathrm{CG,TS}}}{\ell_{\mathrm{ICR}}} \tag{8.38}$$

The second term describes the influence of the tire-sprung mass on the wheel load transfer. It impedes the design of the kinematic because the parameters h_{ICR} and ℓ_{ICR} have to be considered independently and therefore two parameters have to be analyzed. In order to determine whether this fraction must be considered, an analysis of its impact is conducted. For an ℓ_{ICR} of 0.8 m, the ratio of this force to the overall load transfer amounts to 5 %. Below that value, however, the fraction highly increases, so that it is required to assure a distance to the ICR of at least 0.8 m in order to minimize the impact of the wheel mass.

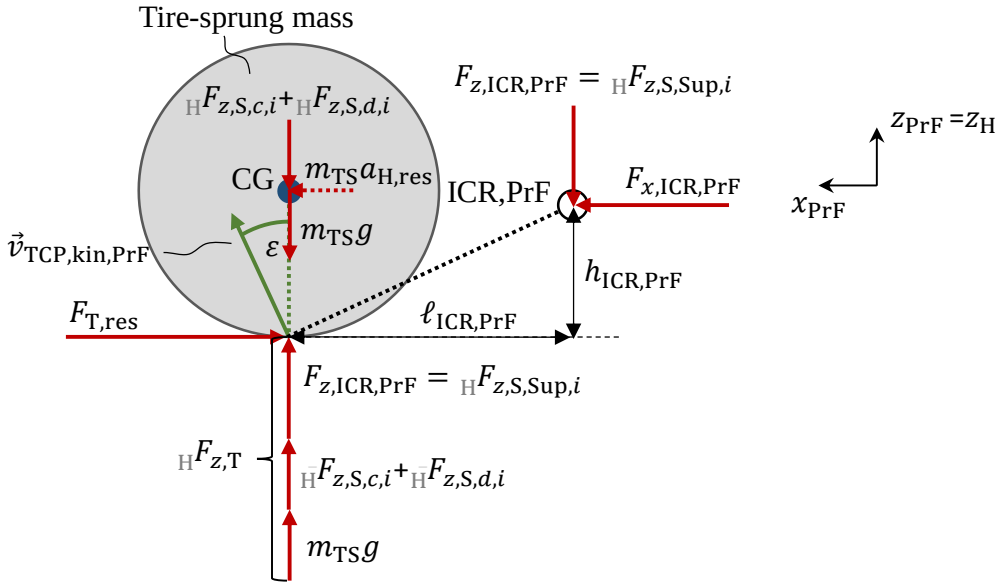

Figure 8-17: Force relations at the tire-sprung mass in the plane of the resultant tire force.

This makes it possible to neglect the second term for the design of the kinematics and the following calculation for the support force is applied:

$${}_{\mathrm{H}}F_{z,\mathrm{S},\mathrm{Sup},i} = \left(F_{\mathrm{T,res},i} - m_{\mathrm{TS}}a_{\mathrm{H,res}}\right)\frac{h_{\mathrm{ICR}}}{\ell_{\mathrm{ICR}}} = \left(F_{\mathrm{T,res},i} - m_{\mathrm{TS}}a_{\mathrm{H,res}}\right)\tan\varepsilon_i \tag{8.39}$$

The acceptability of this neglect will be investigated in the validation. Equation (8.39) shows that an adaption of the support angle ε or of the tire force $F_{\mathrm{T,res}}$ to the force direction at the wheel $\xi_{\mathrm{W},i}$ is required to support the load transfers in Figure 8-16. The adaption of the tire

force is not feasible because it is dependent on the force $F_{\mathrm{H,res}}$ resulting from the motion control (MC). For example, at a force direction of 90° (only lateral acceleration, no yaw acceleration) the force at the front wheel were required to be zero to avoid a vertical support force. This, however, would result in a yaw acceleration because no force would compensate the moments resulting from the forces at the rear wheels. Hence, only an adaption of the support angle is possible. Based on these considerations, the applicability of support angles for the reduction of pitch and roll motions is analyzed in the following.

Steered Kinematic: A steered kinematic would result in a constant support angle in wheel direction. For example, if only longitudinal forces were to act at the tire, the support angle would be constant for all force directions ξ because the kinematic velocity vector $\vec{v}_{\mathrm{TCP,kin}}$ from Figure 8-4 would be rotated together with the tire force. This would result in a constant line in Figure 8-16, so that the required support force is only achievable for two force directions ξ. However, even if at one wheel the support force and the load transfer are equal for a given ξ, this optimum is not met by the other wheels due to the shift of the load transfers at the respective wheels. Hence, no reduction of the pitch and roll movements would be possible with a steered kinematic. In most operation points, the behavior even deteriorates because the support forces result in additional spring forces and therefore higher suspension stroke.

Non-Steered Kinematic: For a non-steered kinematic, the direction of the velocity vector $\vec{v}_{\mathrm{TCP,kin}}$ is fixed in the vehicle frame. Therefore, the fraction of this velocity in the force direction $\vec{v}_{x,\mathrm{TCP,kin,PrF}}$ changes with varying ξ, so that an adaption of the effective support angle to the direction of the horizontal force occurs. For example, for the motion state shown in Figure 8-4 the effective support angle would be zero for a force direction of 90°, which would lead to the desired support force from Figure 8-16. Following from that, the support angles can be applied to reduce pitch and roll motions if a non-steered kinematic is chosen. The negative comfort impact of the diagonal springing is small on normal asphalt roads and is therefore accepted for the sake of reduced angular motions and suspension strokes.[111]

8.5.1.4 Caster Trail and Caster Angle

A caster trail results in steering-induced horizontal and, in combination with a caster angle, vertical motions of the WMDS due to a deflection of the tire contact point relative to the WMDS. Additionally, the required steering moments are increased. On the other hand, no advantages result from the implementation of a caster trail because no steering feedback is required as in passenger cars. Therefore, the aim of the kinematic steering parameter design should be to avoid static and dynamic caster trails. Coordination of the dynamic caster angle and the suspension-induced motion of the tire contact point could be applied in order to minimize the occurring caster trail values.

[111] Cf. Matschinsky, W.: Radführungen der Straßenfahrzeuge (2007), p. 129.

Steered Kinematic: The position of the steering axis cannot be influenced by the steered kinematic. However, angular motions of the WMDS body generate an angle of the steering axis, which would result in a caster trail. A kinematic motion of the tire could compensate this trail by moving the tire contact point into the intersection between the ground plane and the steering axis, as shown in the appendix in Figure C.1 - 1 on the left.

On the other hand, as shown in Figure C.1 - 1 on the right, driving surface-induced vertical motions of the wheel would also result in a deflection of the tire contact point. Because of inertia, no pitch-angle is generated in the first moment after driving over the unevenness and the steering axis inclination remains zero. The motion of the tire contact point would now generate an undesirable caster trail relative to that steering axis. Hence, the kinematic design is a tradeoff between the generation of caster trails through angular motions of the WMDS body and through driving surface unevenness. The case of angular motion is less critical in that case because it is generated by horizontal forces. Due to Weber's Law described in section 2.4.4 the subject is less sensitive to disturbances resulting from caster trails because of the already acting accelerations. Hence, the kinematic motion of the wheel should be avoided to mitigate the influences resulting from driving surface-induced disturbances.

Non-Steered Kinematic: For the non-steered kinematic, no relative motion between the steering axis and tire contact point is possible, so that no compensation of resulting caster trails can be conducted. Hence, the change of the caster angle over wheel stroke should be as small as possible.

8.5.1.5 Kingpin Inclination and Scrub Radius

In addition to the negative impact of vertical motion resulting from steering motions, which was already described in section 8.5.1.4, the scrub radius generates steering torques from the longitudinal tire forces. These have to be controlled by the steering motor, which impedes the control coordination and increases the energy demand of the steering system. Hence, the kingpin inclination and the scrub radius are undesirable. The compensation of the scrub radius generated by a steering axis inclination through angular motions of the WMDS is discarded due to the same reasons as for the caster.

8.5.1.6 Summary

Summarizing, the following kinematic parameters have static and dynamic target values of zero:

- Toe angle
- Caster angle and trail
- Kingpin inclination and scrub radius

The support angle is applicable to reduce the angular motions and suspension strokes of the WMDS if a non-steered kinematic is implemented. Further investigations are required to

determine target values. Especially the coordination between support angles and the force distribution between the wheels given by the motion control needs to be investigated.

The static and dynamic camber angle relative to the ground should be kept to zero. To achieve this aim, the suspension should be designed to compensate body inclinations with counteracting inclinations of the wheel relative to the body. The required target values for the kinematic are dependent on the occurring body inclinations and suspension strokes and the correlation between them, which are on the other hand dependent on the support angles. Therefore, the design of the support angles is conducted first. Subsequently, the desired kinematic inclinations are derived.

8.5.2 Design of Support Angles and Motion Control

The aim of the support angle design is to avoid suspension strokes and associated pitch and roll angles resulting from horizontal accelerations of the WMDS. Ideally, the vertical support forces must be equal to the load transfers resulting from the horizontal accelerations in all relevant operational states of the simulator. Hence, the following condition for the optimum support angle $\varepsilon_{\mathrm{opt},i}$ at a wheel is derived from equations (8.34) and (8.39) with the overall load transfer ${}_{\mathrm{H}}\Delta F_{z,\mathrm{S},\mathrm{sum},i}$ and the tire force $F_{\mathrm{T,res},i}$, which are both dependent on the magnitude $a_{\mathrm{H,res}}$ and direction ξ_{res} of the acceleration of the WMDS:

$$\tan \varepsilon_{\mathrm{opt},i} = \frac{{}_{\mathrm{H}}\Delta F_{z,\mathrm{S},\mathrm{sum},i}\left(a_{\mathrm{H,res}}, \xi_{\mathrm{res}}\right)}{\left(F_{\mathrm{T,res},i}\left(a_{\mathrm{H,res}}, \xi_{\mathrm{res}}\right) - m_{\mathrm{TS}} a_{\mathrm{H,res}}\right)} \tag{8.40}$$

The tire force $F_{\mathrm{T,res},i}$ is dependent on the applied motion control (MC). The following section aims at the investigation of the influence of the MC on the support angle design and the derivation of MC adaptions to address the demands of the suspension.

8.5.2.1 Influence of Motion Control on Support Angle Design and Concept Development

For an initial investigation and the derivation of necessary adaptions, the currently applied MC that is presented in section 2.6.2.2 is analyzed. The determination of the overall tire force demand is split into translational and yaw demand according to Figure 2-6. Both aspects are analyzed separately.

The yaw demand fraction of the tire forces generates no pitch and roll moments and therefore the support forces are required to be zero to avoid the insertion of tire-force-induced motions. It is advantageous that the directions of the yaw forces $\xi_{\mathrm{yaw},i}$ at the tires in the leveled simulator coordinate system are the same for all operational states, so that this is only required for these specific directions. Hence, the following conditions must be fulfilled:

$$\varepsilon_{\mathrm{opt,f}}\left(\xi_{\mathrm{f}} = \xi_{\mathrm{yaw,f}} = 90° \;\&\; 270°\right) = 0° \tag{8.41}$$

$$\varepsilon_{\mathrm{opt,rl}}\left(\xi_{\mathrm{rl}} = \xi_{\mathrm{yaw,rl}} = 30° \,\&\, 210°\right) = 0° \tag{8.42}$$

$$\varepsilon_{\mathrm{opt,rr}}\left(\xi_{\mathrm{rr}} = \xi_{\mathrm{yaw,rl}} = 150° \,\&\, 330°\right) = 0° \tag{8.43}$$

Optimum support for all operational states is only achievable if the required support angles for the translational force demand also meet these conditions, which is analyzed in the following. The described MC concept divides the overall translational force demand on the wheels dependent on the wheel load ${}_{\mathrm{H}}F_{z,\mathrm{T},i}$ in order to achieve an equal friction utilization. Therefore, it is referred to as **friction-optimized motion control (FMC)** in the following. The magnitudes of the desired tire forces for the translational acceleration demand $a_{\mathrm{H,res,dem}}$ are calculated as follows:[112]

$$F_{\mathrm{T,res},i} = {}_{\mathrm{H}}F_{z,\mathrm{T},i}\mu_{\mathrm{res}} = {}_{\mathrm{H}}F_{z,\mathrm{T},i}\frac{a_{\mathrm{H,res,dem}}}{g} \tag{8.44}$$

The following considerations assume that the acting acceleration $a_{\mathrm{H,res}}$ is equal to the demanded acceleration. Additionally, the force directions at the wheels ξ_i are equal to the direction of the resultant force respectively acceleration ξ_{res}. The wheel loads ${}_{\mathrm{H}}F_{z,\mathrm{T},i}$ are calculated similarly to the suspension forces ${}_{\mathrm{H}}\Delta F_{z,\mathrm{S,sum},i}$ but instead of only considering the body mass, the WMDS is assumed as a rigid body and the total mass and center of gravity is applied for the calculation of the wheel loads. This results in the following descriptions:

$${}_{\mathrm{H}}F_{z,\mathrm{T,f}} = \frac{m_{\mathrm{tot}}g}{3} - \frac{2h_{\mathrm{CG,tot}}}{\sqrt{3}\ell_{\mathrm{t}}}m_{\mathrm{tot}}a_{\mathrm{H,res}}\cos\xi_{\mathrm{res}} \tag{8.45}$$

$${}_{\mathrm{H}}F_{z,\mathrm{T,rl}} = \frac{m_{\mathrm{tot}}g}{3} - \frac{2h_{\mathrm{CG,tot}}}{\sqrt{3}\ell_{\mathrm{t}}}m_{\mathrm{tot}}a_{\mathrm{H,res}}\cos(120° - \xi_{\mathrm{res}}) \tag{8.46}$$

$${}_{\mathrm{H}}F_{z,\mathrm{T,rr}} = \frac{m_{\mathrm{tot}}g}{3} - \frac{2h_{\mathrm{CG,tot}}}{\sqrt{3}\ell_{\mathrm{t}}}m_{\mathrm{tot}}a_{\mathrm{H,res}}\cos(240° - \xi_{\mathrm{res}}) \tag{8.47}$$

Inserting these equations in (8.40) yields the following optimum support angles for the FMC with equation (8.44):

$$\tan\varepsilon_{\mathrm{opt,f,FMC}} = \frac{2\sqrt{3}gh_{\mathrm{CG,B}}m_{\mathrm{B}}\cos\xi_{\mathrm{res}}}{m_{\mathrm{tot}}\left(2\sqrt{3}a_{\mathrm{H,res}}h_{\mathrm{CG,tot}}\cos\xi_{\mathrm{res}} - g\ell_{\mathrm{t}}\right) + 3g\ell_{\mathrm{t}}m_{\mathrm{TS}}} \tag{8.48}$$

$$\tan\varepsilon_{\mathrm{opt,rl,FMC}} = \frac{2\sqrt{3}gh_{\mathrm{CG,B}}m_{\mathrm{B}}\cos(120° - \xi_{\mathrm{res}})}{m_{\mathrm{tot}}\left(2\sqrt{3}a_{\mathrm{H,res}}h_{\mathrm{CG,tot}}\cos(120° - \xi_{\mathrm{res}}) - g\ell_{\mathrm{t}}\right) + 3g\ell_{\mathrm{t}}m_{\mathrm{TS}}} \tag{8.49}$$

$$\tan\varepsilon_{\mathrm{opt,rr,FMC}} = \frac{2\sqrt{3}gh_{\mathrm{CG,B}}m_{\mathrm{B}}\cos(240° - \xi_{\mathrm{res}})}{m_{\mathrm{tot}}\left(2\sqrt{3}a_{\mathrm{H,res}}h_{\mathrm{CG,tot}}\cos(240° - \xi_{\mathrm{res}}) - g\ell_{\mathrm{t}}\right) + 3g\ell_{\mathrm{t}}m_{\mathrm{TS}}} \tag{8.50}$$

The conditions (8.41) to (8.43) for the yaw demand are fulfilled by this approach. However, it is recognizable that the optimum support angle for the FMC depends on the magnitude of

[112] Cf. Betz, A.: Diss., Feasibility and Design of WMDS (2014), p. 62.

the resultant acceleration $a_{\mathrm{H,res}}$, as shown in Figure 8-18 for the front wheel. Hence, it would be necessary to continuously adapt the support angles to the current acceleration of the simulator in order to realize an optimum force support. Additionally, the optimum support angle is dependent on the direction of the acceleration. Positive accelerations (0-90° and 270-360°) require a higher support angle at the front wheel than negative accelerations (90-270°).

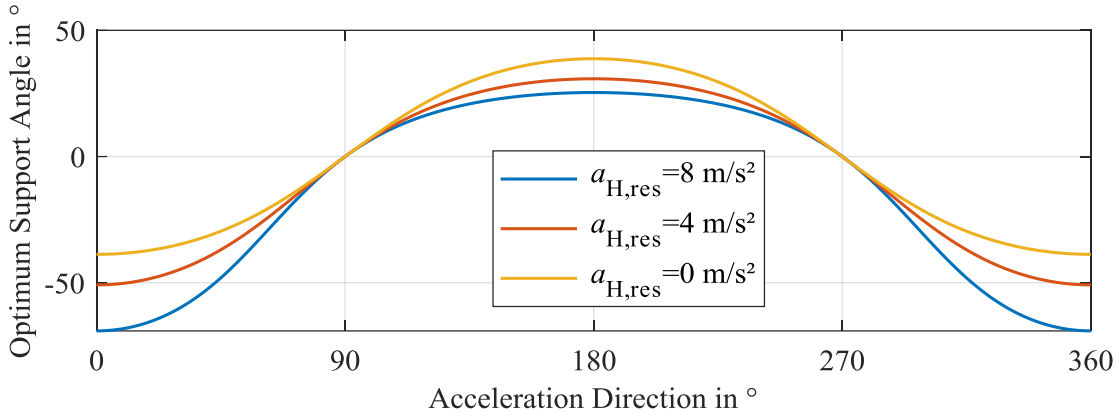

Figure 8-18: Required support angles for optimum force support at the front wheel for friction-optimized motion control (FMC) at different acceleration magnitudes and directions.

The reason for this behavior is the friction-focused force distribution. This is explained exemplarily for the front wheel. The amount of wheel load transfer and, therefore, the required vertical support force for an acceleration direction of 0° is the same as for 180°. However, the sign of the wheel load transfer changes, so that the front wheel has an increased wheel load at 180° and a reduced wheel load at 0°. This results in different longitudinal forces dependent on the direction of acceleration. The low longitudinal force for an acceleration direction of 0° requires a high support angle according to equation (8.40) to generate the necessary support force. At an acceleration direction of 180° however, the longitudinal force at the front wheel is high while the same amount of support force is required. This needs to be compensated by a reduced support angle. For an acceleration of zero, no wheel load transfer would occur and the tire forces would be distributed equally. Therefore, the course in Figure 8-18 is point symmetric between 0 and 180°. However, this is a theoretical state because for an acceleration of zero no support angles would be required. A higher acceleration results in a higher shift of the optimum support angle to the negative region.

The dependency on the magnitude of acceleration would require a force-sensitive switching of the support angle. This could be achieved by implementing elastically mounted joints, which change their position depending on the acting force. However, this would result in latencies and undesired dynamics of the horizontal forces. Therefore, an alternative MC approach is aspired to avoid the described shortcomings.

The dependency on magnitude and direction of the acceleration results from the wheel load dependent force division of the FMC. An alternative approach would be the **equal distribution** of the wheel forces, in the following referred to as **EMC**. This means that each wheel generates a third of the overall translational force demand:

$$F_{\mathrm{T,res},i} = \frac{m_{\mathrm{tot}} a_{\mathrm{H,res,dem}}}{3} \tag{8.51}$$

This results in the following optimum support angles:

$$\tan \varepsilon_{\mathrm{opt,f,EMC}} = \frac{2\sqrt{3} h_{\mathrm{CG,B}} m_{\mathrm{B}} \cos \xi_{\mathrm{res}}}{(3m_{\mathrm{TS}} - m_{\mathrm{tot}}) \ell_{\mathrm{t}}} \tag{8.52}$$

$$\tan \varepsilon_{\mathrm{opt,rl,EMC}} = \frac{2\sqrt{3} h_{\mathrm{CG,B}} m_{\mathrm{B}} \cos(120° - \xi_{\mathrm{res}})}{(3m_{\mathrm{TS}} - m_{\mathrm{tot}}) \ell_{\mathrm{t}}} \tag{8.53}$$

$$\tan \varepsilon_{\mathrm{opt,rr,EMC}} = \frac{2\sqrt{3} h_{\mathrm{CG,B}} m_{\mathrm{B}} \cos(240° - \xi_{\mathrm{res}})}{(3m_{\mathrm{TS}} - m_{\mathrm{tot}}) \ell_{\mathrm{t}}} \tag{8.54}$$

This corresponds to the optimum support angles of the FMC at an acting acceleration of zero. The course of this support angle for the front wheel is depicted as the yellow line in Figure 8-18. It is only dependent on the acceleration direction but due to the symmetric behavior, no switching of the support angles is required between positive and negative accelerations. Additionally, the conditions for the yaw demand are fulfilled. Hence, ideal force support is possible. A shortcoming of this approach is that the tire forces are not adapted to the acting wheel load. This is not critical as long as the friction coefficient is not exceeded at any wheel. The front wheel reaches this limit at an acceleration of 4.5 m/s² for an acceleration direction of 0°.

Consequently, this force distribution leads to a reduction of the acceleration potential. In addition, from this acceleration, full support is no longer possible because the front wheel cannot build up any additional support forces to compensate for the increasing wheel load transfer. For this reason, only a hybrid variant is possible for this approach, in which the force distribution is adjusted when reaching a certain coefficient of friction μ_{lim} so that reaching the adhesion limit of the tires μ_{max} is prevented. If the following criterion is fulfilled, a switching to an MC approach, which adjusts the horizontal tire forces according to the wheel load, is conducted:

$$\mu_{\mathrm{act},i} = \frac{(m_{\mathrm{tot}} a_{\mathrm{H,res,dem}})/3}{{}_{\mathrm{H}}F_{z,\mathrm{T},i}} \geq \mu_{\mathrm{lim}} \tag{8.55}$$

In order to increase the limit of the acceleration from which the adhesion limit is reached, a purely direction-dependent force distribution can be applied (**direction-dependent MC, DMC**), which, however, does not depend on the magnitude of the acceleration. Thus, for example, a significantly greater horizontal force can be transferred to the wheel, which is loaded under the acting direction of acceleration. Although this does not achieve an even friction coefficient utilization, this is not problematic until the adhesion limit is reached. An approach is the horizontal force distribution based on the wheel load ${}_{\mathrm{H}}F_{z,\mathrm{T},i,\mathrm{aFix}}$ at one specific acceleration, which is independent of the demanded acceleration:

$$F_{\mathrm{T,res},i} = {}_{\mathrm{H}}F_{z,\mathrm{T},i,\mathrm{aFix}} \frac{a_{\mathrm{H,res,dem}}}{g} \tag{8.56}$$

The wheel loads ${}_{\mathrm{H}}F_{z,\mathrm{T},i,\mathrm{aFix}}$ are calculated with the equations (8.45) to (8.47) but instead of the resultant acting acceleration, a fixed dimensioning acceleration $a_{\mathrm{H,Fix}}$ is inserted:

$${}_{\mathrm{H}}F_{z,\mathrm{T,f,aFix}} = \frac{m_{\mathrm{tot}}g}{3} - \frac{2h_{\mathrm{CG,tot}}}{\sqrt{3}\ell_{\mathrm{t}}} m_{\mathrm{tot}} a_{\mathrm{H,Fix}} \cos\xi_{\mathrm{res}} \tag{8.57}$$

$${}_{\mathrm{H}}F_{z,\mathrm{T,rl,aFix}} = \frac{m_{\mathrm{tot}}g}{3} - \frac{2h_{\mathrm{CG,tot}}}{\sqrt{3}\ell_{\mathrm{t}}} m_{\mathrm{tot}} a_{\mathrm{H,Fix}} \cos(120° - \xi_{\mathrm{res}}) \tag{8.58}$$

$${}_{\mathrm{H}}F_{z,\mathrm{T,rr,aFix}} = \frac{m_{\mathrm{tot}}g}{3} - \frac{2h_{\mathrm{CG,tot}}}{\sqrt{3}\ell_{\mathrm{t}}} m_{\mathrm{tot}} a_{\mathrm{H,Fix}} \cos(240° - \xi_{\mathrm{res}}) \tag{8.59}$$

If a value of 8 m/s² is chosen, the uniform friction coefficient utilization among the three wheels is achieved at that acceleration, which is necessary due to reaching the adhesion limit (maximum friction coefficient of 0.8). The maximum friction coefficient is not exceeded at lower accelerations.

The optimum support angle for the DMC approach is calculated according to the other motion control concepts by dividing the required suspension forces by the tire forces:

$$\tan\varepsilon_{\mathrm{opt,f,DMC}} = \frac{2\sqrt{3}gh_{\mathrm{CG,B}}m_{\mathrm{B}}\cos\xi_{\mathrm{res}}}{m_{\mathrm{tot}}\left(2\sqrt{3}a_{\mathrm{H,FixMC}}h_{\mathrm{CG,tot}}\cos\xi_{\mathrm{res}} - g\ell_{\mathrm{t}}\right) + 3g\ell_{\mathrm{t}}m_{\mathrm{TS}}} \tag{8.60}$$

$$\tan\varepsilon_{\mathrm{opt,rl,DMC}} = \frac{2\sqrt{3}gh_{\mathrm{CG,B}}m_{\mathrm{B}}\cos(120° - \xi_{\mathrm{res}})}{m_{\mathrm{tot}}\left(2\sqrt{3}a_{\mathrm{H,Fix}}h_{\mathrm{CG,tot}}\cos(120° - \xi_{\mathrm{res}}) - g\ell_{\mathrm{t}}\right) + 3g\ell_{\mathrm{t}}m_{\mathrm{TS}}} \tag{8.61}$$

$$\tan\varepsilon_{\mathrm{opt,rr,DMC}} = \frac{2\sqrt{3}gh_{\mathrm{CG,B}}m_{\mathrm{B}}\cos(240° - \xi_{\mathrm{res}})}{m_{\mathrm{tot}}\left(2\sqrt{3}a_{\mathrm{H,Fix}}h_{\mathrm{CG,tot}}\cos(240° - \xi_{\mathrm{res}}) - g\ell_{\mathrm{t}}\right) + 3g\ell_{\mathrm{t}}m_{\mathrm{TS}}} \tag{8.62}$$

The comparison of these support angles with that of the FMC in equations (8.48) to (8.50) reveals that the DMC is independent of the acting acceleration and hence, no switching of the support angles is required, which would depend on the magnitude of the force. Additionally, the yaw demand conditions are fulfilled as for the other MC concepts. However, this approach also implies a direction dependency as the FMC. This directionality cannot be resolved if the utilization of the maximum acceleration potential of the tires is desired. Since accelerations are always associated with wheel load transfers, the tire forces must be increased or reduced accordingly at the respective wheels. This results in the behavior of different support angles in positive and negative acceleration direction outlined above. Another approach, which does not involve the direction and constantly assigns more force to a wheel, would only lead to a lower traction potential than the uniform distribution (EMC) in an unfavorable direction of acceleration.

The acceleration-direction dependency would require a switching support angle, which is sensitive to the force direction. This is theoretically possible by implementing overrunning-clutches or by dividing tension and compression functions of the suspension onto different joints. However, this is not feasible due to the situation depicted in Figure 8-19 in the x-z-

plane of the simulator coordinate system. The initial position of the tire-sprung mass is indicated by the grey body. Driving surface unevenness generates a motion of the tire-sprung mass around the instantaneous center of rotation (ICR). During this motion, a horizontal acceleration direction of 0° is assumed, which results in the green motion of the body. If a change of the horizontal acceleration direction were to occur at the upper end of the tire-sprung mass motion, the ICR would switch and the body would move according to the blue vector. At the end of this driving surface induced motion, the tire-sprung mass motion would end at another point than it started as indicated by the blue body. This is a relevant scenario, because the motion due to driving surface unevenness and the horizontal acceleration, which generates a discrete switching of the ICR, are not correlated. Hence, within a period, the tire-sprung mass would retract due to this behavior.

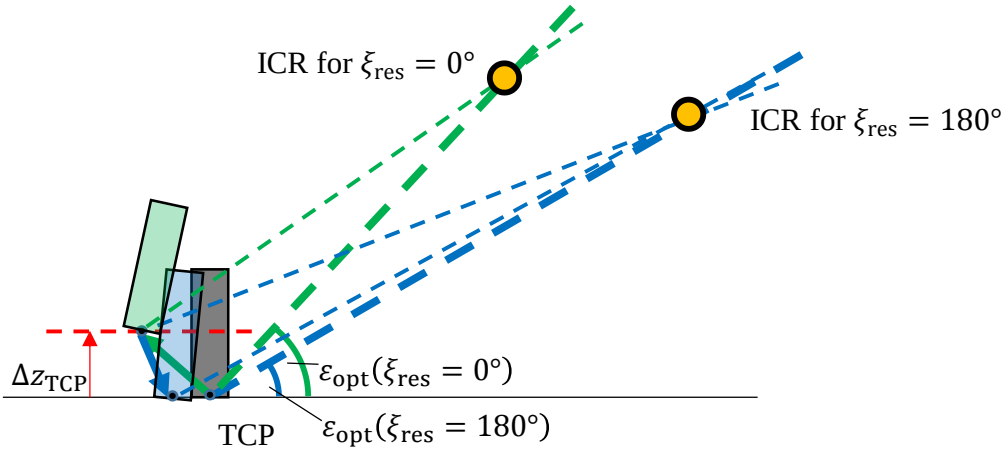

Figure 8-19: Impact of a switching instantaneous center of rotation (ICR) during driving surface-induced motions.

Therefore, the discrete switching of the support angle respectively the ICR is only possible for a rotationally symmetrical body because in that case the difference between start- and endpoint is not recognizable. This would require a rotation characteristic of the wheel over suspension stroke, which is dependent of the tire force direction in the simulator coordinate system. Hence, a transmission of this motion between steered and non-steered part as well as between sprung and unsprung part of the simulator would be necessary. Additionally, ideal support would still only be possible in the direction of the longitudinal tire force, because in the lateral direction no rotational symmetry exists. Thus, even if the high effort of this kinematic arrangement would be feasible it would still not be possible to completely avoid suspension strokes and, therefore, pitch and roll angles. Hence, this solution is not aspired.

Alternatively, instead of a discrete switching of the support angles, the ICR could be adapted continuously along a centrode. However, this leads to deviations from the desired support angles in the transition state. One possible concept is the implementation of hinge points that are only effective in one direction, by separating tie and push rods, for example by providing one-sided stops. This separation must take place at a clearly defined point so that the kinematic does not change during movements. However, since there are two different pivot points, a compression movement in which one of the rods is loaded leads to a displacement

of the other rod. If the force direction is changed, the rod must first move back to its stop, resulting in kinematic changes, power-buildup delays, and shocks on reaching the stop. A sufficiently hard damper would mitigate these shocks. However, this would result in a continuous increase in the rod deflection. At one point, a stop must be provided to limit the maximum wheel deflection due to the rod displacements. This would result in a blockage of the suspension. Hence, this solution is not feasible.

Another approach is the kinematic adjustment of the support angle over the suspension travel. This implies non-ideal force support because only in that case suspension travel would occur. Therefore, this approach is only applicable to mitigate the influences of horizontal accelerations but not to completely avoid pitch and roll motions. Nevertheless, the kinematic influence should be considered and adjusted to improve the behavior.

Summarizing, no MC concept is able to achieve ideal force support for all relevant accelerations and directions. The next step is the closer investigation and determination of the potential of the different approaches in order to select the most promising. The following MC approaches are investigated:

- Friction-optimized motion control (FMC)
- Direction-dependent motion control (DMC)
- Equal-distribution motion control with switching to FMC at $\mu_{\mathrm{lim}} = 0.7$ (EFMC)
- Equal-distribution motion control with switching to DMC at $\mu_{\mathrm{lim}} = 0.7$ (EDMC)

As outlined above, the optimum support angles are not realizable for the DMC and the FMC. Thus, the actual support angle design with the best behavior is unknown yet. Additionally, the natural frequency of the suspension is variable and affects the support angle design. Hence, a model is required to be able to identify the best design for each MC concept. Afterward, a comparison of the different approaches is possible. The model applied for this investigation is described in the following.

8.5.2.2 Model for the Analysis of the Motion Control Approaches

For this first investigation of the impact of the non-ideal force support, a stationary analytic model is applied. It has already been outlined that the kinematic change of the support angles has an influence on the stationary behavior. The effects of the non-ideal force support resulting from the acceleration magnitude and direction asymmetry can be partly compensated by adjusting the support angles over the suspension stroke w_{S}, which is defined as follows:

$$w_{\mathrm{S},i} = {}_{\mathrm{H}}z_{\mathrm{W},i} - {}_{\mathrm{H}}z_{\mathrm{B,W},i} \cong -{}_{\mathrm{H}}z_{\mathrm{B,W},i} \tag{8.63}$$

With the vertical body motion at the respective wheels ${}_{\mathrm{H}}z_{\mathrm{B,W},i}$, which is calculated according to the kinematic equations (4.11) to (4.13). The tire elasticity is neglected, so that the wheel motion is set to zero because it has no influence on the support forces. The sign is chosen so that a positive suspension stroke results in a spring compression and therefore a positive

spring force on the body. The effect of changing support angles is implemented with the following linear description:

$$\varepsilon_i(\xi_{\mathrm{res}}) = \varepsilon_{\mathrm{stat},i}(\xi_{\mathrm{res}}) + \delta\varepsilon_{\mathrm{kin},i}(\xi_{\mathrm{res}}) w_{\mathrm{S},i} \tag{8.64}$$

With the direction-dependent gradient of the support angle $\delta\varepsilon_{\mathrm{kin},i}(\xi_{\mathrm{res}})$. Assuming a plane motion of the wheel, the following description of the acceleration direction dependency is formulated:

$$\delta\varepsilon_{\mathrm{kin,f}}(\xi_{\mathrm{res}}) = |\delta\varepsilon_{\mathrm{kin}}| \cos(\xi_{\mathrm{res}}) \tag{8.65}$$

Equation (8.22) together with the description of the vertical support force in equation (8.39) yields the following description for the stationary vertical suspension force:

$${}_{\mathrm{H}}\Delta F_{z,\mathrm{S,sum},i}(w_{\mathrm{S},i}) = F_{\mathrm{T,res},i} \tan(\varepsilon_{\mathrm{stat}} + \delta\varepsilon_{\mathrm{kin}} w_{\mathrm{S},i}) + c_{\mathrm{S}} w_{\mathrm{S},i} \tag{8.66}$$

The gradient $\delta\varepsilon_{\mathrm{kin},i}$ is typically negative for an acceleration direction of 180° because the instantaneous center of rotation is lifted together with the sprung mass. This results in an increase of the support force if the body moves upwards, which leads to a further lifting of the body, the so-called jacking effect. If the spring stiffness is too low to compensate this increasing support force, the system becomes unstable and the wheel is pushed under the simulator. A stable system requires a positive gradient of the overall suspension force over the suspension stroke. Based on this criterion, unstable suspension configurations (e.g. too high kinematic support angle change, too low spring stiffness) are identified and excluded.

The overall load transfers ${}_{\mathrm{H}}\Delta F_{z,\mathrm{S,sum,req},i}$, which have to be supported by the suspension, are calculated with the equations (8.31) to (8.33). These have to be equal to the sum of the suspension forces according to equation (8.66). The tire forces $F_{\mathrm{T,res},i}$ are determined with equation (8.44) for the FMC, (8.56) for the DMC and (8.51) for the EMC, which is switched to the FMC respectively DMC if criterion (8.55) is fulfilled.

In order to determine the suspension strokes resulting from these force relations, the following equation is solved numerically:

$$\frac{F_{\mathrm{T,res},i} \tan(\varepsilon_{\mathrm{stat}} + \delta\varepsilon_{\mathrm{kin}} w_{\mathrm{S},i}) - {}_{\mathrm{H}}\Delta F_{z,\mathrm{S,sum,req},i}}{c_{\mathrm{S}}} + w_{\mathrm{S},i} = 0 \tag{8.67}$$

The motions of the WMDS, which are generated by these suspension strokes, are then calculated for different acceleration magnitudes and directions with the following kinematic equations, which result from a rearrangement of the equations (4.11) to (4.13):

$${}_{\mathrm{H}}\varphi_{\mathrm{B}}(a_{\mathrm{H,res}}, \xi_{\mathrm{res}}) = \frac{w_{\mathrm{S,rr}} - w_{\mathrm{S,rl}}}{\ell_{\mathrm{t}}} \tag{8.68}$$

$${}_{\mathrm{H}}\vartheta_{\mathrm{B}}(a_{\mathrm{H,res}}, \xi_{\mathrm{res}}) = \frac{-w_{\mathrm{S,rl}} - w_{\mathrm{S,rr}} + 2w_{\mathrm{S,f}}}{\sqrt{3}\ell_{\mathrm{t}}} \tag{8.69}$$

$${}_{\mathrm{H}}z_{\mathrm{B,CG}}(a_{\mathrm{H,res}}, \xi_{\mathrm{res}}) = -w_{\mathrm{S,f}} + {}_{\mathrm{H}}\vartheta_{\mathrm{B}} \frac{1}{\sqrt{3}} \ell_{\mathrm{t}} \tag{8.70}$$

The lift of the center of gravity (CG) ${}_{\mathrm{H}}z_{\mathrm{B,CG}}$ results in another self-reinforcing effect. A higher CG results in increased load transfers, so that the conducted calculations of the suspension forces would change. This problem is solved by an iterative approach. At the end of each iteration of the described calculations, the height of the CG is adjusted by the lift from equation (8.70) and the suspension forces are calculated with this corrected CG. Another iteration is started and the calculations are conducted for the new CG height until the error between corrected and original suspension force is below 10 N.

Based on the derived model, a design of the support angles for different MC approaches is conducted in the next step.

8.5.2.3 Design of Support Angles for the MC Approaches

The MC approaches are different concerning the free parameters of the support angle development. The static design of the EMC approaches is already given by the optimum support angles from equations (8.52) to (8.54). The advantage of ideal force support up to an acceleration of 4.5 m/s², which is the most relevant range occurring during an urban driving scenario (cf. Figure 3-5), is considered very valuable. The potential reduction of motions at higher accelerations is rated as less important because of the low occurrence and the high reference stimulus, which reduces the sensitivity to disturbances according to Weber's Law from section 2.4.4. Hence, only the kinematic slope of the support angle is designed for this MC in order to compensate the motions at higher accelerations.

The DMC and the FMC, on the other hand, have different optimum static support angles depending on the sign of the acceleration. Thus, it is necessary to find a static support angle design that provides the best compromise between the acceleration directions. Therefore, both parameters, the static and the kinematic support angle, have to be designed for these MC concepts.

Additionally, the design of both parameters is dependent on the natural frequency of the suspension, which is not finally determined yet. A low natural frequency requires less kinematic change of the support angle because of the required positive gradient of the overall suspension force from equation (8.66) over the stroke in order to ensure stability.

In order to identify the most suitable design configurations, acceleration magnitudes between zero and 8 m/s² and directions between 0° and 350° are simulated with the model from section 8.5.2.2 for the four MC approaches. The support angle design and the natural frequency are varied. The parameter **static support angle** for the FMC and the DMC is the amplitude of the static support angle course over the acceleration direction, e.g. the value at an acceleration of 180° at the front wheel. The desired symmetric directional behavior of the support angle is formulated according to equation (8.52) as follows:

$$\varepsilon_{\mathrm{stat,f}}(\xi_{\mathrm{res}}) = |\varepsilon_{\mathrm{stat}}| \frac{\operatorname{atan}(\cos \xi_{\mathrm{res}})}{\operatorname{atan}(1)} \tag{8.71}$$

The scaling with $\mathrm{atan}(1)$ is required to generate an amplitude of $|\varepsilon_{\mathrm{stat}}|$ at an acceleration direction of 180°. For the rear wheels, the same description is applied with a shift of 120°.

The considered output parameter for the evaluation of the different design variations is the maximum suspension stroke of all three wheels within all acceleration magnitudes and directions. For each natural frequency, the support angle design that offers the minimum suspension stroke is selected. However, for the DMC and the FMC, different combinations of the static and kinematic support angle yield similar suspension strokes. Therefore, designs that are within a suspension stroke of 1 mm around the optimum configuration are also considered because it increases the freedom concerning the design of the practical implementation. The resulting configurations of the static support angle $|\varepsilon_{\mathrm{stat}}|$ and the kinematic support angle slope $|\delta\varepsilon_{\mathrm{kin}}|$ are depicted for the FMC in dependency of the natural frequency in Figure 8-20.

It is recognizable that the flexibility concerning the combination of static and dynamic support angle increases at higher natural frequencies. At low natural frequencies, only a few suitable configurations are available because of the limited range of stable kinematic support angles.

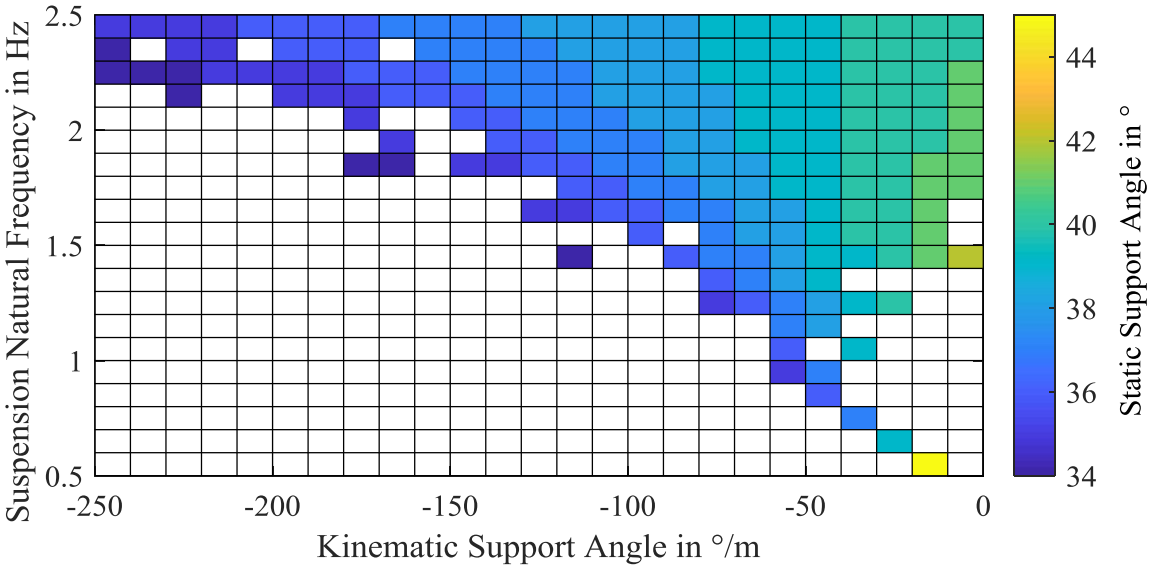

Figure 8-20: Suitable support angle configurations for the FMC depending on the natural frequency of the suspension determined with the model from 8.5.2.2 by minimizing the suspension stroke over different acceleration magnitudes between 0 and 8 m/s² and directions between 0° and 360°.

The comparison to the optimum support angles for the FMC in Figure 8-18 shows that the desired symmetric static support angle is between the optimum support angle for positive (60°) and negative (22°) acceleration directions at a magnitude of 8 m/s² and, hence, is a compromise between them. The reason for this behavior is that an extreme design that only focusses on positive acceleration directions would strongly deteriorate the behavior at negative acceleration directions. For example, for ideal force support at the front wheel for an acceleration direction of 0°, a support angle of 60° would be required because of the low tire force that is assigned to the unloaded wheel by the FMC. Due to the symmetry of the support

angles, the 60° would also act at an acceleration direction of 180°. In that case, however, the tire force would be much higher because the front wheel has an increased wheel load. Therefore, according to equation (8.39), the support force would be much higher than required from the pitch moments and a heave of the body would occur. Thus, even though for an acceleration direction of 0° ideal force support is achieved at the front wheel, the behavior in the opposite direction is impeded and the required suspension strokes are higher. Even worse is that the support angles at the rear wheels are shifted. Therefore, these wheels are in the non-ideal range of the acceleration direction. Even if ideal force support at the front wheel is achieved at 0° acceleration direction, this does not apply for the rear wheels. Hence, a compromise for the support angle design in the middle of both acceleration directions is preferable.

The suitable support angle configurations for the DMC are determined in the same way. The results are given in the appendix in Figure C.1 - 2. The methodology for the determination of the desired support angle configuration of the EMC approaches is the same. However, only the kinematic support angle is varied. The results for this variation are shown in Figure 8-21. The desired kinematic support angle slopes are smaller at low natural frequencies.

Based on the determined support angle designs, the evaluation and selection of the different MC approaches is conducted in the next step. For the FMC and the DMC, different possible design combinations within a suspension stroke range of 1 mm were derived. However, for the evaluation, the configuration with the lowest suspension stroke is applied.

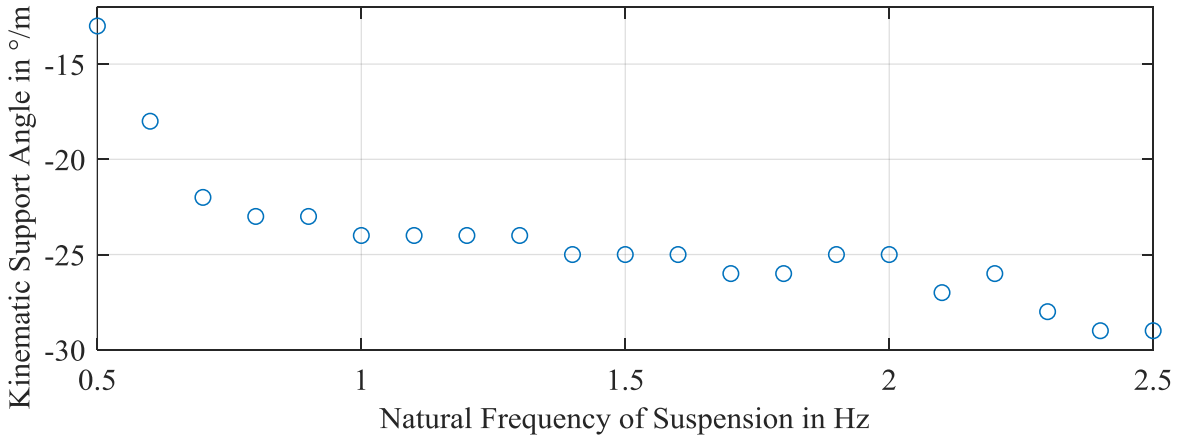

Figure 8-21: Desired kinematic support angle configurations for the EFMC depending on the natural frequency determined with the model from 8.5.2.2 by minimizing the suspension stroke over different acceleration magnitudes between 0 and 8 m/s² and directions between 0° and 360°.

8.5.2.4 Evaluation of MC Approaches

The developed motion control approaches and the respective support angle designs are investigated based on the model developed in section 8.5.2.2. The considered evaluation parameters, which are the relevant characteristics that should be reduced by the suspension, are as follows:

- Suspension Stroke
- Pitch-Angle
- Roll-Angle
- Lift of CG

The minimum and maximum occurring values for these characteristics within all acceleration magnitudes and directions are shown dependent on the natural frequency in Figure 8-22 for the different MC approaches and for the case without support angles.

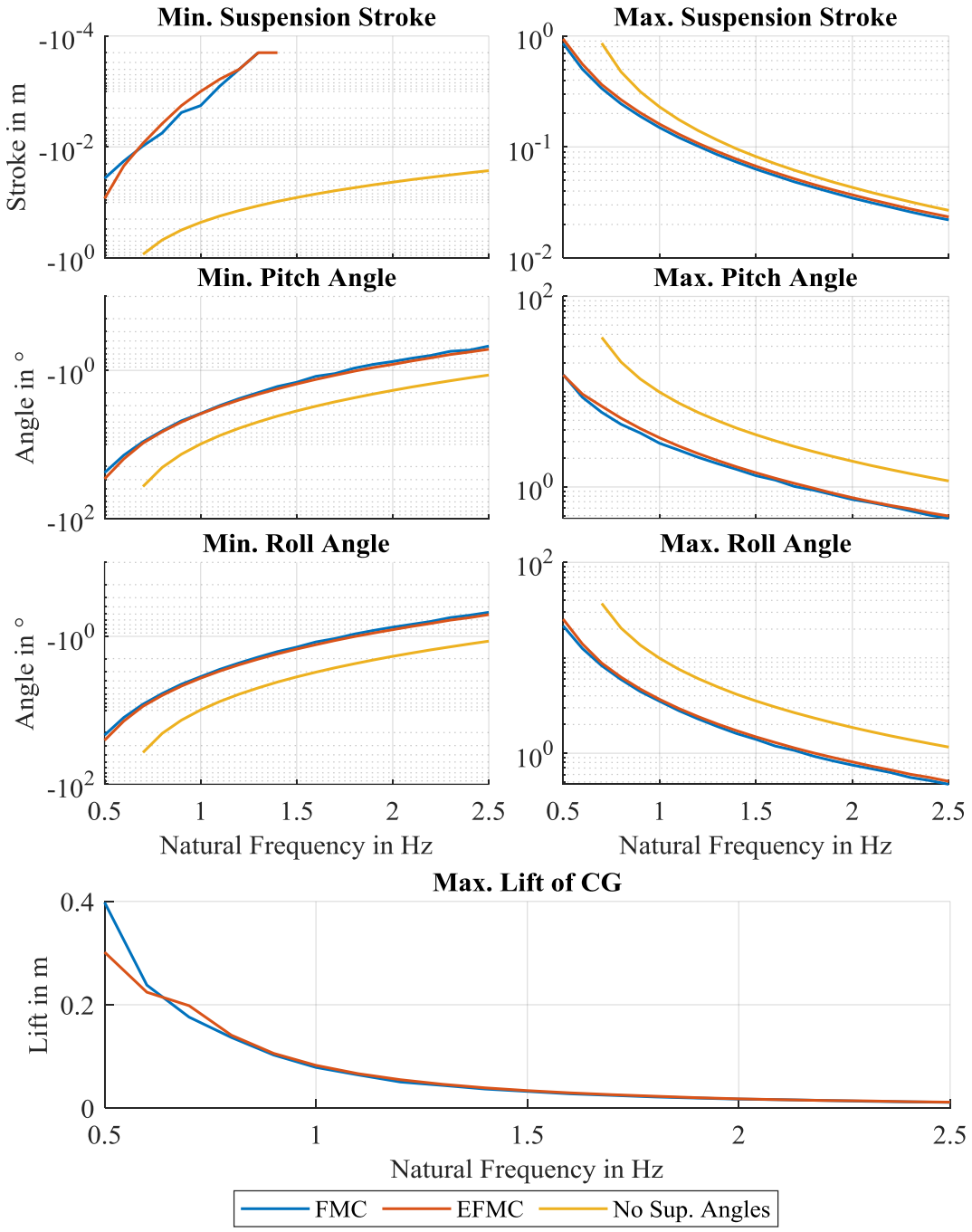

Figure 8-22: Comparison of MC approaches concerning the maximum values of evaluation parameters during straight acceleration maneuver with acceleration magnitudes between 1 and 8 m/s² and directions between 0° and 350° determined with model from 8.5.2.2.

The DMC/EDMC is not shown separately because the support angles and the tire force division are the same as for the FMC/EFMC at the maximum acceleration of 8 m/s². Therefore, both have the same results concerning the maximum value considered here. Only the behavior for lower accelerations is different.

Only a slight difference exists between the MC approaches. The FMC has a lower maximum suspension stroke, pitch and roll angle than the EFMC. The reason for this is that the FMC support angles are optimized to the minimum overall suspension stroke, whereas the EMC approaches are adjusted to the optimum support angles of the equal distribution to enable ideal force support at low accelerations. This is associated with a slight deterioration of the behavior at higher accelerations.

Compared to the behavior of a suspension without support angles, a clear improvement is recognizable with both MC approaches. At a natural frequency of 1 Hz, the maximum suspension stroke with the FMC is 80 mm (-34 %) less than without support angles. This results in a reduction of the maximum pitch angles by 7° (-71 %) and the roll angles by 6.4° (-65 %). The biggest advantage of the support angles is the minimum suspension stroke. At a natural frequency of 1 Hz, only 2 mm of negative suspension stroke, which means a compression of the suspension spring, are required, which is negligible compared to the 229 mm without support angles.

This has positive effects on the suspension design and the implementation into the overall WMDS concept. The space that has to be provided between the body and tire-sprung mass is low because both parts almost do not move closer to each other despite horizontal accelerations. Therefore, the required raising of the body and, hence, of the center of gravity is reduced. Additionally, a low ground clearance as in the current concept can be maintained. This enables the application of the current safety concept with external braking pods without considerably increasing the initiation time. Though the results from Figure 8-22 indicate an advantage of the FMC approach, an extended investigation is needed that differentiates between the acting acceleration magnitudes rather than just considering the maximum values. The results of this analysis are shown in Figure 8-23.

The advantage of the EMC approaches is obvious. Up to an acceleration of 4.5 m/s², which is the switching point from EMC to FMC (calculated with equation (8.55) for $\mu_{\mathrm{lim}} = 0.7$), no suspension stroke or motions of the body occur. This is a major advantage because most of the accelerations acting during an urban driving scenario are below that value according to Figure 3-5. Additionally, the motions of the body are less disturbing at higher reference stimuli. The increase of the maximum suspension stroke at an acceleration of 8 m/s² compared to the FMC and DMC is marginal. The comparison between EDMC and EFMC shows that the EFMC is advantageous in the range from 4 to 8 m/s². Thus, the EFMC is selected as the preferable MC approach.

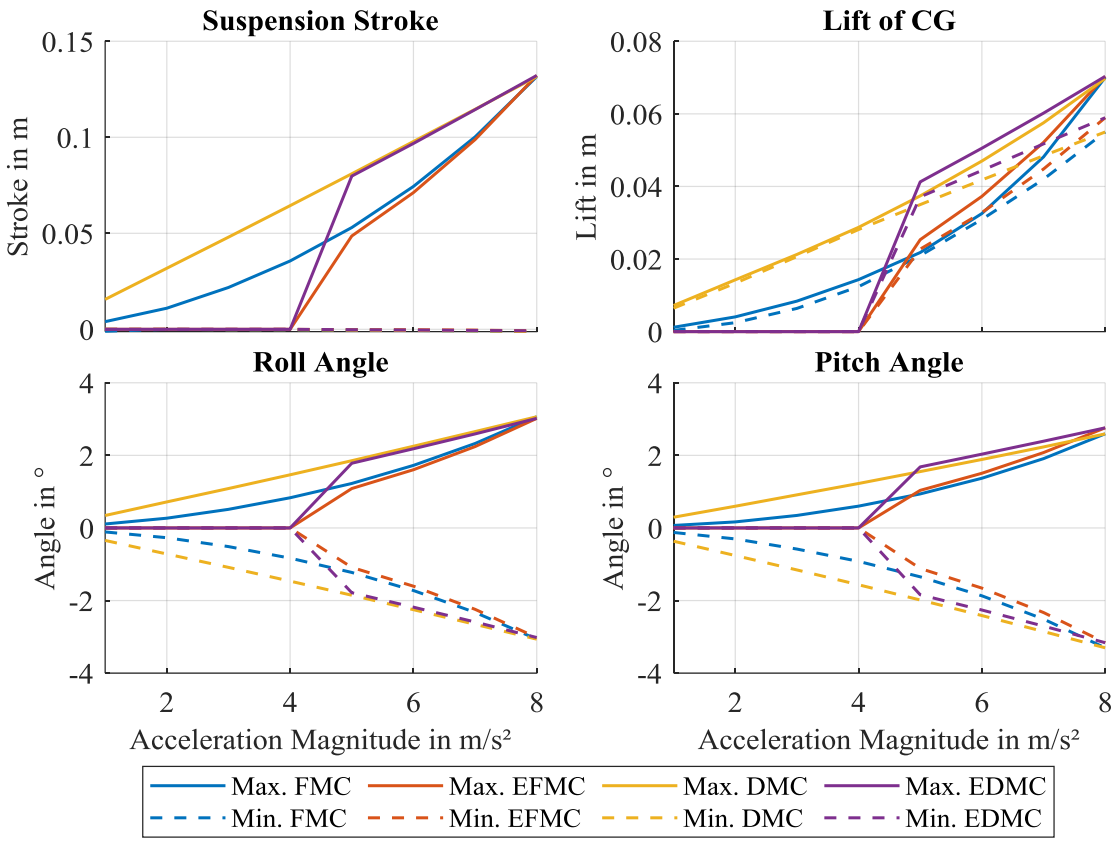

Figure 8-23: Comparison of MC approaches concerning the maximum and minimum values of the evaluation parameters during straight acceleration maneuver with acceleration directions between 0° and 350° determined with the model from section 8.5.2.2 for a natural frequency of 1 Hz.

8.5.3 Target Values for Kinematic Inclination of the Wheel

In order to determine the required inclination of the wheel relative to the body over suspension stroke, it has to be analyzed, which inclinations of the body correspond to which suspension stroke. This correlation is not constant but dependent on the acceleration direction and magnitude. For example, a suspension stroke of zero at the front wheel could occur at an acceleration direction of 90° due to the missing wheel load transfer, whereas at the other wheels the non-ideal force support results in suspension strokes and, hence, inclinations of the body. At an acceleration magnitude of zero, the suspension stroke at the front wheel would also be zero but no inclination of the body would appear. Therefore, a range of the desired target inclination has to be defined. For this purpose, the model from section 8.5.2.2 is applied. Acceleration magnitudes between 0 and 8 m/s² and directions between 0° and 350° are simulated for the optimum configuration of the EFMC and the resulting combinations of body inclination and suspension stroke are evaluated. The range of the angles occurring at different suspension strokes are indicated by the hull curves in Figure 8-24 exemplarily for a natural frequency of 1 Hz.

It is recognizable that at the highest suspension stroke of 0.13 m a positive wheel inclination around the pitch axis of 2.6° to 3.1° (for the front wheel, axis is shifted by 120° respectively

240° for the other wheels) relative to the body would reduce the camber angle relative to the ground. A negative inclination at zero suspension stroke would also reduce the camber in some operation states. However, this static camber angle is undesired because it would disturb the drive at zero or low accelerations. Therefore, an increase of the inclination from 0° at the minimum suspension stroke up to 3° at the maximum is demanded for the pitch axis.

For the roll axis, a symmetry around the x-axis is recognizable. A wheel inclination could only compensate the roll angle in one direction, which would impede the behavior in the other. Therefore, a persistent target inclination of 0° is demanded from minimum to maximum suspension stroke around the roll axis.

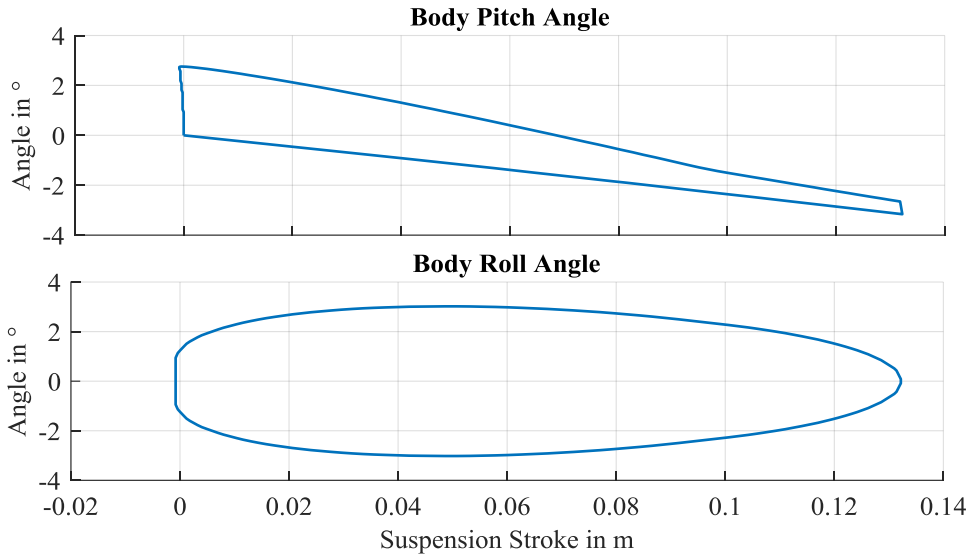

Figure 8-24: Range of occurring body angles depending on the suspension stroke during straight acceleration maneuver with acceleration directions between 0° and 350° determined with the model from section 8.5.2.2 for a natural frequency of 1 Hz.

8.5.4 Summary

The analysis of the demands on the suspension due to the horizontal dynamics of the simulator results in the following findings:

- The kinematic parameters toe angle, camber angle, caster angle, caster trail, kingpin inclination and scrub radius should be kept to zero statically and dynamically.
- The relative kinematic inclination between wheel and body can be applied to reduce the ground-related camber resulting from the inclination of the body.
- The implementation of support angles results in a high reduction of angular motions and suspension stroke compared to a system with no support angles. This enables lower natural frequencies of the suspension and therefore an improved vibration isolation behavior.
- The compression of the suspension is almost completely avoided if support angles are applied. Hence, almost no increase of the center of gravity or the ground clearance is required to implement the suspension.

- An MC that distributes the tire forces equally up to an acceleration of 4.5 m/s² and then switches to a friction-optimized motion control (EFMC) is preferable because it completely avoids suspension motions up to the switchover.
- The application of support angles requires a non-steered kinematic with isolated wheels so that only the DoF positions 3 to 5 are suitable for this configuration. A steered kinematic should have a support angle of 0°.
- The optimum support angles for the EFMC are shown in Figure 8-18 as yellow curve.
- The desired slope of the kinematic change of the support angles over suspension stroke are shown in dependency of the natural frequency in Figure 8-21.
- The required suspension strokes due to horizontal dynamics are shown in Figure 8-22 depending on the natural frequency and for different MC support angle combinations (including no support angles).

8.6 Practical Feasibility and Design of Suspension

Based on the derived demands on the suspension due to horizontal dynamics and vibration isolation, the next step is the design of the suspension and the validation of its practical feasibility. The limiting factor concerning the practical feasibility is the suspension stroke, which generates a lower limit for the natural frequency that has to be as small as possible for optimum vibration isolation according to Figure 8-13. The first step is to analyze which combination of DoF-position and natural frequency is practically feasible and results in the best vibration isolation behavior. For example, DoF position 1 at the wheel hub offers the highest potential concerning vibration isolation. However, if DoF position 3 enables a lower natural frequency due to the possibility of the implementation of support angles, this could result in better vibration isolation.

The problem is approached by an iterative procedure. Because of the highest vibration isolation potential, the DoF-position 1 is initially analyzed concerning its attainable natural frequency. This is done by identifying limiting components at the DoF-position and determining the suspension stroke achievable with them. Other DoF-positions that enable a lower natural frequency and, therefore, have a higher vibration isolation potential are analyzed subsequently until the combination with the best vibration isolation is found.

8.6.1 Analysis of DoF-Position 1 (Wheel Hub)

The limiting component of this DoF-position is the torque transmission between drive motor and wheel, which has to enable a vertical motion of the wheel. This requires a minimum axial distance between motor and wheel for e.g. joint shafts with limited angular offsets or couplings. The distance between wheel and motor in the current configuration is short in order to reduce the moments of inertia for the steering. Although an increase of this distance

is possible, a maximum of 237 mm between transmission-output and wheel cannot be exceeded because of the danger of a collision with other parts during a steering motion.

Based on a research for joint shafts and couplings and on contacts to several suppliers for drivetrain solutions, a parallel crank coupling is identified as a suitable solution for the limited axial installation space.[113] The concept is shown in the appendix in Figure C.2 - 1. This coupling enables an overall vertical motion of 160 mm. A comparison to the required suspension strokes from Figure 8-22 shows that a minimum natural frequency of 1.6 Hz is required to comply with this available range of motion.

Additionally, this DoF has following disadvantages:

- The steering moment of inertia increases due to the higher distance between wheel and motor.
- The compression motion of the suspension requires a higher ground clearance and therefore, a greater distance of the safety system to the ground. This results in increased initiation times of the safety system.
- According to Figure 8-22, the angular motions at that natural frequency are 3 times higher than at DoF-position 3, which makes use of support angles.

The position of the DoF at the steering bearing (2 and 3) achieves better vibration isolation at a natural frequency of 1.4 Hz. Thus, the next step is to analyze if these natural frequencies are practically feasible at these DoFs. The steered DoF-position 2 is not expected to reduce the attainable natural frequency because no support angles can be implemented at that point. Therefore, no advantage results from position 2 and only position 3 is further investigated.

8.6.2 Analysis of DoF-Position 3 (Above Steering Bearing)

As for DoF-position 1, the torque transmission between the sprung and unsprung part of the WMDS is a limiting factor for the feasible suspension stroke. For this DoF, a transmission of the steering torque is required. However, contrary to the previous DoF, the suspension moves axially to the direction of the torque. This enables the application of a steering crank, which theoretically allows an unlimited suspension stroke as long as the levers of the crank are long enough. Of course, this is practically limited by the radial installation space, which is approximately half of the required suspension stroke. Nevertheless, even the required suspension stroke of 0.4 m at a natural frequency of 0.6 Hz could theoretically be provided. Hence, other limiting factors have to be analyzed to identify the lower frequency boundary:

- Kinematic nonlinearities due to suspension motion, which impede the support of horizontal forces (e.g. the wheel folding away).

[113] Cf. Haberhauer, H.: Kupplungen und Bremsen (2014), pp. 117–119.

- The practically feasible tradeoff between elasticity and load capacity of available springs.

The first aspect requires the development of a kinematic that fulfills the demands determined in subchapter 8.5 in order to identify the nonlinearity-limit. Based on this kinematic, the development of a spring-system is possible in order to analyze the second limitation.

8.6.2.1 Design and Practical Limitations of Kinematic

The target kinematic parameters are summarized in section 8.5.3. The desired support angles from equations (8.52) to (8.54) require a horizontal velocity of the respective tire contact points in the direction of the connecting line between the center of gravity and the wheels. Otherwise, a non-zero support angle would arise at acceleration directions of 90° and 270° at the front wheel (or shifted by 120° for the rear left and 240° for the rear right wheel) and therefore impede ideal force support. Additionally, a steering axis inclination of zero is aspired statically and dynamically, so that no rotation of the wheel around the connection line between the center of gravity and the wheel should occur. Hence, the suspension kinematic has to generate a motion of the tire-sprung mass in the plane spanned by the connection line from the center of gravity to the respective wheel and the vertical axis of the leveled vehicle frame, as depicted in Figure 8-25. In the following, this plane is referred to as suspension plane, which is shifted around the vertical axis by 120° for each wheel. In order to enable a motion that lies in this suspension plane, the rotation axes of the implemented joints have to be normal to it.

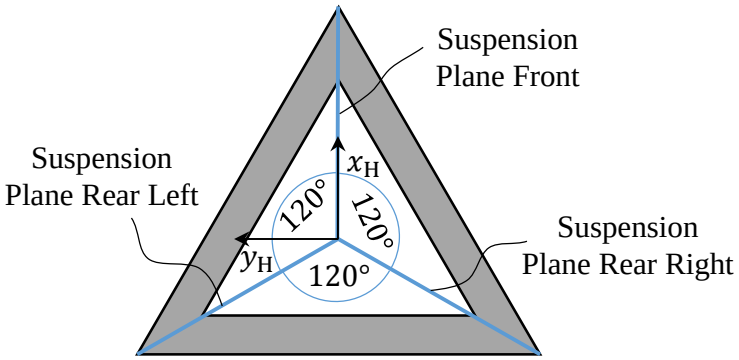

Figure 8-25: Suspension planes.

The determination of the amount and the position of the joints is based on the target values of the kinematic parameters. The considered DoF-position enables a reduction of the originally defined kinematic parameters. The inclination of the steering axis in the suspension plane is equal to the overall inclination of the tire-sprung mass for the considered non-steered DoF. Therefore, the three parameters kingpin inclination, caster angle and camber angle are combined to the inclination of the tire-sprung mass in the suspension plane.

Concerning the target value for the inclination of the tire-sprung mass relative to the ground, it has already been illustrated that 0° is aspired. However, due to the requirements on the

other kinematic parameters, deviations probably have to be accepted. Therefore, an acceptable range is defined. The most critical aspect concerning the inclination is the ground clearance of the parts of the tire-sprung mass. Especially the drive motor, which has a high lateral distance from the tire contact point and is already close to the ground at zero inclination, has to be considered. The tire has a radius of 150 mm, which is reduced by an elastic deflection of 7 mm at the maximum wheel load (cf. Figure 4-2). The drive motor has a radius of 114 mm so that the static distance to the ground is 29 mm at the full deflection of the tire and the maximum distance to the tire-contact point amounts to 241 mm. A safety factor is introduced by assuming a factor of 2 for the elastic tire deflection. This results in a maximum acceptable inclination of the tire-sprung mass relative to the ground of 5.2°.

As described in sections 8.5.1.2 and 8.5.3, the kinematic inclination of the tire-sprung mass is defined relative to the body. The inclination relative to the ground is given by the superposition of this kinematic inclination and the angular body motions. The ranges for the latter have been determined in section 8.5.3 and have to be added to the kinematic inclination determined in this chapter.

The stability of the suspension kinematic is limited by the gradient of the support angle over suspension stroke. If the gradient changes its sign, the wheel begins to rotate in the direction of the moment induced by the horizontal tire force. At this point, a support of the horizontal tire force is impeded and the tire-sprung mass begins to fold in. Therefore, the suspension stroke at which the sign of the gradient changes should be as high as possible to achieve a low natural frequency.

Summarized, the following kinematic parameters have to be attained by the suspension:

1. Support angle: target value at acceleration directions 0° and 180°: 39.6°
2. Kinematic support angle change at a suspension stroke of 0 mm: target value between 10 and 40 °/m
3. Maximum inclination of tire-sprung mass relative to the ground: target between 0° and 5.2°
4. Suspension stroke, at which the sign of the gradient of the support angle changes: target value as high as possible to achieve a low natural frequency

The next step is the design of a suitable kinematic to attain these values. According to Ersoy, suspensions are classified by the number of their linkages.[114a] The desired motion in the suspension plane and the support angles could theoretically be attained with a one-link suspension, which connects tire-sprung mass and body with one joint. However, this concept generates high changes in the inclination of the tire-sprung mass because of the body-fixed instantaneous center of rotation (ICR).[114b] Therefore, a spherical concept with two suspension links is selected, which has a variable position of the ICR relative to the body over the suspension travel. This enables a constant horizontal motion of the tire contact point while

[114] Cf. Ersoy, M.: Achsen und Radaufhängungen (2013). a: p. 427; b: p. 442.

minimizing the rotation of the tire-sprung mass. Thus, four joints have to be defined. Each joint has two free coordinates in x- and z-direction of the respective plane that have to be determined. The y-direction does not affect the rotation behavior of the wheel in the considered plane. Hence, eight coordinate parameters have to be defined.

Although the range of investigated coordinates is reduced based on analytical considerations (e.g. parallel links cannot generate vertical support forces), a high amount of possible joint configurations to achieve the aforementioned specifications exists. To determine a suitable configuration, different practically feasible joint configurations are tested for their kinematic parameters in a computer-aided pre-investigation. From all investigated joint configurations, the one that is closest to the kinematic target values 1 to 3 and has the maximum value for parameter 4 is selected. Afterward, a fine-tuning of the selected configuration is conducted by investigating the impact of slight changes of the coordinates on the kinematic parameters and generating a tuning matrix. The final kinematic is derived by iteratively adjusting the coordinates according to the desired behavior given by the tuning matrix. Due to the spherical behavior of the suspension, a multibody model is applied for the described investigations in order to identify the influence of the changing ICR. Additionally, the component model of the suspension is the basis for the validation of the overall system.

Based on this analysis, the kinematic shown in Figure 8-26 for the initial static and the rebounded state at the critical suspension stroke is derived. Due to the high lengths of the suspension links, they are dissolved into two links symmetrical to the suspension plane in order to support the moments resulting from the tire forces. This is also advantageous in terms of installation space since the joints are directly above the triangle frame and therefore no elements to bridge the distance between frame and joint are required. The high position of the joints leads to the desired static support angles. The shorter upper link results in a low change of the inclination of the tire-sprung mass by rotating it contrary to the translational motion at high strokes. This also leads to an almost constant movement direction of the tire contact point and therefore the desired low change of the support angles.

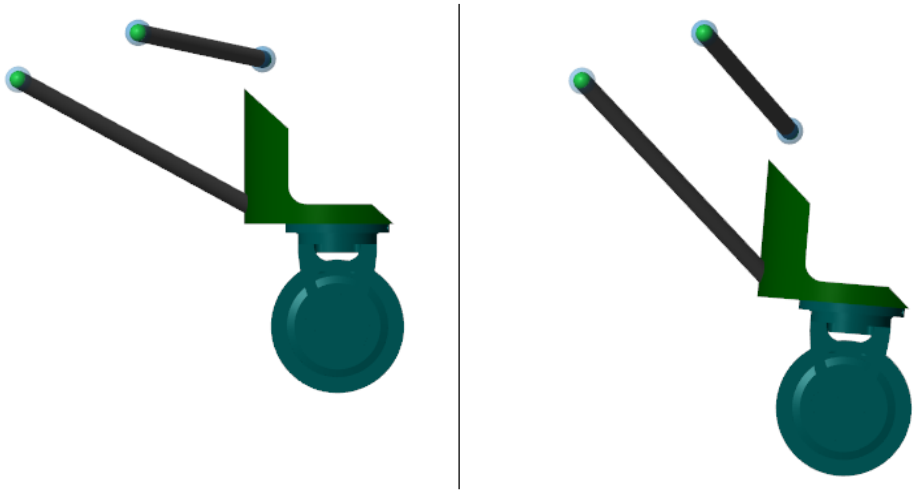

Figure 8-26: Kinematic in static equilibrium state (left) and at critical suspension stroke (right).

This behavior is also recognizable in the representation of the kinematic parameters for the front wheel in Figure 8-27. The real static support angle at an acceleration direction of 0° amounts to 38.8° compared to the optimum angle of 39.6°. The course over the acceleration direction shows a qualitative agreement, even though the support angles are slightly smaller in the practical implementation. The effects of this deviation have to be investigated in the validation.

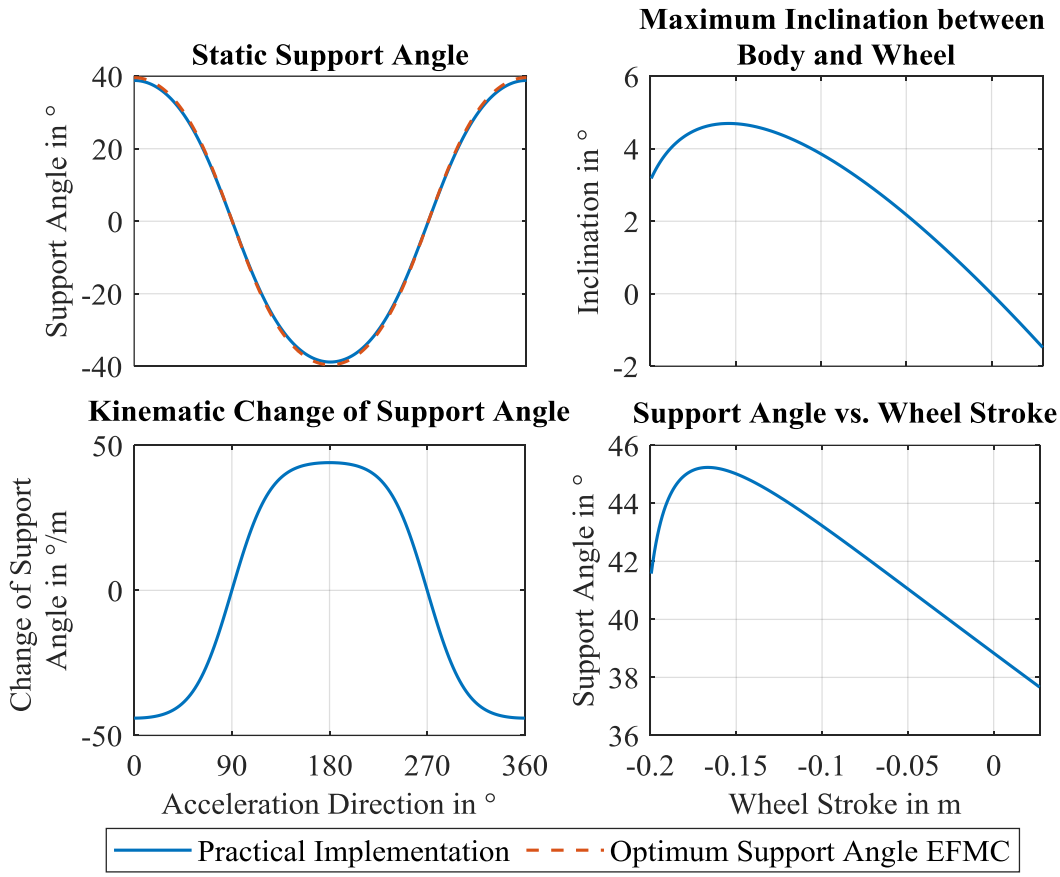

Figure 8-27: Parameters of the developed kinematic determined with multibody model.

The kinematic change of the support angle at an acceleration direction of 0° amounts to -44°, which is slightly lower than the demanded range. However, the reduction of the maximum inclination in combination with the high static support angle requires this tradeoff. The maximum inclination of the tire-sprung mass relative to the body in the suspension plane amounts to 4.7°. This maximum inclination opposes the inclination from the angular motions of the body shown in Figure 8-24 so that a reduction of the ground-related inclination of the wheel is achieved. The relative inclination at medium wheel strokes of 50 mm could also act in the same direction as that of the body depending on the direction and magnitude of the current acceleration. Nevertheless, based on the relative inclination between body and wheel and the body inclinations calculated with the model from section 8.5.2.2, an exceedance of the maximum inclination relative to the ground is not expected. This is proven during the validation. Hence, the kinematic offers the demanded static and dynamic support angles while maintaining an acceptable inclination of the tire-sprung mass.

Concerning the acceptable suspension stroke, which is limited by the sign change of the gradient of the support angles, a maximum of -166 mm is acceptable. A comparison with the required suspension strokes from Figure 8-22 shows that this corresponds to a minimum acceptable natural frequency of 1 Hz. The next step is to investigate if the determined limiting natural frequency is practically realizable with a spring-system.

8.6.2.2 Design and Practical Limitations of Spring-Damper System

The following requirements on the spring system are given by the aforementioned considerations and the system characteristics of the driving simulator:

- Static load capacity: 3400 N
- Natural frequency: 1 Hz
- Maximum Compression: 30 mm (Resulting from driving surface excitations)
- Maximum Rebound: 150 mm (Resulting from horizontal dynamics, cf. Figure 8-22)

These requirements are wheel-related, which means that the spring is mounted vertically and above the tire contact point. This is not possible because of the space conflict with the steering unit. Therefore, an additional conversion is required.

Research for industrial springs yields a suitable spring (cf. appendix, Figure D.2 - 1), which requires a conversion of 1.1 in order to achieve the given natural frequency. This conversion is realized by a lever that enables the preferable installation of the spring between the suspension links. An adjustable rotational damper is mounted at the lever's axis of rotation.

8.6.2.3 Design of Steering Crank

The steering crank has to transmit the steering torque from the body-fixed steering unit to the wheel carrier while allowing the vertical motion of the wheel as well as the rotations resulting from kinematic constraints at all steering angles between 0° and 360°. In order to enable the suspension stroke, rotational degrees of freedom at the base-points of the steering crank (at the steering unit and the wheel carrier) as well as between both cranks are required normal to the plane spanned by both crank arms. Additionally, the crank has to enable an additional angular motion in the perpendicular vertical plane to adjust the crank angle to the angle between both base points, which changes due to the wheel deflection. Therefore, cardan joints are required at the two base-points. The connection between both levers is realized by a revolute joint.

8.6.2.4 Overall Suspension Concept

The derived suspension concept for the second DoF is depicted in Figure 8-28. The considered DoF-position allows a minimum natural frequency of 1 Hz. This natural frequency improves the vibration isolation compared to the suspension at DoF-position 1. Additionally,

the vibration isolation at this natural frequency is better than that of the higher DoF-positions according to Figure 8-13, even if their natural frequency could be reduced to the stability limit. Therefore, no further potential is recognizable in the consideration of other DoF-positions, so that the concept is validated in the following.

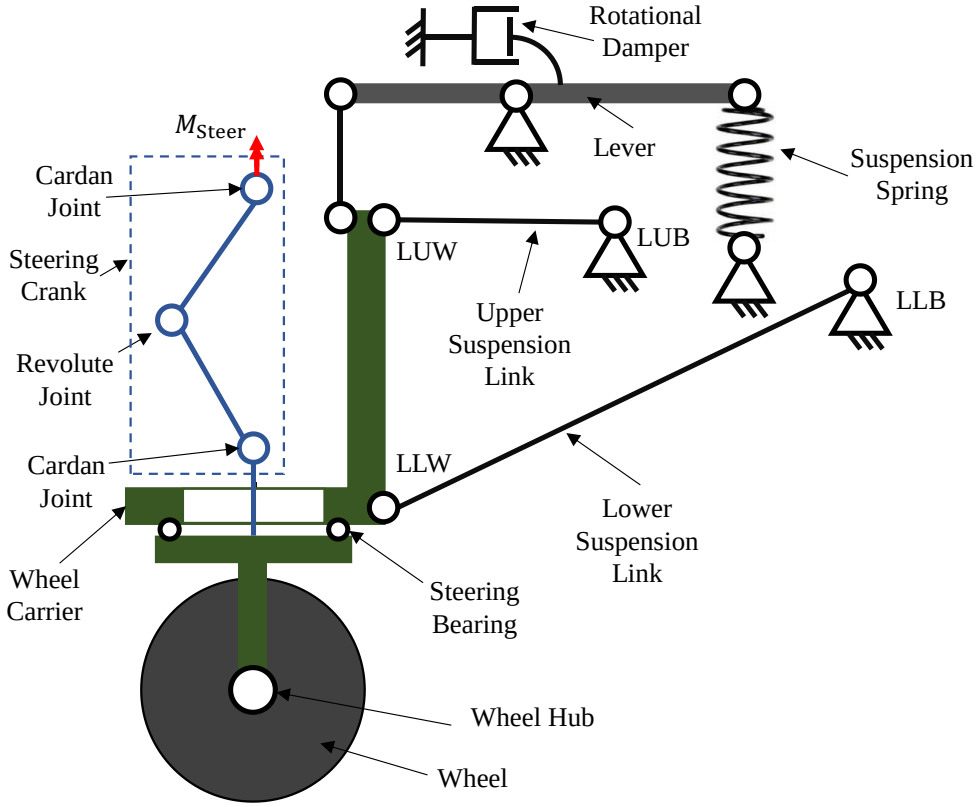

Figure 8-28: Suspension concept.

The implementation of the described suspension concept into the MORPHEUS prototype is shown in Figure 8-29.

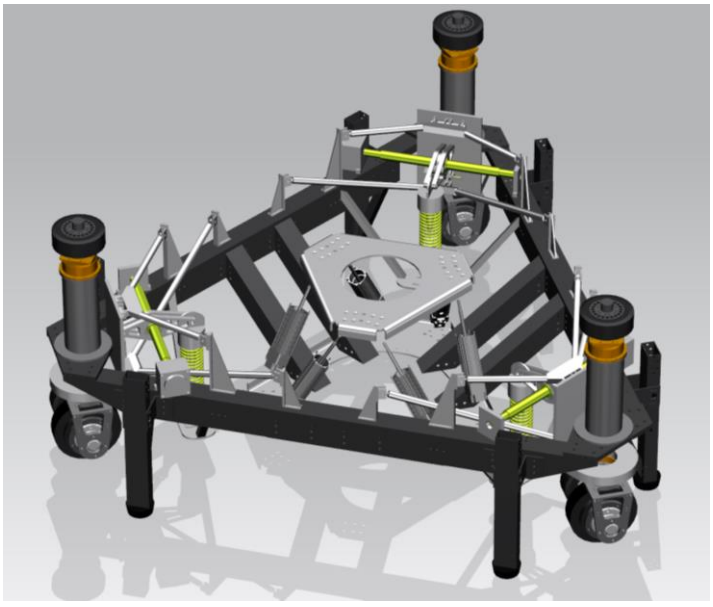

Figure 8-29: Implementation of the suspension concept in the MORPHEUS prototype.

8.7 Theoretical Validation

The following subchapter aims at validating the developed suspension concept. The first step is the development of a model for the theoretical validation. Based on this model, a comparison with the analytic model from section 8.5.2.2 is conducted. Additionally, the inclination between wheel and ground, which is not represented by the analytical model, is investigated with the validation model. Subsequently, the robustness of the suspension is investigated by analyzing the impact of varying parameters, which could impede the desired function of the force support.

8.7.1 Validation and Evaluation Model

The validation of the analytic model from section 8.5.2.2 requires the application of an alternative modeling approach. The analytic model involves the following idealizations, which have to be addressed by the new model:

- No control, drivetrain and tire dynamics
- Deviations from the optimum force distribution resulting from tire-force characteristics and wheel load oscillations
- Negligence of the tire-sprung mass in the calculation of the support forces
- No changes of the wheel distances due to suspension motions
- No nonlinear kinematic change of support angle
- No nonlinear spring force characteristic
- No changes of the support angles due to pitch and roll angles of the body (e.g. a positive pitch angle has to be added to the body-related support angle for the determination of the effective acting support angle[115])

A multibody model is selected for the purpose of the validation. Contrary to the analytic model, which calculates the resultant vertical support force based on given support angles, the multibody model considers the kinematic arrangement that generates the support forces and the motions of the wheels. The model structure is depicted in Figure 8-30.

In order to account for the influence of the non-ideal control, drivetrain and tire characteristics, the component models described in the sections 2.6.2 and 3.5 are implemented. The suspension model consists of the suspension links and joints as described in section 8.6.2.1 and the spring-damper system including the lever kinematics. The body platform is modeled as a rigid body with translational and rotational inertia properties. The hexapod multibody model from section 7.5.1 is mounted on the bottom platform. The output are the motions of the subject on the top plate, which are transformed to the position of the subject's head.

[115] Cf. Matschinsky, W.: Radführungen der Straßenfahrzeuge (2007), 150 ff.

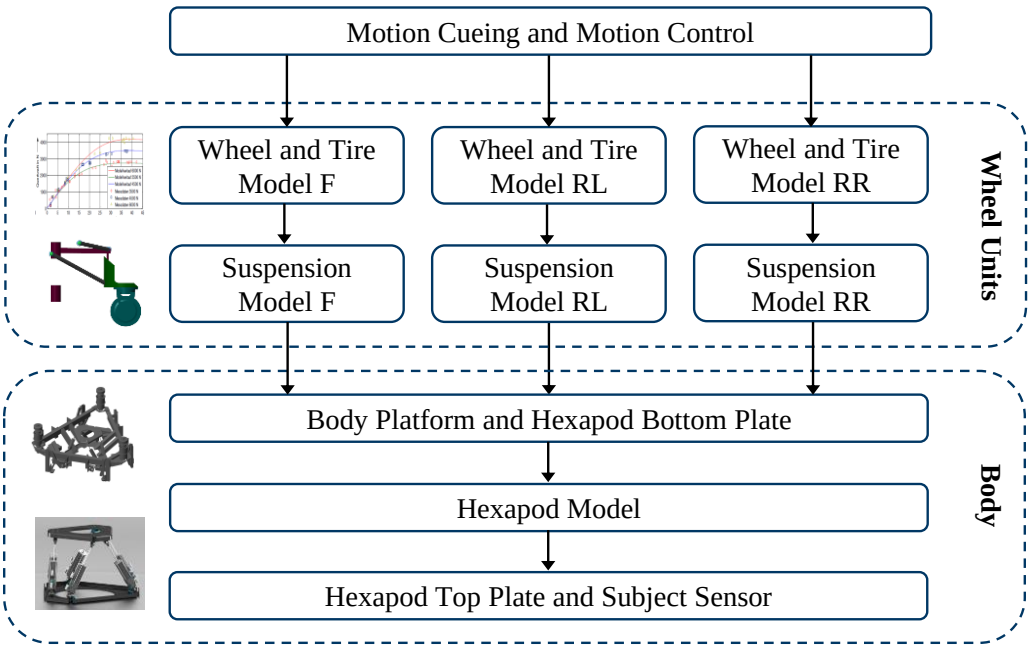

Figure 8-30: Structure of multibody model applied for validation and evaluation.

8.7.2 Comparison between Analytic and Multibody Model

In order to increase the trust in the applied models and to assess the influence of the idealizations of the analytic model, a comparison is conducted. For this purpose, different acceleration magnitudes between 1 and 8 m/s² and directions between 0° and 350° are simulated with the developed multibody model and the analytic model from section 8.5.2.2. For the comparison, the kinematic parameters of the analytic model are adapted to the values of the practical implementation of the kinematic from Figure 8-27. The results of both models concerning the evaluation parameters from section 8.5.2.1 are shown in Figure 8-31.

Especially in the range of low accelerations up to 4 m/s², a high agreement of the models is recognizable. At accelerations above the switching point of the equal distribution motion control (EMC) to the friction optimized motion control (FMC), the deviations increase. Between 5 and 7 m/s², the multibody model shows higher suspension strokes than the analytic model. This results from the nonlinearity of the spring system. The rotation of the lever reduces the transmission ratio of the spring force and therefore requires a higher suspension stroke to support the pitch and roll motions. An alternative model setup that neglects the spring system's kinematic and instead applies a spring with high length placed above the wheel to reduce the nonlinearities due to suspension motions is used to verify this. For this model, the maximum suspension stroke at an acceleration of 5 m/s² amounts to 51 mm, which corresponds with the results of the analytic model. At higher accelerations, however, other effects become dominant.

At an acceleration of 8 m/s², the maximum suspension stroke, pitch and roll angles of the multibody model are lower than those of the analytic model, whereas the lift of the CG is

higher. This results mainly from the inaccuracies of the analytic model concerning the acting support angle. The first influence is the nonlinear characteristic of the support angle over wheel stroke. According to Figure 8-27, the slope of the support angle reduces for higher wheel strokes, whereas it is assumed to be constant in the analytic model. The second effect is the influence of pitch and roll angles on the effective support angle. For example, a positive pitch angle increases the support angle at the front wheel and reduces those at the rear wheels.[115]

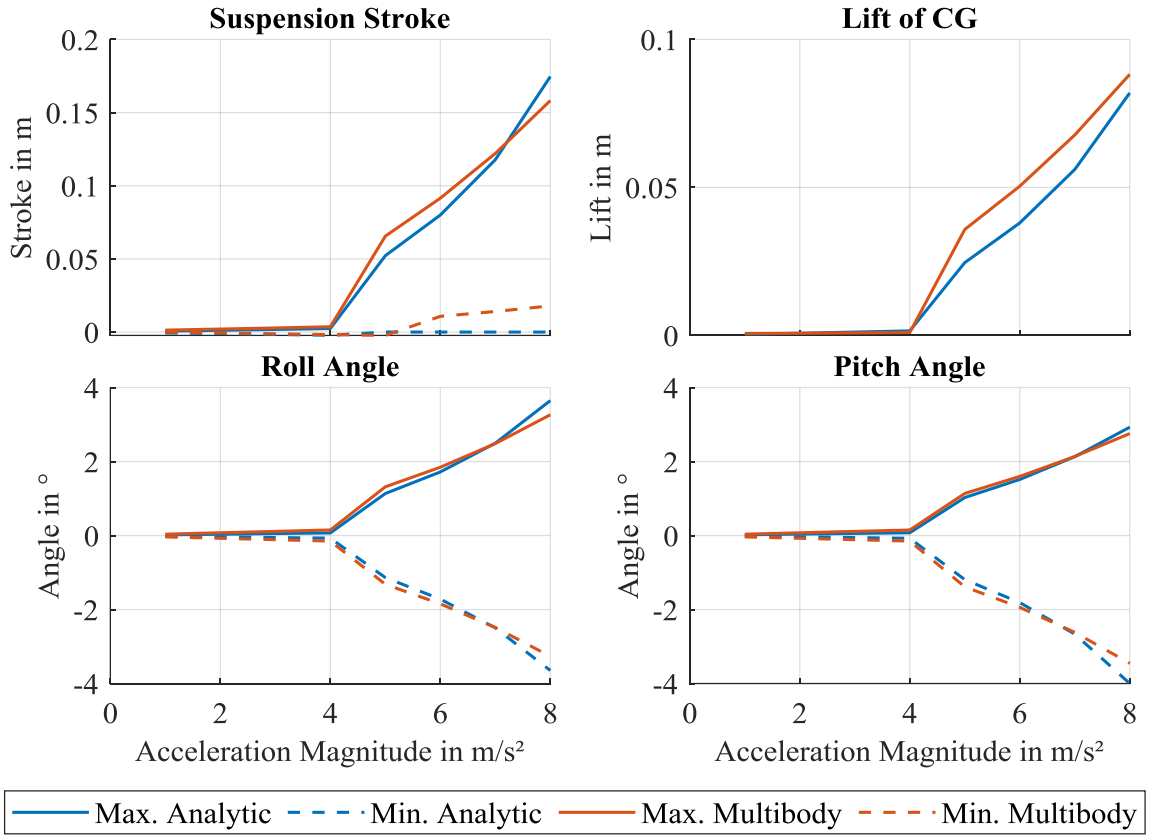

Figure 8-31: Comparison between analytic model from section 8.5.2.2 and multibody model from section 8.7.1 with the parameters of the developed suspension. Shown are the maximum and minimum values of the evaluation parameters during a straight acceleration maneuver with acceleration directions between 0° and 350° for different acceleration magnitudes.

First, an acceleration direction of 180°, which is the worst case concerning the suspension stroke for the analytic model, is considered. The support force at the front wheel is too high due to the optimization of the support angles to the equal force distribution, so that the body is lifted. The reduction of the effective support angle by the nonlinear kinematic and the pitch angle decreases this effect, resulting in a reduced suspension stroke. For an acceleration direction of 180°, the analytic model calculates an effective support angle of 46.6°, whereas the multibody model has an effective support angle of 42.0°. Based on equation (8.39), an approximated support force difference of 800 N is calculated, which corresponds to a suspension stroke of 59 mm for the natural frequency of 1 Hz. The difference of the suspension strokes of both models at the considered acceleration direction amounts to 64 mm, which verifies that the difference of the support angles is the main impact on the deviation between

both models. However, this high difference is not recognizable in the maximum suspension strokes in Figure 8-31.

The reason is the contrary effect of the pitch angle at an acceleration direction of 0°. As for the acceleration direction of 180°, a negative pitch angle is generated. In this case, however, the support force at the front wheel is not sufficient to compensate for the wheel load transfer. The reduction of the effective support angle by the pitch angle worsens this effect, resulting in an increased suspension stroke. The effective support angle of the analytic model amounts to 44.2°. The multibody model calculates an angle of 41.7°. The support force difference of 420 N results in an estimated increase of the suspension stroke of 31 mm in the multibody model. The actual difference amounts to 37 mm, which confirms the impact of this inaccuracy of the multibody model.

Summarizing, the prediction of the simple analytic model, which considers the support angle as given, confirms the function of the practical kinematic implementation in the multibody model. On the other hand, the multibody model considers important effects that are neglected by the analytic model, increasing the accuracy of and trust in the results.

8.7.3 Wheel Inclination to the Ground

The maximum occurring inclinations of the wheel relative to the ground resulting from simulations of different acceleration magnitudes from 1 to 8 m/s² and directions from 0° to 350° are shown in Figure 8-32. As for the other motions shown in Figure 8-31, almost no inclinations occur below 4.5 m/s². Maximum acceleration leads to a considerable inclination. Nevertheless, it is still below the maximum allowed value of 5.2° defined in section 8.6.2.1.

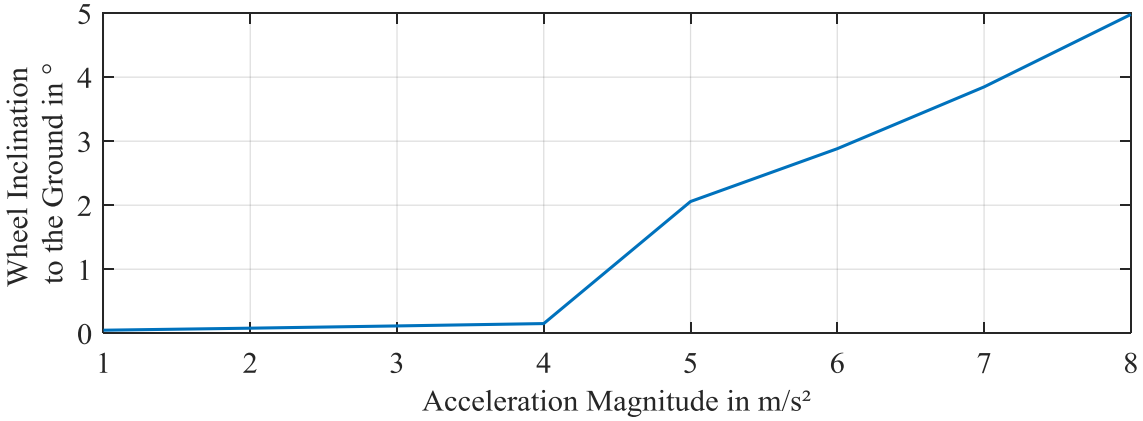

Figure 8-32: Maximum inclination of the wheel relative to the ground during straight acceleration maneuvers with acceleration directions between 0° and 360° for different acceleration magnitudes. Determined with multibody model from 8.7.1 with parameters of developed suspension.

8.7.4 Robustness of Suspension Design

The support angle design is sensitive to all effects that influence the relation between wheel load transfer and horizontal tire forces or that affect the support angle itself. The wheel load

transfer is influenced by the geometric properties of the driving simulator according to equation (8.31). Especially the vertical position of the center of gravity could impede the vertical force support because its determination is accompanied by high inaccuracies and it varies statically (e.g. due to changing subject weights or different system configurations) and dynamically (e.g. due to motions excited by the driving surface). The horizontal tire forces are affected by all inaccuracies from the control to the tire force generation. Especially the acting tire forces could highly differ from the desired optimum forces calculated by the motion control. Sources of disturbances are horizontal force oscillations due to wheel load changes and undesired lateral forces, which arise due to high steering angle gradients at the reversal points of the driving simulator motion. Summarizing, the following effects have to be investigated concerning their influence on the suspension function:

- Deviations of the height of the center of gravity
- Deviations from the desired tire forces

The first aspect is investigated in the following by synthetically inducing a center of gravity deviation into the system. The occurrence of the last aspect is highly dependent on the driven simulation scenario and its realization by the control of the simulator (e.g. high steering angle velocities are prevented by an internal logic). Therefore, the influence is investigated as part of the evaluation of a representative urban driving scenario in section 8.8.4.

8.7.4.1 Center of Gravity Deviations

To investigate the robustness of the developed suspension concerning variations of the center of gravity (CG), the multibody model from section 8.7.1 is simulated with the same input acceleration magnitudes and directions as in the previous sections. The CG height is varied. Relative to the reference height, which is the determined CG height for the current system configuration with consideration of the subject, a reduction of -40 mm is analyzed. This approximately corresponds to the difference between a test drive without a subject and with a subject with a mass of 102.5 kg (95%-percentile of males[116]). This difference is also applied in positive direction in order to investigate a worst-case scenario, which could result from two subjects driving the simulator. The results are presented in Figure 8-33.

The results show that a reduction of the CG height resulting from a lower subject mass or a drive without subject improves the behavior in every aspect. This results from the support angles of the practical implementation, which is slightly lower than the determined optimum.

For the high CG, the wheel inclination at maximum acceleration amounts to 5.2° and is therefore exactly at the limit of the acceptable ground clearance of the drive motor. The maximum suspension stroke of 168 mm is 2 mm above the determined limit from section 8.6.2.1, but still below the stability limit. However, no margins for other disturbances exist

[116] Jürgens, H. W.: Anthropometrische Maße (2004), p. 14.

anymore. Therefore, an increase of the CG above the reference height should be avoided. An increase above 40 mm is not acceptable without increasing the natural frequency.

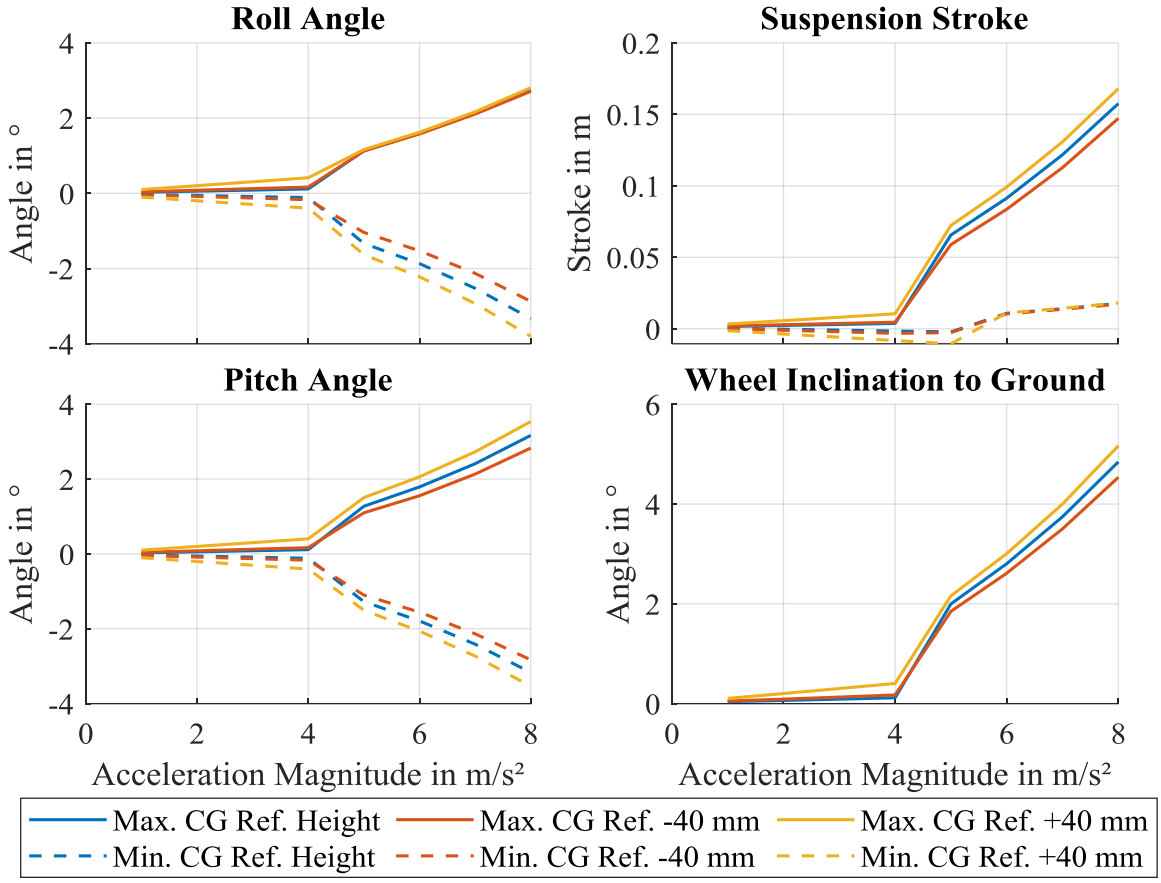

Figure 8-33: Minimum and maximum displacement characteristics during straight acceleration maneuvers with acceleration directions between 0° and 350° for different acceleration magnitudes and with varying center of gravity (CG) height. Determined with multibody model from section 8.7.1 with the parameters of the developed suspension.

8.8 Evaluation

The next step is the evaluation of the developed concept. As for the controlled tire-sprung system from chapter 7, the acceptable driving surface quality, the disturbances of horizontal accelerations due to wheel load variations, and the hexapod requirements are analyzed. Additionally, the impact of horizontal dynamics on the disturbance motions of the platform is investigated. Contrary to the tire-sprung system, these motions are now relevant due to the introduced DoF and the soft springs.

8.8.1 Acceptable Driving Surface Quality

In the following section, the acceptable driving surface quality is assessed for solid and pneumatic tires. The acceptable driving surface quality is determined with the methodology from

subchapter 3.1. A detailed description of the application of the methodology is given for the passive tire-sprung system in section 4.1.1. The acceptable driving surface is determined with the model from section 8.7.1 for pure vertical accelerations without additional disturbances due to horizontal accelerations. For reduced computation time, the suspensions are approximated by prismatic joints instead of the complete kinematic for this investigation. The results for both tire types are presented in Figure 8-34.

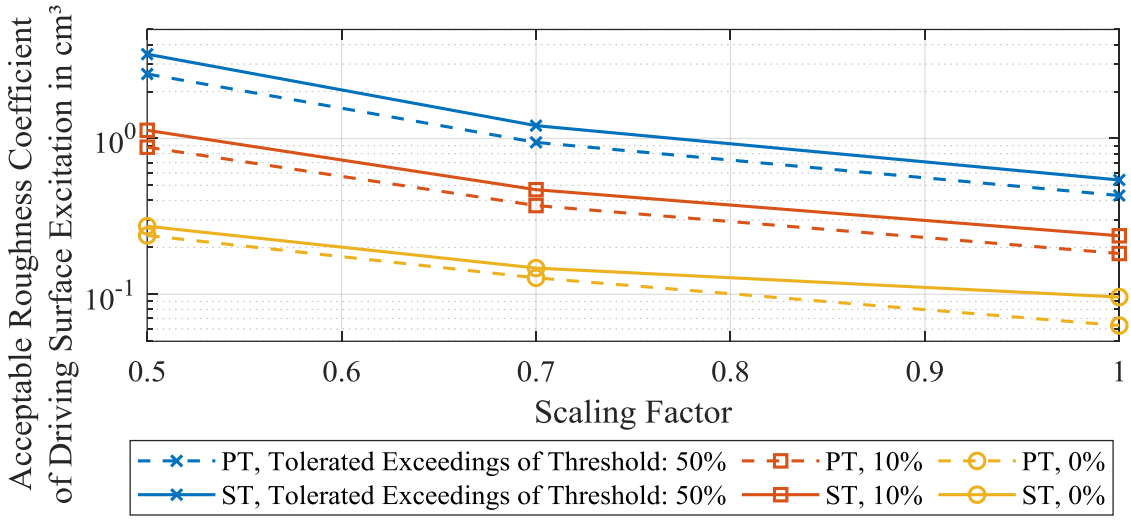

Figure 8-34: Acceptable driving surface qualities for solid (ST) and pneumatic (PT) tire with suspension system and closed-loop control for different scaling factors and allowed exceedings of threshold. The quality was determined with the model from section 8.7.1 (kinematic approximated by prismatic joints) in an urban driving scenario by iteratively reducing the surface roughness until the total vibration value (section 2.4.2) is below the perception threshold.

The range of the depth gauges is between 0.545 mm and 3.492 mm for the pneumatic tire and 0.672 mm and 4.043 mm over a length of 4 m for the solid tire according to equation (3.4). The solid tire is slightly preferable. The higher stiffness yields an increased second natural frequency, which is further away from the sensitive range of the human motion perception. It is recognizable, that with scaling factors of 0.7 and 0.5 the target value of 1 cm³ defined in section 2.5.2 is achieved, if a limited exceeding of the acceleration threshold is tolerated. If an exceeding of the acceleration threshold is not acceptable, the required driving surface quality is one order of magnitude higher than the target value. Hence, the developed system is suitable to only a limited extent for the application on asphalt or concrete driving surfaces of achievable quality.

8.8.2 Impact of Wheel Load Variations

The Weber ratios resulting from the disturbance of horizontal accelerations through wheel load variations are shown in Figure 8-35 for different reference accelerations and for solid (ST) and pneumatic tires (PT). It is recognizable that the impact of wheel load variations increased compared to the tire-sprung systems. This results from the division of wheel and body mass and the focus on the vibration isolation of the subject. This enables the application on a low driving surface quality that induces higher wheel load variations, while the subject

disturbances remain small. Especially between 1 and 4 m/s² and at accelerations above 6 m/s² the perception threshold is exceeded with the solid tire.

The reason for this varying behavior over the reference acceleration is resulting from the combination of tire force characteristic and evaluation parameter. At low accelerations, the longitudinal force deviations due to wheel load variations are increasing linearly, while the reference quantity, the perception threshold, remains the same until 2 m/s². Then the Weber Law described in section 2.4.4 applies, while the force deviations remain almost constant, resulting in reducing Weber ratios. At higher accelerations, the force deviations increase because a compensation of the wheel load reductions by increasing slip is limited due to the tire nonlinearities.

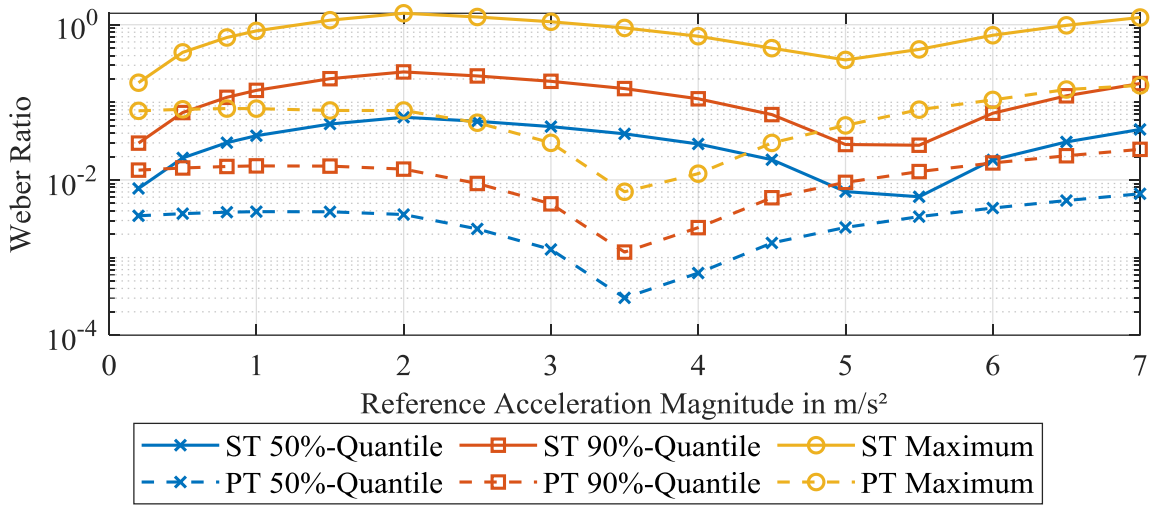

Figure 8-35: Disturbance of horizontal reference acceleration through wheel load variations by means of Weber ratio (cf. equation (3.5), perception threshold: 1). Determined from wheel load variations on acceptable driving surface from section 8.8.1 with isolated horizontal tire model (cf. subchapter 3.5) and different input moments corresponding to the shown reference acceleration.

Although exceedances of the perception thresholds occur for specific acceleration ranges with the solid tire, the occurrence of these situations is low. In 90 % of the simulation scenario, the disturbances remain far below the perception thresholds. The impact of the rare perceptible disturbances has to be further investigated in subject studies.

In comparison, the behavior of the pneumatic tire is more advantageous. The maximum Weber ratio is at 17 %, leaving a high margin to the perceptions thresholds for other disturbances. As discussed in section 6.2.2 this results from the higher slip stiffness of the pneumatic tire.

8.8.3 Hexapod Requirements

The requirements on the hexapod resulting from the active compensation of driving surface-induced disturbances on different surface qualities are summarized in Figure 8-36 for the solid (ST) and pneumatic tire (PT) together with the respective limitations of the Mevea Hexapod. The requirements are calculated based on the validation model from section 8.7.1

for pure vertical excitations without horizontal forces. The considered control approach is the closed-loop architecture.

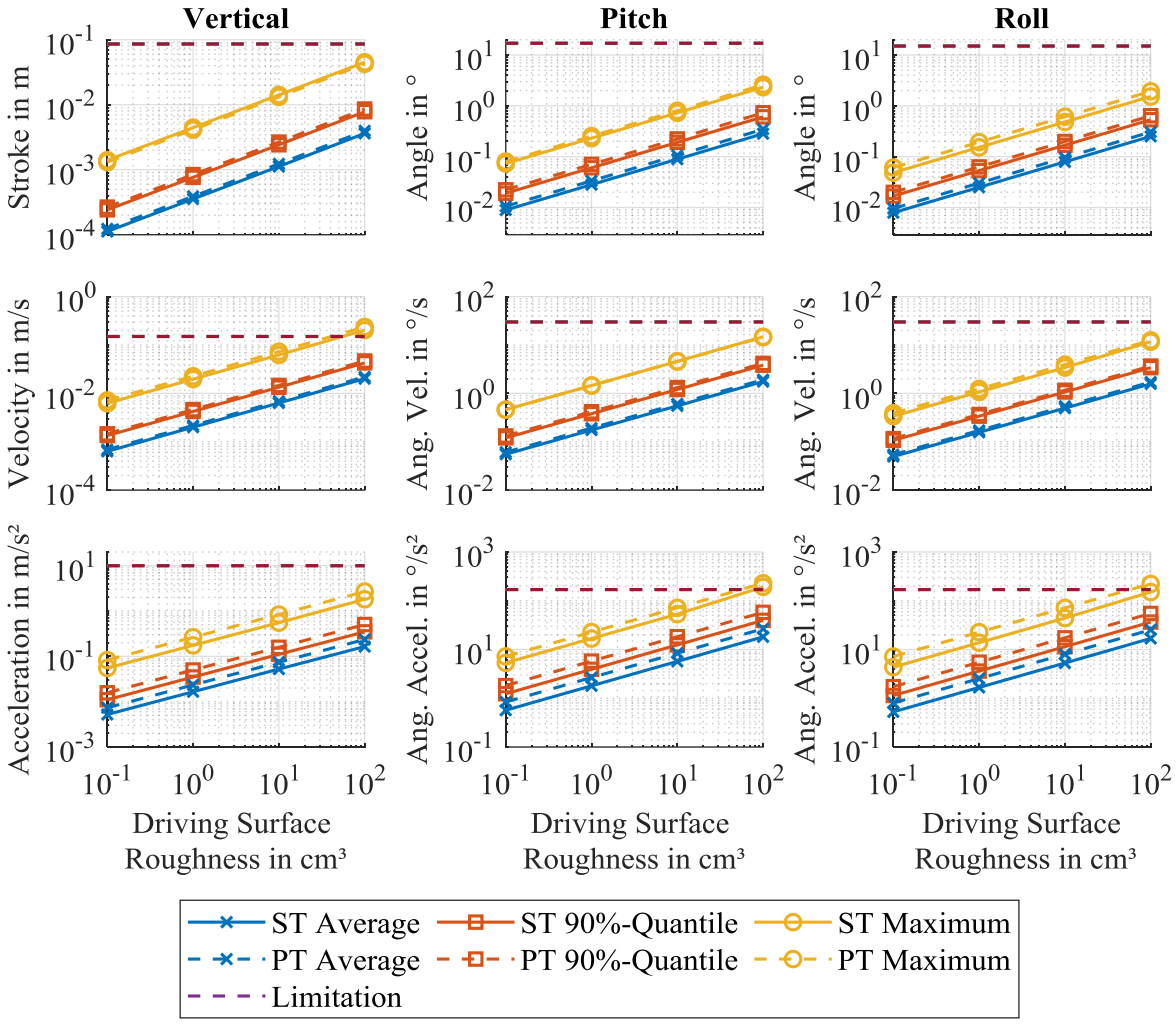

Figure 8-36: Hexapod requirements for solid (ST) and pneumatic tires (PT) determined with the multibody model from section 8.7.1 in urban driving scenario on different driving surface qualities.

Shown are the heave, pitch and roll DoF on position, velocity and acceleration level. For the solid tire, an exceedance of the maximum vertical velocity (200 vs. 150 mm/s) as well as the angular acceleration in pitch direction (192 vs. 170 °/s²) are recognizable at the lowest driving surface quality (corresponds to a class D surface according to Table 2-2). For roughness coefficients below 50 cm³ all limitations are maintained. Compared to the solely tire-sprung system, a reduction from 102 °/s² to 8 °/s² at a roughness coefficient of 0.1 cm³ is achieved for the critical roll accelerations. Especially the pitch and roll angles, which are the most relevant characteristics due to the main function of tilt coordination, remain small. The maximum pitch angle amounts to 2.3°, which corresponds to a reduction of the tilt potential by 13 %. For the roll angle, a maximum of 1.5° and a reduction of the tilt capability by 10 % is determined.

For the pneumatic tire, higher requirements are recognizable on acceleration level. The maximum vertical acceleration is 48 % higher, the angular accelerations are 19 % higher in pitch

direction and 51 % in roll direction. The increase results from the lower second natural frequency of the tire-sprung mass that is within a range controllable by the hexapod actuator. The attempt of the hexapod actuator to control this peak results in a higher acceleration demand.

8.8.4 Impact of Horizontal Dynamics

The investigation of the disturbances arising from the horizontal dynamics of the WMDS is divided into two parts. First, straight acceleration steps of different magnitudes and directions are analyzed as in subchapter 8.7 in order to determine the disturbance behavior for all possible states of operation. Subsequently, an urban driving scenario is investigated in order to assess the impact of the horizontal dynamics in a representative application scenario of WMDS. The validation model from section 8.7.1 is applied for these investigations.

8.8.4.1 Straight Accelerations

As discussed in section 3.4.3 the disturbances resulting from the horizontal dynamics of the simulator consist of two fractions. The first aspect is that undesired vertical and angular accelerations occur during the transient buildup phase of the horizontal acceleration step. This aspect is evaluated based on the absolute perception thresholds.

The second aspect is the static deviation of the simulated acceleration resulting from the tilt of the subject, which generates a horizontal disturbance due to the tilted gravitational acceleration. This part is investigated based on the Weber-ratio introduced in section 3.4.2 for the deviation of the resultant acceleration magnitude. Additionally, the directional deviation of the disturbed horizontal acceleration is analyzed. The results for the first aspect are shown in Figure 8-37.

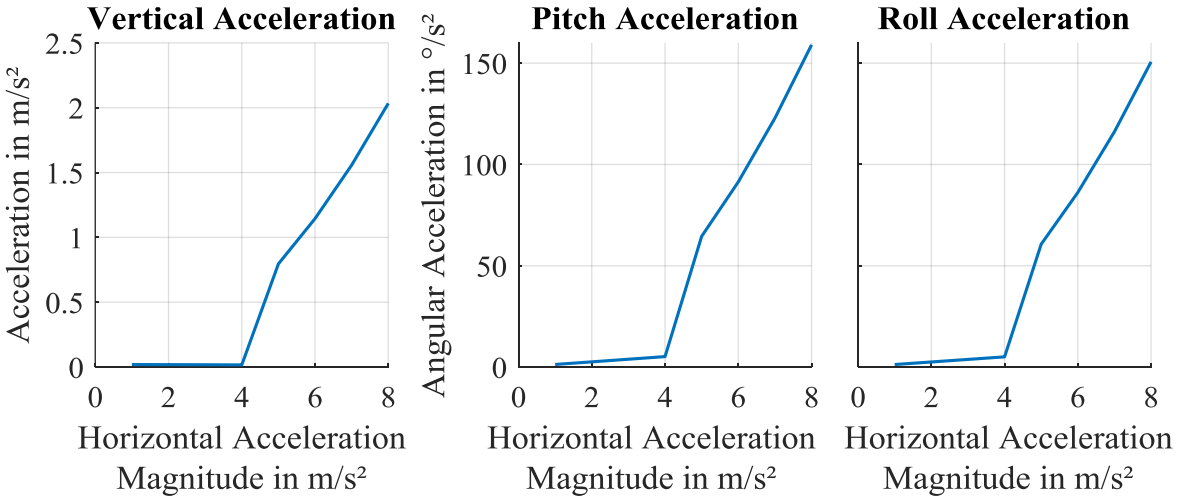

Figure 8-37: Maximum disturbance accelerations during transient phase of straight horizontal acceleration step with acceleration directions between 0° and 350° for different acceleration magnitudes. Determined with multibody model from 8.7.1 with the parameters of the developed suspension.

Up to a horizontal acceleration of 4.5 m/s², which is the range of the equal force distribution and therefore approximately ideal force support, the disturbances remain below the perception thresholds (z: 0.016 m/s², ϑ: 5.2 °/s², φ: 5.0 °/s²). At accelerations above the switching point from EMC to FMC, the disturbance accelerations rise strongly and exceed the absolute perception thresholds by far. However, it is unclear how high the practical impact of these disturbances is. The duration of the high acceleration oscillation is just about 1 s, while at the same time high transient horizontal accelerations are acting. The resulting disturbance of the immersion might be acceptable. The perception of these combined accelerations is not assessable with the given objective values. Therefore, the impact of these disturbances has to be further investigated in subject studies. Nevertheless, up to 4.5 m/s², the behavior of the system is as desired.

The results for the second aspect in Figure 8-38 show a similar characteristic. The Weber fractions at accelerations below 4 m/s² are less than 5 % of the perception threshold. At the highest acceleration, the disturbance of the acceleration magnitude still remains below the perception threshold, although a ratio of 71 % does not leave much margin for other disturbances as the wheel load variations.

The maximum direction deviation of the horizontal acceleration direction amounts to 3.3° and is therefore below the perception threshold of 6°. Summarizing, the influence of the tilt of the subject resulting from suspension motions is below the perception threshold even at the highest acceleration.

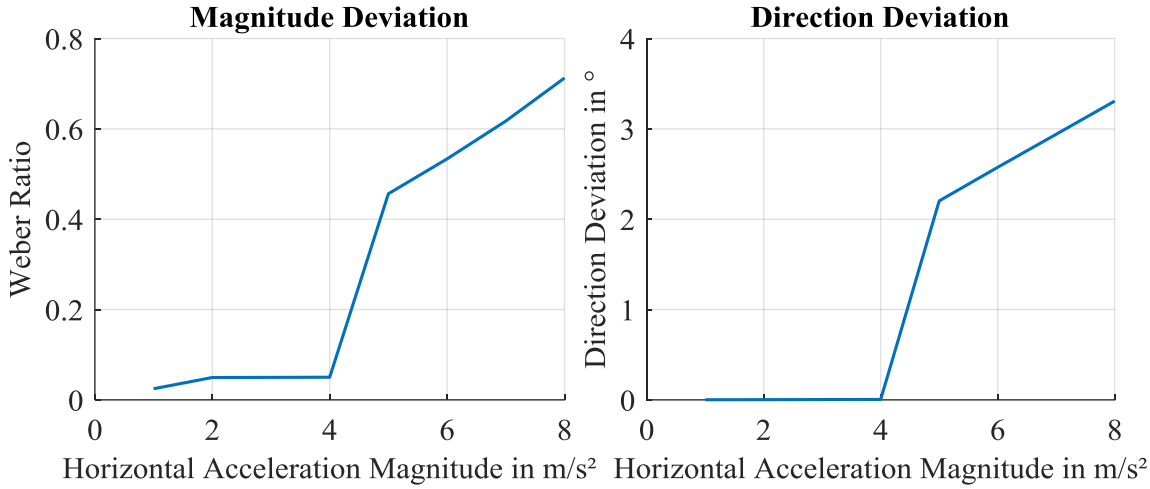

Figure 8-38: Disturbance of acceleration magnitude by means of the Weber ratio from equation (3.5) and direction resulting from tilt of the subject during straight acceleration maneuver. Shown are the maximum values over acceleration directions between 0° and 350° for different acceleration magnitudes. Determined with multibody model from section 8.7.1 with the parameters of the developed suspension.

8.8.4.2 Urban Driving Scenario

To evaluate the impact of the horizontal dynamics of the WMDS on the disturbance motions, the urban driving scenario from section 3.3 is simulated with the multibody model from

section 8.7.1. To assess the robustness of the results, an increase of the CG height by 50 mm is also investigated. The suspension stroke and the wheel inclination in Figure 8-39 do not exceed their acceptable values within the whole scenario. The maximum rebound suspension stroke is -70 mm, the maximum compression is 37 mm. These values are within the range that is achievable with the developed kinematic from section 8.6.2. The maximum wheel inclination to the ground of 2.5° is far below the value of 5.2° that would imperil the ground clearance of the motors. Additionally, the 99%-quantile of 0.26° is in a range that will probably not affect the tire force generation. An increased center of gravity (CG) results in a slightly higher median and 99%-quantile, whereas the maximum values are almost the same.

The disturbances resulting from pitch and roll motions are given in Figure 8-40 as a cumulative distribution function. The deviation from the desired resulting acceleration magnitude is given as Weber-ratio. Additionally, the direction deviation between the disturbed acceleration and the desired acceleration is shown. The 99%-quantile for the Weber-ratio amounts to 0.12, which is far from the perception threshold of 1 and leaves enough margin for other disturbances of the horizontal accelerations as the wheel load variations. The 99%-quantile increases up to 0.25 due to an increase in the CG height, which is still far enough from the threshold. The maximum values are 1.2 for both CG heights. Although this means a slight exceedance of the perception threshold, this occurs rarely throughout the whole scenario.

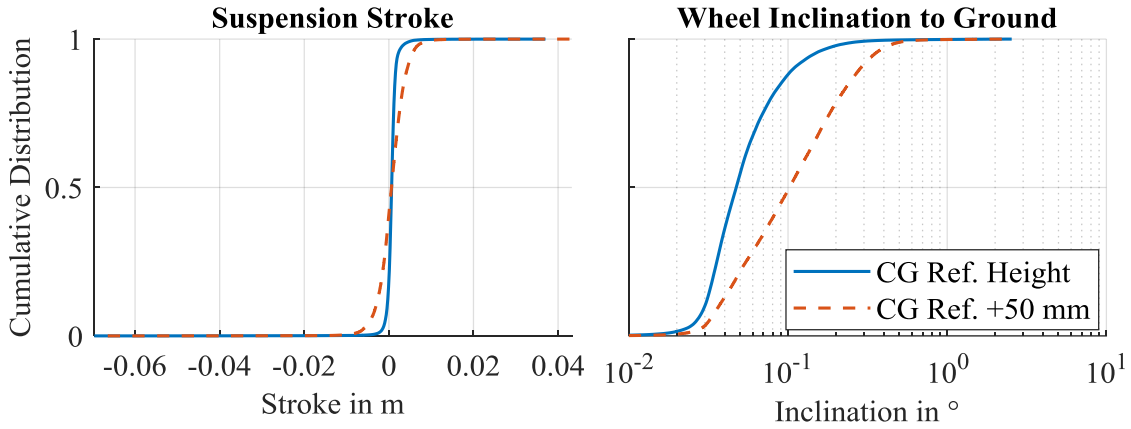

Figure 8-39: Cumulative distribution of suspension stroke and inclination between wheel and ground occurring during an urban scenario for different heights of the center of gravity (CG). Determined with multibody model from section 8.7.1 with the parameters of the developed suspension.

The 99%-quantile of the direction deviation is 1.2° for the reference height and 2.5° for the increased CG. These values are not perceptible. The maximum value of 16° for both heights is above the perception threshold of 6°. However, the duration of this exceedance is only 100 ms and it occurs one time in an overall scenario length of 48 minutes.

A similar characteristic is found for the disturbance accelerations, which are presented in Figure 8-41. The 99%-quantiles of the accelerations are below the perception thresholds (z: 0.03 m/s², ϑ: 3.2 °/s², φ: 3.2 °/s²), whereas the maximum values exceed them by far (z: 2.74 m/s², ϑ: 172.2 °/s², φ: 166.7 °/s²). The increase of the CG results in slightly higher disturb-

ances, which are, however, below the perception threshold. The 99%-quantile and the maximum values also apply for the increased CG. The perception thresholds are exceeded in 7 situations throughout the scenario duration of 48 minutes. An analysis of these situations shows that high steering angle velocities are the source of the disturbance motions. The steering motion occurs because of singular wheel positions, which arise due to the washout of the WMDS.[117a] The WMDS moves away from its origin due to an acceleration demand. If this demand is omitted, the washout generates accelerations that move the WMDS back to its initial position. At the outer point of the simulator trajectory, the sign of the velocity changes. If the motion was exactly in the radial direction, this would be detected by a logic and the wheel rotation direction would be reversed. However, deviations from the radial movement direction result in fast steering motions in order to change the sign of the velocity. These steering motions generate a wrong direction of the longitudinal force and generate slip angles that additionally result in lateral disturbance forces. These deviations from the desired forces calculated from the motion control result in wrong support forces and therefore induce motions of the WMDS body. However, even without a suspension, false cues are generated by the fast steering motions because the horizontal accelerations are also disturbed. Therefore, this is a problem of WMDS in general even though the interaction with a suspension increases its impact.

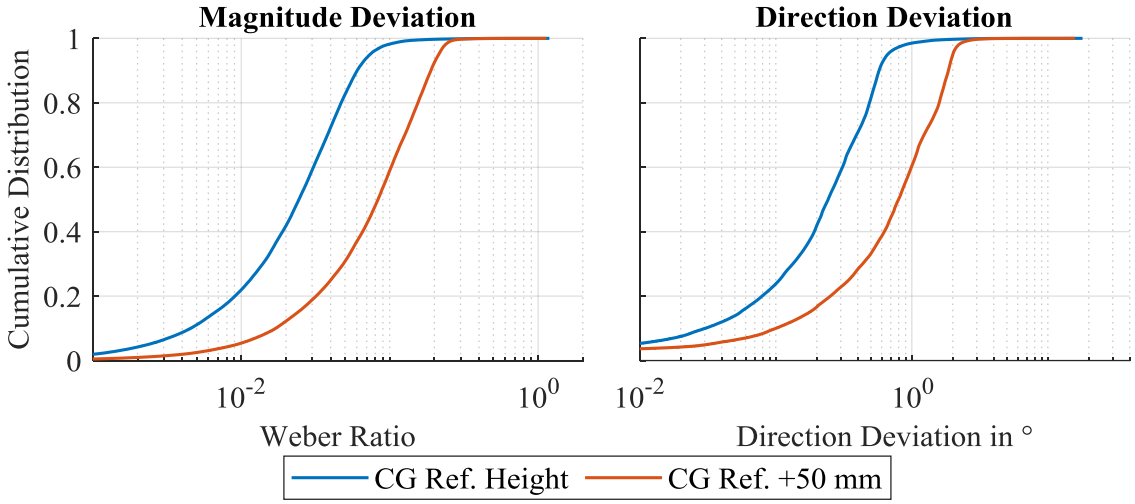

Figure 8-40: Disturbance of acceleration direction and magnitude by means of the Weber ratio from equation (3.5) resulting from tilt of the subject during urban driving scenario for different heights of the center of gravity (CG). Determined with multibody model from section 8.7.1 with the parameters of the developed suspension.

Solutions for this problem based on adjustments of the WMDS trajectory already exist.[117b] These approaches achieve a reduction of the occurring singular wheel configurations by 93%, which results in the low overall occurrence during the urban scenario. However, these approaches are mainly focused on the reduction of steering power. Further research is required to reduce the false cues arising from undesired steering motions.

[117] Cf. Betschinske, D.: BaTh, Verringerung Lenkleistungsbedarf WMDS (2016). a: p. 18 ff.; b: -.

Summarizing, despite the disturbances resulting from the described steering motions of the WMDS, the motions of the body that occur during a representative urban scenario due to the introduced suspension DoF with a soft spring are acceptable. Therefore, the main purpose of WMDS is not impeded by the suspension, while it enables the application on driving surfaces of much lower quality.

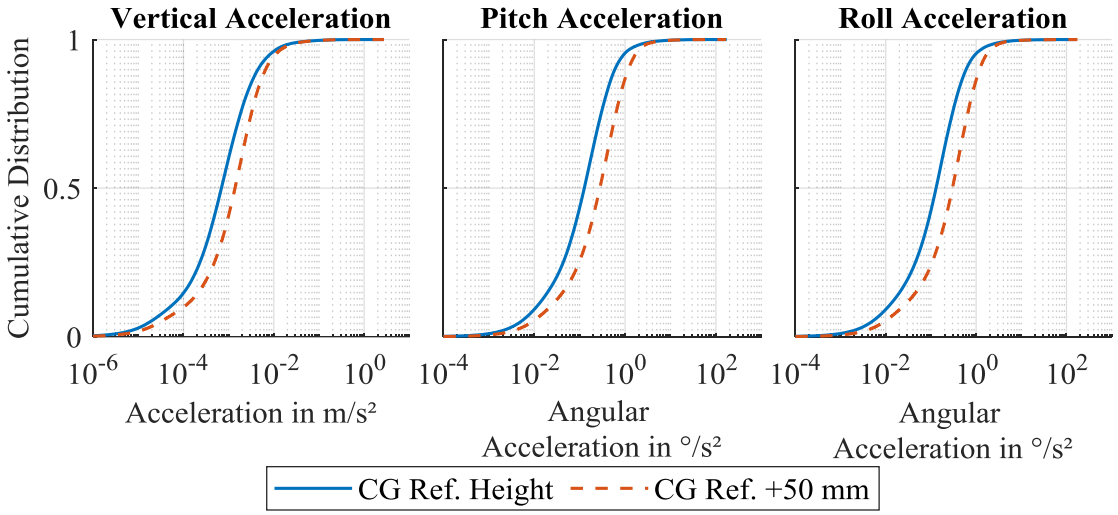

Figure 8-41: Disturbances by transient accelerations due to horizontal motions of the WMDS occurring during urban driving scenario for different heights of the center of gravity (CG). Determined with multibody model from section 8.7.1 with the parameters of the developed suspension.

8.9 Summary and Discussion

In this chapter, a passive suspension and an active hexapod control were developed in order to reduce the vibration disturbances resulting from driving surface excitations. The results of the previous subchapters show that the suspension design is a trade-off between the acceptable driving surface quality for the application of the WMDS and the disturbances resulting from body motions due to suspension strokes. The developed approach offers a balanced compromise that suppresses body motions at accelerations below 4.5 m/s², which is the most relevant range occurring during urban driving scenarios according to Figure 3-5, while maintaining a low natural frequency of 1 Hz. This low frequency offers high vibration isolation, especially in combination with the applied controller. The acceleration range could be increased to 5.4 m/s² by applying pneumatic tires with a higher friction coefficient

Of course, the suitability only applies to the considered urban scenarios. As discussed in section 8.8.4.1, scenarios with higher acceleration demands could worsen the behavior. Even though the determined disturbance accelerations are above the perception thresholds it is unclear which effect this has on the immersion of the subject. Motions of the vehicle are expected during the acceleration-buildup phase so that the disturbance motions probably feel real. In these cases, however, the low natural frequency and damping of the suspension could

worsen the behavior, because the motions of the simulator do not match to the system behavior of the virtual vehicle.

For simulation scenarios with high acceleration requirements, an adaptable spring-damper characteristic could be introduced. A higher stiffness would reduce the disturbances arising from high horizontal accelerations and additionally converge the behavior of simulator motion and virtual vehicle. However, in this case, the amount of suitable driving surfaces is reduced. Nevertheless, even if both demands are not achievable at the same time, the developed approach offers the flexibility to adapt to the respective simulation scenario.

Another aspect that was neglected in the considerations of this chapter are breakaway forces of the suspension. The requirement of not exceeding the perception thresholds of the subject could be impaired even by small adherence effects and significantly reduce the performance of the suspension. This aspect has to be further investigated in the future. The multibody model developed in this work is applicable for that by implementing friction models into the suspension joints.

9 Overall Comparison and Evaluation

For a final comparison and evaluation of the developed concepts, the PSD spectra depicted in Figure 9-1 are analyzed. Shown are the vertical frequency-weighed accelerations. The advantage of the early filtering effect of the suspension is clearly recognizable. The square slope of the acceleration over frequency results in high magnitudes of the tire-sprung systems. The low damping increases this problem due to the high peaks at the natural frequency. The active control mitigates this problem by damping the peak, but still the magnitudes are higher than that of the passive suspension due to the mentioned effect. Even in the high-frequent regions the magnitudes of the tire-sprung system are comparable to the maximum of the suspension system.

Generally, the main target of the active approach to damp the natural frequencies is achieved for all developed concepts, while the robustness requirements for the tire-sprung system impede the control behavior. The influence of additional peaks due to the feedback loop is minimized in the relevant frequency range of human motion perception.

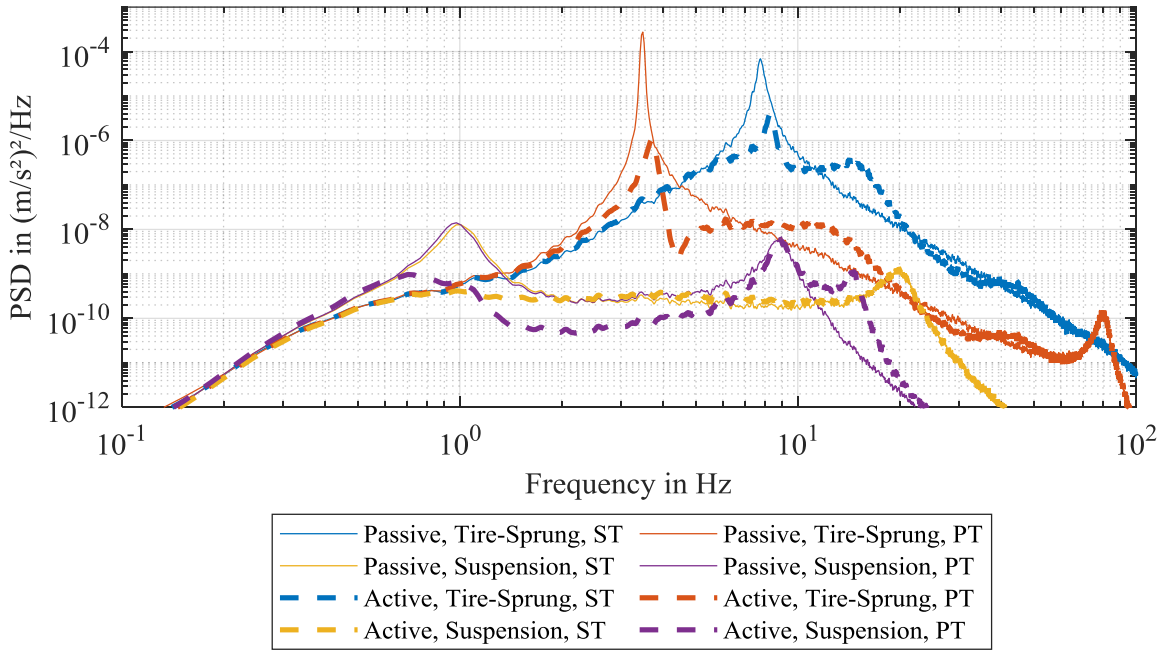

Figure 9-1: PSD spectra of vertical frequency-weighed acceleration determined in an urban driving scenario with scaling 1 on the reference driving surface quality from subchapter 4.5 with a roughness coefficient of 0.036 mm³. Shown are passive and active tire-sprung and suspension systems in combination with solid (ST) and pneumatic (PT) tires. The applied models of the respective system configurations are described in sections 4.2, 6.1, 7.5.1 and 8.7.1.

The findings are also reflected in the time domain, which is shown in Figure 9-2 by means of the total vibration values occurring during an urban driving scenario. The maximum disturbance accelerations of the initial system configuration are reduced by two orders of mag-

nitude through the implementation of a suspension and an active hexapod control. Both solution approaches contribute to this improvement by approximately one order of magnitude, although the impact of the suspension is slightly higher. The highest difference between solid and pneumatic tire is recognizable for the active tire-sprung approach. For the suspension system, the solid tire is preferable in terms of vibration isolation due to the higher second natural frequency outside the sensitive range of human motion perception. However, the difference amounts to approximately 25 %, which is small according to the logarithmic scale of the classification of driving surfaces from Table 2-2. Thus, the tire selection should be based on other criteria than the vibration isolation. Especially the higher friction coefficient and the associated extension of the range of ideal force support, the lower nonlinearity and the reduced impact of wear yield the pneumatic tire as the preferred concept.

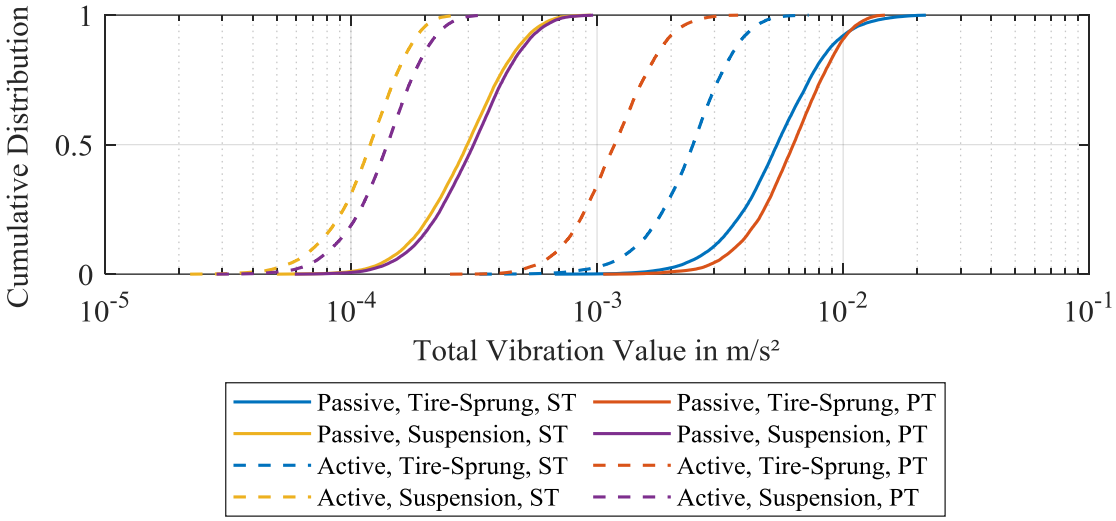

Figure 9-2: Total vibration value (cf. 2.4.2) occurring during an urban driving scenario with scaling 1 on a reference driving surface quality from subchapter 4.5 with a roughness coefficient of 0.036 mm³. Shown are passive and active tire-sprung and suspension systems in combination with solid (ST) and pneumatic (PT) tires. The applied models of the respective system configurations are described in sections 4.2, 6.1, 7.5.1 and 8.7.1.

The reduction of the total vibration values by the improvement approaches are also reflected in the overview of the acceptable driving surface qualities shown in Table 9-1.

Table 9-1: Overview of acceptable driving surface qualities in terms of roughness coefficient and depth gauge for a scaling factor of 0.7 and no exceedings of the perception thresholds.

	Acceptable Roughness Coefficients in mm³			
	Tire-Sprung		Suspension	
Tire Type	Solid	Pneumatic	Solid	Pneumatic
Passive	0.036	0.047	11.8	12.0
Active	0.348	0.931	147.4	127.6
	Acceptable Depth Gauge in mm			
Passive	0.013	0.015	0.236	0.238
Active	0.041	0.066	0.833	0.775

The application of a suspension increases the acceptable roughness coefficient by 3 orders of magnitude compared to the tire-sprung system. The implementation of the active hexapod control extends the range by an additional order of magnitude for both vibration system configurations. Thus, the implementation of a suspension reduces the required driving surface quality significantly. Even if a driving surface would be able to achieve the required quality of the tire-sprung system, it is expected that the costs for the construction of the surface will be reduced by the suspension, resulting in a lower acquisition barrier for potential users. The disadvantage of increased motions induced by the horizontal dynamics of the driving simulator is negligible in the typical application scope of urban driving scenarios.

The active hexapod control has a high improvement potential at almost no additional costs except the parameterization effort. The acceleration determination is also required for other functions of the WMDS (e.g. localization and control) and therefore is available anyway.

Summarizing, the active suspension approach is clearly preferable in terms of vibration isolation. It is the only concept that achieves an acceptable driving surface that is within the scope of the target value. The difference between solid and pneumatic tire is small for the suspension system. The pneumatic tire is recommended due to the friction coefficient, the suspension force support and the wear behavior.

10 Conclusion and Outlook

10.1 Conclusion

At the beginning of this thesis, the scope of driving surface qualities that are suitable for the application of WMDS was unknown. Thus, the following working hypothesis was stated:

> An ideal driving surface without unevenness is required for the application of WMDS without deterioration of the immersion of the subject.

The aim of this work was to falsify this hypothesis by determining the acceptable driving surface quality for the initial system configuration and to extend it by developing and evaluating improvement measures to reduce disturbances due to unevenness. For the determination of the acceptable driving surface quality, a model-based methodology was applied, which allows the iterative adaption of the surface quality until the tolerable limit is found.

Based on a vertical dynamics model of the respective considered system configuration and a driving surface unevenness model, the simulator-trajectory of a representative urban driving scenario is simulated, which is the most relevant application scenario for WMDS. The resulting disturbance motions are evaluated based on the total vibration value that considers the frequency dependency of the human vibration perception (cf. section 2.4.2). The driving surface roughness is iteratively adapted until the occurrence of exceedings of the perception threshold during this scenario are below different specified values. Although for the adaption of the hypothesis no exceeding is allowed, the sensitivity of the results to the varying human motion perception is estimated by additionally determining the acceptable roughness if partial exceedings are tolerated. Secondary it is analyzed, to which extent the horizontal accelerations are disturbed by wheel load variations occurring on the acceptable driving surface. For that purpose it is evaluated, if the acceleration deviations at different reference stimuli are above the just noticeable difference. For the suspension system, the impact of motions resulting from horizontal accelerations are investigated. Based on this methodology, the following system configurations were investigated.

Initial Situation (Solid tire-sprung system): A model of the current system state is developed based on a thorough system identification and validation with the MORPHEUS prototype on a stochastic driving surface. The results of the described methodology show that a maximum roughness coefficient of 0.036 mm^3 is required, which corresponds to a depth gauge of 0.013 mm over a length of 4 m. The researched driving surface qualities of asphalt or concrete material achieve a minimum roughness of about 1000 mm^3. Thus, with the given system configuration, an application on e.g. automobile testing grounds is not possible without impairing the immersion of the subject. The improvement potential of pneumatic tires is

marginal due to their low damping. Summarizing, the tire-sprung system requires a driving surface of sophisticated quality that strongly restricts the flexibility advantage of WMDS. Thus, improvement measures are needed.

Tire-sprung system and hexapod vertical dynamics control: This active approach is advantageous because it does not require any hardware changes due to the already available hexapod. Two control architectures are developed and investigated: a closed-loop control (CLC) of the acceleration of the hexapod top plate and an open-loop control (OLC) that compensates the motion of the hexapod bottom plate. The great advantage of the OLC is the avoidance of a parameterization. Nevertheless, due to the low damping of the tires and the resulting high group delays, the OLC is unstable for both tire types with the tire-sprung system. The CLC approach strongly improves the vibration isolation and extends the acceptable driving surface quality range by one order of magnitude, although it suffers from the robust design that accounts for variations of the natural frequency of the tires. In combination with the solid tire, the relevant control frequency is slightly lower than the intersection frequency of the phase with 180°, which limits the performance of the active approach. This is mainly due to the high dead time of the hexapod.

Although an improvement of this shortcoming could be expected with the softer pneumatic tires, the low damping and the correlated high group delays result in a sensitivity to parameter variations of the vibration system, which impedes the performance of the controller. Summarizing, although the active approach improves the vibration isolation, the high natural frequencies, the low damping and the varying behavior of the tires in combination with the high dead times of the hexapod impede a higher potential within the tire-sprung system.

Suspension and hexapod vertical dynamics control: In order to avoid the aforementioned problems of the tire-sprung system, a suspension is developed that reduces the natural frequency and introduces additional damping into the system. A kinematic is developed that minimizes the motions of the subject that are induced by horizontal accelerations. Four motion control approaches are investigated concerning the interaction with this kinematic. A hybrid approach that switches the force distribution dependent of the friction utilization of the tires from equal to friction-dependent is preferable in terms of suspension motions. The developed suspension avoids exceeding the perception thresholds due to disturbance motions up to 4.5 m/s^2. The use of pneumatic tires would increase this limit up to 5.4 m/s^2. In urban driving scenarios, the perception thresholds are exceeded less than 1 % of the time, resulting from high steering motions due to shortcomings of the WMDS control.

Concerning the vibration isolation, a high improvement compared to the tire-sprung system is achieved, especially with the active approach. The solid tire is advantageous because of its higher second natural frequency, which is out of the sensitive range of human vibration perception. Nevertheless, the high dead time of the hexapod generates control-induced vibrations within the sensitive frequency range of the human motion perception. This restricts the adjustable controller gain and, thus, the achievable vibration isolation. Therefore, although an improvement is achieved with the hexapod, an alternative actuator that reaches higher frequencies would be preferable.

Generally, the suspension design is a trade-off between the reduction of driving surface-induced vibrations and disturbances due to the horizontal dynamics. For the relevant acceleration range of urban driving scenarios, the developed approach is suitable. Scenarios with higher dynamics could require an increased natural frequency, which reduces the vibration isolation.

10.1.1 Conclusions for WMDS Design

Based on the aforementioned findings, the following recommendations for the design of WMDS are given:

Tire selection: Although the solid tire achieves a slightly better vibration isolation in combination with the suspension and the active control, the use of pneumatic tires is recommended. Especially the higher friction coefficient is advantageous. On the one hand, higher accelerations are possible. On the other hand, and even more important, the acceleration range for an ideal support of pitch and roll motions is extended. Thus, perceptible disturbances resulting from horizontal dynamics are avoided up to 5.4 m/s². Additionally, the tire nonlinearities and the high impact of wear on the tire characteristics are disadvantageous for the solid tire.

Suspension: The implementation of a suspension into the WMDS design is strongly recommended. The demanded high driving surface quality of the tire-sprung system would require the elaborate construction of a special testing ground for the application of the WMDS. This could be a crucial barrier for the broad dispersion of WMDS, especially among potential users with limited budget. The costs for such an accurate surface are expected to exceed the additional costs for a suspension by far. The slight increase of system complexity is worthwhile in comparison.

Hexapod control: The active hexapod vertical dynamics control yields an increase of the acceptable driving surface roughness by one order of magnitude at no additional hardware cost. In combination with a suspension, the OLC approach offers a high vibration isolation at least for the angular DoFs, while the effort for the implementation is low due to the avoidance of a parameterization. Therefore, it is well suitable for the first stages of the system. The CLC approach needs to be adapted to different vibration systems and hexapods, while it offers a higher vibration isolation than the OLC. The methodology described in this work is applicable for an automated parameterization of the controller, so that the additional effort is limited to the system identification for the adaption of the applied models.

10.1.2 Final Evaluation

The findings of this thesis enable the following final adaption of the working hypothesis:

A driving surface with a roughness coefficient of 0.15 cm³ is required for the application of WMDS without deterioration of the immersion of the subject.

Although this is an improvement by 4 orders of magnitude compared to the initial state, this value is still 1 order of magnitude below the target driving surface quality of 1 cm³. Nevertheless, the depth gauge of 0.8 mm over 4 m is only half of the documented achievable values. Additionally, if a slight weakening of the evaluation criterions would be acceptable, the target value is achieved. The human perception of motion is a complex issue that is difficult to assess objectively. In particular, the question to which extent vibrations in the simulator feel realistic and at which point the immersion is significantly disturbed (especially during standstill of the virtual vehicle) offers a high scope for the evaluation of the acceptability of a driving surface. This uncertainty is addressed in this thesis by examining different allowed exceedances in order to estimate the sensitivity to the evaluation parameter. Nevertheless, the objective evaluation of the subjective feeling of disturbance motions is the biggest disadvantage of the applied methodology. But even if a wheeled mobile driving simulator for subject studies is available in the future, the model-based methodology would be required to be able to adapt the driving surface quality to determine the tolerable roughness. Therefore, the methodology should also be applied for future investigations, but in combination with a further refinement of the evaluation criteria through subject studies.

The adjustment of the working hypothesis in this work is based on completely staying below the perception threshold and is therefore a conservative criterion, yielding a lower limit of the acceptable roughness coefficients. Thus, the given working hypothesis is a fundament for future adjustments, either by new findings concerning the human motion perception or through the development of further measures for the reduction of driving surface-induced disturbances.

10.2 Outlook

The two aspects mentioned at the end of the last subchapter should be the main focus of the future research concerning driving surface-induced disturbances in WMDS.

The first aspect is the human motion perception. The further investigation and validation of the evaluation parameters is crucial for a more substantiated assessment of the acceptable driving surface quality. On the one hand, the practical impact of the vibration disturbances on the immersion of the subject has to be identified. On the other hand, the impact of the superposition of the different sources of disturbance requires further investigations. For that purpose, a WMDS that is suitable for subject studies has to be built in order to assess the complex topic of human motion perception.

Based on this prototype, a validation of the developed improvement measures has to be conducted. In particular, the function of the kinematic force support and the active hexapod control require experimental evaluations.

The second aspect is the further development of improvement measures. The following enhancements of the presented approaches are conceivable:

- Online parameter identification of the vibration system parameters in order to adapt the controller parameters of the hexapod control. This would reduce the robustness requirements of the controller and enable a design with higher performance.
- The development of a sophisticated kinematic that superposes a suspension stroke-dependent rotation on the wheel that is dependent on the direction of the tire force, could generate an asymmetric support angle around the y-axis of the suspension planes. This could enable the application of the directional motion control and, thus, vitiate the currently required switching of the motion control. This would reduce the horizontal dynamic disturbances throughout the whole acceleration range.
- The avoidance of high steering angle velocities due to singular wheel configurations would also reduce horizontal dynamic disturbances.

The following additional concepts proposed in this work could be developed in the future:

- Trajectory adaption of the simulator to avoid strong excitations.
- Masking of the driving surface-induced vibrations with synthetic vibrational cues.
- Adaption of the visualization to display oncoming driving surface unevenness.
- If the vibration disturbances turn out to be too large despite the approaches developed in this work, an active approach based on additional actuators with lower dead times than the hexapod could yield a further vibration isolation. An approach to adapt the developed suspension could be an electric motor attached to the spring lever, opposite to the damper.

Finally, the following aspects that have been neglected in this work have to be investigated in the future:

- The aspect of acoustic disturbances due to high-frequent vibrations has to be assessed. It could be sufficient to equip the simulator dome with an acoustic insulation, which will be required anyway due to other disturbance noise as from the drivetrain or airflow. If this is not sufficient, the implementation of rubber elements is required.
- This work focused on whole body vibrations by frequency-weightings. Another aspect are high-frequent vibrations that are mainly perceived with the mechanoreceptors of the skin, which are e.g. transmitted through the steering wheel. This aspect can be investigated with the developed models but with other weighting functions.
- As discussed in subchapter 8.9, breakaway forces of the suspension have been neglected yet. Due to the ambitious requirement of staying below the perception threshold, these forces could significantly impede the performance of the suspension. This aspect can be investigated based on the multibody model developed in this work by implementing friction models into the joints.

A Fundamentals

A.1 Frequency Weighing Functions

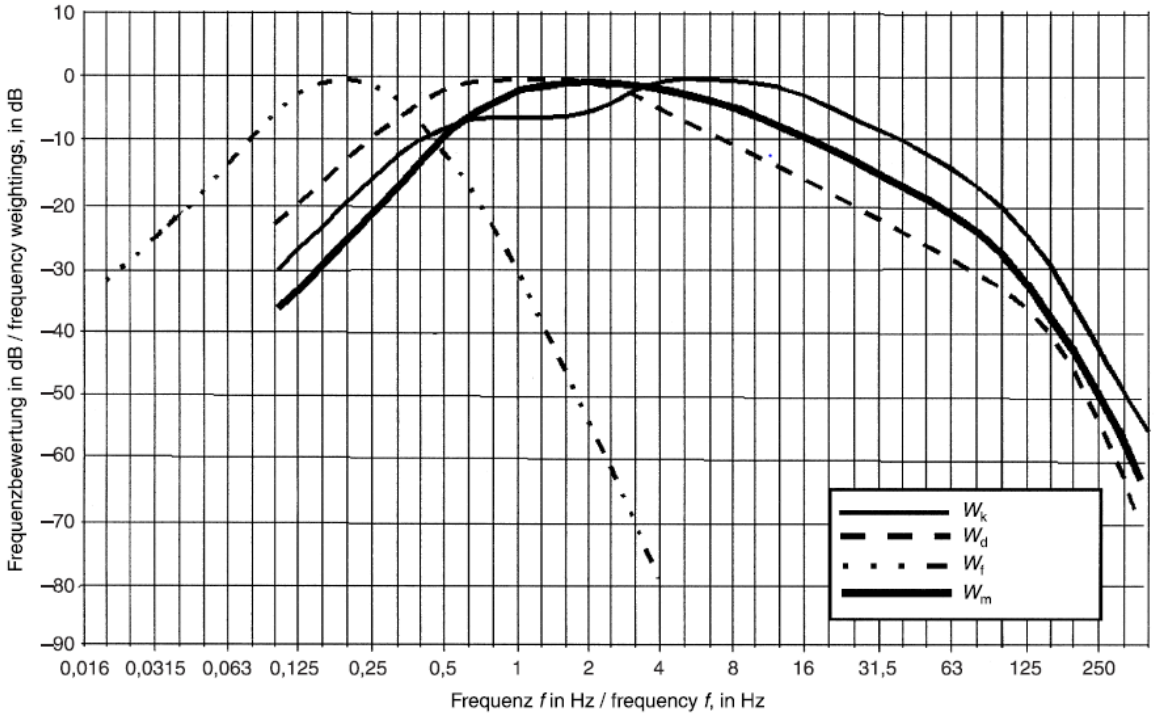

Figure A.1 - 1: Examples for frequency weighting functions (W_k: Assessment of comfort while sitting or standing for z direction; W_d: Assessment of comfort while sitting or standing for x and y direction; W_m: Assessment of comfort with undefined posture; W_f: Assessment of low-frequency z vibrations, which could result in kinetosis)[118]

[118] VDI, Verein Deutscher Ingenieure: VDI 2057 - Ganzkörper-Schwingungen (2017), p. 21.

A.2 Road Profile Measurements

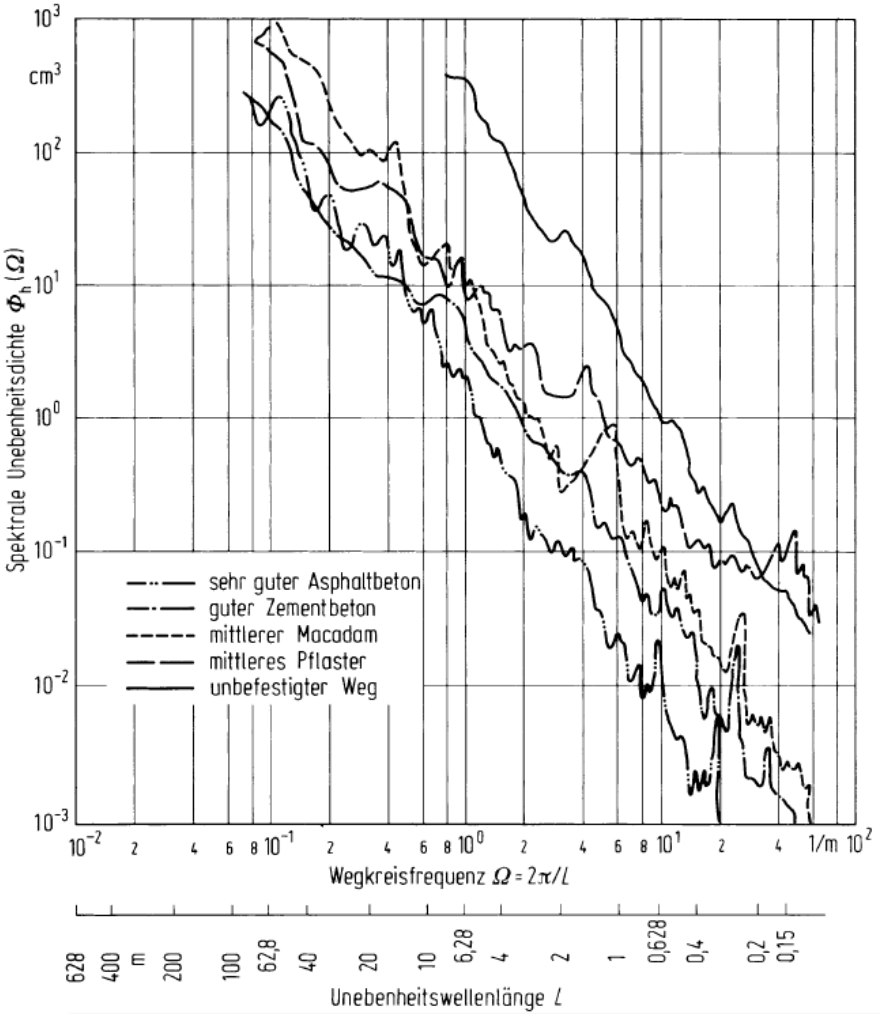

Figure A.1 - 2: Power spectral densities of different road surfaces determined by Braun.[119]

[119] Braun, H.: Diss., Untersuchung von Fahrbahnunebenheiten (1969). According to Mitschke, M.; Wallentowitz, H.: Dynamik der Kraftfahrzeuge (2014), p.342.

A.3 Motion Control Architecture

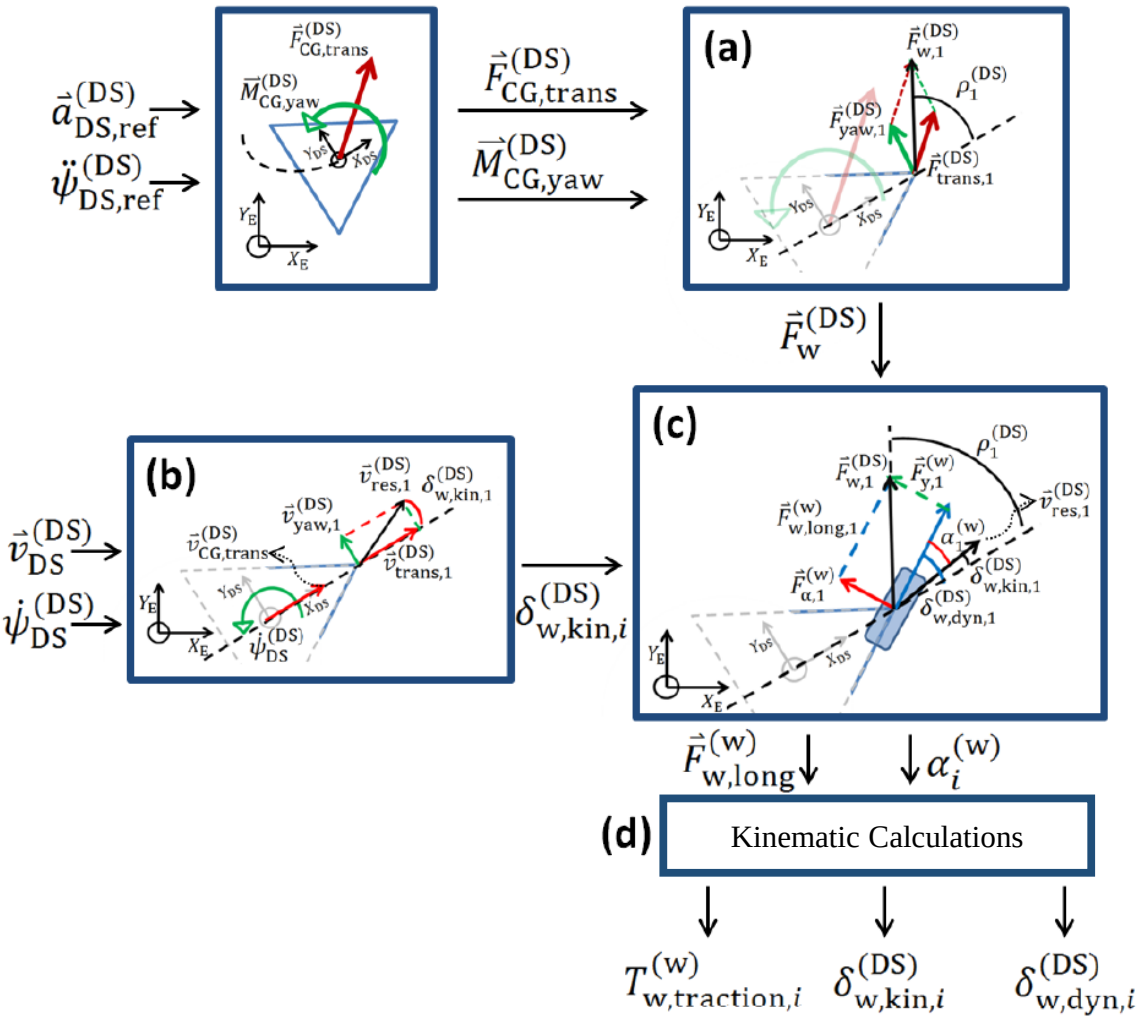

Figure A.1 - 3: Motion control block diagramm.[120]

A.4 Hilbert Transform

Steps of Hilbert-Transform in section 4.1.2.3:

- Calculation of the Fourier transform ${}^{\mathcal{F}}_{\mathrm{H}}\ddot{z}_{\mathrm{CG}}$ of the measured vertical acceleration signal in the CG.
- Cutoff of frequencies below 4 Hz and above 12 Hz by setting them to zero (range around the natural frequency of 8 Hz determined in section 4.1.2.2) in order to limit the influence of high-frequent modes on the Hilbert transform (Result: ${}^{\mathcal{F}}_{\mathrm{H}}\ddot{z}_{\mathrm{CG,Cut}}$).

[120] Betz, A. et al.: Driving Dynamics Control of a WMDS (2013). According to Betz, A.: Feasibility and Design of WMDS (2014), p. 59.

- Multiplication of the remaining frequency spectrum ${}^{\mathcal{F}}_{\mathrm{H}}\ddot{z}_{\mathrm{CG,Cut}}$ with $-\mathrm{jsgn}(f)$ to determine the Hilbert transform ${}^{\mathcal{F}}_{\mathrm{H}}\ddot{z}_{\mathrm{Hil,CG,Cut}}$ of the vertical acceleration in the Fourier domain.
- Inverse Fourier-transform of ${}^{\mathcal{F}}_{\mathrm{H}}\ddot{z}_{\mathrm{Hil,CG,Cut}}$ in order to determine the Hilbert transform ${}_{\mathrm{H}}\ddot{z}_{\mathrm{Hil,CG,Cut}}$ in the time domain.
- Inverse Fourier transform of ${}^{\mathcal{F}}_{\mathrm{H}}\ddot{z}_{\mathrm{CG,Cut}}$ in order to determine the frequency-reduced acceleration ${}_{\mathrm{H}}\ddot{z}_{\mathrm{CG,Cut}}$ in the time domain.
- Determination of the analytic signal: ${}_{\mathrm{H}}\ddot{z}_{\mathrm{An,CG,Cut}} = {}_{\mathrm{H}}\ddot{z}_{\mathrm{CG,Cut}} + \mathrm{j}\,{}_{\mathrm{H}}\ddot{z}_{\mathrm{Hil,CG,Cut}}$
- Determination of the envelope ${}_{\mathrm{H}}\ddot{z}_{\mathrm{Env,CG,Cut}}$ of the acceleration oscillation by calculating the magnitude ${}_{\mathrm{H}}|\ddot{z}|_{\mathrm{An,CG,Cut}}$ of the analytic signal.

B Controller Design

B.1 Suspension Vibration System Model Equations

$$ {}^{\mathcal{L}}G_{\mathrm{DB},z}(s) = \frac{{}^{\mathcal{L}}_{\mathrm{H}}\ddot{z}_{\mathrm{HTP,DB}}(s)}{{}^{\mathcal{L}}_{\mathrm{H}}z_{\mathrm{DSE}}(s)} = \frac{3(c_{\mathrm{T}} + d_{\mathrm{T}}s)(c_{\mathrm{S}} + d_{\mathrm{S}}s)s^2}{(m_{\mathrm{HBP}} + m_{\mathrm{HTP}})m_{\mathrm{W}}s^4 + \left((d_{\mathrm{S}} + d_{\mathrm{T}})(m_{\mathrm{HBP}} + m_{\mathrm{HTP}}) + 3d_{\mathrm{S}}m_{\mathrm{W}}\right)s^3 + \left((c_{\mathrm{S}} + c_{\mathrm{T}})(m_{\mathrm{HBP}} + m_{\mathrm{HTP}}) + 3c_{\mathrm{S}}m_{\mathrm{W}} + 3d_{\mathrm{S}}d_{\mathrm{T}}\right)s^2 + 3(c_{\mathrm{T}}d_{\mathrm{S}} + c_{\mathrm{S}}d_{\mathrm{T}})s + 3c_{\mathrm{S}}c_{\mathrm{T}}} \tag{B1.1} $$

$$ {}^{\mathcal{L}}G_{\mathrm{MRB},z}(s) = \frac{{}^{\mathcal{L}}_{\mathrm{H}}\ddot{z}_{\mathrm{HTP,MRB}}(s)}{{}^{\mathcal{L}}_{\mathrm{H}}z_{\mathrm{Hex,act}}(s)} = \frac{(m_{\mathrm{HBP}}m_{\mathrm{W}}s^4 + \left((d_{\mathrm{S}} + d_{\mathrm{T}})m_{\mathrm{HBP}} + 3d_{\mathrm{S}}m_{\mathrm{W}}\right)s^3 + \left((c_{\mathrm{S}} + c_{\mathrm{T}})m_{\mathrm{HBP}} + 3c_{\mathrm{S}}m_{\mathrm{W}} + 3d_{\mathrm{S}}d_{\mathrm{T}}\right)s^2 + 3(c_{\mathrm{T}}d_{\mathrm{S}} + c_{\mathrm{S}}d_{\mathrm{T}})s + 3c_{\mathrm{S}}c_{\mathrm{T}})s^2}{(m_{\mathrm{HBP}} + m_{\mathrm{HTP}})m_{\mathrm{W}}s^4 + \left((d_{\mathrm{S}} + d_{\mathrm{T}})(m_{\mathrm{HBP}} + m_{\mathrm{HTP}}) + 3d_{\mathrm{S}}m_{\mathrm{W}}\right)s^3 + \left((c_{\mathrm{S}} + c_{\mathrm{T}})(m_{\mathrm{HBP}} + m_{\mathrm{HTP}}) + 3c_{\mathrm{S}}m_{\mathrm{W}} + 3d_{\mathrm{S}}d_{\mathrm{T}}\right)s^2 + 3(c_{\mathrm{T}}d_{\mathrm{S}} + c_{\mathrm{S}}d_{\mathrm{T}})s + 3c_{\mathrm{S}}c_{\mathrm{T}}} \tag{B1.2} $$

$$ {}^{\mathcal{L}}G_{\mathrm{DB},\vartheta}(s) = \frac{{}^{\mathcal{L}}_{\mathrm{H}}\ddot{\vartheta}_{\mathrm{HTP,DB}}(s)}{{}^{\mathcal{L}}_{\mathrm{H}}\vartheta_{\mathrm{DSE}}(s)} = \frac{4}{\sqrt{3}}\frac{(c_{\mathrm{T}} + d_{\mathrm{T}}s)(c_{\mathrm{S}} + d_{\mathrm{S}}s)\ell_t s^2}{2\left(J^{(S)}_{\mathrm{HBP},y} + J^{(S)}_{\mathrm{HTP},y}\right)m_{\mathrm{W}}s^4 + \left(2(d_{\mathrm{S}} + d_{\mathrm{T}})\left(J^{(S)}_{\mathrm{HBP},y} + J^{(S)}_{\mathrm{HTP},y}\right) + d_{\mathrm{S}}m_{\mathrm{W}}\ell_t^2\right)s^3 + \left(2(c_{\mathrm{S}} + c_{\mathrm{T}})\left(J^{(S)}_{\mathrm{HBP},y} + J^{(S)}_{\mathrm{HTP},y}\right) + c_{\mathrm{S}}m_{\mathrm{W}}\ell_t^2 + d_{\mathrm{S}}d_{\mathrm{T}}\ell_t^2\right)s^2 + \ell_t^2(c_{\mathrm{T}}d_{\mathrm{S}} + c_{\mathrm{S}}d_{\mathrm{T}})s + c_{\mathrm{S}}c_{\mathrm{T}}\ell_t^2} \tag{B1.3} $$

$$ {}^{\mathcal{L}}G_{\mathrm{MRB},\vartheta}(s) = \frac{{}^{\mathcal{L}}_{\mathrm{H}}\ddot{\vartheta}_{\mathrm{HTP,MRB}}(s)}{{}^{\mathcal{L}}_{\mathrm{H}}\vartheta_{\mathrm{Hex,act}}(s)} = \frac{\left(J^{(S)}_{\mathrm{HBP},y}m_{\mathrm{W}}s^4 + \left((d_{\mathrm{S}} + d_{\mathrm{T}})J^{(S)}_{\mathrm{HBP},y} + d_{\mathrm{S}}m_{\mathrm{W}}\ell_t^2\right)s^3 + \left((c_{\mathrm{S}} + c_{\mathrm{T}})J^{(S)}_{\mathrm{HBP},y} + c_{\mathrm{S}}m_{\mathrm{W}}\ell_t^2 + d_{\mathrm{S}}d_{\mathrm{T}}\ell_t^2\right)s^2 + (c_{\mathrm{T}}d_{\mathrm{S}} + c_{\mathrm{S}}d_{\mathrm{T}})\ell_t^2 s + c_{\mathrm{S}}c_{\mathrm{T}}\ell_t^2\right)s^2}{2\left(J^{(S)}_{\mathrm{HBP},y} + J^{(S)}_{\mathrm{HTP},y}\right)m_{\mathrm{W}}s^4 + \left(2(d_{\mathrm{S}} + d_{\mathrm{T}})\left(J^{(S)}_{\mathrm{HBP},y} + J^{(S)}_{\mathrm{HTP},y}\right) + d_{\mathrm{S}}m_{\mathrm{W}}\ell_t^2\right)s^3 + \left(2(c_{\mathrm{S}} + c_{\mathrm{T}})\left(J^{(S)}_{\mathrm{HBP},y} + J^{(S)}_{\mathrm{HTP},y}\right) + c_{\mathrm{S}}m_{\mathrm{W}}\ell_t^2 + d_{\mathrm{S}}d_{\mathrm{T}}\ell_t^2\right)s^2 + \ell_t^2(c_{\mathrm{T}}d_{\mathrm{S}} + c_{\mathrm{S}}d_{\mathrm{T}})s + c_{\mathrm{S}}c_{\mathrm{T}}\ell_t^2} \tag{B1.4} $$

$$ {}^{\mathcal{L}}G_{\mathrm{DB},\varphi}(s) = \frac{{}^{\mathcal{L}}_{\mathrm{H}}\ddot{\varphi}_{\mathrm{HTP,DB}}(s)}{{}^{\mathcal{L}}_{\mathrm{H}}\varphi_{\mathrm{DSE}}(s)} = \frac{(c_{\mathrm{T}} + d_{\mathrm{T}}s)(c_{\mathrm{S}} + d_{\mathrm{S}}s)2\ell_t s^2}{\left(J^{(S)}_{\mathrm{HBP},x} + J^{(S)}_{\mathrm{HTP},x}\right)m_{\mathrm{W}}s^4 + \left((d_{\mathrm{S}} + d_{\mathrm{T}})\left(J^{(S)}_{\mathrm{HBP},x} + J^{(S)}_{\mathrm{HTP},x}\right) + 2d_{\mathrm{S}}m_{\mathrm{W}}\ell_t^2\right)s^3 + \left((c_{\mathrm{S}} + c_{\mathrm{T}})\left(J^{(S)}_{\mathrm{HBP},x} + J^{(S)}_{\mathrm{HTP},x}\right) + 2c_{\mathrm{S}}m_{\mathrm{W}}\ell_t^2 + 2d_{\mathrm{S}}d_{\mathrm{T}}\ell_t^2\right)s^2 + 2\ell_t^2(c_{\mathrm{T}}d_{\mathrm{S}} + c_{\mathrm{S}}d_{\mathrm{T}})s + 2c_{\mathrm{S}}c_{\mathrm{T}}\ell_t^2} \tag{B1.5} $$

$$ {}^{\mathcal{L}}G_{\mathrm{MRB},\varphi}(s) = \frac{{}^{\mathcal{L}}_{\mathrm{H}}\ddot{\varphi}_{\mathrm{HTP,MRB}}(s)}{{}^{\mathcal{L}}_{\mathrm{H}}\varphi_{\mathrm{Hex,act}}(s)} = \frac{\left(J^{(S)}_{\mathrm{HBP},x}m_{\mathrm{W}}s^4 + \left((d_{\mathrm{S}} + d_{\mathrm{T}})J^{(S)}_{\mathrm{HBP},x} + 2d_{\mathrm{S}}m_{\mathrm{W}}\ell_t^2\right)s^3 + \left((c_{\mathrm{S}} + c_{\mathrm{T}})J^{(S)}_{\mathrm{HBP},x} + 2c_{\mathrm{S}}m_{\mathrm{W}}\ell_t^2 + 2d_{\mathrm{S}}d_{\mathrm{T}}\ell_t^2\right)s^2 + 2(c_{\mathrm{T}}d_{\mathrm{S}} + c_{\mathrm{S}}d_{\mathrm{T}})\ell_t^2 s + 2c_{\mathrm{S}}c_{\mathrm{T}}\ell_t^2\right)s^2}{\left(J^{(S)}_{\mathrm{HBP},x} + J^{(S)}_{\mathrm{HTP},x}\right)m_{\mathrm{W}}s^4 + \left((d_{\mathrm{S}} + d_{\mathrm{T}})\left(J^{(S)}_{\mathrm{HBP},x} + J^{(S)}_{\mathrm{HTP},x}\right) + 2d_{\mathrm{S}}m_{\mathrm{W}}\ell_t^2\right)s^3 + \left((c_{\mathrm{S}} + c_{\mathrm{T}})\left(J^{(S)}_{\mathrm{HBP},x} + J^{(S)}_{\mathrm{HTP},x}\right) + 2c_{\mathrm{S}}m_{\mathrm{W}}\ell_t^2 + 2d_{\mathrm{S}}d_{\mathrm{T}}\ell_t^2\right)s^2 + 2\ell_t^2(c_{\mathrm{T}}d_{\mathrm{S}} + c_{\mathrm{S}}d_{\mathrm{T}})s + 2c_{\mathrm{S}}c_{\mathrm{T}}\ell_t^2} \tag{B1.6} $$

B.2 Linear Controller Evaluation Pitch and Roll

B.2.1 Tire-Sprung System

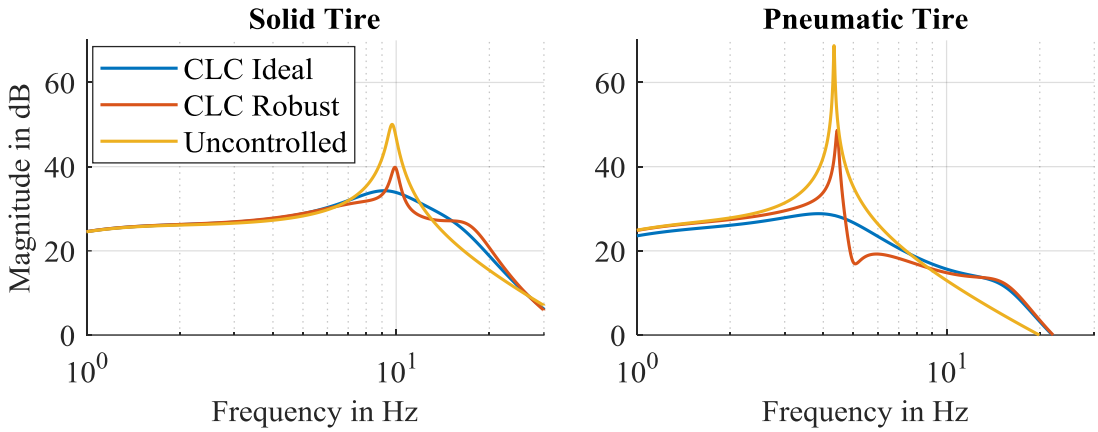

Figure B.1 - 1: Bode plot of frequency-weighed output pitch acceleration (cf. equation (7.25)) comparing the ideal and robust closed-loop control (CLC) approaches to the uncontrolled system. Determined with linear model from subchapter 7.3.

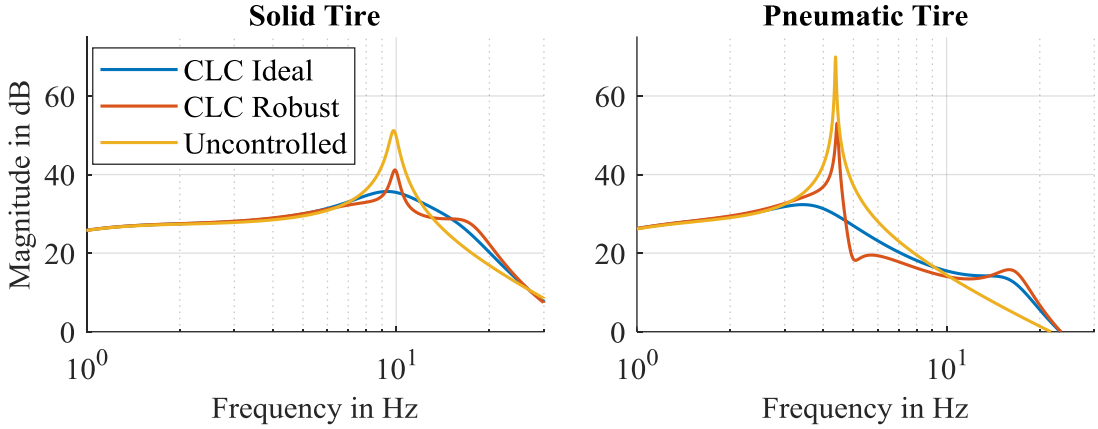

Figure B.1 - 2: Bode plot of frequency-weighed output roll acceleration (cf. equation (7.25)) comparing the ideal and robust closed-loop control (CLC) approaches to the uncontrolled system. Determined with linear model from subchapter 7.3.

B.2.2 Suspension System

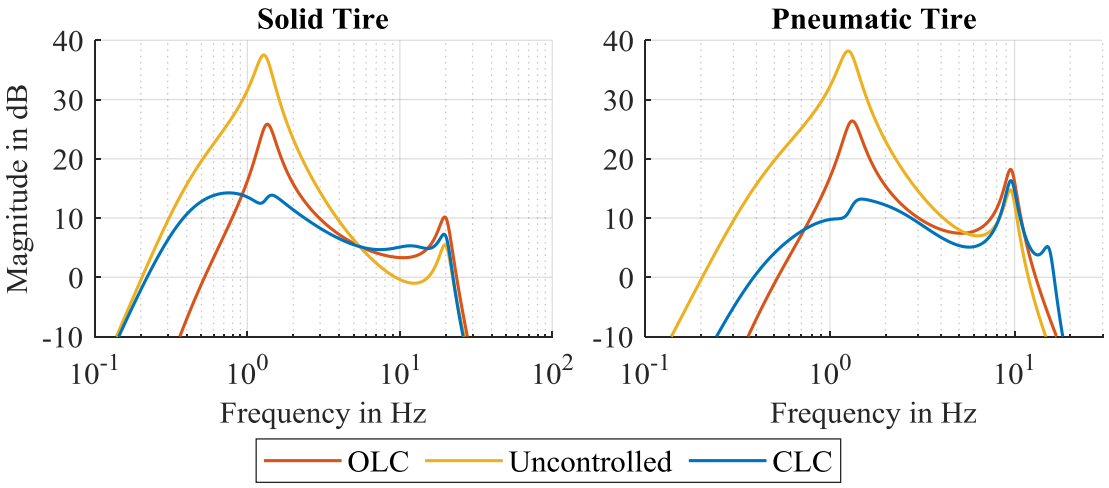

Figure B.1 - 3: Bode plot of frequency-weighed output pitch acceleration (cf. equation (7.25)) comparing the control approaches (open-loop system architecture, OLC; closed-loop system architecture, CLC) to the uncontrolled system. Determined with linear model from subchapter 8.2.2.

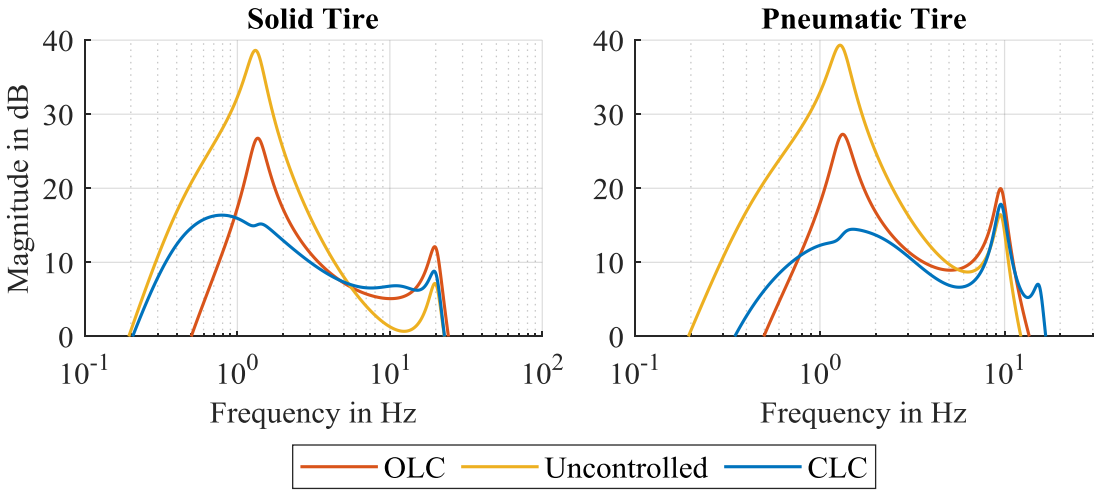

Figure B.1 - 4: Bode plot of frequency-weighed output roll acceleration (cf. equation (7.25)) comparing the control approaches (open-loop system architecture, OLC; closed-loop system architecture, CLC) to the uncontrolled system. Determined with linear model from subchapter 8.2.2.

B.3 Robustness Analysis

B.3.1 Parameter Variations Tire-Sprung System: Pitch and Roll

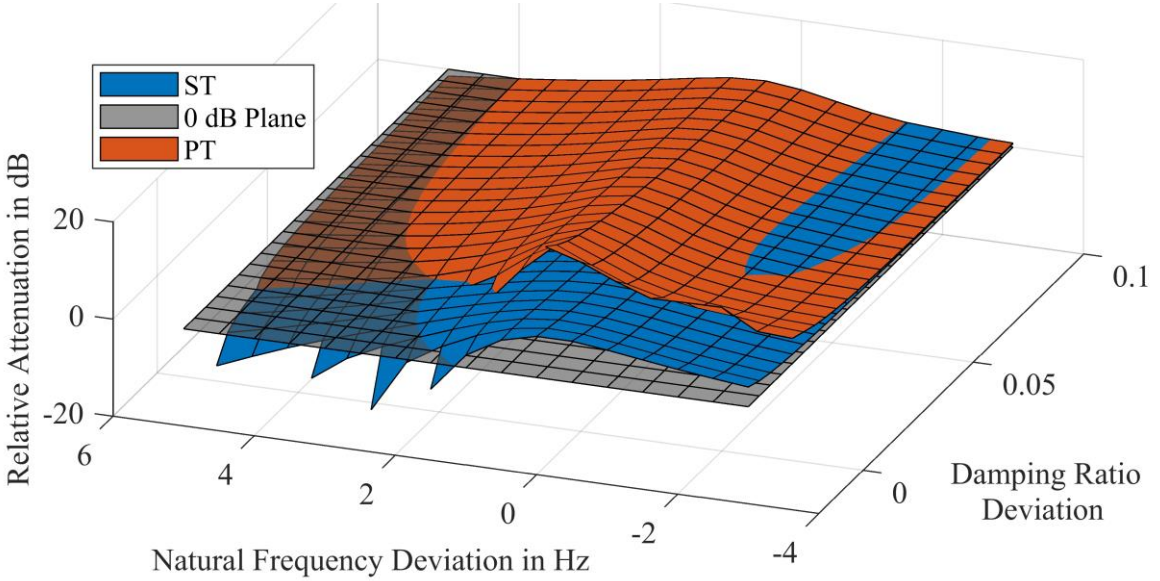

Figure B.2 - 1: Robustness of controller against deviations of vibration parameters for solid (ST) and pneumatic tire (PT) in pitch DoF. Positive values (above 0 dB plane) indicate an improvement by the controller. Determined with linear model from subchapter 7.3 by varying parameters of the vibration system for a fixed control design and evaluating relative attenuation (cf. equation (7.27)).

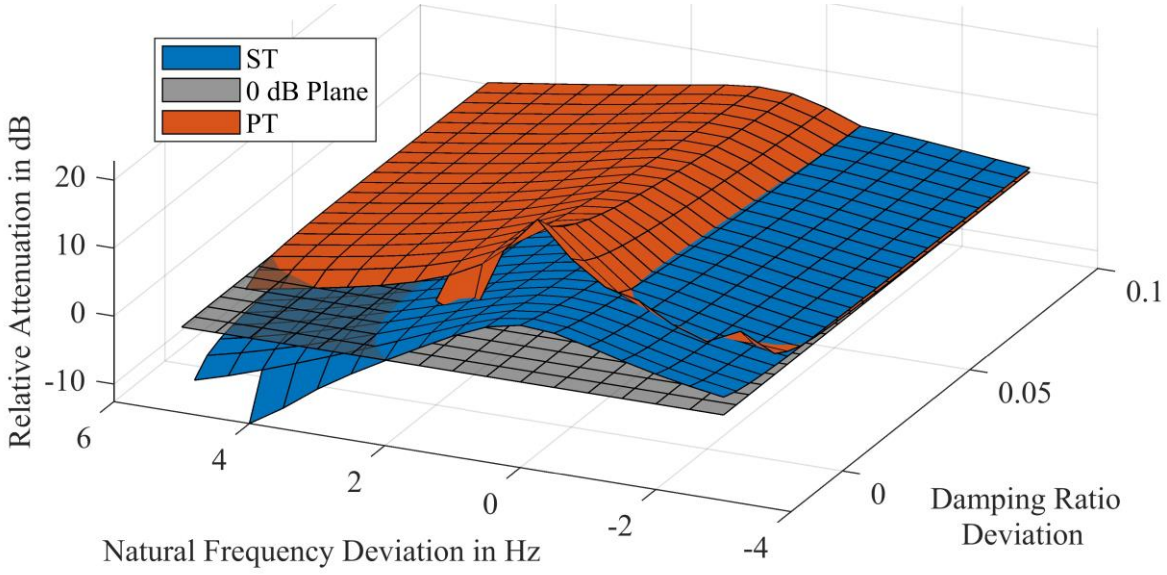

Figure B.2 - 2: Robustness of controller against deviations of vibration parameters for solid (ST) and pneumatic tire (PT) in roll DoF. Positive values (above 0 dB plane) indicate an improvement by the controller. Determined with linear model from subchapter 7.3 by varying parameters of the vibration system for a fixed control design and evaluating relative attenuation (cf. equation (7.27)).

B.3.2 Robustness Dead Time Variations Tire-Sprung System: Pitch and Roll

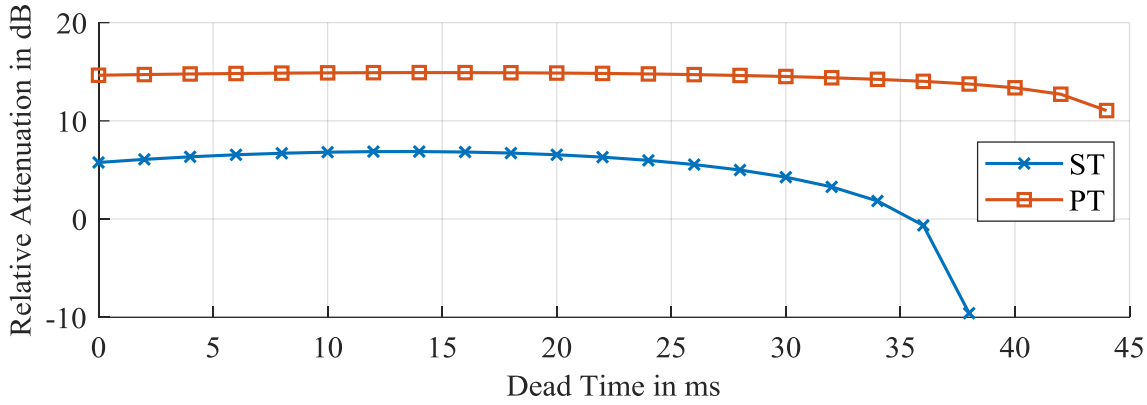

Figure B.2 - 3: Robustness of controller against deviations of dead time for solid (ST) and pneumatic tire (PT) in pitch DoF. Determined with linear model from subchapter 7.3 by varying dead time for a fixed control design and evaluating relative attenuation (cf. equation (7.27)).

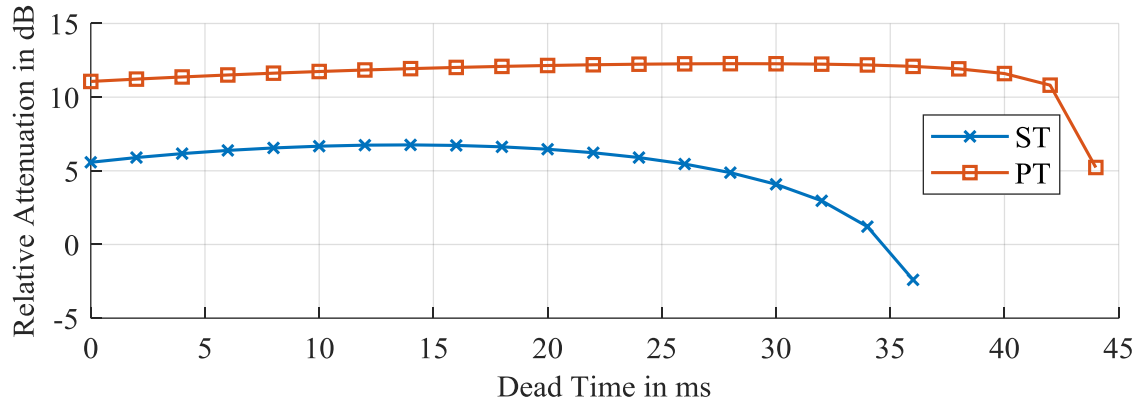

Figure B.2 - 4: Robustness of controller against deviations of dead time for solid (ST) and pneumatic tire (PT) in roll DoF. Determined with linear model from subchapter 7.3 by varying dead time for a fixed control design and evaluating relative attenuation (cf. equation (7.27)).

B.3.3 Parameter Variations Suspension System and Solid Tire: Pitch and Roll

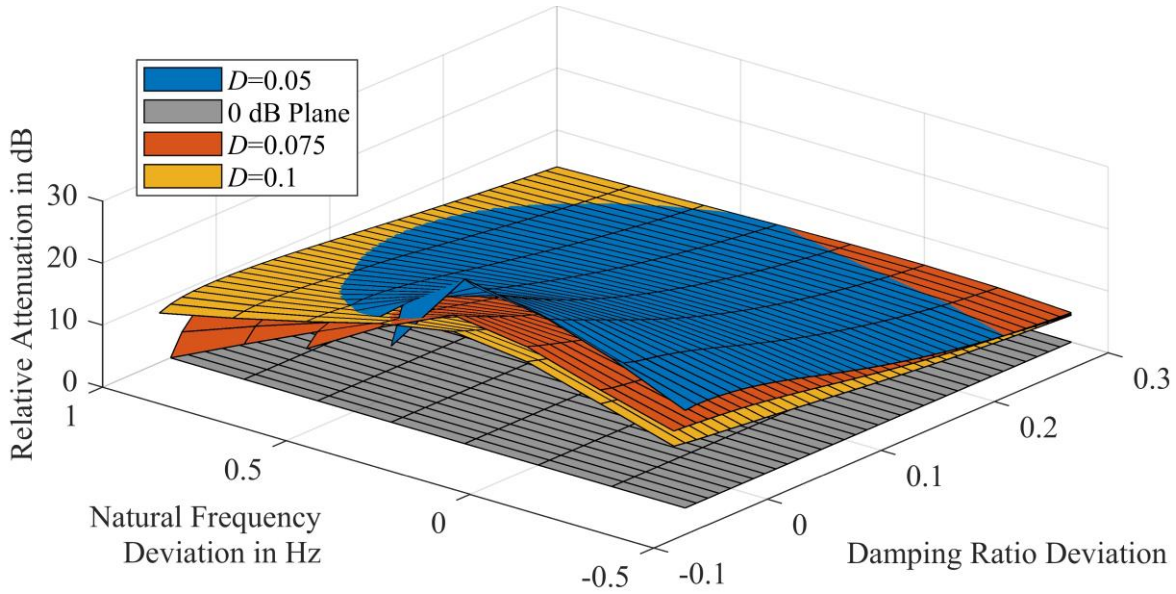

Figure B.2 - 5: Robustness of controller against deviations of vibration parameters for solid tire for different design damping ratios of the controller in pitch DoF. Positive values (above 0 dB plane) indicate an improvement by the controller. Determined with linear model from 8.2.2 by varying parameters of the vibration system for a fixed control design and evaluating relative attenuation (cf. equation (7.27)).

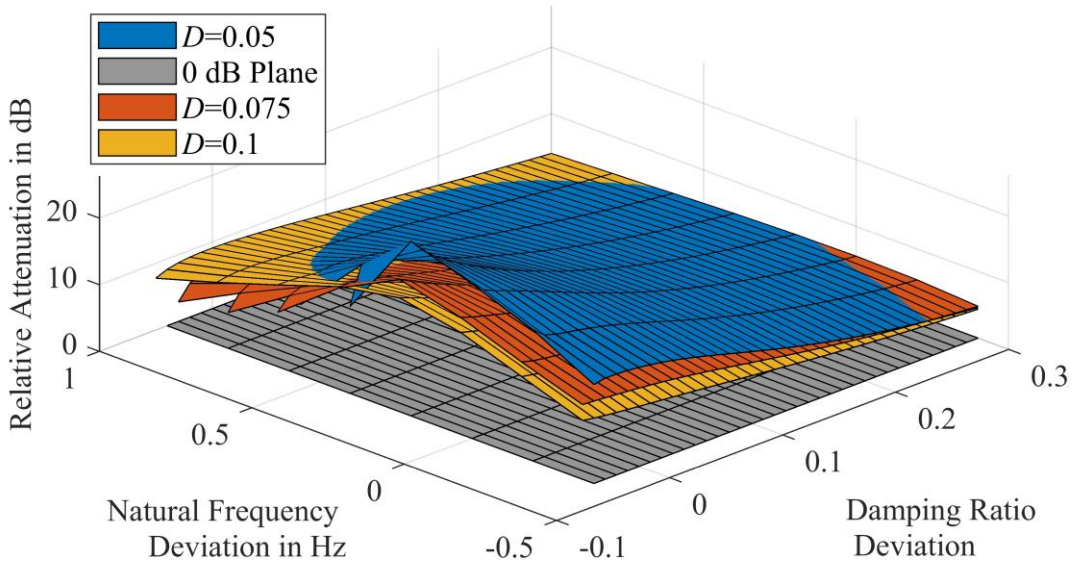

Figure B.2 - 6: Robustness of controller against deviations of vibration parameters for solid tire for different design damping ratios of the controller in roll DoF. Positive values (above 0 dB plane) indicate an improvement by the controller. Determined with linear model from 8.2.2 by varying parameters of the vibration system for a fixed control design and evaluating relative attenuation (cf. equation (7.27)).

B.3.4 Parameter Variations Suspension System and Pneumatic Tire

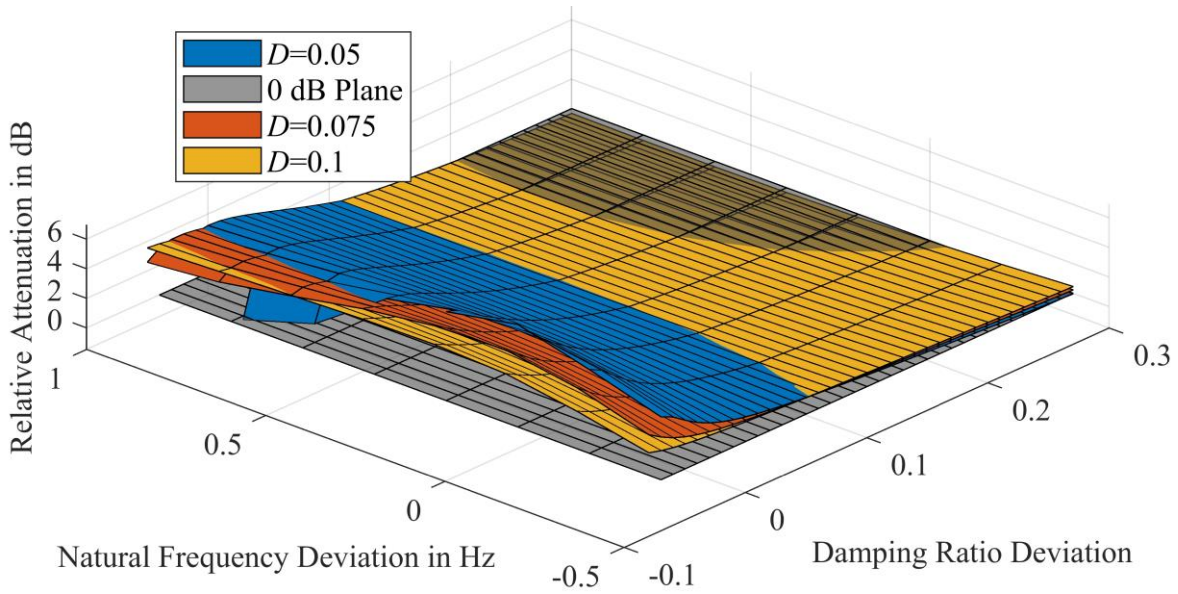

Figure B.2 - 7: Robustness of controller against deviations of vibration parameters for pneumatic tire for different design damping ratios of the controller in vertical DoF. Positive values (above 0 dB plane) indicate an improvement by the controller. Determined with linear model from 8.2.2 by varying parameters of the vibration system for a fixed control design and evaluating relative attenuation (cf. equation (7.27)).

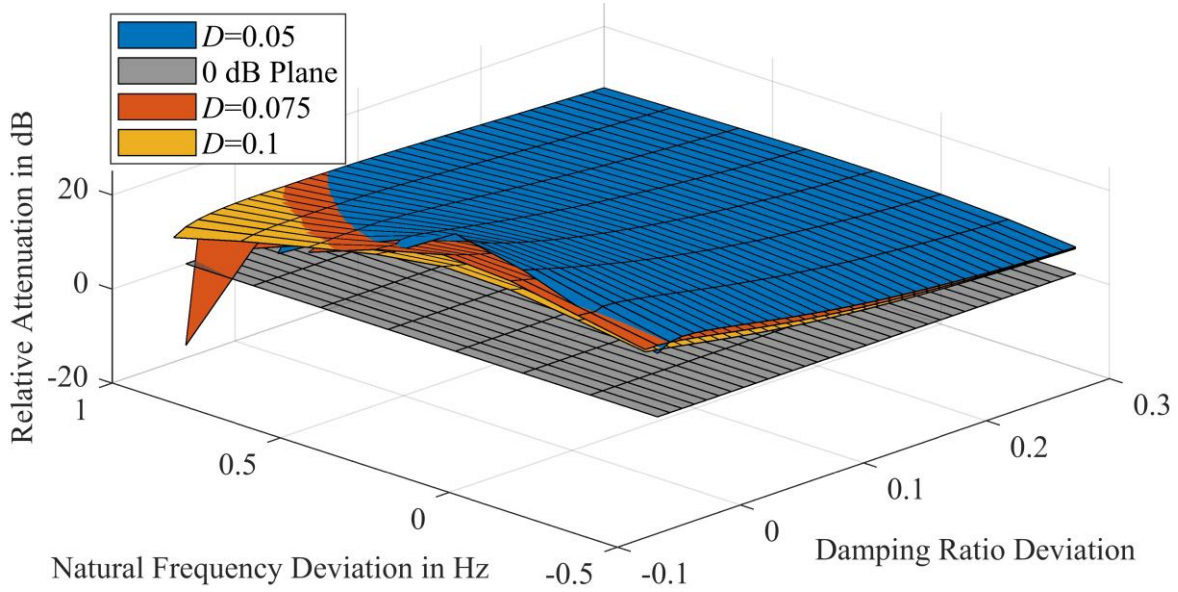

Figure B.2 - 8: Robustness of controller against deviations of vibration parameters for pneumatic tire for different design damping ratios of the controller in pitch DoF. Positive values (above 0 dB plane) indicate an improvement by the controller. Determined with linear model from 8.2.2 by varying parameters of the vibration system for a fixed control design and evaluating relative attenuation (cf. equation (7.27)).

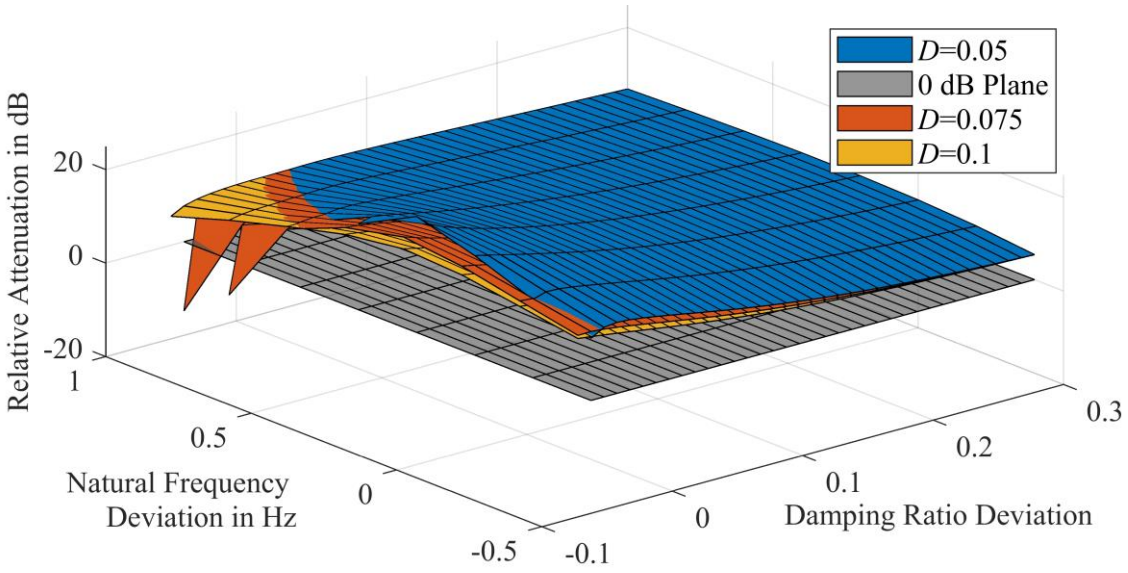

Figure B.2 - 9: Robustness of controller against deviations of vibration parameters for pneumatic tire for different design damping ratios of the controller in roll DoF. Positive values (above 0 dB plane) indicate an improvement by the controller. Determined with linear model from 8.2.2 by varying parameters of the vibration system for a fixed control design and evaluating relative attenuation (cf. equation (7.27)).

B.3.5 Robustness Dead Time Variations Suspension System: Vertical and Roll

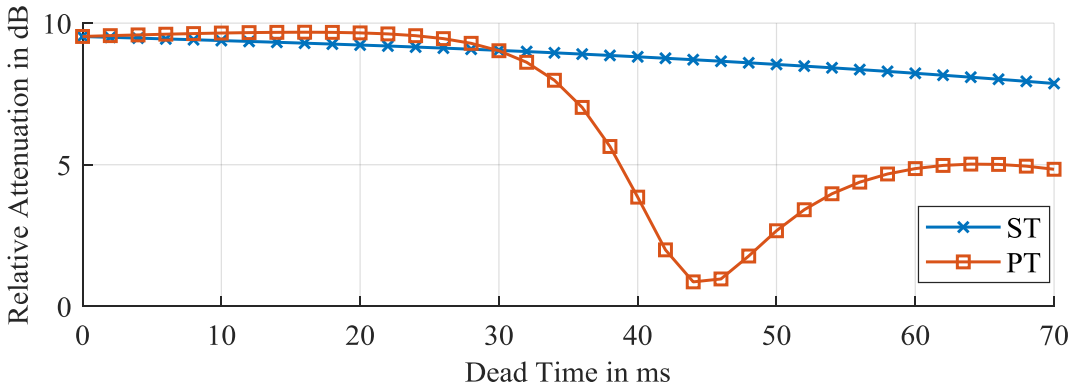

Figure B.2 - 10: Robustness of controller against deviations of dead time for solid (ST) and pneumatic tire (PT) in pitch DoF. Determined with linear model from 8.2.2 by varying dead time for a fixed control design and evaluating relative attenuation (cf. equation (7.27)).

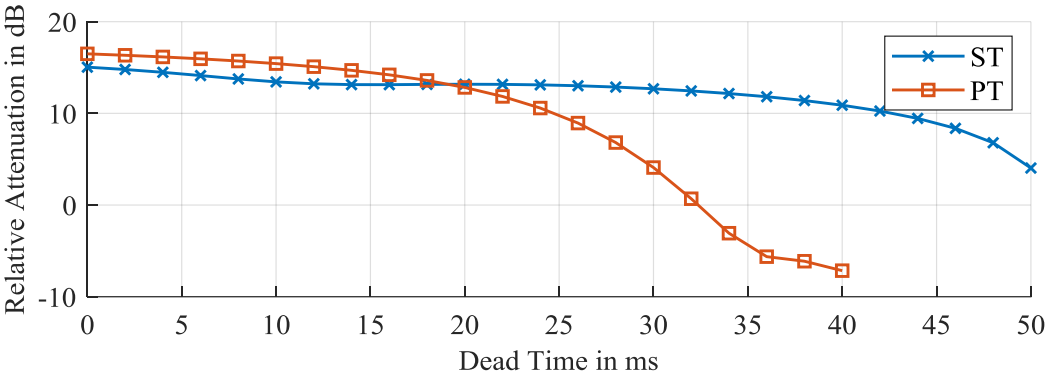

Figure B.2 - 11: Robustness of controller against deviations of dead time for solid (ST) and pneumatic tire (PT) in roll DoF. Determined with linear model from 8.2.2 by varying dead time for a fixed control design and evaluating relative attenuation (cf. equation (7.27)).

C Suspension Design

C.1 Design of Kinematics

C.1.1 Steering Kinematic

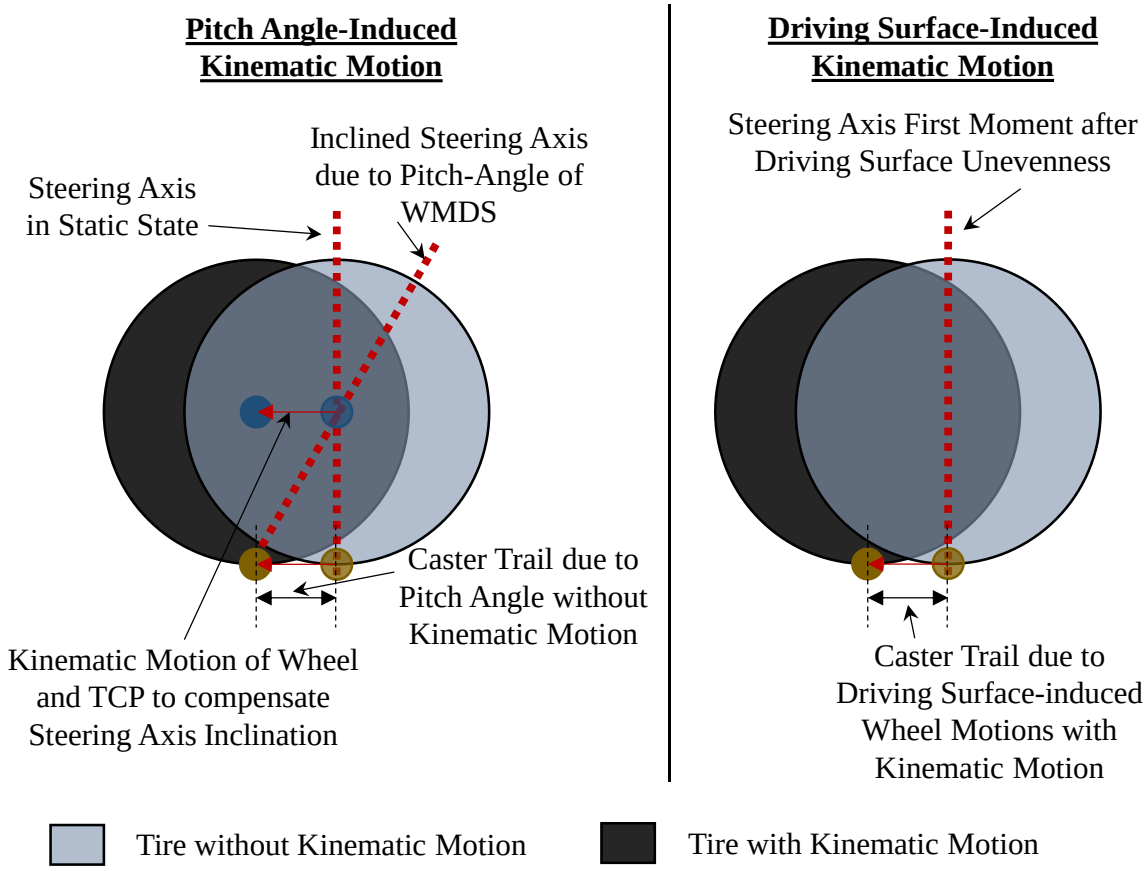

Figure C.1 - 1: Compensation of pitch-induced steering axis inclination through the kinematic motion of the tire contact point

C.1.2 Target Kinematic Change of Support Angle for DMC

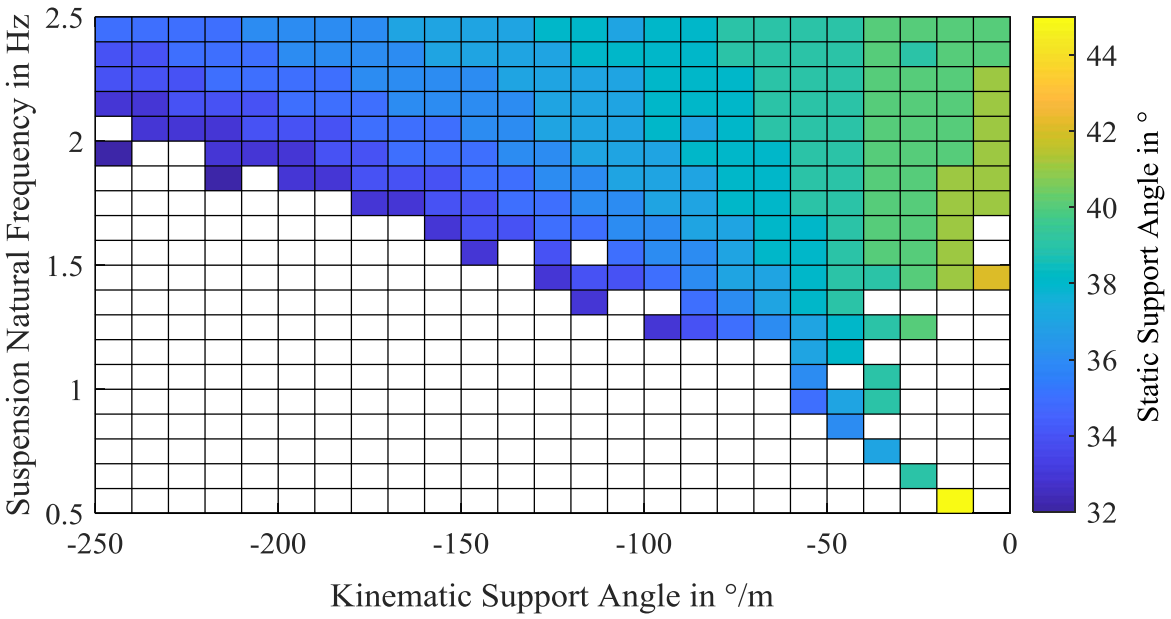

Figure C.1 - 2: Desired static support angle for different kinematic support angle change in dependence of the natural frequency.

C.2 Suspension Concepts

C.2.1 Crank Coupling Concept for DoF Position 1

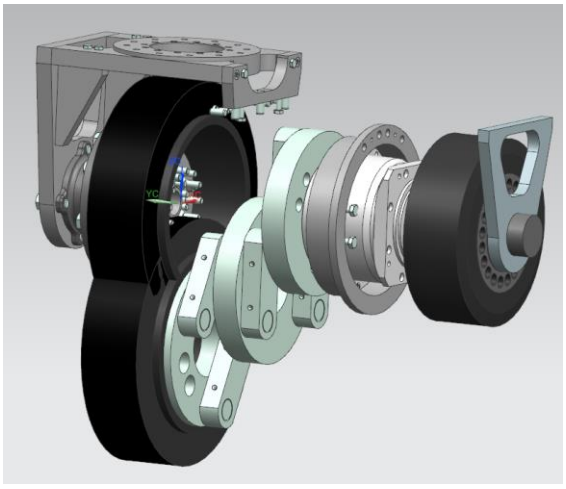

Figure C.2 - 1: Parallel crank coupling concept for torque transmission.

D Component Descriptions and Datasheets

D.1 Hexapod

D.1.1 Representation

Figure D.1 - 1: Mevea motion platform 6DoF 1200E[121]

[121] Directindustry: Mevea Motion Platform 6DOF 1200E (2019).

D.1.2 Hexapod Datasheet

Model	6 DOF 1200E
Degrees of freedom	Surge, Sway, Heave, Roll, Pitch and Yaw
Maximum motions	Surge: ±140 mm Sway: ±130 mm Heave: ±86 mm Roll: ±15 deg Pitch: ±17 deg Yaw: ±22 deg
Maximum velocities	Surge: 280 mm/s Sway: 250 mm/s Heave: 150 mm/s Roll: 30 deg/s Pitch: 30 deg/s Yaw: 50 deg/s
Maximum accelerations	Surge: 0.7 g Sway: 0.7 g Heave: 1.0 g Roll: 170 deg/s^2 Pitch: 170 deg/s^2 Yaw: 200 deg/s^2
Maximum payload	1200 kg
Center of mass	Center of the upper frame and maximum 0.5 m above the upper frame
Current and voltage	400 V 32 A
Dimensions	Upper frame: 0.70 x 0.78 m Lower frame: 1.0 x 1.2 m Height in the lowest position: 0.55 m
Weight	120 kg

Figure D.1 - 2: Specifications of Mevea motion platform 6 DoF 1200E[122]

[122] Mevea Ltd.: Mevea Motion Platform 1200E (2014).

D.1.3 Actuator Datasheet

GSM20 & GSM30 Performance Specifications

Model No.	Frame Size in (mm)	Stroke (nominal)* in (mm)	Screw Lead in (mm)	Continuous Force Rating lb (N) 1 stack/2 stack	Max Velocity in/sec (mm/sec)	Approx. Continuous Motor Torque 1 stack/2 stack lb-in (N-m)	Maximum Static Load lb (N)	Armature Inertia** lb-in-s² (Kg-m²)	Dynamic Load Rating lb (N)	Weight (approx.) lb (kg)
GSM30-0601	3.3 (84)	5.9 (150)	0.1 (2.54)	829/1347 (3688/5992)	5 (127)	16.5/26.8 (1.86/3.03)	1620 (7206)	0.00361 (0.000408)	3310 (14724)	11.5 (5.2)

GSM30 Mechanical and Electrical Specifications

Nominal Backlash	in (mm)	0.008 (.20)
Lead Accuracy	in/ft (mm/300 mm)	0.001 (.025)
Maximum Radial Load	lb (N)	20 (90)
Environmental Rating: Standard/Optional		IP54/IP65

Motor Stator		258
RMS SINUSOIDAL COMMUTATION		
Continuous Motor Torque	lbf-in (Nm)	26.7 (3.02)
Torque Constant (Kt) (+/– 10% @ 25°C)	lbf-in/A (Nm/A)	15.5 (1.75)
Continuous Current Rating	Amps	1.9
Peak Current Rating	Amps	3.8
TRAPEZOIDAL COMMUTATION		
Continuous Motor Torque	lbf-in (Nm)	25.5 (2.88)
Torque Constant (Kt) (+/– 10% @ 25°C)	lbf-in/A (Nm/A)	12.1 (1.37)
Continuous Current Rating	Amps	2.4
Peak Current Rating	Amps	4.7

MOTOR STATOR DATA		
Voltage Constant (Ke)	Vrms/Krpm	106.0
(+/– 10% @ 25°C)	Vpk/Krpm	149.9
Pole Configuration		8
Resistance (L-L)(+/– 5% @ 25°C)	Ohms	14.1
Inductance (L-L)(+/– 15%)	mH	46.2
Brake Inertia	lb-in-sec² (Kg-cm²)	0.00033 (0.38)
Brake Current @ 24 VDC	A	.5
Brake Holding Torque	lbf-in (Nm)	70 (8)
Brake Engage/Disengage Time	ms	19/29
Mechanical Time Constant (tm), ms	min	2.6
	max	4.4
Electrical Time Constant (te)	ms	3.3
Damping Constant	lbf-in/krpm (N-m/krpm)	1.23 (0.14)
Friction Torque	lbf-in (Nm)	2.00 (0.23)
Bus Voltage	Vrms	400
Speed @ Bus Voltage	rpm	3000
Insulation Class		180 (H)

Figure D.1 - 3: Specification of Exlar GSM30 actuators applied in the Mevea Hexapod[123]

[123] Exlar Automation: Exlar GSM (2014).

D.2 Suspension Components

D.2.1 Suspension Spring

Formelzeichen	Wert	Einheit	Beschreibung
Mat	EN 10270-1	-	Werkstoffart
s2		mm	Strecke der Feder gespannt
L2		mm	Länge der Feder gespannt
F2		N	Kraft der Feder gespannt
Fdn	Angelegt und geschliffen	-	Federenden
d	11	mm	Drahtdurchmesser
D	89	mm	Mittlerer Windungsdurchmesser
Dd		mm	Dorndurchmesser
De	100	mm	Äußerer Windungsdurchmesser
Detol	1,5	mm	(+/-) Toleranz für Windungsdurchmesser
Dh		mm	Hülsendurchmesser
F1tol		N	(+/-) Toleranz Kraft der Feder vorgespannt
F2tol		N	(+/-) Toleranz Kraft der Feder gespannt
Fn	4050,469	N	Höchstkraft der Feder
Fntol	166	N	(+/-) Toleranz für statische Höchstkraft
Lk	451	mm	Knicklänge
L0	620	mm	Ungespannte Länge der Feder
L0tol	9,26	mm	(+/-) Toleranz für ungespannte Länge der Feder
L1		mm	Länge der Feder vorgespannt
Ln	265,83	mm	Kleinste Länge der Feder
s1		mm	Strecke der Feder vorgespannt
sn	354,17	mm	Größter Federweg bei statischer Belastung
S	32,919	mm	Steigung der Federn
n	18,5	Stück	Anzahl der federnden Windungen
nt		Stück	Anzahl der Gesamtwindungen
R	11,437	N/mm	Federrate
Fndyn		N	Dynamische Höchstkraft
Fndtol		N	(+/-) Toleranz für dynamische Höchstkraft
Lndyn		mm	Kleinste Länge dynamische Belastung
shdyn		mm	Größter Federweg dynamische Belastung
Gew	4305,7562	g	Gewicht des Artikels
PG	BF	-	Preisgruppe für diesen Artikel

Figure D.2 - 1: Specifications of suspension spring.[124]

[124] Gutekunst + Co.KG Federnfabriken: Compression Spring D-488.

D.2.2 Suspension Damper

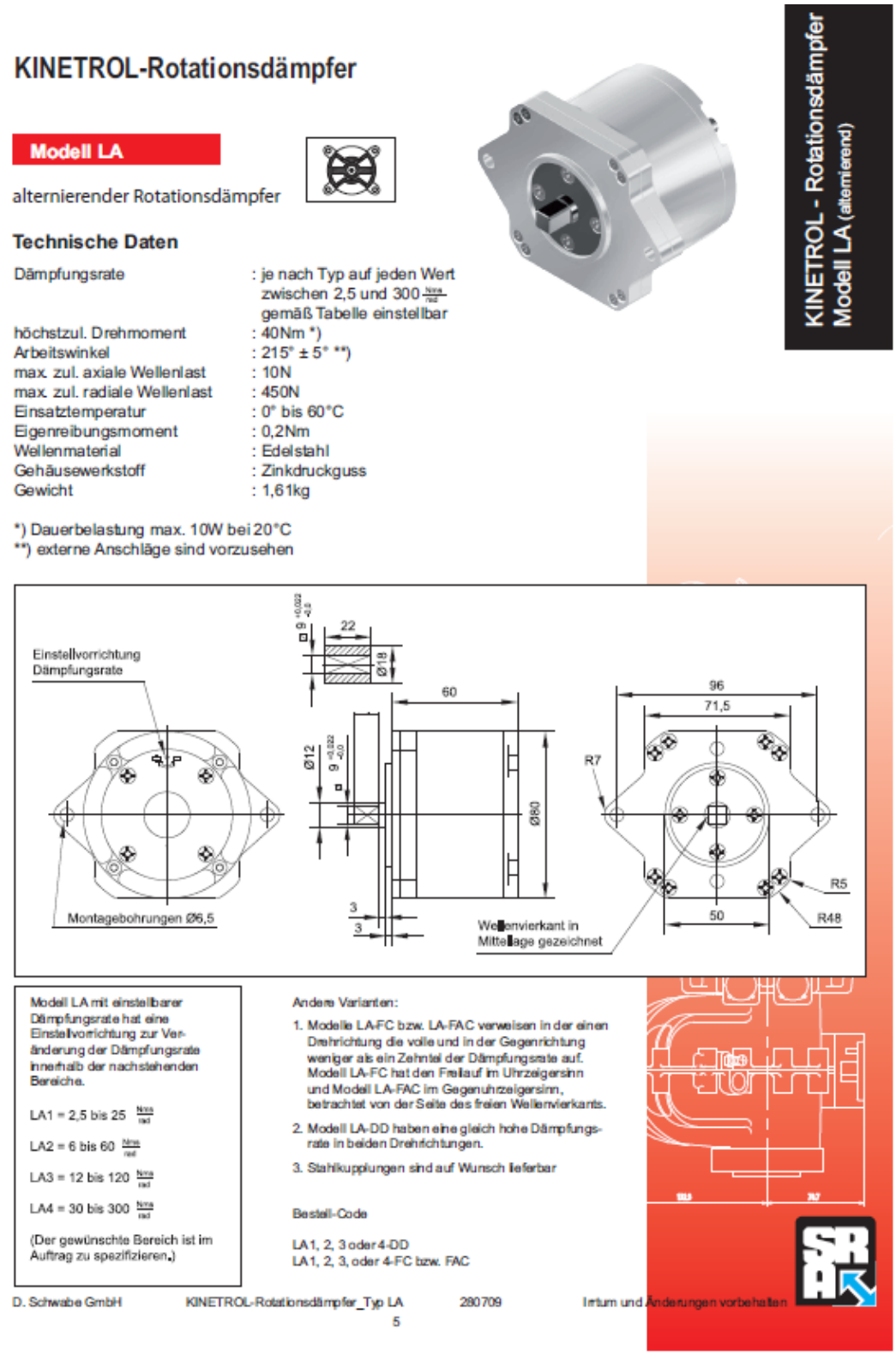

Figure D.2 - 2: Specifications of suspension damper.[125]

[125] D. Schwabe GmbH: Kinetrol Rotationsdämpfer. p. 5.

List of References

A&D GmbH: Vehicle Measurement System Description (2013)
A&D GmbH: Vehicle Measurement System Description, Darmstadt, 2013

Adamski, D.: Simulation Fahrwerktechnik (2014)
Adamski, Dirk: Simulation in der Fahrwerktechnik, ATZ / MTZ-Fachbuch, Springer Vieweg, Wiesbaden, 2014

Ammon, D.: Problems in Road Surface Modelling (1992)
Ammon, Dieter: Problems in Road Surface Modelling, in: Vehicle System Dynamics sup. 1, Issues 20, pp. 28–41, 1992

Banic, M. et al.: Advanced Design Project 82/16, Anlage Vermessung Fahrbahnprofile (2016)
Banic, Michael; Kappes, Aaron; Karabulut, Derya; Kerres, David; Ladewig, Lennart; Mayer, Philipp: Entwicklung einer Anlage zur Vermessung realer Fahrbahnprofile in vertikaler Richtung, Advanced Design Project 82/16
Technische Universität Darmstadt, Darmstadt, 2016

Baumann, G. et al.: How to build Europe's largest eight-axes DS (2012)
Baumann, Gerd; Riemer, Thomas; Liedecke, Christoph; Rumbolz, Philip; Schmidt, Andreas: How to build Europe's largest eight-axes motion simulator, in: Espié, Stéphane; Kemeny, Andras; Mérienne, Frédéric (Eds.): Proceedings of the driving simulation conference Europe 2012, Actes INRETS A 134, INRETS, Bron, 2012

Bellmann, M. A.: Diss., Perception of Whole-Body Vibrations (2002)
Bellmann, Michael A.: Perception of Whole-Body Vibrations: From basic experiments to effects of seat and steering-wheel vibrations on the passenger's comfort inside vehicles, Dissertation Universität Oldenburg, 2002

Berthoz, A. et al.: Motion Scaling for DS (2013)
Berthoz, A.; Bles, W.; Bülthoff, H. H.; Correia Gracio, B. J.; Feenstra, P.; Filliard, N.; Huhne, R.; Kemeny, A.; Mayrhofer, M.; Mulder, M.: Motion Scaling for High-Performance Driving Simulators, in: IEEE Transactions on Human-Machine Systems no. 3,vol. 43, pp. 265–276, 2013

Betschinske, D.: BaTh, Verringerung Lenkleistungsbedarf WMDS (2016)
Betschinske, Daniel: Untersuchung von Methoden zur Verringerung des Lenkleistungsbedarfs des selbstfahrenden Fahrsimulators, BaTh
Technische Universität Darmstadt, Darmstadt, 2016

Betz, A. et al.: Concept Analysis of a WMDS (2012)

Betz, Alexander; Hämisch, Robert; Müller, Marius; Winner, Hermann: Concept Analysis of a Wheeled Mobile Driving Simulator Showing an Omnidirectional Motion Base for Urban Traffic Simulation, in: Berechnung, Simulation und Erprobung im Fahrzeugbau 2012, VDI-Berichte Nr. 2169, VDI-Verl., Düsseldorf, 2012

Betz, A. et al.: Driving Dynamics Control of a WMDS (2013)

Betz, Alexander; Butry, Andreas; Junietz, Phlipp; Wagner, Paul; Winner, Hermann: Driving Dynamics Control of a Wheeled Mobile Driving Simulator Utilizing an Omnidirectional Motion Base for Urban Traffic Simulation, in: Future Active Safety Technology toward zero-traffic-accident, Nagoya, Japan, 2013

Betz, A.: Diss., Feasibility and Design of WMDS (2014)

Betz, Alexander: Feasibility Analysis and Design of Wheeled Mobile Driving Simulators for Urban Traffic Simulation, Dissertation Technische Universität Darmstadt, Darmstadt, 2014

Boer, E. R. et al.: The Role of DS in Developing and Evaluating AD (2015)

Boer, Erwin R.; Penna, Mauro D.; Utz, Hans; Pedersen, Liam; Siehuis, Maarten: The Role of Driving Simulators in Developing and Evaluating Autonomous Vehicles, in: Bülthoff, Heinrich; Kemeny, Andras; Pretto, Paolo (Eds.): Proceedings of DSC 2015 Europe Driving Simulation Conference & Exhibition, Tübingen, 2015

Braun, H.: Diss., Untersuchung von Fahrbahnunebenheiten (1969)

Braun, H.: Untersuchung von Fahrbahnunebenheiten und Anwendungen der Ergebnisse, Dissertation Technische Universität Braunschweig, 1969

Braun, H.: Meßergebnisse von Straßenunebenheiten (1991)

Braun, H.: Meßergebnisse von Straßenunebenheiten, in: VDI, Verein Deutscher Ingenieure (Ed.): Unebenheiten von Schiene und Straße als Schwingungsursache, VDI-Berichte, 1991

Chapron, T.; Colinot, J.-P.: The new PSA Peugeot-Citroën Advanced DS (2007)

Chapron, Thomas; Colinot, Jean-Pierre: The new PSA Peugeot-Citroën Advanced Driving Simulator Overall design and motion cue algorithm, in: Proceedings of the Driving Simulator Conference 2007, Iowa City, Iowa, 2007

Claus, S.: Diss., Kompensation Verzugszeiten semiaktive Fahrwerkregelung (2016)

Claus, Sebastian: Vorausschauende Kompensation von Verzugszeiten im Regelkreis der semiaktiven Fahrwerkregelung, Dissertation Technische Universität Darmstadt, 2016

D. Schwabe GmbH: Kinetrol Rotationsdämpfer

D. Schwabe GmbH: Kinetrol Rotationsdämpfer; https://schwabe-sra.de/wp-content/uploads/2017/11/Katalog-KINETROL-Rotationsdaempfer.pdf, Access 13.05.2019

Deutsches Institut für Normung e. V.: DIN 18202 - Toleranzen im Hochbau (2005)
Deutsches Institut für Normung e. V.: DIN 18202 - Toleranzen im Hochbau - Bauwerke, 2005

Deutsches Institut für Normung e. V.: ISO 8855 - Fahrdynamik Begriffe (2013)
Deutsches Institut für Normung e. V.: ISO 8855 - Straßenfahrzeuge - Fahrzeugdynamik und Fahrverhalten - Begriffe, Beuth, Berlin, 2013

DIN Deutsches Institut für Normung e.V.: ISO 8041-1 - Human Response to Vibration (2017)
DIN Deutsches Institut für Normung e.V.: ISO 8041-1 - Human response to vibration - measuring instrumentation - Part 1: General purpose vibration meters, Beuth Verlag, 2017

Directindustry: Mevea Motion Platform 6DOF 1200E (2019)
Directindustry: Mevea Motion Platform 6DOF 1200E; http://www.directindustry.de/prod/mevea/product-64809-850923.html, 2019, Access 02.05.2019

Dobbeck, R.: Diss., Beschleunigungen in Fahrsimulatoren (1974)
Dobbeck, R.: Darstellung von Beschleunigungen in Fahrsimulatoren bis in den Grenzbereich, Dissertation Technische Universität Berlin, Berlin, 1974

Donges, E.: Fahrsimulator (2002)
Donges, Edmund: Fahrsimulator, Bayrische Motoren Werke AG, Patent DE000010106150A1, Patent application number: 101 06 150.1, 2002

Ersoy, M.: Achsen und Radaufhängungen (2013)
Ersoy, Metin: Achsen und Radaufhängungen, in: Heißing, Bernd; Ersoy, Metin; Gies, Stefan (Eds.): Fahrwerkhandbuch, 4. Edition, Springer Vieweg, Wiesbaden, 2013

Ersoy, M.; Gies, S.: Chassis Handbook Fundamentals (2011)
Ersoy, Metin; Gies, Stefan: Introduction and Fundamentals, in: Heißing, Bernd; Ersoy, Metin (Eds.): Chassis Handbook, 1. Edition, Vieweg+Teubner (GWV), Wiesbaden, 2011

Exlar Automation: Exlar GSM (2014)
Exlar Automation: GSM Series Catalog, Chanhassen, USA, 2014

Fischer, M.: Diss., Motion-Cueing-Algorithmen (2009)
Fischer, Martin: Motion-Cueing-Algorithmen für eine realitätsnahe Bewegungssimulation, Dissertation Technische Universität Braunschweig, 2009

GeneSys Elektronik GmbH: ADMA (2018)
GeneSys Elektronik GmbH: ADMA: Automotive Dynamic Motion Analyzer; https://www.genesys-offenburg.de/index.php?eID=tx_securedownloads&p=25&u=0&g=0&t=1556178624&hash=ded316afffcdf30dd51bc3bc62d47b3a69654a96&file=fileadmin/user_upload/ProdBeschr_ADMA_rel_03.2018.pdf, 2018, Access 24.04.2019

Gipser, M.: FTire (2007)
Gipser, M.: FTire – the tire simulation model for all applications related to vehicle dynamics, in: Vehicle System Dynamics sup. 1, Issues 45, pp. 139–151, 2007

Graupner, M.: Bachelor Thesis, Entwicklung Stadtparcours (2011)
Graupner, Maren: Entwicklung eines repräsentativen Stadtparcours mittels makroskopischer Betrachtung lokaler Verkehrsbereiche, Bachelor Thesis Technische Universität Darmstadt, Darmstadt, 2011

Greenberg, J. et al.: Lateral motion cues during simulated driving (2003)
Greenberg, Jeff; Artz, Bruce; Cathey, Larry: The effect of lateral motion cues during simulated driving, in: Proceedings of the Driving Simulator Conference 2003, Dearborn, Michigan, 2003

Gumasol Rubber-Tec GmbH: Datasheet Gumasol-Softy (2014)
Gumasol Rubber-Tec GmbH: Datasheet Gumasol-Softy, Germersheim, 2014

Gutekunst + Co.KG Federnfabriken: Compression Spring D-488
Gutekunst + Co.KG Federnfabriken: Compression Spring D-488; https://www.federnshop.com/de/produkte/druckfedern/d-488.html, Access 02.05.2019

Haberhauer, H.: Kupplungen und Bremsen (2014)
Haberhauer, Horst: Kupplungen und Bremsen, in: Haberhauer, Horst; Kaczmarek, Manfred (Eds.): Taschenbuch der Antriebstechnik, Fachbuchverl. Leipzig im Hanser, München, 2014

Haken, K.-L.: Grundlagen der Kraftfahrzeugtechnik (2015)
Haken, Karl-Ludwig: Grundlagen der Kraftfahrzeugtechnik, 4. Edition, Hanser, München, 2015

Hüsing, K.: Fahrsimulator (2003)
Hüsing, Kurt: Fahrsimulator, Bayerische Motoren Werke AG, Patent DE000010158101A1, Patent application number: 101 58 101.7, 2003

ISO: ISO 8608-1 - Road surface profiles (1995)
ISO: 1: ISO 8608 - Mechanical vibrations - Road surface profiles - Reporting of measured data, 1995

ISO: ISO 2631-1 - Mechanical Vibration (1997)
ISO: ISO 2631-1 - Mechanical vibration and shock - Evaluation of human exposure to whole-body vibration. Part 1: General requirements, 1997

Jürgens, H. W.: Anthropometrische Maße (2004)
Jürgens, Hans W.: Erhebung anthropometrischer Maße zur Aktualisierung der DIN 33 402 - Teil 2, Schriftenreihe der Bundesanstalt für Arbeitsschutz und Arbeitsmedizin Forschung Arbeitsschutz, Issues 1023, Wirtschaftsverl. N.W Verl. für Neue Wissenschaft, Bremerhaven, 2004

Kässens, A.: Bachelorthesis, Modellbildung Hexapod MORPHEUS (2016)
Kässens, Adrian: Modellbildung des Hexapod des MORPHEUS zur Untersuchung der Eignung für eine Vertikaldynamikregelung, Bachelorthesis
Technische Universität Darmstadt, Darmstadt, 2016

Lunze, J.: Regelungstechnik (2010)
Lunze, Jan: Regelungstechnik, Springer-Lehrbuch, 8. Edition, Springer, Berlin, 2010

Mack, C. A.: Analytic form of PSD (2011)
Mack, Chris A.: Analytic form for the power spectral density in one, two, and three dimensions, in: Journal of Micro/Nanolithography, MEMS, and MOEMS (4), Issues 10, pp. 1–2, 2011

MacNeilage, P. R. et al.: Vestibular heading discrimination (2010)
MacNeilage, Paul R.; Banks, Martin S.; DeAngelis, Gregory C.; Angelaki, Dora E.: Vestibular heading discrimination and sensitivity to linear acceleration in head and world coordinates, in: The Journal of neuroscience : the official journal of the Society for Neuroscience (27), Issues 30, pp. 9084–9094, 2010

Magnus, K. et al.: Schwingungen (2016)
Magnus, Kurt; Popp, Karl; Sextro, Walter: Schwingungen, 10. Edition, Springer Vieweg, Wiesbaden, 2016

Mallery, R. M. et al.: Discrimination of rotational velocities (2010)
Mallery, Robert M.; Olomu, Osarenoma U.; Uchanski, Rosalie M.; Militchin, Valentin A.; Hullar, Timothy E.: Human discrimination of rotational velocities, in: Experimental brain research (1), Issues 204, pp. 11–20, 2010

Mansfield, N. J.; Griffin, M. J.: Difference thresholds automobile seat vibration (2000)
Mansfield, N. J.; Griffin, Michael J.: Difference thresholds for automobile seat vibration, in: Applied Ergonomics (31), pp. 255–261, 2000

Markert, R.: Strukturdynamik (2013)
Markert, Richard: Strukturdynamik, Mechanik, Shaker, Aachen, 2013

Matschinsky, W.: Radführungen der Straßenfahrzeuge (2007)
Matschinsky, Wolfgang: Radführungen der Straßenfahrzeuge, 3. Edition, Springer-Verlag Berlin Heidelberg, Berlin, Heidelberg, 2007

Matsumoto, Y. et al.: Difference Thresholds Whole-Body Vibration (2002)
Matsumoto, Yasunao; Maeda, Setsuo; Oji, Yasushi: Influence of Frequency on Difference Thresholds for Magnitude of Vertical Sinusoidal Whole-Body Vibration, in: Industrial Health (40), pp. 313–319, 2002

Maurer, M. et al.: Autonomes Fahren (2015)
Maurer, Markus; Gerdes, J. C.; Lenz, Barbara; Winner, Hermann: Autonomes Fahren, Springer Vieweg, Berlin, 2015

Mehren, M.: Masterthesis, Hexapod Vertikaldynamikregelung (2017)
Mehren, Michael: Entwicklung von Steuerungen und Regelungen für bestehende Systemarchitekturen einer Hexapod Vertikaldynamikregelung, Masterthesis Technische Universität Darmstadt, Darmstadt, 2017

Mevea Ltd.: Mevea Motion Platform 1200E (2014)
Mevea Ltd.: Specifications Motion Platform 6 DOF 1200E, Lappeenranta, 2014

Mitschke, M.; Wallentowitz, H.: Dynamik der Kraftfahrzeuge (2014)
Mitschke, Manfred; Wallentowitz, Henning: Dynamik der Kraftfahrzeuge, VDI-Buch, 5. Edition, Springer Vieweg, Wiesbaden, 2014

Moroika, M.; Griffin, M. J.: Difference thresholds for intensity perception (2000)
Moroika, Miyuki; Griffin, Michael J.: Difference thresholds for intensity perception of whole-body vertical vibrations: effect of frequency and magnitude, in: Journal of the Acoustical Society of America (1), Issues 107, pp. 620–624, 2000

Müller, T. et al.: JND Longitudinal Acceleration (2013)
Müller, Thomas; Hajek, Hermann; Radić-Weißenfeld, Ljubica; Bengler, Klaus: Can You Feel The Difference?, in: Proceedings of the Human Factors and Ergonomics Society Annual Meeting (1), Issues 57, pp. 1219–1223, 2013

Naseri, A. R.; Grant, P. R.: Human discrimination of translational accelerations (2012)
Naseri, Amir R.; Grant, Peter R.: Human discrimination of translational accelerations, in: Experimental brain research (3), Issues 218, pp. 455–464, 2012

Negele, H. J.: Diss., Konzipierung Fahrsimulatoren (2007)
Negele, Hans J.: Anwendungsgerechte Konzipierung von Fahrsimulatoren für die Fahrzeugentwicklung, Dissertation Technische Universität München, 2007

Oertel, C.; Fandre, A.: Reifenmodell RMOD-K (2001)
Oertel, Christian; Fandre, Andreas: Das Reifenmodellsystem RMOD-K, in: ATZ - Automobiltechnische Zeitschrift (11), Issues 103, pp. 1074–1079, 2001

Pacejka, H. B.; Besselink, I.: Tire and vehicle dynamics (2012)
Pacejka, H. B.; Besselink, Igo: Tire and vehicle dynamics, 3. Edition, 2012

Parchilowskij, J. G.: Verteilungsdichte der Unebenheiten (1961)
Parchilowskij, J. G.: Spektrale Verteilungsdichte der Unebenheiten des Mikroprofils der Straßen und die Schwingungen des Kraftfahrzeuges, in: Automobilnaja Promischlenost, Issues 10, 1961

Pielemeier, W.J., Jeyabalan, V. et al.: JND vertical vibration automobile seat (1997)
Pielemeier, W.J., Jeyabalan, V.; Meier, R. C.; Otto, N. C.: Just noticeable difference in vertical vibration for subjects on an automobile seat, in: United Kingdom Group Meeting on Human Response to Vibration, Southhampton, 1997

Pischinger, S.; Seiffert, U.: Vieweg Handbuch Kraftfahrzeugtechnik (2016)
Pischinger, Stefan; Seiffert, Ulrich (Eds.) Vieweg Handbuch Kraftfahrzeugtechnik, ATZ / MTZ-Fachbuch, 8. Edition, Springer Vieweg, Wiesbaden, 2016

Quarz, V.: Diss., Generierung von Fahrwegstörungen (2004)
Quarz, Volker: Die Generierung von Fahrwegstörungen für vorgegebene Spektraldichten mit Hilfe orthogonaler Funktionen, Dissertation Technische Universität Dresden, 2004

Reason, J. T.; Brand, J. J.: Motion Sickness (1975)
Reason, J. T.; Brand, J. J.: Motion Sickness, Academic Press, London, 1975

Richter, A.; Scholz, M.: The Surveyor's Guide to Automotive Simulation (2016)
Richter, A.; Scholz, M.: "The Surveyor's Guide to Automotive Simulation": Development and Evaluation of Guidelines for Straight forward Road Surveying for Driving Simulator Databases and Test Development of Driver Assistance and Automation Systems, in: Proceedings of DSC 2016 Europe Driving Simulation & Virtual Reality Conference & Exhibition, Paris, France, 2016

Roth, J.: Diss., Kraftübertragung Pkw-Reifen (1993)
Roth, J.: Untersuchungen zur Kraftübertragung zwischen Pkw-Reifen und Fahrbahn unter besonderer Berücksichtigung der Kraftschlusserkennung im rotierenden Rad, Dissertation TH Darmstadt, VDI-Fortschrittsberichte, Reihe 12, Issues 195, Düsseldorf, 1993

Schmeitz, A.J.C.: Diss., Semi-Empirical Pneumatic Tyre Model (2004)
Schmeitz, A.J.C.: A Semi-Empirical Three-Dimensional Model of the Pneumatic Tyre Rolling over Arbitrarily Uneven Road Surfaces, Dissertation TU Delft, 2004

Schmidt, R. et al.: Physiologie des Menschen (2005)
Schmidt, Robert; Lang, Florian; Thews, Gerhard (Eds.) Physiologie des Menschen, 29. Edition, Springer Medizin Verlag, Heidelberg, 2005

Schollmaier, M.: Expert Interview - Quality of Driving Dynamics Area (2017)
Schollmaier, Mathias: Expert Interview - Quality of Opel Driving Dynamics Area Dudenhofen, Workshop: Bad Roads Well Built, 2017

Schöner, H. P.: Erprobung und Absicherung im dynamischen DS (2014)
Schöner, H. P.: Erprobung und Absicherung im dynamischen Fahrsimulator, in: 17. Kongress SIMVEC - Simulation und Erprobung in der Fahrzeugentwicklung 2014 : Berechnung, Prüfstands- und Straßenversuch ; Baden-Baden, 18. und 19. November 2014, VDI-Verl., Düsseldorf, 2014

Schöner, H.-P.: Expectations towards Driving Simulation (2018)
Schöner, Hans-Peter: Automotive Needs and Expectations towards Next Generation Driving Simulation, in: Kemeny, Andras et al. (Eds.): Proceedings of the Driving Simulation Conference 2018 Europe, Antibes, 2018

Schröder, D.: Regelung von Antriebssystemen (2015)
Schröder, Dierk: Elektrische Antriebe - Regelung von Antriebssystemen, 4. Edition, Springer Vieweg, Heidelberg, 2015

Seebold, L. A.: Masterthesis, Hexapod Regelung WMDS (2016)
Seebold, Lisa A.: Entwicklung einer Hexapod-Vertikaldynamikregelung für einen selbstfahrenden Fahrsimulator, Masterthesis
Technische Universität Darmstadt, Darmstadt, 2016

Slob, J. J. et al.: The Wall is the Limit (2009)
Slob, J. J.; Kuijpers, M. R. L.; Rosielle, P. C. J. N.; Steinbuch, M.: A New Approach to Linear Motion Technology: The Wall is the Limit, in: DSC 2009 Europe, INRETS-Renault, Arcueil, 2009

Swart, R. d.: Expert Interview - Bosch Dead Times (2017)
Swart, Rik d.: Expert Interview - Bosch Dead Times, Darmstadt, 2017

Tüschen, T. et al.: Design suspension dynamic driving simulator (2015)
Tüschen, T.; Kocksch, Felix; Rinnert, T.; Breitelschmidt, D.; Prokop, G.: Design of dual suspension kinematics for a highly dynamic driving simulator, in: Proceedings of the 18th ITI Symposium, Dresden, 2015

Tüschen, T. et al.: Suspensions Design of a WMDS (2016)
Tüschen, Thomas; Kocksch, Felix; Beitelschmidt, Denise; Prokop, Günther: “auto.mobile-driving simulator” – Suspensions Design of a Wheel-Based Driving Simulator, in: Pfeffer, Peter (Ed.): 7th International Munich Chassis Symposium 2016, Springer Fachmedien, Wiesbaden, 2016

Tüschen, T.: Diss., Konzeptionierung selbstfahrender Fahrsimulator (2018)
Tüschen, T.: Konzeptionierung eines hochimmersiven und selbstfahrenden Fahrsimulators, Dissertation Technische Universität Dresden, Dresden, 2018

VDI, Verein Deutscher Ingenieure: VDI 2057 - Ganzkörper-Schwingungen (2017)
VDI, Verein Deutscher Ingenieure: VDI 2057 - Einwirkung mechanischer Schwingungen auf den Menschen, Blatt 1: Ganzkörper-Schwingungen, Beuth Verlag, Berlin, 2017

Wagner, P.: Diss., Practical Feasibility WMDS (2018)
Wagner, Paul: Practical Feasibility and Functional Safety of a Wheeled Mobile Driving Simulator, Dissertation Technische Universität Darmstadt, Darmstadt, 2018

Winkel, K. N. de et al.: Perception of angular self-motion (2013)
Winkel, K. N. de; Soyka, F.; Barnett-Cowan, M.; Bülthoff, H. H.; Groen, E. L.; Werkhoven, P. J.: Integration of visual and inertial cues in the perception of angular self-motion, in: Experimental brain research (2), Issues 231, pp. 209–218, 2013

Zaichik, L. et al.: Acceleration perception (1999)
Zaichik, L.; Rodchenko, V.; Rufov, I.; Yashin, Y.; White, A.: Acceleration perception, in: Modeling and Simulation Technologies Conference and Exhibit, Portland,OR,U.S.A, American Institute of Aeronautics and Astronautics, Reston, Virigina, 1999

Zeeb, E.: Daimler's Driving Simulator (2010)
Zeeb, Eberhard: Daimler's New Full-Scale, High-dynamic Driving Simulator - A Technical Overview, in: Kemeny, Andras; Mérienne, Frédéric; Espié, Stéphane (Eds.): Proceedings of the Driving Simulation Conference Europe 2010, Paris, 2010

Zegelaar, P. W.: Diss., Dynamic response of tyres (1998)
Zegelaar, Peter W. A.: The dynamic response of tyres to brake torque variations and road unevennesses, Dissertation TU Delft, TU Delft, Delft, 1998

Zöller, C.: Masterthesis, Reifenmodell WMDS (2015)
Zöller, Chris: Implementierung eines Fahrdynamiksimulations-tauglichen Modells des Bandagenreifen des WMDS sowie Identifikation der relevanten Parameter, Masterthesis
Technische Universität Darmstadt, Darmstadt, 2015

Zöller, C. et al.: Preview Driving Surface Unevenness in WMDS (2018)
Zöller, Chris; Wagner, Paul; Lutwitzi, Melina; Winner, Hermann: Preview of Driving Surface Unevenness in Wheeled Mobile Driving Simulators, in: IEEE (Ed.): 2018 IEEE 21th International Conference on Intelligent Transportation Systems (ITSC), Maui, USA, 2018

Zöller, C. et al.: Vertical Dynamics WMDS (2019)
Zöller, Chris; Wagner, Paul; Winner, Hermann: Tires and vertical dynamics of wheeled mobile driving simulators, in: Transportation Research Part F: Traffic Psychology and Behaviour, Issues 61, pp. 69–83, 2019

Own Publications

Wagner, P.; Zöller, C..; Winner, H.: Safety Analysis for Wheeled Mobile Driving Simulators, in: Proceedings of the Driving Simulation Conference & Virtual Reality Conference & Exhibition Europe - DSC, September 7-9, Paris, France, 2016.

Zöller, C.; Wagner, P.; Winner, H.: Tire Concept Investigation for Wheeled Mobile Driving Simulators, in: Proceedings of the Driving Simulation Conference & Virtual Reality Conference & Exhibition Europe - DSC, September 7-9, Paris, France, 2016.

Wagner, P.; Zöller, C.; Albrecht, T.; Winner, H.: Power, Energy, and Latency Test Drives with the Wheeled Mobile Driving Simulator Prototype MORPHEUS, in: Proceedings of the Driving Simulation Conference & Virtual Reality Conference & Exhibition Europe - DSC, September 6-8, Stuttgart, Germany, 2017.

Zöller, C.; Wagner, P.; Lutwitzi, M.; Winner, H.: Preview of Driving Surface Unevenness in Wheeled Mobile Driving Simulators, in: IEEE (Ed.): 2018 IEEE 21th International Conference on Intelligent Transportation Systems (ITSC), November 4-7, Maui, USA, 2018.

Zöller, C.; Wagner, P.; Winner, H.: Tires and vertical dynamics of wheeled mobile driving simulators, in: Transportation Research Part F: Traffic Psychology and Behaviour, Issues 61, pp. 69–83, 2019.

Winner, H.; Zöller, C.: Fahrsimulatorkonzepte im Wandel, in: Bruder, R; Winner, H. (Ed.): Hands off, Human Factors off? Welche Rolle spielen Human Factors in der Fahrzeugautomation?, 9. Darmstädter Kolloquium Mensch und Fahrzeug, April 2-3, Darmstadt, Germany, 2019.

Zöller, C.; Müller, A.; Eggert, L.; Winner, H.; Abendroth, B.: Applicability of Head-Mounted Displays in Driving Simulation, in: Proceedings of the Driving Simulation Conference & Virtual Reality Conference & Exhibition Europe - DSC, September 4-6, Strasbourg, France, 2019.

Supervised Theses

Jiao, H.: Entwicklung eines Vertikaldynamikmodells des WMDS sowie Identifizierung des vertikaldynamischen Verhaltens, Masterthesis Nr. 596/15, 2016.

Angelov, E.; Dimitrov, D.; Dreier, S.; Gosewinkel, D.; Kratz, C.; Laumeyer, L.; Reichel, M.: Development of a Concept for a Competition Framework for Driverless Formula Student Cars, Advanced Design Project Nr. 70/16, 2016.

Albrecht, T.; Davoodi Memar, A.; Wilczynski, D.; Betancourt Bautista, M.A.; Huber, K.: Fahrwiderstands- und Energiebedarfsbetrachtung des MORPHEUS unter Berücksichtigung der speziellen Eigenschaften der Bandagenreifen, Advanced Design Project Nr. 72/16, 2016.

Kolmer, M.; McCloskey, S.; Morris, B.; Neu, T.; Steuerwald, A.; Szewczyk, D.: Development of a Concept for the Application of Pneumatic Tires in the MORPHEUS Prototype, Advanced Design Project Nr. 77/16, 2016.

Buehler, J.: Acoustic Optimization of the MORPHEUS' drivetrain, International Research Experience, 2014.

Schade, D.: Passive Systeme zur Beeinflussung des Übertragungsverhaltens fahrbahnerregter Schwingungen in Fahrzeugen, Forschungsseminar 155/16, 2016.

Xiaojing, H.: Aktive Systeme zur Beeinflussung des Übertragungsverhaltens fahrbahnerregter Schwingungen in Fahrzeugen, Forschungsseminar 156/16, 2016.

Kässens, A.: Modellbildung des Hexapod des MORPHEUS zur Untersuchung der Eignung für eine Vertikaldynamikregelung, Bachelorthesis Nr. 1264/16, 2016.

Le Floch, A.: Entwicklung eines Konzeptes zur Implementierung automatisierter Fahrfunktionen in ein Formula Student Electric Fahrzeug, Masterthesis Nr. 612/16, 2016.

Seebold, L.A.: Entwicklung einer Hexapod-Vertikaldynamikregelung für einen selbstfahrenden Fahrsimulator, Masterthesis Nr. 615/16, 2016.

Lutwitzi, M.: Entwurf eines Konzepts für eine Umfelderkennung für selbstfahrende Fahrsimulatoren, Bachelorthesis Nr. 1272/16, 2016.

Glatzki, F.: Untersuchung des Einflusses einer Trajektorienüberlagerung auf den Lenkleistungsbedarf eines selbstfahrenden Fahrsimulators, Bachelorthesis Nr. 1273/16, 2016.

Banic, M.; Kappes, A.; Karabulut, D.; Kerres, D.; Ladewig, L.; Mayer, P.: Entwicklung einer Anlage zur Vermessung realer Fahrbahnprofile in vertikaler Richtung, Advanced Design Projekt Nr. 82/16, 2016.

Bonakdar, F.: Verbesserung der Bewegungsregelung eines selbstfahrenden Fahrsimulators, Bachelorthesis Nr. 1275/16, 2016.

Betschinske, D.: Untersuchung von Methoden zur Verringerung des Lenkleistungsbedarfs des selbstfahrenden Fahrsimulators, Bachelorthesis Nr. 1287/16, 2017.

Perschbacher, R.: Untersuchung der Eignung eines Hexapods zur Maskierung von Störeinflüssen aus der Lenkung an einem selbstfahrenden Fahrsimulator, Bachelorthesis Nr. 1288/17, 2017.

Mehren, M.: Entwicklung von Steuerungen und Regelungen für bestehende Systemarchitekturen einer Hexapod Vertikaldynamikregelung, Masterthesis Nr. 643/17, 2017.

Hein, E.; Lamrabet, Y.; Niess, S.; Schmeiß, M.: Entwicklung des selbstfahrenden Fahrsimulators MORPHEUS 2.0, Advanced Design Project Nr. 100/17, 2017.

Sallehsari, K.: Identifikation der Leistungsfähigkeit einer Umfelderfassungskamera für selbstfahrende Fahrsimulatoren, Bachelorthesis Nr. 1292/17, 2017.

Jargon, E.: Entwicklung von Methoden zur Bewegungsraumadaption des Motion Cueing Algorithmus von WMDS, Bachelorthesis Nr. 1299/17, 2018.

Eggert, L.: Untersuchung der Eignung von Head-Mounted Displays für die Anwendung in Fahrsimulatoren, Masterthesis Nr. 666/17, 2018.

Lutwitzi, M.: Entwicklung einer Sicherheitsarchitektur für einen selbstfahrenden Fahrsimulator, Masterthesis Nr. 733/19, 2019.